

TAILORING STRUCTURES USING STOCHASTIC
VARIATIONS OF STRUCTURAL PARAMETERS

Von der Fakultät Bauingenieurwesen und Geodäsie der
Gottfried Wilhelm Leibniz Universität Hannover
zur Erlangung des Grades

DOKTOR-INGENIEUR
DR.-ING

genehmigte Dissertation von
IR. SANDER FRISO VAN DEN BROEK

2023

HERAUSGEBER:

Prof. Dr-Ing. habil. Raimund Rolfes
Institut für Statik und Dynamik
Gottfried Wilhelm Leibniz Universität Hannover
Appelstraße 9A
30167 Hannover
Tel. 0511 - 762 3867
Fax. 0511 - 762 2236
www.isd.uni-hannover.de
info@isd.uni-hannover.de

REFERENT:

Prof. Dr-Ing. habil. Raimund Rolfes
Institut für Statik und Dynamik
Gottfried Wilhelm Leibniz Universität Hannover

KORREFERENT:

Prof. Dr-Ing. Benedikt Kriegesmann
Strukturmechanik im Leichtbau
Technische Universität Hamburg

TAG DER PROMOTION:

14.04.2023

© 2023 Sander Friso van den Broek
Institut für Statik und Dynamik

Alle Rechten, insbesondere das der Übersetzung in fremde Sprachen vorbehalten. Ohne Genehmigung des Autors ist es nicht gestattet, dieses Heft ganz oder teilweise auf fotomechanischem, elektronischem oder sonstigem Wege zu vervielfältigen.

ISSN: 1862-4650

To my family, It, Something, and No one; Everything is finally done...

EIDESSTATTLICHE VERSICHERUNG

Ich erkläre hiermit, dass ich

- 1.) die Regeln der geltenden Promotionsordnung kenne und eingehalten habe und mit einer Prüfung nach den Bestimmungen der Promotionsordnung einverstanden bin,
- 2.) die Dissertation selbst verfasst habe, keine Textabschnitte von Dritten oder eigener Prüfungsarbeiten ohne Kennzeichnung übernommen habe und alle von mir benutzten Hilfsmittel und Quellen in meiner Arbeit angegeben habe,
- 3.) Dritten weder unmittelbar noch mittelbar geldwerte Leistungen für Vermittlungstätigkeiten oder für die inhaltliche Ausarbeitung der Dissertation erbracht habe,
- 4.) die Dissertation noch nicht als Prüfungsarbeit für eine staatliche oder andere wissenschaftliche Prüfung eingereicht habe,
- 5.) nicht die gleiche oder eine in wesentlichen Teilen ähnliche Arbeit und auch nicht eine andere Arbeit bei einer anderen Hochschule als Dissertation eingereicht habe,
- 6.) damit einverstanden bin, dass die Dissertation auch zum Zwecke der Überprüfung der Einhaltung allgemein geltender wissenschaftlicher Standards genutzt wird, insbesondere auch unter Verwendung elektronischer Datenverarbeitungsprogramme.

Hannover, 14.04.2023

Sander F. van den Broek

ABSTRACT

Imperfections, meaning deviations from an idealized structure, can manifest through unintended variations in a structure's geometry or material properties. Such imperfections affect the stiffness properties and can change the way structures behave under load. The magnitude of these effects determines how reliable and robust a structure is under loading.

Minor changes in geometry and material properties can also be added intentionally, creating a more beneficial load response or making a more robust structure. Examples of this are variable stiffness composites, which have varying fiber paths, or structures with thickened patches.

The work presented in this thesis aims to introduce a general approach to creating geodesic random fields in finite elements and exploiting these to improve designs. Random fields can be assigned to a material or geometric parameter. Stochastic analysis can then quantify the effects of variations on a structure for a given type of imperfection.

Information extracted from the effects of imperfections can also identify areas critical to a structure's performance. Post-processing stochastic results by computing the correlation between local changes and the structural performance result in a pattern, describing the effects of local changes. Perturbing the ideal deterministic geometry or material distribution of a structure using the pattern of local influences can increase performance. Examples demonstrate the approach by increasing the deterministic (without imperfections applied) linear buckling load, fatigue life, and post-buckling path of structures.

Deterministic improvements can have a detrimental effect on the robustness of a structure. Increasing the amplitude of perturbation applied to the original design can improve the robustness of a structure's response. Robustness analyses on a curved composite panel show that increasing the amplitude of design changes makes a structure less sensitive to variations. The example studied shows that an increase in robustness comes with a relatively small decrease in the deterministic improvement.

Keywords— Random fields, Robust design, Geodesic random field, Thickness tailoring, Fiber steering

ZUSAMMENFASSUNG

Imperfektionen, d. h. die Abweichungen von einer idealisierten Struktur, können sich durch unbeabsichtigte Variationen in der Geometrie oder den Materialeigenschaften einer Struktur ergeben. Solche Imperfektionen wirken sich auf die Steifigkeitseigenschaften aus und können das Verhalten von Strukturen unter Last verändern. Das Ausmaß dieser Auswirkungen bestimmt, wie zuverlässig und robust eine Struktur unter Belastung ist.

Kleine Änderungen der Geometrie und der Materialeigenschaften können auch absichtlich eingebaut werden, um ein verbessertes Lastverhalten zu erreichen oder eine stabilere Struktur zu schaffen. Beispiele hierfür sind Verbundwerkstoffe mit variabler Steifigkeit, die unterschiedliche Faserverläufe aufweisen, oder Strukturen mit lokalen Verstärkungen.

Die in dieser Dissertation vorgestellte Arbeit zielt darauf ab, einen allgemeinen Ansatz zur Erstellung geodätischer Zufallsfelder in Finiten Elementen zu entwickeln und diese zur Verbesserung von Konstruktionen zu nutzen. Zufallsfelder können Material- oder Geometrieparametern zugeordnet werden. Die stochastische Analyse kann dann die Auswirkungen von Variationen auf eine Struktur für eine bestimmte Art von Imperfektion quantifizieren.

Die aus den Auswirkungen von Imperfektionen gewonnenen Informationen können auch Bereiche identifizieren, die für das Tragvermögen einer Struktur kritisch sind. Die Auswertung der stochastischen Ergebnisse durch Berechnung der Korrelation zwischen lokalen Veränderungen und Strukturtragvermögen ergibt ein Muster, das die Auswirkungen lokaler Veränderungen beschreibt. Die Perturbation der idealen deterministischen Geometrie oder der Materialverteilung einer Struktur unter Verwendung des Musters der lokalen Einflüsse kann das Tragvermögen erhöhen. Anhand von Beispielen wird der Ansatz durch die Erhöhung der deterministischen (ohne Imperfektionen) linearen Knicklast, der Lebensdauer und des Nachknickverhaltens von Strukturen aufgezeigt.

Deterministische Verbesserungen können sich zum Nachteil der Robustheit einer Struktur auswirken. Eine Vergrößerung der Amplitude der auf den ursprünglichen Designentwurf angewendeten Perturbation kann die Robustheit der Reaktion einer Struktur verbessern. Robustheitsanalysen an einer gekrümmten Verbundplatte zeigen, dass eine Struktur durch eine Vergrößerung der Amplitude der Entwurfsänderungen weniger empfindlich

gegenüber Abweichungen wird. Das untersuchte Beispiel zeigt, dass eine Erhöhung der Robustheit mit einem relativ geringen Verlust der deterministischen Verbesserung einhergeht.

Schlüsselwörter— Zufallsfelder, robuster Entwurf, geodätisches Zufallsfeld, Dickenanpassung, Fasersteuerung

ACKNOWLEDGEMENTS

I would like to express my sincere gratitude to all those who have supported me throughout my journey to completing this Ph.D thesis.

First and foremost, I would like to like to thank Prof. Raimund Rolfes for his mentorship and valuable insights. I would also like to thank Eelco Jansen, for his invaluable guidance, encouragement, and support throughout this research.

My gratitude also goes to the following individuals that hosted and supported me at the University of Bristol: Prof. Paul Weaver, Prof. Alberto Pirrera, Sergio Minera, and Mayank Patni, for their insightful comments and suggestions. I would also like to thank Gerd-Jan Schreppers and Tanvir Rahman at DIANA FEA, Johannes Wolff and Christian Hühne at DLR for their support and assistance with my research. A special mention to Prof. Joaquim Martins and Prof. Turaj Ashuri that helped me in deciding to apply for doctoral positions and helped me in the process.

I am deeply grateful to my parents, Eelco and Pam, and my siblings, Lucas and Lisa, for their unwavering support and encouragement throughout my academic journey.

I would also like to thank my friends at ISD: My old office mates, Mehdi, Ayan and Anilkumar, for being able to put up with my constant joking around and being great sparring partners when I needed someone to talk to. In addition, I must acknowledge the friends I have made at the institute, including Aamir, Andreas, Maggie, Marlene, Muzzamil, Nabeel, Stavroula, Stefan and Susanne, for their friendship and support.

Of course, I have to extend my thanks to my friends outside of ISD that I met in Hannover, or before my move to Hannover: Annika, Bianca, Dany, David, Dhansashri, Ethan, Hannie, Henk-Jan, Ilze, Jeroen, Koen, Leyla, Lily, Nena, Ooy, Rachel, Raphaël¹, Rick, Severine, Steffi, Thomas, and all I others

¹ May he and his family rest in peace.

I forgot to mention for their encouragement, support, and understanding.

My research was funded by the European Commission, through Marie Curie Actions, and the German research foundation; I would like to thank both funders for their financial contribution, making this research possible. As part of the Fullcomp ITN, I made friends all over Europe; I would like to thank Alberto, Gabriele, Georgios, Guohong, Ibrahim, Lorenzo, Pietro, and Yanchuan for their friendship and support.

Lastly, I have made many great friends since moving away from Hannover: Charlie, Gianni, Jibs, Vale, Joel "Jugs", Roman, Sara, Sergio and all the others. They have been very supportive and understanding in the final phase of the Ph.D journey, thank you.

Thank you all for being a part of my academic journey and for your contributions to this thesis.

Sander

CONTENTS

Eidesstattliche Versicherung	v
Abstract	vii
Zusammenfassung	ix
List of Figures	xiv
1 INTRODUCTION	1
1.1 Background and motivation	1
1.2 Literature survey	3
1.2.1 Variations due to manufacturing of thin-walled structures	3
1.2.2 Stochastic Finite Element Analysis	10
1.2.3 Tailoring thin-walled structures	21
1.2.4 Sensitivity and robustness analysis of structures	24
1.3 Research aims and objectives	30
1.4 Structure of thesis	32
2 PAPER A: GENERATING GEODESIC FIELDS	35
3 PAPER B: ENHANCING STRUCTURES	55
4 PAPER C: IMPROVING FATIGUE LIFE OF PRINTED STRUCTURES	71
5 PAPER D: ROBUST BUCKLING LOAD IMPROVEMENT OF A COMP. STRUCTURE	87
6 SUMMARY AND FUTURE WORK	101
6.1 Summary	101
6.2 Future work	103
BIBLIOGRAPHY	105
CURRICULUM VITAE	127
DISSEMINATION	129
MITTEILUNGEN DES INSTITUTS FÜR STATIK UND DYNAMIK DER LEIBNIZ UNIVERSITÄT HANNOVER	133

LIST OF FIGURES

- Figure 1.1 Example of laying temperature affecting void content of a carbon/epoxy composite [36], reprinted with permission from Elsevier. 5
- Figure 1.2 Fiber trajectories reconstructed using x-ray tomography [40] ($1\text{px}=1.1\ \mu\text{m}$), reprinted with permission from Elsevier. 6
- Figure 1.3 Fiber waviness measured using computed tomography (CT) scans and generated using extracted spectral density [53–55]. 8
- Figure 1.4 Imperfection pattern and thickness measurement of a cylinder, scaled by a factor 100 [65], reprinted with permission from Elsevier. 10
- Figure 1.5 Comparison between correlation functions. 13
- Figure 1.6 Schematic representation of field P generated using TBM [110], reprinted with permission from John Wiley and Sons. 17
- Figure 1.7 Continuous transition of a FGM between material elements [137], reprinted with permission from Elsevier. 22
- Figure 1.8 Effects of local thickened patches on the postbuckling response. Zero, partial and fully connected designs refer to how the thickened (red areas in sub-figure a) are connected to each other [4], reproduced with permission from World Scientific. 24
- Figure 1.9 Definitions of structural robustness and reliability [153]. Robustness relates to the area near the mean value of the pdf. Reliability relates to the tail-end of a pdf, moving towards the other tail as reliability decreases, reprinted with permission from Elsevier. 25
- Figure 1.10 Comparison of RDO and RBDO approaches [154], reproduced with permission from Elsevier. 29

INTRODUCTION

If you thought that science was certain - well, that is just an error on your part.

— Richard P. Feynman

1.1 BACKGROUND AND MOTIVATION

INDUSTRY design practices make many simplifications and assumptions in daily engineering practice. Simplifications made during structural design include homogeneity of material properties, simplifying boundary conditions, joints between parts, and idealizing geometry to a nominal shape. Making these assumptions simplifies the analysis of structures significantly, as uncertainties are often not quantifiable to designers.

Production processes are not ideal and introduce imperfections. Material properties can be affected by chemical composition, curing, annealing, internal stresses, and material orientation. Some manufacturing processes introduce engineered changes in material properties, such as quenching hot steel, promoting the formation of martensite crystals. However, most variations introduced are unintended and can have a detrimental effect on the structure's performance.

Magnitude and type of variations are highly dependent on the manufacturing processes employed. More expensive and slow production processes are often capable of generating structures with tighter tolerances at a monetary cost. A common practice in engineering is to determine a safety factor empirically and over-design a structure making sure it exceeds the requirements by the set factor.

Using a safety factor does have two significant drawbacks. Designs using a safety factor can be overly conservative, making structures unnecessarily heavy and costly. A safety factor also disregards any insights that can be developed by further analyzing the effects of (local) variations.

Another approach to the design process is to accept variations or tailor these variations to improve the structure's performance. Engineered variations in material properties or minor changes in geometry have already seen widespread use. How structures can be tailored is heavily dependent on the material and manufacturing process used. For instance, within

fiber-reinforced composite structures, variable stiffness can be achieved by steering the fiber filaments during placement to provide different properties in different areas. Engineered stiffness distributions can also be achieved using functionally graded materials (FGM) to achieve an improvement in the mechanical response [1–3]. Structures manufactured through additive manufacturing processes also make it possible to easily tailor a structure’s geometry, thereby tailoring the stiffness. Tailoring can be achieved by varying the thickness, either empirically [4], using periodic functions [5] or by using arbitrary stepwise variations [6]. Another approach is to modify the ideal geometry, using seeded imperfections consisting of scaled mode shapes to make areas less critical to local failure triggered by structural instability [7–9].

Finding where to apply changes can be done by utilizing patterns that indicate how local changes of a parameter within a structure affect the performance. Finding these patterns of influence on local changes is not trivial, as this inherently involves many parameters to define local changes. Traditional optimization studies would have to deal with many variables and constraints to avoid discontinuities that are not manufacturable.

Structures optimized for a conventional deterministic objective can also be susceptible to unintended variations, as optimized designs usually intersect multiple design constraints on a feasibility (Pareto) front. Robust optimization techniques exist but are generally only suitable for traditional parametric optimization, which can be challenging to do with many variables that are also linked to each other.

Therefore, it is of interest to develop a generalized method to find patterns in which to apply these variations and evaluate the statistical response of designs subjected to imperfections. Patterns applied to perturb the original design have to make a tradeoff between deterministic performance and resilience to imperfections introduced during manufacturing or use.

Like traditional optimization approaches, the method aims to improve the performance of a structure. Traditional optimization approaches, however, do this by varying parameters to reach a deterministic optimum. The proposed method does not vary each parameter as an independent variable but instead finds patterns to vary a design parameter. Patterns can be analyzed for their sensitivity to imperfections using the same analysis process used to generate the pattern, making it possible to repeat the process or quantify the robustness of a perturbed design.

1.2 LITERATURE SURVEY

Work done by other authors defines the context in which this thesis should be interpreted. Literature related to imperfections, modeling imperfections, and tailoring using variations are discussed in this section.

1.2.1 *Variations due to manufacturing of thin-walled structures*

Manufacturing processes can affect the local material properties throughout a structure, as well as the finished geometry. These parameters can influence the global mechanical behavior of a structure, leading to variations in properties such as buckling load, fatigue life, stiffness, and stress levels [10–13].

1.2.1.1 *Mechanical properties and orientation*

Local variations in the material properties are very closely related to both the material and manufacturing process used. Both of these are highly dependent on the design of the manufactured (sub)component. Therefore, statistical properties and the distribution of the material properties and geometric deviations are quite challenging to extract from real components, especially a priori.

Laser cutting is an example of a process that introduces local changes in mechanical properties. When materials, such as fiber-reinforced composites, are cut using a high-temperature process, the mechanical properties, such as shear strength, can be negatively impacted within the heat-affected zone [14].

Sufficient modeling and process tuning can make the size of the heat-affected zone well known. However, uncontrolled external parameters such as moisture content can still cause an unknown variance in the mechanical properties within the heat-affected zone [15]. In these cases, the material properties result from a combination of factors, generally unquantifiable, creating uncertainty in the effective material properties.

MECHANICAL PROPERTIES WITHIN ADDITIVE MANUFACTURING

Additive manufacturing (AM) refers to a range of methods to create a structure by selectively adding material to local parts of a structure. Materials can be metals, polymers, ceramic, or composite materials [16, 17]. Lindgren & Lundbäck [18] have had success in modeling certain metal AM

processes using computational welding models, but these are not suitable for all AM processes, which often do not use metals.

Fused Filament Fabrication (FFM) is the most popular AM method used to create polymer and composite structures. Manufacturing parameters' effect on the mechanical properties has been studied extensively for this approach [19–21]. The manufacturing parameters affect the material properties, as does the way a structure is built up. An inherent anisotropy exists in different manufacturing directions. Anisotropy can be exacerbated by varying the primary orientation between layers printed. Varying the layer orientation reduces the fused area between filaments, significantly reducing stiffness and strength in the build-up direction [22, 23].

UNIDIRECTIONAL FIBER-REINFORCED COMPOSITES

Within aerospace engineering composites typically refer to polymer matrix materials, reinforced with fibers, typically made out of glass or carbon. Fibers greatly increase the stiffness and strength in one direction, creating anisotropic material properties. Most structures do not have unidirectional stress and strains, requiring reinforcement in different directions. Structures can be assembled by layering laminas, which consist of tows¹ of unidirectional fibers. The stacking sequence and the laminas' orientation determine the laminate's stiffness and strength properties [24–26].

Multi-stage manufacturing processes introduce uncertainty and variability throughout laminate manufacture. Material imperfections of fiber-reinforced composites can be classified as interface defects, matrix defects, fiber misalignments or breakage. All of these types of imperfections or variations affect the strength, fatigue, and mechanical properties [27].

Interface defects occur when the interface between layers or fibers and the matrix material is not adequately infused or wetted. Air trapped between laminas can flatten during consolidation, resulting in unbound areas. Although significant variations in strength and fatigue life are to be expected, limited experimental data exists, though numerical analyses have been performed in recent years [28–30].

Matrix defects are caused by incomplete curing, or more commonly by voids introduced during manufacturing. Voids are small pockets of air trapped within the matrix [31]. Such pockets can affect the mechanical stiffness and the strength of the material [32]. Manufacturing and material parameters, such as the autoclave pressure, cure temperature, resin viscosity, and vacuum pressure, can affect the number of voids found in a structure

¹ A bundle of fibers impregnated with epoxy-resin.

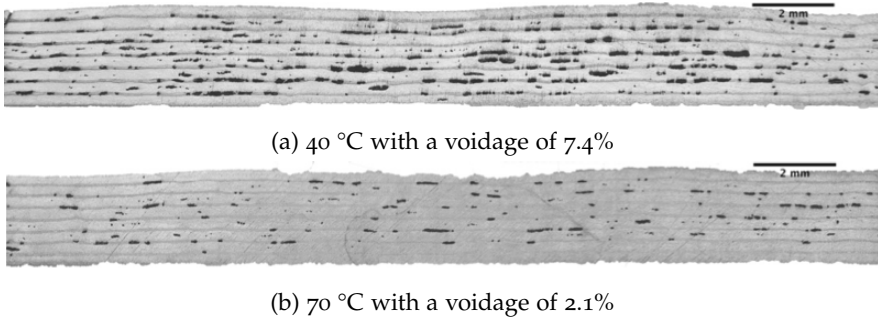


FIGURE 1.1: Example of laying temperature affecting void content of a carbon/epoxy composite [36], reprinted with permission from Elsevier.

[33–35]. Figure 1.1 shows the effect of laying temperature on the void content of unidirectional composites with layup laid by an automated layup and vacuum bag-only cure. The material consists of IMA fibers in a Hexcel M21 resin in an ATL-grade prepreg using single-sided backing paper. Increasing the temperature during the curing process dramatically reduces the void content in the composite.

Misalignment of fibers can occur due to several reasons. Misalignment of laminas inside a laminate can cause an entire layer to deviate from the desired orientation. Local variations within a prepreg are common and result in the fibers having a non-uniform direction in a layer [37, 38]. Such local variations are also possible due to local curvature, stretching, or compressing laminas locally [39]. Measured fiber misalignments of a section of glass-fiber reinforced composite material are shown in fig. 1.2.

Manufacturing using Automated Fiber Placement (AFP) or Automated Tape Laying (ATL) processes increases the manufacturing process's repeatability compared to hand-placed fibers. Both of these processes use robots to lay fibers on a structure in an automated fashion. Fiber orientation can vary significantly throughout a structure, depending on the manufacturing parameters [41]. Deviations from an ideal path can be unavoidable in complex structures, even in ideal manufacturing conditions. Defects should, therefore, best be understood and managed [42].

Deviations of the fiber path can occur at the tow level or within a tow. Paths a tow follows are defined as the center of a tow. Therefore, the tow's edges have a deviation of the fiber path, which depends on the tow width [43]. Decreasing the tow width can improve the fiber alignment while also slowing down production and increasing the number of gaps and overlaps

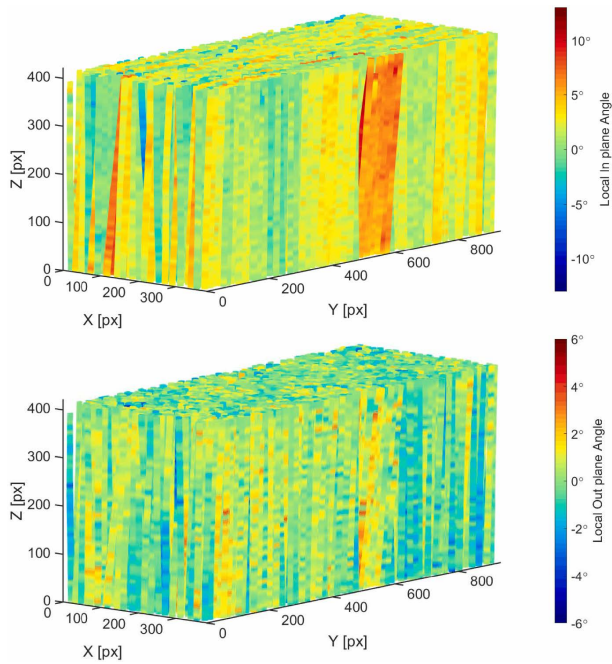


FIGURE 1.2: Fiber trajectories reconstructed using x-ray tomography [40] ($1\text{px}=1.1\ \mu\text{m}$), reprinted with permission from Elsevier.

in a structure [44]. Steering can also cause out-of-plane waviness, as tight turning radii can cause the fiber to buckle [39]. Stiffness and inertia effects of placement machines also can cause deviations in the designed structure [45, 46].

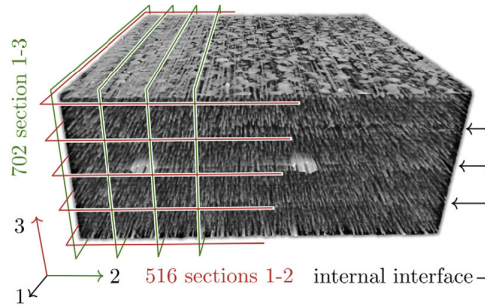
CHARACTERIZING COMPOSITE MATERIAL UNCERTAINTIES

Predicting the local variation in material properties a priori is very complex due to the large number of variables involved. Generating realistic distributions and patterns is therefore much easier using empirical results. Sriramula & Chryssanthopoulos [47] have attempted to quantify the spatial distribution of material properties using many coupons cut out of glass fiber reinforced (GFRP) panels. Sasikumar *et al.* [48] have done a similar series of experiments on a carbon fiber reinforced panel (CFRP). Such approaches can characterize a specific structure and production process but can not predict the influence different geometries and manufacturing process parameters can have on the distributions.

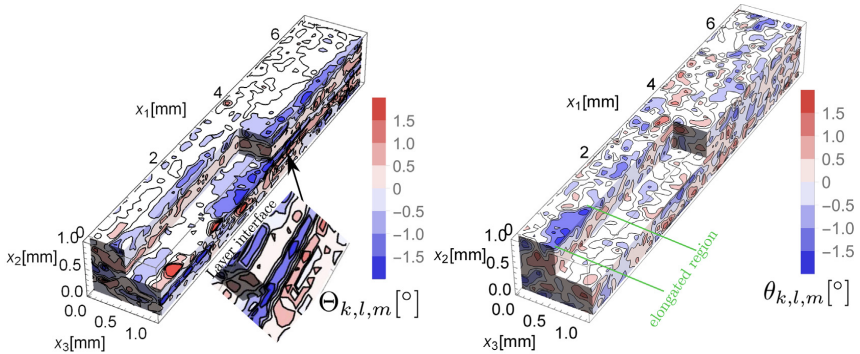
Experimental characterization using coupon testing is expensive and time-consuming, being a destructive form of determining spatial variability. Non-destructive testing (NDT) is a promising approach to mapping spatial variability in fiber orientation, void formation, and interface failures. NDT uses X-rays, ultrasonic measurements, MRI, and other techniques to inspect a structure without compromising its integrity. Using NDT enables engineers to validate the correct manufacturing of structures to tolerances. It also makes it possible to gain insight into the types and distribution of material imperfections resulting from those geometry and manufacturing processes [49–51]. Sutcliffe, Lemanski & Scott [52] have shown that fiber waviness measurements using x-ray imaging can reproduce destructive micrograph measurements. More recently Safdar *et al.* [53] used CT scans to analyze the fiber misalignments in 3D and used extracted spectral information to generate similar misalignments [54, 55], this process is illustrated in fig. 1.3. Daum *et al.* [56] looked into measured data of misalignment of non-crimp fabric laminates to determine their effects on compressive strength.

1.2.1.2 *Geometry and thickness variations in unstiffened cylindrical shells*

Production processes do not only affect the material properties of structures; they also affect the geometry. Pre-stress introduced through manufacturing processes, production tolerances, and other manufacturing parameters can cause deviations from the ideal geometrical shape. Thin-walled structures



(a) A volumetrically scanned image of fiber misalignment using a CT scans



(b) Constructed misalignments in vol- (c) Generated misalignment using spec-
 ume based on data extracted from tral information from measured data
 scans

FIGURE 1.3: Fiber waviness measured using computed tomography (CT) scans and generated using extracted spectral density [53–55].

can be affected by deviations in the mid-plane surface, as well as the local thickness.

Although not necessarily as significant as mid-plane deviations in geometry, deviations of thickness can also influence the structural response. Papadopoulos & Papadrakakis [57] studied the effect of local thickness variations on the structural stability of a cylinder, showing a coefficient of variation of up to 20% using a standard deviation of the thickness variation of 10% the original wall thickness. Thickness deviations occur due to manufacturing processes such as cold forming, welding, or tape laying, which can cause local thickness changes in composites due to gaps, overlaps, and fiber curvature.

Mid-plane surface deviations are a common field of study within the stability of structures. Imperfections such as these are also known as traditional imperfections. Experiments on the buckling of unstiffened cylindrical shells show a large amount of scatter in the results, with a significant decrease from the analytical result. Koiter [58] first identified the source of this spread as traditional imperfections, which are critical to cylindrical shells' stability.

Not all imperfect shapes have the same effect, and some are more critical than others [59]. Certain shapes are more likely to decrease the buckling load or increase local stresses. When analyzing the stability of a structure, imperfections are often added in the shape of linear buckling modes, which are very likely to trigger a decrease in buckling load. Applying imperfections in these shapes causes the buckling load to reduce significantly [60]. Research done by Meurer [61] has shown that worst-case shapes can be filtered into more primitive descriptions of geometry representing critical worst-case patterns that are not in the shape of a linear buckling mode.

Imperfection shapes in real structures can be measured through a variety of techniques [62]. Degenhardt *et al.* [63] used photogrammetry to map the imperfections of cylinders while using ultrasonic measurements for the thickness. Hilburger & Starnes [64] mapped the local thickness by measuring the distance from the inside to the outside of the cylinder. Most recently Lyssakow *et al.* [65] measured the inner and outer surfaces of a cylinder using lasers to increase the measurement resolution and accuracy. Zhao, Tootkaboni & Schafer [66] used lasers to measure geometric imperfections of cold-formed steel structures. An example of a laser scan-generated imperfection field is shown in fig. 1.4.

Over the years, a large number of imperfect shapes for cylinders have been cataloged and are accessible to researchers. Data has been published

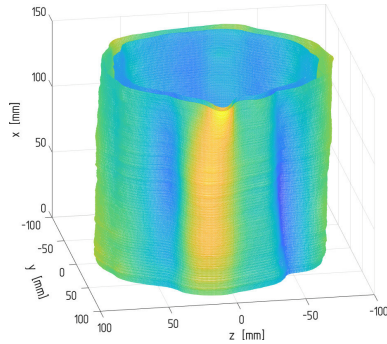


FIGURE 1.4: Imperfection pattern and thickness measurement of a cylinder, scaled by a factor 100 [65], reprinted with permission from Elsevier.

by groups at TU Delft [67, 68], Technion, and CalTech [69] are the most well known, with detailed scans of the imperfect shells being available, together with associated experimental data. Such data can be used to, for instance, find the manufacturing signature of a cylinder [70, sec. 5.6].

1.2.2 Stochastic Finite Element Analysis

Structural problems have been analyzed using analytical tools for most of history [71]. Analytical solutions, though elegant, are not feasible for complex structures, becoming too complex to solve without simplifying the problem.

Finite element analyses are a useful tool in computing deterministic structural problems. Structures with stochastic parameters, such as those discussed in section 1.2.1 can have these stochastic influences work out in their mechanical behavior. Such effects can affect the reliability of structures [72, 73]. Uncertainties are usually taken into account by using a safety factor in the design process, often, but not always, leading to overly conservative designs and not expanding the knowledge of the effects of specific variations [74, 75]. Quantifying and assigning a probability to failure of a (sub)component is pointed out by Tinsley Oden *et al.* [76] as one of the major research directions in computational mechanics.

Stochastic finite elements refer to a variety of approaches that can be used to quantify the effects of stochastic parameters on structures using finite elements [77–81]. Origins of the method are discussed within this section, as well as a variety of common approaches.

1.2.2.1 Finite Element Analysis

Numerical approaches which discretize structures into elements are better suited for such complex problems. Finite elements find their origins in the work of Courant *et al.* [82], in which a hollow shaft is discretized into triangles and analyzed using interpolating stress function. Pushed by the development of computers and aerospace developments in the 1950s the finite element approach was developed even further, leading to widespread adoption in industry as well as academia [83, 84].

Equations used in finite element analysis vary by application and problem [85]. Structural problems relating displacements with forces utilize a stiffness matrix \mathbf{K} . \mathbf{K} is an $n \times n$ matrix relating the forces and displacements acting on a structure as $\mathbf{K}\mathbf{u} = \mathbf{f}$, in which \mathbf{u} represent displacements and \mathbf{f} forces acting on the n degrees of freedom. Linear buckling analyses take stress-dependent stiffness effects into account through a geometric stiffness matrix \mathbf{K}_G , which allows for the solution of $\det(\mathbf{K} + \lambda_{cr}\mathbf{K}_G) = 0$, in which factor λ_{cr} is the load factor $\mathbf{f}_{cr} = \lambda_{cr}\mathbf{f}$, where \mathbf{f}_{cr} is the buckling load and \mathbf{f} an applied load.

Stochastic analysis introduces an additional variation to the matrices in the finite element problem. Changes to material properties result in the stiffness matrix \mathbf{K} being decomposed to a deterministic stiffness \mathbf{K}_0 , and a stochastic component $\Delta\mathbf{K}$, resulting in $(\mathbf{K}_0 + \Delta\mathbf{K})\mathbf{u} = \mathbf{f}$.

Assembly of the stochastic component can be done through a variety of approaches. Local variations are represented using a random field, which contains continuous or discretized values associated with a stochastic parameter. Mapping fields to the structure makes it possible to quantify their numerical effect on the stiffness matrix, resulting in the stochastic component $\Delta\mathbf{K}$. Approaches that can be used to generate fields, and map them to the structure are discussed in the following sections.

1.2.2.2 Random fields

Random fields, also known as stochastic fields, are fields in n dimensional space that spread a parameter in space with a specified statistical distribution. A large variety of methods exist which can be used to generate random fields [86–88]. Values of a random field are generally generated from a normal distribution with an associated mean (μ) value and standard deviation (σ). When other distributions are required normally distributed random variables can be transformed into other distributions using a non-linear mapping. A non-linear mapping links the normal distribution to that

of a different distribution. Transforming random variables does however introduce potential issues, such as differences in the power spectrum and autocorrelation function, requiring careful consideration [81].

Points within a field are correlated in space, this gives a relationship to a point's value and those in its vicinity. Using the expectation operator E , which equals the mean value when an infinite amount of stochastic samples are generated, the definition of correlation between variables X and Y is [89, ch. 10]

$$\rho_{X,Y} = \frac{\text{cov}(X,Y)}{\sigma_X\sigma_Y} = \frac{E[(X - \mu_X)(Y - \mu_Y)]}{\sigma_X\sigma_Y}, \quad (1.1)$$

which is bound between $-1 \leq \rho \leq 1$ where -1 would represent perfect inverse correlation ($y = -x$ for example) and 1 perfect correlation ($y = x$ for instance).

For the generation of fields and other spatial analyses, it is useful to switch to a more convenient relationship of distance with respect to correlation. The two most common definitions of distance-dependent correlation functions are

$$\rho_{exp} = e^{-\frac{\Delta L}{L_c}}, \quad (1.2)$$

$$\rho_{sexp} = e^{-\left(\frac{\Delta L}{L_c}\right)^2}, \quad (1.3)$$

where ΔL is the distance between points, and L_c is the correlation length, a characteristic length scale in which the correlation between points decreases, meaning they become less alike. The correlation functions in eqs. (1.2) and (1.3) are known as the exponential and squared exponential functions. When a correlation function of a field only depends on the distance between points it is known as *stationary*.

Other types of correlation functions exist but must satisfy Bochner's theorem, which is not always the case, particularly with geodesic distances instead of Euclidian distances [90]. The exponential function results in a pointier correlation to a point whereas the squared type has a smoother correlation surface from a point. The squared however does reduce correlation faster than the exponential type, as can be seen in fig. 1.5.

1.2.2.3 Field generation through orthogonal series expansion

Orthogonal series approaches state that a field can be defined in the form of a series [91]

$$f(x) = \bar{f}(x) + \sum_{n=1}^N \sqrt{\lambda_n} \xi_n \phi_n(x), \quad (1.4)$$

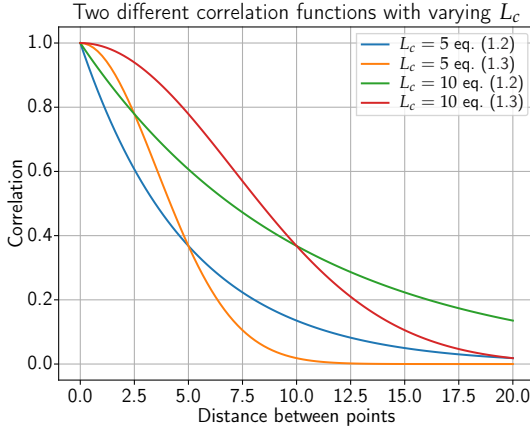


FIGURE 1.5: Comparison between correlation functions.

where $\bar{f}(x)$ is the mean value of the field, λ_n and ϕ_n the eigenvalues and eigenfunctions associated with an autocorrelation function, and value ξ_n is a Gaussian distributed random value. Obtaining the eigenvalues and eigenvectors to generate these random fields can be done through a variety of approaches, the most accurate being the Karhunen-Loève (KL) expansion [78].

Finding the eigenvectors and eigenvalues through the KL approach involves solving the Fredholm integral

$$\int_{\Omega} C_{ff}(x_1, x_2) \phi_n(x_1) dx_1 = \lambda_n \phi_n(x_2), \quad (1.5)$$

in which C_{ff} is the auto-covariance function of the field.

Truncating the series expansion is possible (i.e., setting N to a finite value), limiting the number of eigenvalues to those above a certain threshold can decrease the size of expansion without affecting the fidelity of the random fields. Removing degrees of freedom of a field can lead to the creation of constrained random fields, as shown by Lauterbach, Fina & Wagner [92].

Solving the necessary integral for the KL expansion can be difficult to do in general. Ghanem & Spanos [91] and Spanos & Ghanem [93] show closed-form solutions to a limited set of problems. Numerical solutions are required for most cases, as no closed-form solutions exist, and a variety of approaches exist to solve eq. (1.5) [94, 95].

1.2.2.4 Field generation through decomposition of covariance matrix

Alternatively, a discretized field can be created by decomposing an assembled correlation matrix. Davis [96] first described this approach to generate random fields, which can be implemented relatively easily while representing any correlation function satisfying Bochner's theorem. This is done by first assembling a correlation matrix as a symmetric positive definite matrix in which the correlation of points within the field are defined

$$R_{ij} = \frac{\text{cov}(y_i, y_j)}{\sigma_{y_i} \sigma_{y_j}} = \begin{bmatrix} 1 & \rho(y_1, y_2) & \dots & \rho(y_1, y_n) \\ \rho(y_2, y_1) & 1 & \dots & \rho(y_2, y_n) \\ \vdots & & \ddots & \vdots \\ \rho(y_n, y_1) & \rho(y_2, y_n) & \dots & \rho(y_n, y_n) \end{bmatrix}. \quad (1.6)$$

In which $\rho(y_i, y_j) = \rho(y_j, y_i)$, note that the correlation here can be calculated using eqs. (1.2) and (1.3).

The covariance matrix decomposition method (CMD) calculates a random set of vectors using

$$z_c(\vec{x}_i) = \mathbf{L}\chi, \quad (1.7)$$

in which \mathbf{L} is a decomposed version of the correlation matrix \mathbf{R} and χ , a normally distributed vector with zero mean and unit variance ($\chi \sim N(0, 1)$). This decomposition has to be done in such a way as to generate a vector \vec{x} with a mean of zero and unit variance. Taking the definition of correlation of eq. (1.1) and defining that variables X and Y have a mean value of zero and a unit variance the equation can be simplified to

$$\rho(X, Y) = \frac{\mathbf{E}[(X - \mu_X)(Y - \mu_Y)]}{\sigma_X \sigma_Y} = \mathbf{E}(XY). \quad (1.8)$$

If X and Y are uncorrelated to each other $\mathbf{E}(XY) = \rho = 0$, if they are correlated $\rho \in [-1, 0) \cup (0, 1]$. If X and Y are uncorrelated vectors the correlation is $\rho(X_i, Y_j) = \mathbf{E}(X_i Y_j) = \delta_{i,j}$, meaning that the correlation matrix $\mathbf{R} = \mathbf{I}$.

Using eq. (1.8) it is possible to show that \mathbf{R} can be decomposed into two matrices

$$\begin{aligned} \mathbf{R} &= \text{cov}[\vec{x}, \vec{x}] = \mathbf{E}(\vec{x}, \vec{x}^T) - 0 \cdot 0 \\ &= \mathbf{E}(\mathbf{L}\chi(\mathbf{L}\chi)^T) = \mathbf{L}\mathbf{E}(\chi\chi^T)\mathbf{L}^T = \mathbf{L}\mathbf{I}\mathbf{L}^T = \mathbf{L}\mathbf{L}^T. \end{aligned} \quad (1.9)$$

Decomposition can be done using different methods, the most common methods are through Cholesky or eigenmode factorization. Cholesky decomposition is found in many books in linear algebra and computation methods, e.g. [97, Ch. 7]. Eigenmode decomposition can be done as

$$\mathbf{R} = \mathbf{Q}\mathbf{\Lambda}\mathbf{Q}^T. \quad (1.10)$$

In which $\mathbf{\Lambda}$ is a diagonal matrix with the eigenvalues of \mathbf{R} on the diagonal, and \mathbf{Q} contains the eigenvectors of the matrix. Matrix \mathbf{L} can be extracted from this as

$$\mathbf{R} = \mathbf{Q}\hat{\mathbf{\Lambda}}\hat{\mathbf{\Lambda}}\mathbf{Q}^T = \mathbf{L}\mathbf{L}^T \rightarrow \mathbf{L} = \mathbf{Q}\hat{\mathbf{\Lambda}}, \quad (1.11)$$

in which $\hat{\mathbf{\Lambda}} = \text{diag}(\sqrt{\lambda})$. Term $\mathbf{Q}\hat{\mathbf{\Lambda}}$ can be seen as the equivalent of the term $\sum_{n=1}^N \sqrt{\lambda_n} \phi_n(x)$ in eq. (1.4), with N being the dimension of the correlation matrix (unless it is truncated to only use larger eigenvalues).

As the correlation matrix increases in size, it can become ill-conditioned. When this happens, the matrix is very close to being singular, which can cause numerical problems. In such cases, the Cholesky decomposition may fail, as eigenvalues that are (close to) zero might show up as negative values in the algorithm. Numerical results may include imaginary eigenvalues, which are not realistic. Setting eigenvalues that are below a certain threshold to zero can resolve this. A comparative study showed that eigenmode decomposition is slightly more accurate in generating the random fields [98, Sec. 4.2]. A further advantage is that random fields can be generated by only calculating the dominating eigenvectors [87, 99]. It is necessary to first analyze the error relative to the field size to make sure that the field is not unduly constrained.

Decomposition of the correlation matrix can become computationally intensive for large array sizes. Work has been done over the years to approximate this decomposition using a variety of numerical approaches. Dietrich & Newsam [100] approximated the square root of the covariance matrix using Chebyshev polynomials. Circular embedding can be used to more efficiently calculate the covariance matrix's eigenvalues using FFT, though it can only be used for rectangular or linear meshes [101, 102]. Another approach is to approximate the covariance matrix using a hierarchical matrix. Hierarchical matrices approximate some matrix segments while using exact representations for others [103, 104].

1.2.2.5 Spectral approaches to random field generation

Spectral methods use an expansion of periodic functions to generate a stochastic field. Methods include the Discrete Fourier Transform (DFT), Fast

Fourier Transform (FFT.) [105]. Both of these methods calculate the value at discrete points using a series expansion in the form of [105, 106]

$$f(x) = \sum_{n=0}^{N-1} A_n \cos(\kappa_n x + \phi_n^{(i)}), \quad (1.12)$$

in which $A_n = \sqrt{2S_{ff}(\kappa_n) \Delta\kappa}$, with S_{ff} being the spectral density function of the random field. Other terms are defined as $\kappa_n = n\Delta\kappa$, $\Delta\kappa = \kappa_u/N$ and $n = 0, 1, 2, \dots, N-1$. Parameter k_u is the cut-off wave number after which the power of the spectral density function S_{ff} can be considered zero for mathematical or physical reasons.

The DFT and FFT method are closely related, the FFT utilizing a faster way to calculate the A_n and θ_n coefficients. FFT methods perform well but can have issues if they are not used well [107, Ch. 2]. To generate a well-performing field it is necessary to extend the field beyond the structure, the extent of which depends on the spectral density of the field. Likewise, the resolution of the field must correlate well with the spectral density. A field with a low resolution can have issues related to the Nyquist limit of the function.

When experimental data exists defining the spectral density instead of the correlation function, the spectral density can be used to generate random fields using these types of approaches directly. An example is the work done by Safdar in which he recreates fiber waviness in composites using spectral density measured through CT scans [54].

1.2.2.6 Other approaches to generate random fields

A range of alternative methods also exist, such as the turning bands method (TBM), moving average (MA), and Local Average Subdivision Method (LAS). Details on their implementation can be found in this section's referred literature, which mainly focuses on giving a brief overview of the methods.

The turning bands method (TBM) is schematically shown in fig. 1.6 for 2D fields (3D fields are also possible). Unidimensional stochastic processes are generated on i lines that emanate from an origin point. Lines have an equal spacing θ_i between 0 and 2π . Values on the field P are calculated as a projected sum of these unidimensional processes. Extracting the value at position N is done by creating a position vector \mathbf{x}_N , which is projected on each line as $z_s(\mathbf{x}_N) = \frac{1}{\sqrt{L}} \sum_{i=1}^L z_i(\mathbf{x}_N \cdot \mathbf{u}_i)$, with \mathbf{u}_i being the unit direction vector of line i . The accuracy of the TBM method depends on the number of lines used and the domain's size, becoming computationally inefficient as

locally without the risk of aliasing or mirroring the random field, it requires computational effort during each iteration. There are also potential issues with the variance of the field and can be challenging to implement [108, 113].

1.2.2.7 Discretization and mapping of random fields

Fields generated using the methods described in sections 1.2.2.3 to 1.2.2.6 can be either continuous (e.g. spectral approaches) or discretized (e.g. CMD), depending on the approach used. Continuous fields can be evaluated using global-local coordinate transformations during matrix assembly. Discrete methods require points to be evaluated, which are defined during field generation.

Field discretization usually follows that of the underlying structure, either at its nodes or integration points. Such discretization often leads to unnecessary complexity and the amount of points. Unlike structural discretization, which is refined to increase accuracy in areas subject to stress gradients, random fields' optimal discretization depends on the correlation function used. Li & Der Kiureghian [114] analyzed the optimal discretization and found the range of $\frac{L_c}{10}$ to $\frac{L_c}{5}$ for the exponential definition (eq. (1.2)) and between $\frac{L_c}{4}$ to $\frac{L_c}{2}$ for other the squared exponential (eq. (1.3)) [114–116].

Points can be evaluated at integration points of elements, but this greatly increases the number of evaluated points. Evaluating nodes of the structure and interpolating values at integration points is one approach to reduce the size of the discretization, enabling the reuse of element shape functions already used in structural FEA. Interpolation of field values is done as

$$\hat{H}(\vec{x}) \sum_{i=1}^q N_i(\vec{x}) z_c(\vec{x}_i) \quad x \in \Omega_e, \quad (1.15)$$

where N_i is the shape function (usually polynomial), Ω_e is the domain of an element and \vec{x}_i are the values of the i^{th} node [117]. Expanding on this is the Optimal Linear Estimation (OLE) method, in which a continuous surface is made of the random field by minimizing the variance of the approximation error at each point [114].

Another approach is taken by the Spatial Average method (SA). In this method, the field over an element is described by the spatial average of the field over the element.

$$\hat{H}(\vec{x}) = \frac{\int_{\Omega_e} H(\vec{x}) d\Omega_e}{\int_{\Omega_e} d\Omega} = \bar{z}_c(\vec{x}_c) \quad (1.16)$$

This creates stepwise discontinuities along the boundaries of the elements [117]. There are a few limitations to this method, its nature makes it very hard to be used for anything other than Gaussian distributions [118]. The averaging process will also reduce the variance in the spatially averaged field [86, sec. 7.6],[77].

It should finally be noted that not all discretization methods can be combined with all random field generation methods. The CMD method is easy to combine with the OLE and SA methods. The OLE uses an eigendecomposed covariance matrix to find the optimal shape functions, which is also used in the CMD method. Similarly, the SA method can be easy to implement in the CMD, as it can use the covariance between two local averages. The LAS method implicitly utilizes the SA method in its refining process. It is also possible to combine the FFT method with the SA method, though it is not as straightforward [119].

1.2.2.8 Second moment estimation of structural response

Using random fields can make it possible to numerically analyze the effects of spatially distributed variations in the structure. The reliability of the structure is the main topic of most stochastic analyses. Mathematically this involves estimating the first (mean) and second (variance) moments of the structural response. Three main approaches exist to quantify a structure's reliability, which can generally be quantified as a scalar characterizing a structure, such as maximum displacement, buckling load, and maximum stress.

The most straightforward way of estimating the first and second moments of a stochastic process is through sampling n analyses and analyzing their statistics. Called a Monte-Carlo analysis, it is considered the most straightforward approach to finding the statistical moments while also being quite robust [120, 121]. The standard Monte Carlo method estimates the mean and variance of a stochastic process $f(i)$ using n samples as

$$\bar{f} = \frac{1}{n} \sum_{i=1}^n f(i),$$

$$s^2 = \frac{1}{n-1} \sum_{i=1}^n (f(i) - \bar{f})^2.$$

Estimating the number of samples N required to converge to accurate values for the mean and variance is not trivial and depends on both the structure analyzed and the accuracy required. Increasing the number of samples increases the computational cost of the analysis, limiting large complex analyses. Several strategies exist to reduce the computational time in Monte Carlo analyses [81, ch. 4] [79].

One approach is to reduce the variance of the samples. Doing this requires some knowledge of the statistical response. When low-probability responses are of interest, selectively sampling areas of interest can increase the resolution of the statistics quite effectively. Such an approach is called importance sampling and requires some knowledge of the statistical distribution, for instance, by running a limited amount of standard Monte Carlo samples [122].

When the distribution is unknown, another approach is to spread the samples more effectively, making sure they are not too similar to previous ones. Creating bins of equal probability samples can be generated in limited probability density function areas, creating a lower variance and better fit to stochastic analyses. Spreading out samples in such a manner is called Latin Hypercube Sampling (LHS) [123]. Line sampling is another approach that attaches an importance direction to more effectively sample a stochastic problem without a prior estimate of variance [124].

Instead of analyzing a problem with a Monte Carlo analysis, it is also possible to use alternative approaches. The perturbation method uses a Taylor expansion of a stochastic finite element matrix in the form

$$K(\mathbf{a}) = K_0 + \sum_{i=1}^N K_i^I a_i + \frac{1}{2} \sum_{i=1}^N \sum_{j=1}^N K_{ij}^{II} a_i a_j + \dots, \quad (1.17)$$

where K^I and K^{II} are the partial derivatives $K_i^I = \left. \frac{\partial K}{\partial a_i} \right|_{\mathbf{a}=0}$ and $K_{ij}^{II} = \left. \frac{\partial^2 K}{\partial a_i \partial a_j} \right|_{\mathbf{a}=0}$ and \mathbf{a} a random vector with N entries. Similar expansions are also used for the displacement and load vectors.

Computing the derivatives can be computationally intensive, particularly for systems with many stochastic parameters N . Estimates of the variance work well for small coefficients of variation but can deviate due to the nature of the Taylor expansion. Including higher-order terms can improve the accuracy but comes at the cost of disproportionate computational expense [125].

Kriegesmann *et al.* [126] used finite differences to numerically compute the derivatives of an objective function created through a Mahalanobis transformation of measured outputs. Using this semi-analytical approach, it was possible to quickly estimate the statistical moments of the structure being analyzed, composite cylindrical shells [127, 128] and panels [129] in this case.

Spectral stochastic finite element method (SSFEM) first introduced by Ghanem & Spanos [91] directly incorporates the KL approach of eq. (1.4) allowing normally distributed variations to be incorporated in the stiffness matrix generation as

$$\mathbf{k}^e(\theta) = \mathbf{k}_o^e + \sum_{i=1}^{\infty} \mathbf{k}_i^e \xi_i(\theta) \quad (1.18)$$

where \mathbf{k}_o^e is the mean element stiffness matrix and \mathbf{k}_i^e a deterministic matrix defined as $\mathbf{k}_i^e = \sqrt{\lambda_i} \int_{\Omega_e} \varphi_i(\mathbf{x}) \mathbf{B}^T \cdot \mathbf{D}_o \cdot \mathbf{B} d\Omega_e$, with \mathbf{B} being the strain-displacement matrix, and \mathbf{D}_o the mean value of the constitutive (elasticity) matrix. Assembly of the stiffness matrix leads to the equilibrium equation

$$\left[\mathbf{K}_o + \sum_{l=1}^{\infty} \mathbf{K}_l \xi_l(\theta) \right] \mathbf{u}(\theta) = \mathbf{F} \quad (1.19)$$

with $\mathbf{u}(\theta)$ being a random vector of nodal displacements. Obtaining these nodal displacements should be done by solving eq. (1.19), however no closed-form solution exists to this problem. Solutions are generally obtained by using Wiener chaos polynomials [130]. Material and geometric nonlinearities can not be analyzed with SSFEM at this time, nor has any other field generation approach than the KL-expansion been used thus far.

When variables are not normally distributed they can be represented using a polynomial chaos expansion

$$\mathbf{K}(\theta) = \mathbf{K}_o + \sum_{i=0}^M \hat{\mathbf{K}}_i \Psi_i(\theta), \quad (1.20)$$

where M is the total number of chaos polynomials, $\hat{\mathbf{K}}_i$ the deterministic fluctuation matrix, and $\Psi_i(\theta)$ the polynomial basis function acting on random variables θ .

1.2.3 Tailoring thin-walled structures

Variations discussed in section 1.2.1 refer to unintended deviations from an idealized design, subject to stochastic analyses described in section 1.2.2.

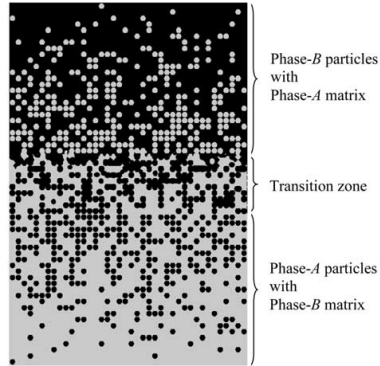


FIGURE 1.7: Continuous transition of a FGM between material elements [137], reprinted with permission from Elsevier.

Variations in material properties or local geometry can also be intentional. When material properties are altered locally by, for instance, changing the composition, these are called functionally graded materials. Effective material properties can also be altered by altering the orientation of orthotropic materials, for instance, by changing the fiber orientation in an FRP. Local changes to the geometry by slightly perturbing the ideal geometry or thickness can also tailor a structure's response. This section presents an overview of different engineered variations that exist.

1.2.3.1 *Functionally graded materials*

Functionally graded materials (FGM) constitute a type of material in which the composition changes spatially throughout a structure. Transitions can be continuous or discontinuous (fig. 1.7), depending on the materials and the manufacturing process used. Mechanical, electrical, or thermal properties can be optimized to improve a structure [131–134]. FGM consist of different types of material, such as metal-ceramic, metal-metal, polymer-ceramic

Many manufacturing processes exist to create FGM [134, 135]. The majority of these processes limit the variability to a single direction, such as methods that use centrifugal force, while other approaches, such as additive manufacturing, allow a great deal of design freedom in the topological gradation [136].

1.2.3.2 *Fiber paths in fiber-reinforced composite structures*

Automated fiber placement (AFP) makes it possible to steer tows of fibers along a path during the manufacturing process of a composite [138]. Changing the fiber angle of a lamina changes the stiffness properties of a laminate spatially, potentially improving a structure's behavior. Gurdal & Olmedo [139] first coined the term variable stiffness composites (VSC) to refer to these types of structures.

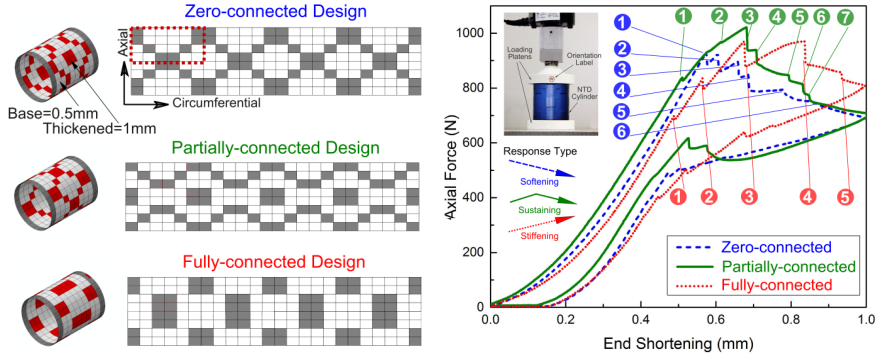
Clever use of varying stiffness can increase the strength of a structure [140], or increase the buckling load of structures [141–143]. Combining pre-stress, it is also possible to create structures with multiple equilibria [144, 145]. Recent work by Lincoln *et al.* [146] showed that varying the fiber angle in a cylinder can result in a structure more insensitive to geometric imperfections.

1.2.3.3 *Geometry and thickness of unstiffened shell structures*

Local thickness changes result in stiffness properties that vary along with the topology of a structure [147]. Townsend & Kim [148] used topology optimization to improve the buckling load of shell structures by optimizing the shape of thickened patches. Results showed that while increasing the buckling load, compliance is also increased, resulting in a necessary trade-off in the optimized solution. Non-uniform thickened patches were used by Hu & Burgueño [4] to control the post-buckling response of a cylinder, which were then analyzed using 3D printed specimens, patch patterns and experimental responses are shown in fig. 1.8. Similarly, Steltner *et al.* [149] optimized local thickness of a stiffened panel, improving both deterministic and robust performance in a fully geometrically nonlinear analysis.

Adding small variations to structures can tailor the behavior of a structure. Hu & Burgueño [9] controlled the post-buckling path of a cylinder by adding seeded geometric imperfections in the shape of linear buckling modes. Cox *et al.* [8] showed that it is possible to nudge structures towards a certain post-buckling path, and thereby reduce the sensitivity towards imperfections [4, 150].

Work done by Minera *et al.* [151] and Minera [152] demonstrates how deterministic improvements can be achieved by performing element-wise variations and mapping sensitivities. Sensitivities obtained this way are also not necessarily continuous but indicate which parts of a structure contribute most to the stiffness. Using these relative contributions to find locations,



(a) Thickened sections on cylinders, (b) Post-buckling response of tested cylinders, shaded areas are twice as thick as unshaded areas markers indicate critical events in the post-buckling path

FIGURE 1.8: Effects of local thickened patches on the postbuckling response. Zero, partial and fully connected designs refer to how the thickened (red areas in subfigure a) are connected to each other [4], reproduced with permission from World Scientific.

cutouts were added to a structure without significantly influencing the structure’s performance, thereby reducing the mass.

1.2.4 Sensitivity and robustness analysis of structures

Stochastic analysis of structures can help quantify structures’ effects on randomly distributed structural parameters in a structure. Quantifying the distribution of an objective function relative to set inputs helps determine the structure’s robustness and reliability.

The terminology used in stochastic analysis and structures’ reliability can be ambiguous from the terminology used in other fields. To clarify terms, the definitions used in [153, 154] are used within this thesis.

Uncertainty can refer to insufficient knowledge of a parameter or its inherent variability. This uncertainty introduces variability in the system, which can affect performance. Structures that are tolerant to variations of the structure or environment are called *robust*. When analyzing the chance of failure or another incident to occur, the *reliability* of a structure is analyzed. Reliability quantifies the chance that a parameter will drop below or climb over a limit state. In the probability density function (pdf) of a response, the

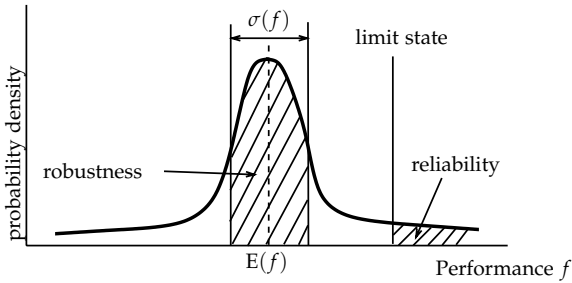


FIGURE 1.9: Definitions of structural robustness and reliability [153]. Robustness relates to the area near the mean value of the pdf. Reliability relates to the tail-end of a pdf, moving towards the other tail as reliability decreases, reprinted with permission from Elsevier.

robustness focuses on the variance around the expectation (mean) value, while reliability affects values at the pdf's tails, as is illustrated in fig. 1.9.

Section 1.2.4.1 discusses examples of stochastic analyses done on structures to quantify their variability under a set of uncertainties. Improvements to structures are discussed in section 1.2.4.2, starting with defining design objectives and then discussing methods that can be used to improve the objective's value.

1.2.4.1 Uncertainty quantification of shell structures

Quantifying the effects of random variations makes it possible to evaluate the robustness and reliability of a structure. Stochastic analysis techniques have been used on a wide array of structures in order to quantify their responses.

Papadopoulos has published a wide range of reference results, analyzing local variations in thickness and material properties of a cylindrical panel [155] and cylindrical shell [57]. Later extensions have introduced imperfect load introduction [156] and non-Gaussian distributions [157].

Material property variations analyzed by Shang & Yun [158] quantify the effects Young's modulus variation has on flat panels, circular segments, and a retaining wall example. Analysis of variability of functionally graded materials has recently been performed by Do *et al.* [159], using two random fields to simulate both materials. Geodesic random fields used by Scarth *et al.* [160] simulate composite material elastic variability of a blade structure's free-vibration and linear buckling modes. Fiber angle variations in variable stiffness composites can also affect the buckling load [13] and stress level

and failure onset of composite structures [161]. Balokas *et al.* [162–165] used 1D random fields to distort yarns in textile-reinforced composites, analyzing the effects of disturbances on the mechanical properties.

Effects of geometric imperfections have also been analyzed using random field approaches. Schenk & Schuëller [166] analyzed the buckling of cylindrical shells, later extending the analysis to include cut-outs [167]. Alfano & Bisagni [168] further studied cylindrical sandwich composite shells under a variety of imperfection sources, quantifying their individual contribution to buckling load reduction. Constrained random fields developed by Lauterbach, Fina & Wagner [92] make it possible to create local geometric imperfections, for instance, in shear walls, but also on cylinders, and flat plates, amongst others. Geometric imperfections on I-section beams were studied by Schillinger *et al.* [169], later extended by Papadopoulos, Soimiris & Papadrakakis [170] to include portal frames.

Vryzidis, Stefanou & Papadopoulos [171] applied geometric imperfections on steel tubes using an evolutionary power spectrum derived from experimental measurements. Using experimental measurements make it possible to reproduce more realistic imperfection patterns, but limited amounts of data can make it challenging to produce useful correlation functions on a structure. Using fuzzy probabilistic Fina, Weber & Wagner [172] increased the usability of finite measurement data to create realistic imperfection patterns, later extending it to include sensitivities [10].

Work done by Kriegesmann *et al.* [126, 127, 173] on composite cylindrical shells and panels [129] combined different types of imperfections. The analyses included traditional geometric imperfections as well as non-traditional imperfections such as wall thickness, material properties, loading and boundary conditions. It should be noted that the choice was made for some parameters (such as wall thickness) to vary as a constant all over the structure rather than locally. Meurer *et al.* [174] proposed a probabilistic perturbation load approach (PPLA) that incorporates perturbing loads instead of geometric imperfections, as well as other non-traditional imperfections. The PPLA design approach was applied on composite unstiffened cylindrical shells, generating less conservative design loads than equivalent NASA standards.

Other types of structures can also be analyzed with random fields. Chen *et al.* [175] analyzed geometric imperfections of reticulated space-frame structures. Microstructure analysis of composites' material properties by Stefanou, Savvas & Papadrakakis [176] couples the effects of mesoscale configurations to microstructure models. Teixeira & Soares [12] analyzed

the effects of corrosion damage on the collapse strength of panels found in bulk carriers.

1.2.4.2 *Improving design of thin-walled structures*

Improving design can mean different things, depending on the objective of the design. Traditional deterministic designs are often optimized to find a (global) optimum, minimizing an objective function. Different optimality definitions can be used when dealing with uncertainties, including the mean and standard deviation or probability of failure. Traditional deterministic design objectives, robust design, and reliability-based design objectives are defined and discussed in this section.

DETERMINISTIC PARAMETRIC DESIGN OPTIMIZATION

Deterministic optimization encompasses a wide range of approaches that try to find an optimum for a function $f(\mathbf{x}, \mathbf{p})$ subject to constraints [177]. Mathematically this problem can be defined as

$$\begin{aligned} & \underset{\mathbf{x}}{\text{minimize}} && f(\mathbf{x}) \\ & \text{subject to} && \mathbf{g}(\mathbf{x}) \leq 0 \\ & && \mathbf{x}^- \leq \mathbf{x} \leq \mathbf{x}^+, \end{aligned} \tag{1.21}$$

in which \mathbf{x} is the design variable being optimized, \mathbf{x}^- and \mathbf{x}^+ define the lower and upper bounds of \mathbf{x} , and $\mathbf{g}(\mathbf{x})$ is a constraint function.

Deterministic optimization suffers from several shortcomings [178]:

- A deterministic optimum is based on a deterministic model of a structure, it is bound with assumptions and simplifications put into the model. Any optimization therefore only optimizes the model, not necessarily the structure. Assumptions and simplifications made in the model may directly affect and alter the optimum.
- When an optimal model is found, it is impossible to recreate this precisely due to variations in manufacturing processes. An optimum is, therefore, often only a theoretical design that can not realistically be produced.
- A function gives a static optimum, and the world is dynamic. When external factors affect the model the optimum depends on their current state. An example would be temperature-dependent material properties, a bridge might need more material on a hot day than

on a calm day if the material strength is degraded. A deterministic optimum design is therefore often also dynamic depending on the environment and other external factors.

The feasibility boundary usually constrains deterministic optima, meaning that any small change in the parameters can cause the structure to violate the constraint function \mathbf{g} . Marczyk [179] wrote that "Optimization is actually just the opposite of robustness," referring to this inherent sensitivity of deterministic optima.

ROBUST DESIGN OPTIMIZATION

Robust design optimization (RDO) comes forth from the work of Genichi Taguchi [180], which focuses on making designs insensitive to the effects of uncertainties. Extending the deterministic optimization formulation of eq. (1.21) to

$$\begin{aligned} & \underset{\mathbf{x}}{\text{minimize}} && \tilde{f}(\mathbf{x}) = F(\mu_f(\mathbf{x}), (\sigma_f(\mathbf{x}))) \\ & \text{subject to} && \mathbf{g}(\mathbf{x}) \leq 0 \\ & && \mathbf{x}^- \leq \mathbf{x} \leq \mathbf{x}^+, \end{aligned} \quad (1.22)$$

where $F(\mu_f(\mathbf{x}), (\sigma_f(\mathbf{x})))$ is the reformulated design objective which is a function of the mean (μ_f) and standard deviation (σ_f) of the optimization objective f . Simple examples of the reformulated objective would be a weighted sum or weighted vector product.

The optimum value found in RDO consists of the optimal value given the variation in the design parameter. Figure 1.10a illustrates this by showing that the robust optimum x_2 is to the right of the deterministic optimum x_1 . The variation of x_1 with $\pm\Delta x$ leads to configurations outside the feasible region. Configuration x_2 remains in the feasible region with variations of $\pm\Delta x$. Quantitatively, integrating x_2 over $x_2 \pm \Delta x$ will result in a lower value than the equivalent over x_1 and stay in the feasible region.

RELIABILITY-BASED DESIGN OPTIMIZATION

Reliability-based design optimization (RBDO) seeks an optimum with an accepted chance of failure. Extending the mathematical definition of eq. (1.21) to

$$\begin{aligned} & \underset{\mathbf{x}}{\text{minimize}} && \tilde{f}(\mathbf{x}) = \mu_f(\mathbf{x}) \\ & \text{subject to} && P(\mathbf{g}(\mathbf{x}) \leq 0) \geq \mathbf{r} \\ & && \mathbf{x}^- \leq \mathbf{x} \leq \mathbf{x}^+, \end{aligned} \quad (1.23)$$

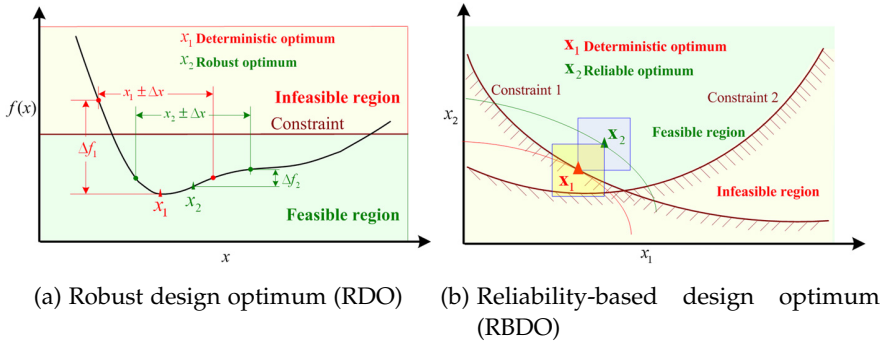


FIGURE 1.10: Comparison of RDO and RBDO approaches [154], reproduced with permission from Elsevier.

in which P indicates the probability of occurrence, which is limited by the values set in vector \mathbf{r} . Applying this reliability constraint moves the optimum found away from the feasible boundary. Figure 1.10b shows how this allows a degree of variation to the new optimum found.

RDO and RBDO can also be combined, with the minimization function of RDO and the reliability constraint of RBDO, this is referred to as *reliability-based robust design optimization* (RBRDO) [181].

APPROACHES TO IMPROVE STOCHASTIC RESPONSE IN STRUCTURAL ANALYSIS

Improving the robustness or reliability of structures can be done through a variety of approaches. Kriegesmann *et al.* [128] optimized fiber lay-up of a composite cylinder, comparing four different approaches to imperfection sensitivity and analyzing their robustness to geometric imperfections.

Traditional deterministic optimization approaches have extensions that incorporate uncertainties [154, 178, 182–184], using the modified optimization criteria discussed earlier in this section. Not all approaches are equally suited for stochastic optimization using the stochastic finite element approach detailed in section 1.2.2. Doltsinis & Kang [153] as an example applied sequential quadratic programming (SQP) to robustly minimize compliance of truss structures.

In addition to these parametric approaches, topology optimization techniques have also seen extensions for uncertainties [185–188]. Most research has gone into compliance-based objective functions, but research has also

been done on non-linear buckling optimization under uncertainty by Jansen, Lombaert & Schevenels [189].

1.3 RESEARCH AIMS AND OBJECTIVES

Literature outlined in section 1.2 shows that many methods exist to analyze and improve a structure stochastically. The work presented in this thesis aims to contribute to the existing literature in two main directions.

Most existing methods of generating random fields focus on generating fields in Euclidian space. The Euclidian distance can be a lousy measure of correlated imperfections for thin-walled structures. Structures with many curvatures, such as Ω shaped brackets, would benefit from fields generated using distances on the surface or volume of the part. Distances on a surface of geometry are known as geodesic distances. Geodesic distances are generally only used when conveniently computed, such as for cylindrical shells. Research on a general approach in generating geodesic random fields in finite elements is still quite limited [160].

This thesis presents a finite element implementation of Crane's heat method [190]. This approach applies a heat flux to a single point of a structure and uses that to compute the shortest path from that source to other points. Due to its quick computation, it becomes possible to compute the geodesic distances of points on a mesh very efficiently. Applying these distance arrays to existing random field methods makes it possible to generate geodesic fields on any finite element model with less computational effort than previously published methods. Modifications and extensions to the approach are used to generate anisotropic and intercorrelated random fields, both of which can be applied to structural problems, such as layered composite structures.

As discussed in section 1.2.2, determining a structure's reliability can only be done with accurate information on the imperfections. However, a structure's robustness can be analyzed using assumed or fictional local variations. Improvements in robustness can then lead to a reduction in the response's standard deviation.

The variability of a structure undergoing local changes in geometry or material properties can be quantified by analyzing stochastic results. Information about the local variation can also be post-processed by calculating their correlation. The resulting pattern describes the topology of a structure's relative contribution to a response. Such a pattern of relative contribution shows which areas are the most critical for varying parameters.

Knowledge obtained can improve inspection routines and the performance of a structure by perturbing the design. Such small perturbations are particularly useful when the design already exists but can be slightly modified by varying the manufacturing process. Minor variations in structural parameters can be achieved relatively easily in additive manufacturing processes or tow-steered structures.

Tailoring the topology of a structure to a design parameter using traditional parametric optimization techniques can quickly become cumbersome when the values at discrete locations (such as nodes or elements) are considered separate design variables. Using such an approach has several disadvantages:

- Loss of physical insight of local effects to a design objective
- Design solutions are not necessarily continuous, requiring additional optimization constraints
- Lack of a direct way to analyze the effect of localized variations affecting regions instead of single parameters

To some extent, these goals can be achieved through filtering of a gradient or solution, see for example [191]. The use of filters to avoid singularities and continuity of design variables requires additional processing and complexity in the design workflow.

The work presented in this thesis presents a generalized method to apply random fields on finite element models and improve a structure's performance by processing the statistical samples found in a stochastic analysis by calculating their correlation to a design objective. Using such an approach makes it possible to analyze a parameter's global and local effects deviations. These local effects can then be used to add minor changes to a structure consisting of minor perturbations in a structure's material properties or geometry. The effects of the changes can then be further analyzed or iterated by analyzing the effects of deviations on the new structural configuration. The nature of the approach and workflow make it most suitable for structures in the later stages of the design process or structures with a relatively fixed shape (due to, e.g., aerodynamic requirements).

Through this research, the following things are aimed to achieve:

- Increase understanding of the local sensitivity to local variations due to, e.g., local material property or thickness fluctuations.
- Use knowledge from the sensitivity towards local deviations to improve structural performance.

- Understand how these improvements affect the robustness and sensitivity of a structure to local imperfections.

Realization of these aims is done through the following research objectives:

- Develop and implement a general, computationally efficient method to apply spatially correlated geodesic random variations on finite element models.
- Improve the linear buckling load of a finite element model of plates and panels using data from stochastic analyses.
- Improve the fatigue life of 3D printed structures by tailoring the local thickness.
- Experimentally validate the improved design of the thickness-tailored 3D printed structure.
- Tailor the post-buckling behavior of a fiber-reinforced composite curved panel to promote a particular response by perturbing the fiber paths.
- Analyze the effects perturbations in fiber orientation have on the stochastic moments of the fiber-reinforced composite curved panel.

1.4 STRUCTURE OF THESIS

Chapter 2 presents the heat method's implementation for geodesic distance calculation in finite elements. Geodesic distances are used to generate random fields, with examples showing the effects of using geodesic distances. Generating correlated fields is demonstrated and analyzed using an example of a composite cylindrical shell.

Chapter 3 shows how applying random variations in thickness, or material properties can lead to a correlation pattern. Linear buckling load is applied using this pattern to tailor the local Young's modulus or thickness of a flat panel and cylindrical shell.

Using a similar approach chapter 4 uses an increase of a 3D-printed structure's fatigue life as its objective. Variations to the local thickness are applied using random fields. Numerically obtained fatigue life improvements are experimentally validated using 3D printed polylactic acid (PLA) specimens, showing a significant improvement in the fatigue life reliability without increasing mass.

Fiber paths of a composite panel are varied in chapter 5, to increase the structure's limit-point buckling load. Correlation patterns of the fiber variations are applied over a range of fiber deviation ranges and scaling parameters. Deterministic solutions are compared with their stochastic responses, showing that structures with the greatest deterministic improvement were also the most sensitive to deviations in the prescribed fiber path. Further analyses were done on perturbed designs to analyze the robustness of local fiber misalignments. Further analyses of the structure illustrate an inherent tradeoff between deterministic optimum and robustness, affecting reliability.

Chapter 6 gives an overview of the results and conclusions of the thesis. Extensions to increase computational time are discussed, as well as other potential future uses of the approach.

PAPER A: GENERATING GEODESIC FIELDS

Elk nadeel heb zijn voordeel.

— Johan Cruijff

The paper presented in this chapter describes how geodesic random fields are generated using the heat approach. It was first published as van den Broek, S., Jansen, E. & Rolfes, R. Efficient generation of geodesic random fields in finite elements with application to shell buckling. *Thin-Walled Structures* **179**, 109646. ISSN: 02638231. doi:10.1016/j.tws.2022.109646 (Oct. 2022).

AUTHOR CONTRIBUTIONS

SANDER VAN DEN BROEK The principal author of the paper, prepared and ran all examples, and developed code necessary for pre and post-processing.

EELCO JANSEN Provided technical suggestions and input during the development of the approach.

RAIMUND ROLFES Provided technical suggestions and input during the development of the approach.



Full length article

Efficient generation of geodesic random fields in finite elements with application to shell buckling

Sander van den Broek^{a,*}, Eelco Jansen^b, Raimund Rolfes^a

^a Leibniz University Hannover, Germany

^b Rotterdam University of Applied Sciences, The Netherlands



ARTICLE INFO

Keywords:
Geodesic length
Heat method
Random field
FEM

ABSTRACT

Structures contain inherent deviations from idealized geometry and material properties. Quantifying the effects of such random variations is of interest when determining the reliability and robustness of a structure. Generating fields that follow complex shapes is not trivial. Generating random fields on simple shapes such as a cylinder can be done using series-expansion methods or analytically computed distances as input for a decomposition approach. Generating geodesic random fields on a mesh representing complex geometric shapes using these approaches is very complex or not possible. This paper presents a generalized approach to generating geodesic random fields representing variations in a finite element setting. Geodesic distances represent the shortest path between points within a volume or surface. Computing geodesic distances of structural points is achieved by solving the heat equation using normalized heat gradients originating from every node within the structure. Any element (bar, beam, shell, or solid) can be used as long as it can solve potential flow problems in the finite element program. Variations of the approach are discussed to generate fields with defined similarities or fields that show asymmetric behavior. A numerical example of a gyroid structure demonstrates the effect of using geodesic distances in field generation compared to Euclidean distances. An anisotropic cylinder with varying Young's modulus and thickness is taken from literature to verify the implementation. Variations of the approach are analyzed using a composite cylinder in which fiber angles are varied. Although the focus of this paper is thin-walled structures, the approach works for all types of finite element structures and elements.

1. Introduction

How a structure performs under loads depends on many parameters such as geometry, material properties, and the direction and magnitude of applied loads. These parameters are often considered constant and known, but in reality, they vary and introduce an element of uncertainty in structural analysis. As structures become more efficient and lightweight, the behavior of these uncertainties and their effect becomes more important.

Stochastic analysis of finite element problems has been around for many years [1–4]. It is possible to model the effects of spatially varying material properties or thickness variations in thin-walled structures using these approaches. Applying imperfections is done by assigning a randomly generated value to the local coordinates within a structure. This field of values in space is often referred to as a *random field* or, less commonly, *stochastic field*.

Random field values at different points inside the spatial domain are correlated; if the correlations are positively-valued, points close to each other tend to have similar field values. Correlation between points on a

field is generally a function of the distance between points, decreasing as the distance increases. The correlation of points in space can be defined using a correlation function, which goes from 1 to 0 as a function of distance and possibly other parameters. When the covariance between the pair (x, y) only depends on the difference $(x - y)$, the field is considered *weakly homogeneous*. Similarly, the correlation between points might have a directional dependency. When the relationship between distance and correlation is the same irrespective of direction, the covariance is only a function of the magnitude $\|x - y\|$. Such a field is *isotropic*. Conversely, if there is a directional dependency, the field is *anisotropic*.

What these correlations look like in actual structures is a topic of ongoing research. Recent work has been done to find these patterns experimentally using coupon testing [5–7]. Investigating the spatial correlation of random variations in material properties in such a manner has many challenges. Not only do many samples have to be tested to gain relevant results, but these results might also only be valid for a specific production process and geometry. Using a different batch of

* Corresponding author.

E-mail address: S.vandenBroek@isd.uni-hannover.de (S. van den Broek).

material or having different environmental conditions can affect these variations.

Therefore, a promising method to gain statistical information on structures is to use non-destructive investigation (NDI). Applying such methods to composite structures makes it possible to gain information on the void content, fiber alignment, fiber volume fraction, and other parameters using ultrasonic and infrared thermography [8–10]. The information gained using these methods could potentially be used to map the correlation function of a structure more accurately.

Many approaches exist to generate and apply random fields [11–14]. A distinction can be made between methods that define the values of fields as a continuous function and those that discretize the field and evaluate values at specific locations.

Continuous methods represent the field through a sum of functions. Such a sum can be composed of a series of orthogonal functions, often done through a Karhunen–Loève (KL) expansion [4]. KL expansions require solving the Fredholm integral, which is only possible analytically for a limited set of correlation functions and geometries [2,15]. Other geometries and correlation functions require a numerical solution to solve the eigenvalues and eigenfunctions of the Fredholm integral [16]. Alternatively, fields can be represented using a Fourier series [17] in which the Fourier coefficients and phase shifts match a desired spectral density.

Discrete approaches define values at discrete points within the domain, such as integration points, nodes, or element centers. This can be done through decomposition of the covariance matrix [18], discretized fast Fourier series [19], and local average subdivision [20], among others. These discretized values can then be interpolated among the field using shape functions [21], optimal linear estimation (OLE) [22], or spatial averaging [23].

Through the use of a correlation function and statistical properties, the stochastic response of a structure to random variations can be quantified. This can be used to design under uncertainty [24,25], simulating the effects of random geometric imperfections on the ultimate load [26, 27], geometric imperfections affecting stability [28–36], effects fiber angle misalignments have on stability [37,38]. Some authors have also analyzed the effects of material property variations [39] or combined material and geometry variations [40–43]. Teixeira and Soares [44] investigated using random fields to study the effects of corrosion on the ultimate strength of plates. Recent work by the authors has analyzed the effects local thickness deviations can have on the fatigue life of a 3D printed component [45]. Analysis of soil mechanics is also done, where random variations in soil properties are represented using random fields [46–50]. Recent work by Zhang et al. [51] used an information-theoretic model to ensure non-Gaussianity of the random field. They used this to perturb the mesh while ensuring that faces do not intersect each other.

Fields generated in most of the previously mentioned analyses are generated and applied on thin-walled structures such as a flat panel or a cylindrical shell. For those structures, computing distances between points using coordinate transformations is straightforward. Though this works well for specific structures, this is not possible or trivial for most structures. Generating fields on domains with a concave surface, such as thin-walled structures containing curvature or a volume with a concave surface, necessitates a different approach. Using the Euclidean distance in computing the correlation will result in significant deviations from the intended correlation matrix unless the correlation length is short compared to the curvature of the structure.

A better approach is to use geodesic distance, which is the distance on the surface or within the volume of the structure. Computing shortest distances between points is a classic problem in computational geometry and has many different approaches [52]. Using geodesic random fields in structural problems was recently discussed by Scarth et al. [53], where use was made of a mesh flattening “MMP” approach [54]. Within this approach, the shortest geodesic path between two points is found using a continuous Dijkstra-type approach. Within the Dijkstra

algorithm [55], the shortest path between two points is found by slowly expanding out from the origin point. This approach can give accurate results for the geodesic length but at a high computational cost. The order of operations is $O(n^2)$, which can cause this approach to become unfeasible for larger structures.

Recent work by Feng et al. [56], Liang et al. [57] tried a different approach using a machine-learning powered isometric feature mapping algorithm to reduce the dimension of the geodesic problem after flattening the geodesic problem to a problem in 2D Euclidean space. The geodesic distance can then be recovered using traditional methods like the classic Dijkstra algorithm. Limitations in this approach do exist. The approach does not work for all shapes and cannot easily be used for non-homogeneous and anisotropic random fields. The approach in the current form is also not suitable for recovering geodesic distances in non-shell elements.

Previously discussed approaches to computing the geodesic distances have limitations in suitable geometry. Methods are generally incompatible with higher-order or non-surface elements and not capable of computing anisotropic and non-stationary random fields. Scaling of operations also limits many approaches from being used effectively in generating random fields. The work presented in this paper discusses a computationally efficient way of computing distances in finite elements and using those to generate random fields. Based on the method presented by Crane [58] it is capable of computing geodesic distances using shell, beam and volume elements. Instead of using mesh flattening, the approach uses principles of heat conduction first to find the path of the shortest distance using the heat gradient and then solve the Poisson equation to recover the geodesic distance. Solving the Poisson equation can be done by pre-factoring the sparse equations, requiring minimal computational time to solve the distances between all points in a field. Geodesic distances computed through the geodesic heat method in finite elements are used to compute the autocorrelation matrix of a field encompassing the domain of the finite element model. Decomposing the autocorrelation matrix makes it possible to generate random fields with a designated correlation through a simple matrix-vector multiplication. Unlike many methods found in literature, this approach works for any complex geometry and element type and does not make assumptions about the geometry of a structure.

Novel variations of the approach can allow for more accurate models for a class of engineering problems. Using the geodesic heat approach makes anisotropy in random fields possible through anisotropic heat conductivity. Another variation discussed is an approach to creating similar fields, which can be used in layered structures or coupled parameters.

2. Methodology

Random fields in this study are randomly generated patterns, but values are still correlated with each other. The correlation between the field values at two different points depends on the distance between the points for stationary fields. Generating random fields requires the desired autocorrelation to be given as an input. Functions used to determine the autocorrelation between points usually vary only with the distance between points. Not all functions can be used, as the autocorrelation matrix has to be positive definite. Correlation functions must satisfy Bochner’s theorem, which states that functions must be symmetric, non-negative definite, and bounded in variation [14, sec. 3.6.3]. For correlation functions that only depend purely on distance, Bochner’s theorem is equivalent to having a non-negative integrable spectral density (the integrability ensures a bounded variation).

When considering correlation functions on geodesic surfaces, it is essential to note that correlation functions that satisfy Bochner’s theorem using Euclidean distances may not satisfy the theorem when using geodesic distances [59–61]. In general, the admissibility of a covariance function must be checked before being used on geometry or type of distance. Not doing so could potentially lead to non-positive-definite matrices [62, post. 2.10]. Issues were not encountered in the

examples discussed in this paper but could arise in other shapes or with other types of correlation functions.

Two functions often found in literature (e.g. [4,63,64]) are the exponential type

$$\rho = e^{-\frac{L}{L_c}} \tag{1}$$

and the square exponential function

$$\rho = e^{-\frac{L^2}{L_c^2}} \tag{2}$$

where ρ is the defined correlation between two points, L is the distance between points, and L_c is the correlation length. The correlation functions decrease from 1 to 0 as distance increases. The speed of which depends on the function used and the correlation length. The correlation function of Eq. (1) decreases slower than that of Eq. (2). The way that the correlation evolves with distance can be related to a spectral density function using the Wiener–Khinchin theorem [11,65].

2.1. Calculation of geodesic distances

Geodesic distances are calculated using an implementation of Keenan Crane’s heat method [58]. Crane’s approach is an extension of the work done by Varadhan [66], which sought to find an elegant solution to the heat equation. Distances from a point a to other points are calculated by calculating a normalized heat gradient from heat applied at point a , followed by solving the Laplacian to find the distance between points. Numerically this approach is fast and can be pre-factored for large systems.

Initially developed in a computational geometry framework, this paper reformulates the approach by Crane et al. into a finite element environment. Using potential flow tools commonly found in finite element solvers to solve thermal problems, the approach to computing geodesic distances is straightforward to implement in many other finite element solvers.

The examples used in this paper utilize an implementation that has been developed using the library of potential flow elements already built into DIANA [67], a commercial finite element solver.

The product of the calculation is to generate a length array $\mathbf{L} \in \mathbb{R}^{n \times n}$, with n the number of points in the array, in this case, nodes of the structure. The length array should be symmetric as distances are not direction-dependent. Meaning that $L_{a,b} = L_{b,a}$, the diagonal is filled with zeros. Resulting in an array in the form of

$$\mathbf{L} = \begin{bmatrix} L_{a,a} = 0 & L_{a,b} & \cdots & L_{a,n} \\ L_{b,a} & 0 & \cdots & L_{b,n} \\ \vdots & \vdots & \ddots & \vdots \\ L_{n,a} & L_{n,b} & \cdots & 0. \end{bmatrix} \tag{3}$$

As described in [67, sec. 81.4] and [68, ch. 12] a heat conduction problem can be formulated using finite elements as

$$\mathbf{K}\phi + \mathbf{C}\dot{\phi} = \mathbf{q}_i \tag{4}$$

where \mathbf{K} is the conductivity matrix, \mathbf{C} is the capacity matrix and \mathbf{q}_i is a combination of external heat flux, heat generation and boundary convection vectors. The vector quantity ϕ is the potential term and equals the temperature within a thermal problem.

Computing the distance at every point i of a mesh requires the right-hand side to be updated n times. Every calculation uses a different external heat flux \mathbf{q}_i , where heat is added to the structure at a single node using unit values for heat conductivity, heat capacity, and external heat flux. Combining all of these into one expression results in

$$\mathbf{K}\Phi + \mathbf{C}\dot{\Phi} = \mathbf{Q} \tag{5}$$

where the matrix \mathbf{Q} can be thought of as an identity matrix \mathbf{I}_n , and Φ contains the potential terms associated with all i points.

In order to calculate the distances, the heat conduction problem has to be solved, meaning that a hypothetical heat source is added to the structure. This is done using explicit Euler forward time integration. Hypothetically the results should become exact when the time step $t \rightarrow 0$. In practice, however, small time steps lead to numerical instability. The optimum time step, therefore, has to be given as input. The optimum value for the time step depends on the mesh. Crane et al. [58] recommend $t = \delta^2$, where δ is the mean edge length of the mesh analyzed. When SI units are used in the analysis t is in seconds and δ in meters.

Through numerical integration Eq. (4) can be rewritten into the form of

$$\mathbf{K}^* \phi^* = \mathbf{Q}^* \tag{6}$$

where \mathbf{K}^* , ϕ^* and \mathbf{Q}^* are the effective matrix, nodal potential and fluxes [67, eqn. 81.18].

The solution ϕ^* provides a thermal flux of the structure originating from the node specified in \mathbf{Q}^* . Normalizing this gradient is carried out by removing the magnitude of the flux

$$\mathbf{X}_a = -\frac{\nabla \phi_a}{|\nabla \phi_a|} \tag{7}$$

which is unique for every node a . By integrating this normalized flux over the elements using the gradient of the element shape function N^1

$$\mathbf{d}_a = \iint \mathbf{X}_a \nabla N(\xi, \eta) d\xi d\eta \tag{8}$$

a vector \mathbf{d}_a containing incremental distances between nodes is generated.

Using the vector \mathbf{d} it is now possible to easily calculate the distance vector for all the points from node a as

$$\mathbf{s}_a = (\mathbf{K}^*)^{-1} \mathbf{d}_a \tag{9}$$

Note that the same inverted matrix used to solve Eq. (6) is used to solve this equation. As mentioned by Crane the solution for Eq. (9) is only unique up to an additive constant. By adding the minimum value of the calculated length vector the distances can be calculated.

The performance of the approach scales very well with the size of the model. Pre-factoring of the left-hand side of the equation scales sub quadratically, and even close to linearly [69]. Solving distances to other points scales linearly with the number of points of the model. Recent work on geodesic distances computed on shell elements by Scarth et al. [53] used a method first proposed by Mitchell et al. [54]. The exact method does not allow pre-computation and scales with $O(n^2 \log n)$, where n is the number of nodes in the model.

A performance comparison done between these approaches by Crane et al. [69] showed that for a 1.6M triangle Ramses model, the computation of distances from one point is approximately four times faster using the heat method, even with pre-factoring included. Different distances from another point of the model can be solved almost 200 times faster than the exact algorithm, with a mean error of only 0.24%. As generating an autocorrelation matrix requires the distances from all points to each other, the additional speedup of the implementation becomes essential for larger models.

This approach works on solid, shell, truss and beam elements as long as they are capable of solving potential flow problems.

2.2. Generation of random fields

Discretized random fields consist of points representing randomly generated variables in space. Values within the field have a predefined correlation to each other.

¹ Using a 2D shell element as an example.

Correlation between two random variables X and Y is defined mathematically as [70, ch. 10]

$$\rho(X, Y) = \frac{\text{Cov}(X, Y)}{\sqrt{\text{Var}(X)\text{Var}(Y)}} = \frac{E[(X - E[X])(Y - E[Y])]}{\sqrt{\text{Var}(X)\text{Var}(Y)}} \quad (10)$$

where E is the expectation operator. If we define that X and Y have a mean value of zero, and a unit variance, the equation can be simplified to

$$\rho(X, Y) = E(XY). \quad (11)$$

If X and Y are uncorrelated to each other; $E(XY) = \rho = 0$. If they are correlated $\rho \in [-1, 0) \cup (0, 1]$.

Gathering all points of a random field into a vector \mathbf{z} the correlation between points in an uncorrelated random field is $\rho(X_i, Y_j) = E(X_i Y_j) = \delta_{i,j}$, meaning that the correlation matrix $\mathbf{R} = \mathbf{I}$. When values are correlated to each other, the off-diagonal entries of the array become populated with values between 0–1.

To generate correlated random fields using uncorrelated random Gaussian vectors, a lower triangular matrix \mathbf{T} is introduced to map uncorrelated values into correlated values as

$$\mathbf{z} = \mathbf{T}\mathbf{x}, \quad (12)$$

with \mathbf{z} being a correlated Gaussian random vector with zero mean and unit variance. Vector \mathbf{x} is an uncorrelated Gaussian random vector with zero mean and unit variance. Substituting Eq. (12) into the simplified definition of correlation of Eq. (11) the correlation matrix can be rewritten as

$$\begin{aligned} \rho(\mathbf{z}_1, \mathbf{z}_2) &= \mathbf{R} = E(\mathbf{z}_1 \mathbf{z}_2^T) \\ &= E(\mathbf{T}\mathbf{x}_1 \mathbf{x}_2^T \mathbf{T}^T) \\ &= \mathbf{T} E(\mathbf{x}_1 \mathbf{x}_2^T) \mathbf{T}^T \\ &= \mathbf{T}\mathbf{T}^T \\ &= \mathbf{T}\mathbf{T}^T \end{aligned} \quad (13)$$

Meaning that the correlation matrix can be written as

$$\rho(\mathbf{z}_1, \mathbf{z}_2) = \mathbf{R} = \mathbf{T}\mathbf{T}^T, \quad (14)$$

where \mathbf{R} can be given as an input, giving the correlation between points as an input, using, for instance, Eqs. (1) and (2), which define an input correlation as a function of the distance between points. Distances from the length array computed in the previous section can be used to compute values in the correlation matrix. Doing this will lead to an array in the form of

$$\mathbf{R} = \begin{bmatrix} 1 & \rho_{1,2} & \dots & \rho_{1,n} \\ \rho_{2,1} & 1 & \dots & \rho_{2,n} \\ \vdots & \vdots & \ddots & \vdots \\ \rho_{n,1} & \rho_{n,2} & \dots & 1 \end{bmatrix} = \mathbf{T}\mathbf{T}^T. \quad (15)$$

There are different ways to factorize the correlation matrix \mathbf{R} into an upper and lower triangular matrix. The two most common approaches are using Cholesky decomposition and using eigenmode decomposition. For larger systems, eigenmode decomposition has fewer numerical issues and can also be done using a limited number of modes without significant loss of accuracy [71]. Another advantage is, although theoretically, a symmetric positive definite matrix only has positive eigenvalues. Numerical issues can cause these eigenvalues to become very small negative values. This can also be corrected by manually setting these eigenvalues to zero [72].

Eigenvalue decomposition can be done by calculating the eigenvalues and eigenvectors of the correlation matrix as

$$\mathbf{R} = \mathbf{Q}\mathbf{\Lambda}\mathbf{Q}^T, \quad (16)$$

where \mathbf{Q} is an array containing the eigenvectors of the array, and $\mathbf{\Lambda}$ is a diagonal array with the squared eigenvalues. Taking the square root of the diagonal array, $\hat{\mathbf{\Lambda}} = \text{diag}(\sqrt{\lambda})$ Eq. (16) can be rewritten as

$$\mathbf{R} = \mathbf{Q}\hat{\mathbf{\Lambda}}\mathbf{Q}^T = \mathbf{T}\mathbf{T}^T \rightarrow \mathbf{T} = \mathbf{Q}\hat{\mathbf{\Lambda}}. \quad (17)$$

For a large number of random fields, this decomposition only has to be done once. To calculate more fields, this decomposed matrix simply has to be multiplied by an uncorrelated zero mean unit variance Gaussian random vector using Eq. (12). An overview of the entire procedure to generate geodesic random fields is shown in algorithm 1.

Fields generated in this manner have unit variance and zero-mean. Scaling of the field is done when it is applied to a structural parameter in the finite element model. Alternatively, fields can be generated with a specified variance by factorizing the covariance matrix ($\mathbf{C} = \sigma^2 \mathbf{R}$) the same way the correlation matrix \mathbf{R} was factorized in Eq. (13).

Algorithm 1: Heat method for finite element random fields

```

input : Mesh,  $t$ 
output:  $n$  samples of  $\mathbf{z}$ 
1 Compute  $\mathbf{K}^*$  using  $t$ ; /* Distance calculation */
2 Solve the Poisson equation for  $\phi^*$  (Eq. (6));
3 Normalize flux to obtain  $\mathbf{X}_a$  (Eq. (7));
4 Compute incremental distances  $\mathbf{d}_a$  (Eq. (8));
5 for Every point  $a$  in mesh do
6 | Compute distances  $s_a$  from point  $a$  (Eq. (9));
7 | Subtract minimum distance  $s_a = s_a - \min(s_a)$ ;
8 Assemble all distances  $s_a$  into a distance array  $\mathbf{L}$ ;
9 Force symmetry of  $\mathbf{L}$ ,  $\mathbf{L} = 0.5(\mathbf{L} + \mathbf{L}^T)$ ;
10 Compute  $\mathbf{R}$  using  $\mathbf{L}$  (e.g. Eqs. (1) and (2)); /* RF
generation */
11 Decompose  $\mathbf{R}$  into triangular form  $\mathbf{T}$  (Eq. (14));
12 for  $i = 1:n$  do
13 |  $\mathbf{z}_i = \mathbf{T}\mathbf{x}_i$  (Eq. (12))
    
```

Examples in Section 4 utilize shell elements. Using shell elements is useful in demonstrating the effects of geodesic distances. The approach described in Section 2 is not limited to shell elements. Fig. 1 shows a distance calculation and random field generated on a 3D tetrahedral model of a compressor blisk.

2.2.1. Applying fields on a structure

The implementation used within this paper utilizes an identical mesh for the random field and the structure. Using the element's shape function, scalar quantities, such as Young's modulus, thickness, or material orientation (angle), can easily be mapped from nodes to integration points. The value of these quantities is computed as

$$a_i = a_y + z_i a_\sigma, \quad (18)$$

in which a_i is a scalar quantity used in the model (such as thickness or Young's modulus), a_y the mean value of a , z_i the value of the random field, a_σ the standard deviation of a , all evaluated at point i .

Geometric imperfections are not a scalar quantity, as they require a direction for the imperfection to act in. Assuming the structure is modeled using shell elements, geometric imperfections can be defined as a translation of nodes normal to its surface. Finding the normal direction of a shell is done by first finding the tangential components of the element coordinate system (ξ, η) in the global coordinate system. Partial derivatives of shape function have the property of transforming coordinates into vectors oriented in the derivative direction. The direction normal to the surface is found by computing the cross product of the shape function derivatives in the in-plane direction. With this in mind, the unit normal vector of point i on element j is

$$\mathbf{n}_i = \frac{\mathbf{X}_j \frac{\partial N(\xi, \eta)}{\partial \xi} \times \mathbf{X}_j \frac{\partial N(\xi, \eta)}{\partial \eta}}{\left| \mathbf{X}_j \frac{\partial N(\xi, \eta)}{\partial \xi} \times \mathbf{X}_j \frac{\partial N(\xi, \eta)}{\partial \eta} \right|}, \quad (19)$$

where ξ, η are the element coordinates as shown in Fig. 2, \mathbf{X}_j are node coordinates of element j . As an example, to calculate the normal of node 1 of a quadratic shell element shown in Fig. 2 the values $\eta = \xi = -1$ are used. \mathbf{X}_j being an array of the coordinates of all the nodes of the element. Nodes which are part of multiple elements take the average normal calculated using all elements.

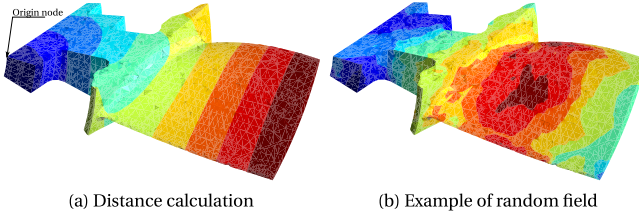


Fig. 1. Example of geodesic distance calculation and random field generation on a tetrahedral mesh model of a compressor blisk, model courtesy of authors of [73].

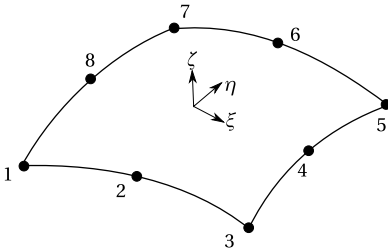


Fig. 2. Element numbering and coordinates of a quadratic shell element.

This approach for geometric imperfection only works on structures that consist of one surface. Applying geometric imperfections generated by random fields on structures consisting of multiple surfaces (such as an I-beam) is more involved but can be done by decomposing the deformation into local and global components [74,75].

2.3. Extensions of random field generation approach

What has been presented up to now can be used to generate isotropic homogeneous random fields that are uncorrelated with each other. However, certain structural problems could benefit from extensions to this approach, allowing for better modeling of certain variations. Therefore, within this section two extensions are introduced which can make it possible to generate more realistic imperfections in, for instance, layered orthotropic structures such as composites.

2.3.1. Generation of correlated random fields

In some analyses, the imperfections correlate with each other. In those cases, it is of interest to generate random fields which have a pre-determined inter-correlation. An example can be the different lamina in a composite structure. In these structures, imperfections can have different sources. Errors due to initial fiber placement would be independent of each other in every layer, but errors due to curing would affect the structure more uniformly. One way to model these coupled imperfection patterns is to generate fields that are correlated with each other.

How to generate correlated random fields is very similar to the approach used to generate random fields in Section 2.2. A correlation matrix defines the relationship between random fields. A series of n intercorrelated fields requires an $n \times n$ symmetric correlation matrix. The correlation between fields can be constant or can be neighbor dependent. It may be that neighboring layers in a composite structure are more correlated to each other than layers on the outer surface. The similarity between random fields is defined through a symmetric

correlation matrix describing the similarity of fields generated in a grouping using

$$\mathbf{R} = \begin{bmatrix} 1 & \rho_{1,2} & \dots & \rho_{1,n} \\ \rho_{2,1} & 1 & \dots & \rho_{2,n} \\ \vdots & \vdots & \ddots & \vdots \\ \rho_{n,1} & \rho_{n,2} & \dots & 1 \end{bmatrix} = \mathbf{T}\mathbf{T}^T \quad (20)$$

where n is the number of correlated random vectors. Decomposing this in the form shown in Eq. (14) it is possible to create correlated random vectors as

$$\mathbf{Y} = \mathbf{T}\mathbf{X}, \quad (21)$$

where \mathbf{Y} is an array with correlated random vectors as its columns, \mathbf{X} a matrix with uncorrelated random vectors as its columns and \mathbf{T} the decomposed matrix of Eq. (15). Using these correlated random vectors, correlated random fields can be generated using Eq. (12).

Section 4.3 discusses an example in which the correlation of fiber misalignments through different layers of a composite shell are analyzed. Intercorrelated, through-thickness varying and independent fields are compared for their relative influence on structural buckling.

2.3.2. Tailoring of thermal conductivity to generate asymmetric random fields

The approach originally presented by Crane [58] utilizes a thermal capacity $C = 1 \frac{J}{K}$ and thermal conductivity $k = 1 \frac{W}{m K}$. When solving the heat equation, this converges to the geodesic length between points. Using anisotropic heat conductivity enables the generation of a metric in which points on the structure are connected through a scaled pseudo-distance. This concept was first studied by [76]. Introducing an anisotropic pseudo-distance to determine the correlation between points on a structure makes it possible to generate fields that show different correlation behavior in different axes, such as limiting variation in a particular direction while showing more in the other direction.

One approach often used in literature (e.g. [46,53,77]) is to define a correlation length per axis. For instance converting Eqs. (1) and (2) to

$$\rho = e^{-\sqrt{\frac{L_x^2}{L_{c,x}^2} + \frac{L_y^2}{L_{c,y}^2}}} \quad (22)$$

and the square exponential function

$$\rho = e^{-\left(\frac{L_x^2}{L_{c,x}^2} + \frac{L_y^2}{L_{c,y}^2}\right)} \quad (23)$$

in which L_x and L_y are the x and y components of the distance between points, and $L_{c,x}$ and $L_{c,y}$ the correlation length in those directions.

Decomposing a distance to (local) coordinates is not a trivial task, except for simple geometries such as cylindrical shells and flat plates. Using the approach presented in this paper, it is possible to directly represent this asymmetric behavior by influencing the heat flow in the geodesic distance calculation.

The heat conductivity used in the geodesic distance calculation of Section 2.1 is inversely proportional to the distance calculated.

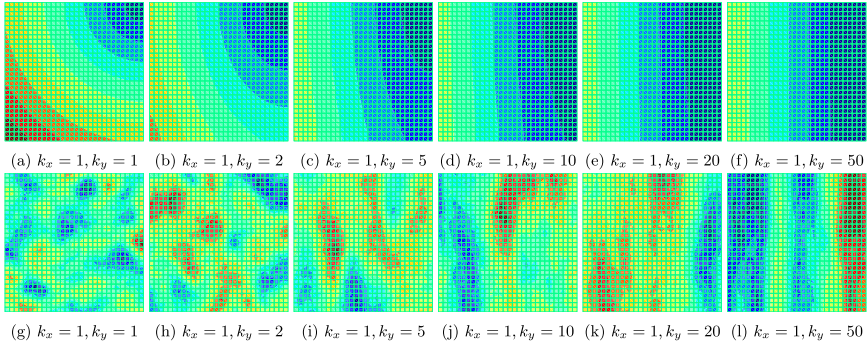


Fig. 3. Pseudo-distances from the top right corner (a–f), and fields generated on a 10×10 m flat plate using a correlation length of 1 m and correlation function Eq. (23) (g–l). Thermal conductivity is constant in the horizontal (x) direction and varies in the vertical (y) direction.

Assuming homogeneous orthotropic thermal properties, the correlation functions in Eqs. (22) and (23) can be reproduced by implementing this orthotropy into the correlation lengths $L_{c,x}$ and $L_{c,y}$ as

$$L_{c,x} = aL_c, \tag{24}$$

$$L_{c,y} = bL_c. \tag{25}$$

where a and b are scaling parameters of the thermal conductivity in the element's x and y directions

$$k_x = ak, \tag{26}$$

$$k_y = bk. \tag{27}$$

This effectively replaces the geodesic distance with a weighed pseudo distance, in which the effective correlation length is the product of the thermal conductivity and the axis-independent correlation length. Examples of distance and random fields generated using anisotropic thermal conductivity are shown in Fig. 3. Increasing anisotropy is applied to the thermal properties resulting in increasing anisotropy in the random fields.

Orientation of the material can be defined in the global coordinate system or a local coordinate system. Local material orientation can be defined through a parametric equation or as a manual input to the nodes or centroid of elements. Material anisotropy in the heat conductivity used to compute pseudo-distances makes generating anisotropic random fields on complex geometry possible.

This approach can also generate non-homogeneous fields by varying the thermal conductivity at areas with different correlation behavior (e.g., seams and edges). Increasing the thermal conductivity in these areas can cause the variations to have a shorter correlation length than their surroundings. Decreasing thermal conductivity can cause the local variation to become more constant. The use of locally varying thermal conductivity is not further explored within this paper.

3. Analysis of accuracy and time step of geodesic distance calculation

Numerical algorithms should converge to an exact solution with increased refinement. In order to verify that the implementation described in Section 2 complies with this paradigm, a number of analyses were performed. These analyses compared the computed geodesic distance and compared it to one obtained analytically. These studies were performed on a flat plate, cube, and cylindrical shell. For the sake of brevity, only the cylindrical shell is discussed in more detail.

3.1. Optimal time step and error of geodesic distance calculation

As mentioned by Crane [58] it is not trivial to find an optimal time step for geodesic length calculation. The ideal time step depends on the size, shape, and average edge length of the elements within a mesh. The geodesic calculation becomes more accurate with a finer mesh, while the ideal time step decreases with an increasing mesh size.

The error in distance calculation between the length arrays in the form of Section 2.1 obtained analytically (L_A) and numerically (L_N) is calculated as

$$\epsilon = \frac{L_N - L_A}{L_A + I}. \tag{28}$$

Array ϵ contains all the relative errors between points in the model. Within the results shown here, the RMS value of the array entries is taken as a comparative measure. The RMS is defined as

$$\text{RMS Error} = \sqrt{\frac{\epsilon_{1,1}^2 + \epsilon_{2,1}^2 + \dots + \epsilon_{n,1}^2 + \dots + \epsilon_{n,n}^2}{n}} \tag{29}$$

where n is the number of nodes of the mesh.

3.1.1. Numerical example of distance calculation

Cylindrical shells are often found in many structures in engineering and are therefore of particular interest. Different discretizations are analyzed to find the optimal time step depending on the geometry. Discretizing a shell into m circumferential elements and n axial elements, nodes are located every $\alpha = \frac{360}{m}$ degrees on the circumference. Due to the discretization, the circumference of a meshed cylindrical shell is less than an analytical cylinder. Using the equation for a chord of a circle segment [78, sec. 3.8] $c = 2R \sin \frac{\alpha}{2}$. The perimeter of the geometry represented by the discrete mesh is therefore $d = 2mR \sin \frac{360}{m}$ (in degrees). Results generated using the heat method are compared to the analytical solution

$$L_{a,b} = \sqrt{\left(2miR \sin \frac{360}{2m}\right)^2 + \left(\frac{jL}{n}\right)^2}, \tag{30}$$

in which i is the number of elements between nodes a and b in the circumferential direction. j is the number of elements between nodes a and b in the axial direction. A discretization of one of the analyzed cylinders can be found in Fig. 4(a), with an example of a distance calculation shown in Fig. 4(b).

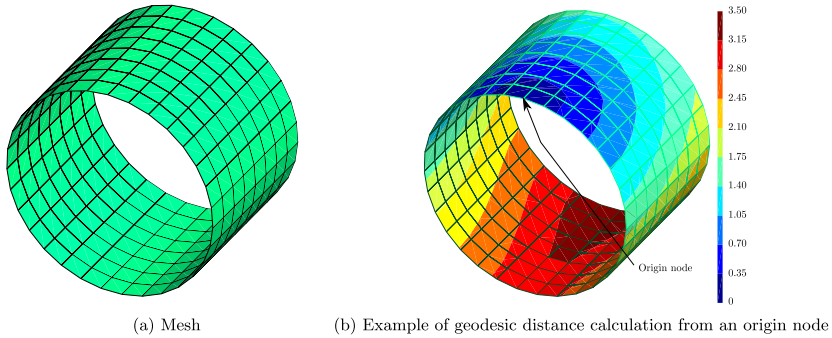


Fig. 4. Example of cylindrical shell mesh $R=1$, $L=1.5$, $\delta=0.2$.

3.1.2. Numerical results and trends

Fig. 5 shows how the RMS error in distance calculation changes with differing time steps when analyzing a cylinder with radius $R = 1$ and length $L = 2$. The analyses show that the RMS error decreases with a decreasing time step up to a certain point. At this point, it rapidly increases or does not converge. Minimization of the time step does not occur when the time goes to zero. Analyses done by Crane et al. [69, App. A] show that as the time step goes towards the limit of zero, the computed distances become a combinatorial distance, e.g., the distance product computed converges to $L = x + y$ instead of $L = \sqrt{x^2 + y^2}$. Increasing the time-step smooths out the fluxes computed, smoothening the distances computed and reducing accuracy. The exact curves vary with the aspect ratio/model size, as shown in Fig. 6. These are generated using a fixed radius of 1 m with a varying length between 1–3 m. Accuracy in the distance calculation improves with mesh size, as shown in Fig. 6(a).

Time steps in which the RMS error is minimized were computed using Brent’s method [79]. The ideal time step for cylindrical shells was close ($R^2 = 0.947$) to

$$t = \delta^{1.7}, \tag{31}$$

where δ is the mesh’s mean edge length. This relationship is a similar result to that recommended by Crane ($t = \delta^2$). Better fits were found with long polynomial expressions, but none of these expressions were accurate for different geometries. The recommendation of Crane is therefore a good starting point for meshes in general.

3.1.3. Anisotropic heat conduction

Utilizing pseudo-distances to create anisotropic fields was discussed in Section 2.3.2. This section analyzes the pseudo-distances relationship to (scaled) distance. This is done by varying the conductivity ratios² $\frac{k_z}{k_{x,y}}$ of a cylindrical shell. Ratios ranging from 0.1 to 10 were computed and compared to the analytical result found by modifying Eq. (30) to

$$L_{a,b} = \sqrt{\left(2miRk_{x,y} \sin \frac{360}{2m}\right)^2 + \left(\frac{jL}{nk_z}\right)^2}, \tag{32}$$

with k_z being the axial thermal conductivity and $k_{x,y}$ the thermal conductivity in the circumferential direction. Fig. 7 shows the minimized RMS error for different conductivity ratios. These minimized errors were obtained using Brent’s method. Results show that with an increasing anisotropy, the direct relationship with distance becomes unclear. Though not necessarily an issue for generating inhomogeneous random fields, this should nevertheless be considered when the correlation function is defined.

² z being the axial direction.

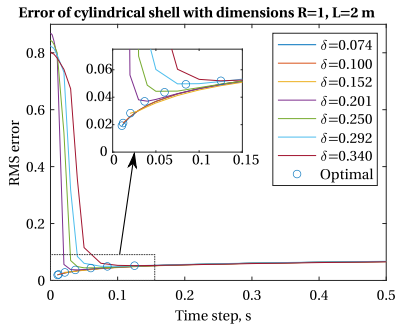


Fig. 5. RMS error in distance calculation of a cylindrical shell using different mean element size δ and time steps.

4. Numerical examples

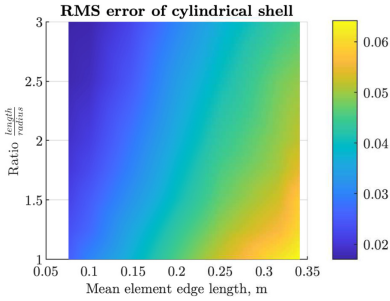
A series of numerical analyses verify the implementation in Diana and demonstrate its use on structures, including how the extensions of Section 2.3 can be used. Numerical analyses focus on cylindrical shells as these are easy to model, and using geodesic length can considerably influence results. In addition to this, cylindrical shells benefit from having many examples analyzed in detail in published literature.

Verification of the random field implementation is done by analyzing Young’s modulus and thickness variations of an isotropic cylinder. Following this analysis, a cylindrical shell’s geometric imperfections are analyzed and compared to those published in literature. A final numerical study is performed to analyze variations in the fiber angle of a composite cylindrical shell’s buckling load.

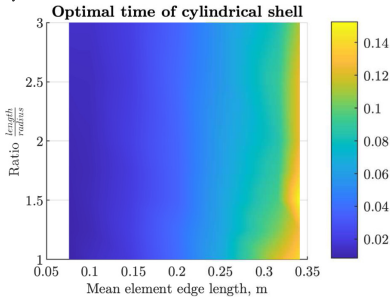
The last part of the section demonstrates some other structures in which fields were generated, showing its use in more complex structures.

4.1. Gyroid structure

Gyroid structures are a form of a minimal surface first described by Schoen [80]. Minimal surfaces are surfaces for which the mean



(a) Lowest RMS error found in the distance computation of cylindrical shell



(b) Time step in which the lowest RMS distance error is achieved, s

Fig. 6. RMS geodesic distance error minimization achieved and the time steps in which it is achieved over a variety of element sizes and geometric ratios.

curvature equals zero. Gyroids can be described mathematically as a surface defined by

$$\sin x \cos y + \sin y \cos z + \sin z \cos x = 0. \tag{33}$$

Recent work showed that gyroid shapes are very strong porous structures that efficiently use space [81], and can be fabricated using additive manufacturing techniques. The effective strength of the structure is directly related to the wall thickness, and the size of the periodic gyroids [82–84]. Additive manufacturing techniques can cause local variations in thickness. Within the current analysis, fictional variations in thickness are introduced, where the x -displacement at the loaded edge $y = 0$ is measured. Comparing the stochastic response of the structure with the random field-generated imperfections using geodesic and Euclidean distances gives an impression of the relative influence both measures have.

4.1.1. Numerical analysis

A series of gyroids with 100 mm sides are assembled in a 2×3 configuration as shown in Fig. 8. The model is discretized into 8558 analytically integrated triangular shell elements. Mesh convergence is done to check if the end displacement converges with the chosen refinement. A shear load of 10 N/mm is applied to the edges where $y=0$. Displacements of nodes located at $y = 0$ are tied together, making them equal on one edge of the gyroids. Clamped boundary conditions are applied to the edge where $y = 300$ mm. Numerical modeling of

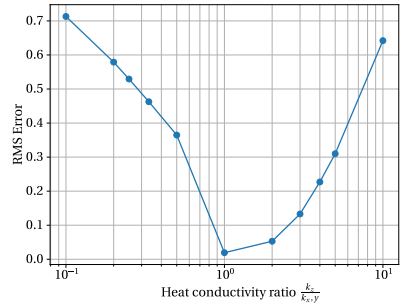


Fig. 7. RMS error of best time step found of various conductivity ratios within a cylindrical shell of $R=1, L=2$.

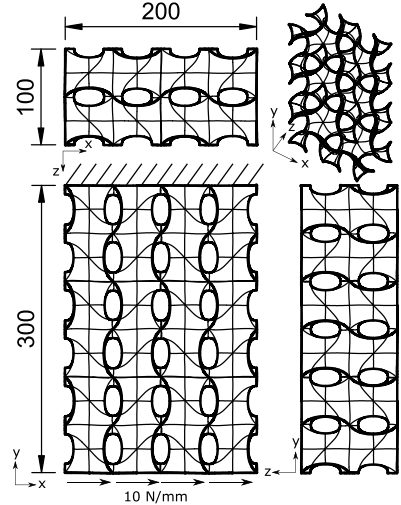


Fig. 8. Gyroid geometry, boundary conditions, and load. Dimensions in mm.

the structure is done using bilinear triangular shell elements. Thickness varies through a Gaussian distributed random field. Table 1 lists the parameters of the random field and the material properties used in the analyses. Thickness variations in the shell are applied as scalar variations on the shell element using Eq. (18). One thousand samples are generated for both types of distance calculations. A 100 mm correlation length is used as it is of a similar order of magnitude as the structure. Very small or large correlation lengths will not show as much of a distinctive difference. In theory, a Gaussian distribution can result in a locally negative thickness that would not be physically possible. However, the chance of this happening with a standard deviation of 0.1t is negligible. Computing the probability using the cumulative distribution function leads to a probability of $\frac{1}{\sqrt{3.142} \cdot 10^{25}}$ and is not considered an issue in this analysis. For more significant standard deviations, a lognormal distribution would be more appropriate. The

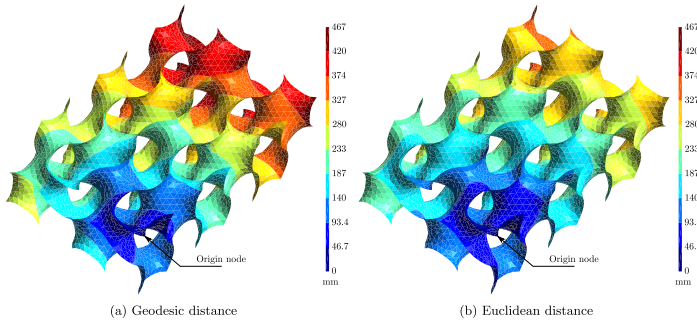


Fig. 9. Distances computed from a corner of gyroid.

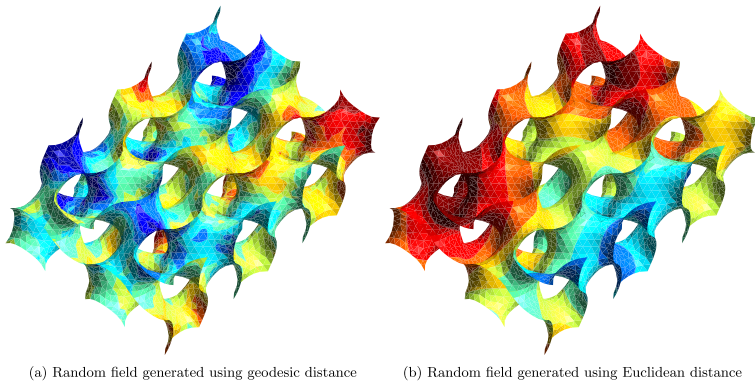


Fig. 10. Random fields generated using two different distance metrics and $L_c = 100$ mm.

Table 1
Deterministic and statistical properties of gyroid structure.

Property	Value
E	210 GPa
ν	0.3
Thickness	Gaussian random field:
	$\mu = 0.5$ mm
	$\sigma = 0.05$ mm (CoV 10%)
	$L_c = 100$ mm

Table 2
Statistical properties of analyses of the x-direction displacement of the loaded edge of the gyroid using different distance metrics in the random field generation.

	μ , mm	σ , mm	CoV
Geodesic	1.626	0.134	8.24%
Euclidean	1.617	0.158	9.78%
Relative difference	-0.5%	18.1%	18.7%

second-order estimate generated is directly affected by the distribution of the random-field variables. Switching distributions, therefore, results in different results in general. This study analyzes only the effects of geodesic vs. Euclidean distances, which is possible to do qualitatively using a Gaussian distribution.

4.1.2. Results

Geodesic distances computed differ significantly from Euclidean distances between points. Fig. 9 illustrates this through a difference that reaches up to 25% for this example. Generating fields with this differing length and correlation matrix also leads to a different looking field. Fig. 10 shows examples of fields generated using both distance metrics

in the correlation function. Fields generated using a geodesic distance show more variation within the structure than fields using Euclidean distance.

Fig. 11 shows the probability density function (pdf) of the displacement of both statistical analyses. Statistical properties of these distributions are shown in Table 2.

Comparing the two analyses, it is clear that a significant deviation of the statistical properties can be present when the distance used for random field generation does not reflect the actual geodesic distance. This deviation depends on the actual structure (curvature and size), and the correlation function used to generate the fields.

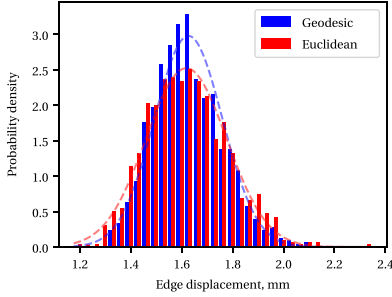


Fig. 11. Displacement in x -direction of loaded edge ($y=0$) of the gyroid structure.

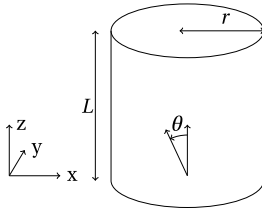


Fig. 12. Cylinder geometry definition.

4.2. Isotropic cylindrical shell with scalar variations

The second example analyzed deals with variations in thickness and Young’s modulus in a cylinder. These results verify the implementation by comparing them with published results. Arbozcz and Abramovich [85] published a series of geometric imperfection measurements of isotropic cylindrical shells referred to as the A-shells. The average property of shells A-7 to A-14 is often used in related imperfection analysis research. Imperfections that are analyzed are not just in nominal shape, but also local changes in thickness, Young’s modulus, or a combination of these [86–89]. Only the independent local variations of thickness and Young’s modulus are analyzed independently within the current work.

4.2.1. Numerical analysis

The analyzed cylinder has a length of $L = 202.3$ mm, radius of $r = 101.6$ mm. Two series of analyses are performed in which either Young’s modulus or the thickness is varied. When one is varied, the other is fixed to the mean value listed in Table 3.

Using linear, curved shell elements, the cylinder is discretized into 213 circumferential elements and 67 axial, totaling 14271 elements. Using the coordinate system of Fig. 12, the edge at $z = 0$ is constrained in all translations and rotation in the z -axis. At the edge $z = L$, translations in x and y directions are constrained, as well as rotations in the z -axis. Translations in the z -axis tied together on the top edge $z = L$, with distributed load is applied of -1.56649 N/m in the z -direction, giving a total of 1 N in compression. Results are normalized by the

Table 3
Material and thickness properties of the isotropic cylinder.

Property	Value
E	Gaussian random field: $\mu = 104.41$ GPa $\sigma = 10.441$ GPa (CoV 10%) $L_c = 50 - 500$ mm
ν	0.3
Thickness	Gaussian random field: $\mu = 0.11597$ mm $\sigma = 0.011597$ mm (CoV 10%) $L_c = 50 - 500$ mm

Note: Young’s modulus and thickness variations are not applied simultaneously. When one is applied as a random field, the mean value of the other is used as a deterministic value.

analytically obtained buckling load of the perfect cylinder calculated as

$$\lambda_{\text{analytical}} = \frac{2\pi E t^2}{\sqrt{3(1-\nu^2)}} = 5339 \text{ N.} \tag{34}$$

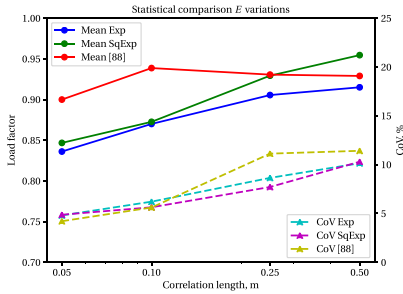
Variations are applied using the exponential correlation function of Eq. (1), as well as the squared exponential function of Eq. (2). A series of correlation lengths are used to generate Gaussian random fields ranging between 50–500 mm, the same range used by the study done by Papadopoulos and Papadrakakis [88] on this structure. Analyzing results over various correlation lengths makes it possible to identify the influence correlation lengths of imperfections have on the structure. Correlation lengths selected range from $\frac{L_c}{R} \approx 0.5$ to more large scale imperfections of $\frac{L_c}{R} \approx 5$. The standard deviation of the variations is 10% of the nominal value of both the thickness and Young’s modulus series of analyses. Although Gaussian fields can potentially result in non-physical values of Young’s modulus and thickness, this is not an issue for this particular example [89, sec. 7.1]. However, analyses with larger variations should switch to a lognormal distribution or other distribution that guarantees positive values. Results in this analysis are directly compared with published results generated using a Gaussian distribution, making direct comparison possible. In the general case when experiments are reproduced, for instance, the distribution of the input variable has to be carefully reproduced to generate an estimate of the variance.

A series of 250 analyses were performed for every correlation length analyzed, the same amount as the referred paper. The convergence of statistical properties was checked qualitatively after the analysis and found to show reasonable convergence. The applied load is slowly increased during the geometrically non-linear analysis using a Newton-based approach until the tangential stiffness matrix contains a negative eigenvalue, meaning the bifurcation buckling load is reached.

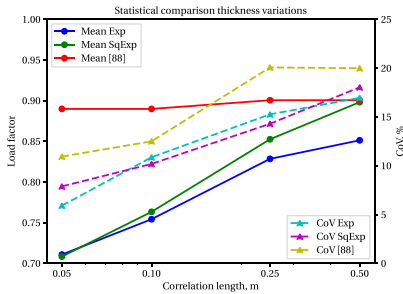
4.2.2. Results

Results found in Fig. 13 show the statistical properties of analyses that apply local Young’s modulus or thickness variations. Fields generated in the referred literature [88] use a squared exponential correlation function. Overall, fields generated using the squared exponential correlation function show a higher mean value for the critical load, while the coefficient of variation ($\frac{\sigma}{\mu}$) is only slightly lower.

Verifying results generated with the current approach and those published by Papadopoulos and Papadrakakis [88], there is an apparent discrepancy in the mean value of the stochastic results. Lower correlation lengths result in a higher value for the buckling than those generated using the geodesic approach. Papadopoulos et al. were aware of the deviation between their model’s results and results that are obtained using a considerably finer mesh. However, they asserted that such a deviation would be consistent in their stochastic results and not affect the stochastic response. This deviation was emphasized within the paper’s geometric imperfections analysis, in which a 15% increase



(a) Statistical properties of structures affected by local Young's modulus variations



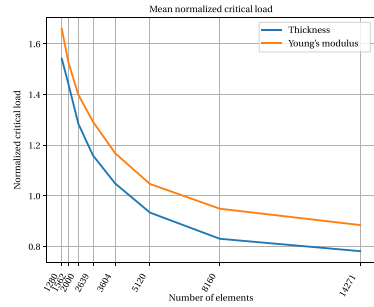
(b) Statistical properties of structures affected by local thickness variations

Fig. 13. Statistical properties of the critical load factor of analyses run with random fields of varying correlation lengths affecting the local Young's modulus or thickness.

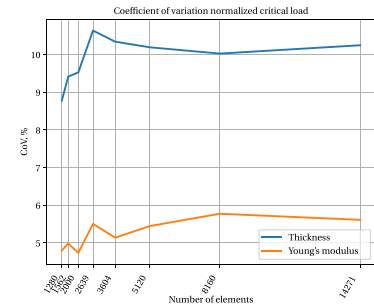
in mean buckling load was found compared to results from Schenk and Schuëller [86].

Checking this hypothesis was done by slowly refining the mesh for one particular configuration and analyzing the convergence of the stochastic results. Fig. 14 shows the stochastic convergence of stochastic parameters of structures with imperfections applied with a square exponential correlation function and a 0.1 m correlation length. Comparing the mean buckling values of Figs. 13 and 14, the mean normalized buckling load of the referred literature seems to be overestimated, corresponding to values obtained with a mesh in the order of 5000–8000 elements.

Comparing the coefficient of variation between the results shows a closer fit, particularly with Young's modulus variations. Stochastic results of the thickness varying analyses show a more significant deviation, however, not just in the variance but also in the mean value. The larger discrepancy is due to the additional refinement needed to properly evaluate the more significant change in local stiffness attributed to local thickness changes. Unlike the linear relationship with Young's modulus variations, thickness changes have a cubic relationship to bending stiffness. Such more distinctive gradients in bending stiffness require a more refined mesh to evaluate accurately, indicating that the assumption made in [88] is only valid when the stiffness gradients are not very large. Recent work from Feng et al. [56] reproduces the thickness variation example and shows a similar discrepancy compared to the original publication, with results being closer to those in the current work.



(a) Mean normalized buckling load computed with different mesh sizes



(b) Coefficient of variation of normalized buckling load computed with different mesh sizes

Fig. 14. Convergence of statistical properties of the cylindrical shell with different mesh sizes under the influence of imperfections in thickness or Young's modulus. Fields applied are generated using a square exponential correlation function and correlation length of 0.1 m.

Table 4
Material properties of Water's composite shell [90] and stochastic parameters used for fiber misalignments.

Property	Value
E_1	127,629 GPa
E_2	11,3074 GPa
G_{12}	6,00257 GPa
ν_{12}	0.300235
Fiber misalignment of θ_i , $i \in \{1 \dots 8\}$	Gaussian random fields: $\mu = 0^\circ$ $\sigma = 2^\circ$ $L_c = 50 - 500$ mm
Thickness	1.01539 mm

4.3. Waters' shell

Effects of fiber angle variations and geometric imperfections are demonstrated using a composite cylindrical shell. Dimensions and properties used are identical to the shell initially analyzed by Waters [90] and consequently used by other researchers, e.g. [91–93].

The cylinder is 355.6 mm tall with a 203.18603 mm radius, consisting of 8 layers with a total nominal thickness of 1.01539 mm with a $\{\pm 45, 0, 90\}$, layout. Material properties of the lamina can be found in Table 4.

Top and bottom edges at $z = 0$ and $z = L$ in Fig. 12 are constrained in the radial direction, leaving the axial direction free. One node on the bottom edge is constrained in the z direction to remove the rigid body mode. The cylinder is discretized into a mesh of 6 536 analytically integrated triangular elements. Mesh is converged to reproduce buckling results published in [93, tab. 3.13]. Results obtained are normalized using the linear buckling load found for the perfect cylinder (without variations applied), which equals $\lambda_{lin} = 135.7$ N/mm.

This example aims to analyze the structure's geometrically non-linear behavior. Accurately representing the complex geometric behavior requires sufficient fidelity in the displacement field. Analyzing the criticality of geometric imperfections demands a displacement field to be accurate enough to represent a given imperfection pattern. The discretization has a mean element size of 12.7 mm. The amount of elements needed to represent a local variation depends on the correlation function, correlation length, and structure. A minimum of five elements over the correlation length is used within this analysis, meaning a minimum of 50 mm is used. 50 mm equals around 14% of the axial length and 4% of the circumference of the cylinder. Fields are generated using a Gaussian distribution, which closely matches imperfections found in real structures [77].

4.3.1. Analysis of critical loads with fiber-misalignments applied

Stochastic variations on the fiber layup are applied using Gaussian random fields with a standard deviation of $\theta_\sigma = 2^\circ$. These imperfections are applied through fields generated over a range of correlation lengths, using the squared exponential correlation function (Eq. (2)). The effects of anisotropic heat coefficients in calculating pseudo-distance calculations and inter-field correlation are discussed in Section 2.3. Anisotropy in the distance measurements of the fields is achieved by applying $k_z = 50$ in the distance calculation. The z -axis is defined in Fig. 12 as the axial direction of the cylinder. The inter-field correlation Σ used in the analyses are:

Equicorrelation, (c_ρ) All fields in a run have an equal correlation to one another,

$$\Sigma = \begin{bmatrix} 1 & \rho & \rho & \dots & \rho \\ \rho & 1 & \rho & \dots & \rho \\ \vdots & \vdots & \vdots & \ddots & \vdots \\ \rho & \rho & \rho & \dots & 1 \end{bmatrix}, \tag{35}$$

where $\rho \in [0.3 \ 0.5 \ 0.9]$, making all fields equally similar to each other. Such a series of fields suitable for modeling, for example, fiber imperfections which are influenced by curing in an equal manner between layers (for instance, in very thin structures).

Identity (I) All fields are completely independent from each other, $\Sigma = I_S$. Generating a set of fields using an identity correlation matrix implies that fields are completely independent. This is equivalent to generating the fields separately without taking others into account.

Material gradient (mat) Fields in a structure are less correlated the more distance they have between them,

$$\Sigma = \begin{bmatrix} 1.00 & 0.90 & 0.80 & 0.70 & 0.60 & 0.50 & 0.40 & 0.30 \\ 0.90 & 1.00 & 0.90 & 0.80 & 0.70 & 0.60 & 0.50 & 0.40 \\ 0.80 & 0.90 & 1.00 & 0.90 & 0.80 & 0.70 & 0.60 & 0.50 \\ 0.70 & 0.80 & 0.90 & 1.00 & 0.90 & 0.80 & 0.70 & 0.60 \\ 0.60 & 0.70 & 0.80 & 0.90 & 1.00 & 0.90 & 0.80 & 0.70 \\ 0.50 & 0.60 & 0.70 & 0.80 & 0.90 & 1.00 & 0.90 & 0.80 \\ 0.40 & 0.50 & 0.60 & 0.70 & 0.80 & 0.90 & 1.00 & 0.90 \\ 0.30 & 0.40 & 0.50 & 0.60 & 0.70 & 0.80 & 0.90 & 1.00 \end{bmatrix}, \tag{36}$$

meaning that the field of layer 1 is correlated by layer 2 with 0.9 for instance, but only 0.3 with layer 8. Using such a correlation structure could potentially take curing imperfections of fiber misalignments into account for thicker structures or structures with larger curvatures where curing effects vary through thickness.

Five hundred samples are computed for each of these runs. The critical load is defined as the limit point load in which a tangential stiffness matrix becomes singular. A Newton–Raphson solver is used to compute the critical load using automatic load-step resizing. The number of samples required was determined in a convergence study. This study involved performing 1000 analyses for a few different configurations and analyzing when the mean and standard deviation values stabilize.

4.3.2. Results of stability analyses with fiber-misalignments applied

A total of 45 000 analyses were performed in 90 different configurations, as shown in Figs. 15 and 16. Isotropic results, in which $k_x = k_y = k_z = 1$ have the correlation of points on a field directly coupled to the geodesic distance are shown in Figs. 15(a) and 15(b), with two example structures shown in Figs. 18 and 19. Anisotropic results which use a pseudo-distance to generate correlation values are shown in Figs. 16(a) and 16(b), with two example structures shown in Figs. 20 and 21.

Results show that both the critical load and coefficient of variation vary significantly depending on the correlation length used. Mean critical load values go up as the correlation length increases. Physically these represent smoother and less local fiber angle variations.

The coefficient of variation of the results also varies significantly with the correlation length used. Values initially increase with the correlation length up to 75 mm for isotropic and 37.5 for anisotropic fields, after which the value drops to almost half of its peak value at 150–200 mm (isotropic) or 100–350 (anisotropic). It then goes up with increasing correlation length.

Comparing the isotropic and anisotropic fields, it is clear that a change in the critical correlation (pseudo-)length affects the results. Anisotropic fields generated have less variation in the axial direction. These more consistent variations can cause larger deviations from the axisymmetric deformation of an ideal cylinder, causing slightly lower buckling loads and more variation than the isotropic analyses.

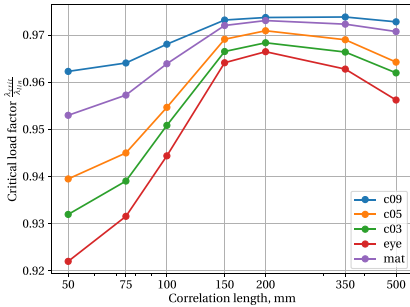
Inter-field correlation has a significant effect on both the mean value and the coefficient of variation in the analyses performed. Overall the critical value decreases as fields become more independent while at the same time increasing the variance. An essential factor is that the quasi-isotropic layup of the structure can show more anisotropic behavior when fields vary independently. Behavior such as compression-twist coupling can have a more significant effect in such cases.

Variation in the results computed is limited, with a coefficient of variation below 2%. It is important to note that the results do illustrate that inter-correlation and correlation length both have a significant effect on the variance obtained. The amplitude of the resulting analyses can increase significantly when the amplitude of variations is increased, or if the structure being analyzed has unstable nonlinear paths for instance.

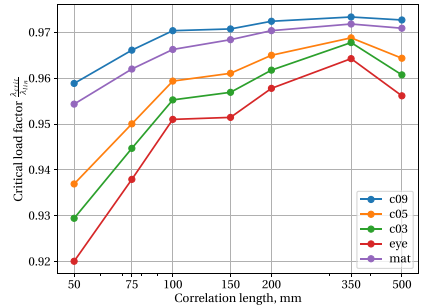
4.3.3. Analysis of critical loads with geometric imperfections applied

Geometric imperfections are also applied to the Waters shell using the procedure described in Section 2.2.1. Geometric imperfections are applied with a standard deviation equal to $\sigma = 0.1r \approx 0.1$ mm from the nominal coordinate. This value is within the maximum range measured for a cylinder by NASA [94]. It should be noted that this value would likely differ in real structures depending on the length scale of variations, e.g., the correlation length. The same value is used for all analyses for the sake of consistency.

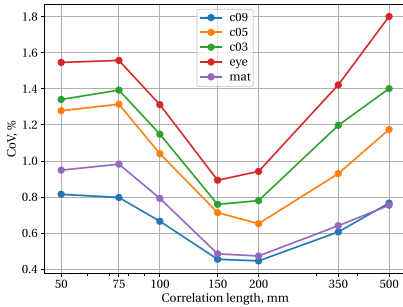
The analyses are solved the same way the fiber deviation analyses are, using a Newton–Raphson approach with automatic step resizing to find the structure's limit-point load.



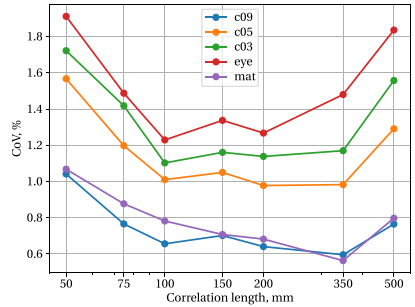
(a) Mean value of normalized critical buckling load of configuration with isotropic (geodesic) random fields with random fields of different correlation lengths



(a) Mean value of normalized critical buckling load of configuration with anisotropic random fields of different correlation lengths



(b) Coefficient of variation of critical buckling load of configuration with isotropic (geodesic) random fields of different correlation lengths



(b) Coefficient of variation of critical buckling load of configuration with anisotropic random fields of different correlation lengths

Fig. 15. Waters shell critical load $\lambda_{cr,0}$ under fiber orientation variations of different correlation lengths, and different inter-layer correlation. Configurations mentioned in the legend are discussed in Section 4.3.1. Correlations with a field use the geodesic distance generated using isotropic thermal conductivity in the geodesic distance calculation.

Fig. 16. Waters shell critical load $\lambda_{cr,0}$ under fiber orientation variations of different correlation lengths, and different inter-layer correlation. Configurations mentioned in the legend are discussed in Section 4.3.1. Correlations with a field use the geodesic distance generated using anisotropic thermal conductivity in the geodesic distance calculation, creating pseudo-distances which are used in the correlation function.

4.3.4. Results of stability analyses with geometric imperfections applied

Fig. 17 shows the statistical properties of geometrically imperfect analyses. The mean value's overall trends are similar to those of the fiber deviation, with a general increase in the correlation length. Variance, however, shows different behavior to that of fiber angle variations. There is a general decrease in the variance as the correlation length increases. Trends in the variance values are similar between the isotropic and anisotropic analyses, with values in the isotropic analyses being approximately 60%–70% higher.

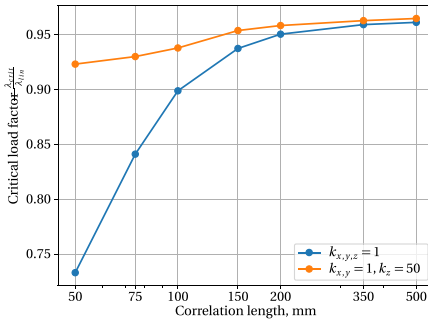
Imperfections representing the out-of-plane displacement use the same standard deviation for every correlation length. Therefore, shorter correlation lengths contain a higher degree of local curvature as the size of imperfections decreases, but the amplitudes remain the same.

Variance decreases with an increase in correlation length. As imperfections become more smoothed out and less localized, they are less likely to have an aggressive influence.

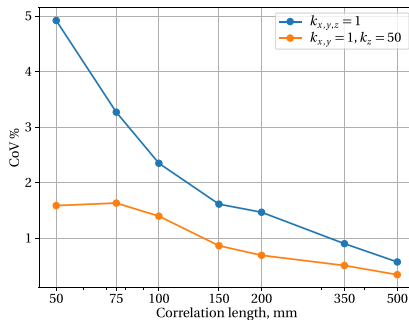
5. Discussion and conclusions

Adaption in finite elements of the heat method has dramatically simplified and accelerated the computation of geodesic random fields in structural mechanics. A random field is used to represent deviations from an ideal geometry or material property. A cylindrical shell is used to demonstrate the geodesic distance calculation. As the number of elements increases and the time step t decreases, the geodesic calculations converge to the exact analytical solution.

Substituting isotropic heat conductivity for anisotropic coefficients makes it possible to generate "pseudo-distances" scaled with the material orientation. These pseudo-distances lead to anisotropic fields, which can have an anisotropic correlation. Anisotropic fields can potentially better represent defects in specific structures introduced during manufacturing processes.



(a) Mean value



(b) Coefficient of variation

Fig. 17. Waters shell critical load λ_{crit} with geometric imperfections of different correlation lengths. Distances used in the correlation length use either isotropic (leading to geodesic distances) or anisotropic (leading to pseudo-distances) thermal conductivity.

Compared to previous work done on geodesic random fields in structural analysis, the approach presented has the following benefits:

Speed Computationally, the approach to geodesic distance calculation is very efficient and scales almost linearly with the number of points evaluated. Compared to the exact “MMP” approach [54] used by Searth et al. [53], the time to compute distances can easily be several orders of magnitude faster.

Anisotropy The MMP method only generates isotropic random fields, as the distances cannot be scaled to generate a directional dependency. Changing the heat conductivity could also change the correlation length locally by scaling the computed “pseudo-distance”, leading to non-stationary fields.

Element order The MMP method described in [54] can be used to compute geodesic distances on polyhedral surfaces. As a first step, the polyhedral has to be triangulated. Triangulation adds a step to the distance calculation (assuming the model does not use linear triangular shell elements) and limits the type and effective order of elements used. Elements that use higher-order

shape functions have to be linearized locally, losing curvature information and accuracy.

Element type The approach presented is not limited to a specific element type. The numerical examples use shell elements, but the approach is also fully functional for bar, beam and solid elements. The more extensive element library makes it possible to accurately model structures or materials requiring different elements.

A few examples are used to demonstrate the approach in structural mechanics. The first example illustrates that it is vital to use geodesic distances when a structure has curvature. The spread of imperfections can cause significant discrepancies in results when substituted by correlations obtained with Euclidean distance. The gyroid example showed a discrepancy of 20% for end displacement under shear loading.

Replicating an example from literature in which Young’s modulus and thickness vary in a cylindrical shell shows a potential source of error in computation. Structures susceptible to very local imperfections (e.g., structures with buckling modes with a short wavelength) need to be discretized and modeled in a sufficiently refined model to represent the mechanical behavior accurately. Therefore, mesh convergence studies should focus on the shortest correlation length of fields applied to a structure.

A final example analyzes the effect of local fiber misalignment. Both isotropic and anisotropic heat conductivity is used in the random field generation. Additionally, different types of correlation between layers of the composite are analyzed. These parameters both significantly influence the statistical response of a structure to imperfections.

Overall the approach presents a significant computational improvement in generating geodesic random fields. It uses existing capabilities found in finite element solvers to solve potential flow problems in the computation of geodesic distances, simplifying implementation. The generality of the formulation makes it possible to apply the approach to a variety of element types without any inherent limitations.

CRedit authorship contribution statement

Sander van den Broek: Conceptualization, Methodology, Software, Validation, Writing – original draft, Visualization. **Eelco Jansen:** Writing – review & editing, Supervision, Project administration, Funding acquisition. **Raimund Rolfs:** Writing – review & editing, Supervision, Project administration, Funding acquisition.

Declaration of competing interest

The authors declare the following financial interests/personal relationships which may be considered as potential competing interests: First author was hosted for a research stay at Diana FEA B.V. the concept of our paper came forth from that research stay. They only supported the authors with their time and software access, not through any financial means.

Acknowledgments

This project has received funding from the European Union’s Horizon 2020 research and innovation program under the Marie Skłodowska-Curie grant agreement No. 642121.



The authors would like to acknowledge the help of Gerd-Jan Schreppers and Tanvir Rahman of Diana FEA B.V. for their assistance in the numerical implementation within Diana, and for hosting one of the authors during a research stay.

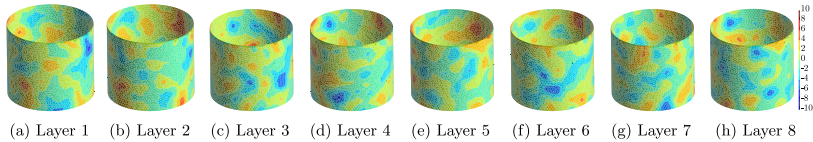


Fig. 18. Degrees fiber deviation of fields generated with $L_x = 50$ mm, isotropic distance, and equal correlation to each other of $\rho = 0.5$ ($\rho(0.5)$) per Eq. (35).

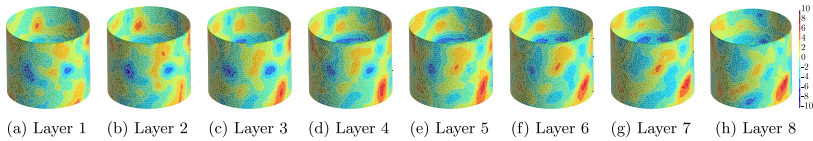


Fig. 19. Degrees fiber deviation of fields generated with $L_x = 50$ mm, isotropic distance, and a field correlation that reduces with increasing distance between fields (mat) per Eq. (36).

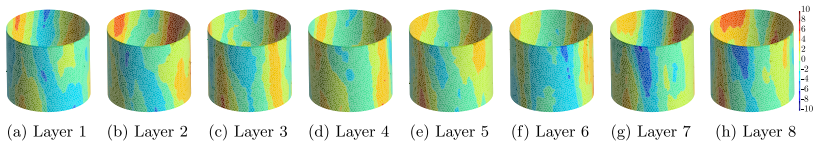


Fig. 20. Degrees fiber deviation of fields generated with $L_x = 50$ mm, anisotropic ($k_x = 1, k_y = 50$) distance, and equal correlation to each other of $\rho = 0.5$ ($\rho(0.5)$) per Eq. (35).

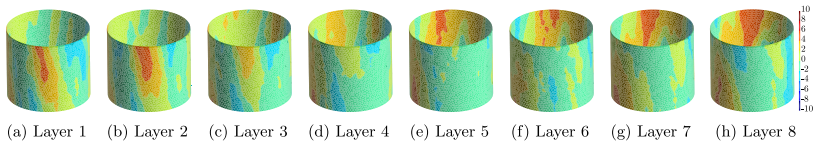


Fig. 21. Degrees fiber deviation of fields generated with $L_x = 50$ mm, anisotropic ($k_x = 1, k_y = 50$) distance, and a field correlation that reduces with increasing distance between fields (mat) per Eq. (36).

References

- [1] G. Stefanou, The stochastic finite element method: Past, present and future, *Comput. Methods Appl. Mech. Engrg.* 198 (9–12) (2009) 1031–1051.
- [2] R.G. Ghanem, P.D. Spanos, *Stochastic Finite Elements: A Spectral Approach*, Springer-Verlag New York, 1991, p. 222.
- [3] A. Der Kiureghian, J.-B. Ke, The stochastic finite element method in structural reliability, *Probab. Eng. Mech.* 3 (2) (1988) 83–91.
- [4] B. Sudret, A. Der Kiureghian, Stochastic finite element methods and reliability: A state-of-the-art report, Univ. Calif. Berkeley (November) (2000) 189.
- [5] P. Sasikumar, R. Suresh, P.K. Vijayaghosh, S. Gupta, Experimental characterisation of random field models for CFRP composite panels, *Compos. Struct.* 120 (2015) 451–471.
- [6] S. Sriramula, M.K. Chryssanthopoulos, An experimental characterisation of spatial variability in FRP composite panels, *Struct. Saf.* 42 (2013) 1–11.
- [7] S. Sriramula, M.K. Chryssanthopoulos, Quantification of uncertainty modelling in stochastic analysis of FRP composites, *Composites A* 40 (11) (2009) 1673–1684.
- [8] L. Junyan, L. Lijiang, W. Yang, Experimental study on active infrared thermography as a NDI tool for carbon-carbon composites, *Composites B* 45 (1) (2013) 138–147.
- [9] D. Saez-Castillo, M. Martín, S. Calvo, F. Rodriguez-Lence, A. Giemes, Effect of processing parameters and void content on mechanical properties and NDI of thermoplastic composites, *Composites A* 121 (January) (2019) 308–320.
- [10] A. Manta, M. Gressil, C. Soutis, Infrared thermography for void mapping of a graphene/epoxy composite and its full-field thermal simulation, *Fatigue Fract. Eng. Mater. Struct.* (October 2018) (2019) 1–13.
- [11] E.H. Vanmarcke, *Random Fields: Analysis and Synthesis*, The MIT Press, 1983, p. 382.
- [12] P.D. Spanos, B.A. Zeldin, Monte Carlo treatment of random fields: A broad perspective, *Appl. Mech. Rev.* 51 (3) (1998) 219.
- [13] G.A. Fenton, *Simulation and Analysis of Random Fields*, (Ph.D. thesis), PhD, (June) 1990, p. 189.
- [14] D.T. Hristopulos, *Basic Notions of Random Fields*, Springer Nature B.V., 2020, pp. 83–125.
- [15] P.D. Spanos, R.G. Ghanem, Stochastic finite element expansion for random media, *J. Eng. Mech.* 115 (5) (1989) 1035–1053.
- [16] W. Betz, I. Papaioannou, D. Straub, Numerical methods for the discretization of random fields by means of the karhunen-loève expansion, *Comput. Methods Appl. Mech. Engrg.* 271 (2014) 109–129.
- [17] B. Kriegesmann, R. Rolles, C. Hühne, J. Tefmer, J. Arboez, Probabilistic design of axially compressed composite cylinders with geometric and loading imperfections, *Int. J. Struct. Stab. Dyn.* 10 (04) (2010) 623–644.
- [18] M.W. Davis, Production of conditional simulations via the LU triangular decomposition of the covariance matrix, *Math. Geol.* 19 (2) (1987) 91–98.
- [19] M. Shinzuka, G. Deodatis, Simulation of multi-dimensional Gaussian stochastic fields by spectral representation, *Appl. Mech. Rev.* 49 (1) (1996) 29–53.
- [20] G.A. Fenton, E.H. Vanmarcke, Simulation of random fields via local average subdivision, *J. Eng. Mech.* 116 (8) (1990) 1733–1749.
- [21] S. van den Broek, S. Minera, A. Pirrera, P.M. Weaver, E. Jansen, R. Rolles, Enhanced deterministic performance of panels using stochastic variations of geometry and material, *AIAA J.* 58 (5) (2020) 2307–2320.

- [22] C.-C. Li, A. Der Kiureghian, Optimal discretization of random fields, *J. Eng. Mech.* 119 (6) (1993) 1136–1154.
- [23] E. Vannacker, M. Grigoriu, Stochastic finite element analysis of simple beams, *J. Eng. Mech.* 109 (5) (1983) 1203–1214.
- [24] B. Kriegesmann, R. Rolles, E.L. Jansen, I. Ellishakoff, C. Hühne, A. Kling, Design optimization of composite cylindrical shells under uncertainty, *Comput. Mater. Contin.* 32 (3) (2012) 177–200.
- [25] J. Zhao, C. Wang, Robust structural topology optimization under random field loading uncertainty, *Struct. Multidiscip. Optim.* 50 (3) (2014) 517–522.
- [26] E. Bielewicz, J. Górski, Shells with random geometric imperfections simulation - based approach, *Int. J. Non-Linear Mech.* 37 (4–5) (2002) 777–784.
- [27] G. Chen, H. Zhang, K.J. Rasmussen, F. Fan, Modeling geometric imperfections for reticulated shell structures using random field theory, *Eng. Struct.* 126 (2016) 481–489.
- [28] C.C. Bienstock, J.T. Mentzer, The use of response surface methodology estimation of composite engineering structures, 16, (2) 1995, pp. 197–226.
- [29] E. Bielewicz, J. Górski, R. Schmidt, H. Walukiewicz, Random fields in the limit analysis of elastic-plastic shell structures, *Comput. Struct.* 51 (3) (1994) 267–275.
- [30] S. Lauterbach, M. Fina, W. Wagner, Influence of stochastic geometric imperfections on the load-carrying behaviour of thin-walled structures using constrained random fields, *Comput. Mech.* 62 (5) (2018) 1107–1125.
- [31] I. Vryzidis, G. Stefanou, V. Papadopoulos, Stochastic stability analysis of steel tubes with random initial imperfections, *Finite Elem. Anal. Des.* 77 (2013) 31–39.
- [32] M. Fina, P. Weber, W. Wagner, Polymorphic uncertainty modeling for the simulation of geometric imperfections in probabilistic design of cylindrical shells, *Struct. Saf.* 82 (November 2018) (2020) 101894.
- [33] M. Fina, L. Panther, P. Weber, W. Wagner, Shell buckling with polymorphic uncertain surface imperfections and sensitivity analysis, *ASCE-ASME J. Risk Uncertain. Eng. Syst. Part B: Mech. Eng.* 7 (2) (2021).
- [34] C.A. Schenk, G.I. Schuëller, Buckling analysis of cylindrical shells with cutouts including random boundary and geometric imperfections, *Comput. Methods Appl. Mech. Engrg.* 196 (35–36) (2007) 3424–3434.
- [35] Y. Luo, J. Zhan, P. Liu, Buckling assessment of thin-walled plates with uncertain geometrical imperfections based on non-probabilistic field model, *Thin-Walled Struct.* 145 (May) (2019) 106435.
- [36] H. Wang, J. Guilleminot, B.W. Schafer, M. Tootkaboni, Stochastic analysis of geometrically imperfect thin cylindrical shells using topology-aware uncertainty models, *Comput. Methods Appl. Mech. Engrg.* 393 (2022) 114780.
- [37] A. Pagani, A.R. Sanchez-Majano, Stochastic stress analysis and failure onset of variable angle tow laminates affected by spatial fiber variations, *Compos. Part C: Open Access* 4 (October 2020) (2021) 100091.
- [38] S. van den Broek, S. Minera, E. Jansen, R. Rolles, Robust improvement of the asymmetric post-buckling behavior of a composite panel by perturbing fiber paths, *Compos. Struct.* 270 (April) (2021) 114011.
- [39] S. Shang, G.J. Yun, Stochastic finite element with material uncertainties: Implementation in a general purpose simulation program, *Finite Elem. Anal. Des.* 64 (2013) 65–78.
- [40] V. Papadopoulos, D.C. Charmpis, M. Papadrakakis, A computationally efficient method for the buckling analysis of shells with stochastic imperfections, *Comput. Mech.* 43 (5) (2009) 687–700.
- [41] L. Graham, E. Siragy, Stochastic finite-element analysis for elastic buckling of stiffened panels, *J. Eng. Mech.* 127 (1) (2001) 91–97.
- [42] J. Kepple, M.T. Herath, G. Pearce, B. Gangadhara Prusty, R. Thomson, R. Degenhardt, Stochastic analysis of imperfection sensitive unstiffened composite cylinders using realistic imperfection models, *Compos. Struct.* 126 (2015) 159–173.
- [43] N.D. Lagaros, V. Papadopoulos, Optimum design of shell structures with random geometric, material and thickness imperfections, *Int. J. Solids Struct.* 43 (22–23) (2006) 6948–6964.
- [44] A.P. Teixeira, C.G. Soares, Ultimate strength of plates with random fields of corrosion, *Int. Structure and Infrastructure Engineering*, Vol. 4, (5) 2008, pp. 363–370.
- [45] S. van den Broek, J. Wolff, S. Scheffer, C. Hühne, R. Rolles, Improving the fatigue life of printed structures using stochastic variations, *Prog. Addit. Manuf.* (0123456789) (2022).
- [46] A. Johari, A. Sabzi, A. Gholamnejad, Reliability analysis of differential settlement of strip footings by stochastic response surface method, *Iran. J. Sci. Technol. - Trans. Civ. Eng.* 43 (1) (2019) 37–48.
- [47] A. Johari, A. Talebi, Stochastic analysis of piled-raft foundations using the random finite-element method, *Int. J. Geomech.* 21 (4) (2021) 04021020.
- [48] A. Johari, A. Heydari, Reliability analysis of seepage using an applicable procedure based on stochastic scaled boundary finite element method, *Eng. Anal. Bound. Elem.* 94 (December 2017) (2018) 44–59.
- [49] A. Johari, A. Talebi, Stochastic analysis of rainfall-induced slope instability and steady-state seepage flow using random finite-element method, *Int. J. Geomech.* 19 (8) (2019) 04019085.
- [50] A. Johari, H. Fooladi, Comparative study of stochastic slope stability analysis based on conditional and unconditional random field, *Comput. Geotech.* 125 (June) (2020) 103707.
- [51] H. Zhang, J. Guilleminot, L.J. Gomez, Stochastic modeling of geometrical uncertainties on complex domains, with application to additive manufacturing and brain interface geometries, *Comput. Methods Appl. Mech. Engrg.* 385 (2021) 114014.
- [52] K. Crane, M. Livesu, E. Puppo, Y. Qin, A survey of algorithms for geodesic paths and distances, 1, (1) 2020.
- [53] C. Scarth, S. Adhikari, P.H. Cabral, G.H.C. Silva, A.P.d. Prado, P. Higinio, G.H.C. Silva, A.P.d. Prado, Random field simulation over curved surfaces: Applications to computational structural mechanics, *Comput. Methods Appl. Mech. Engrg.* 345 (2019) 283–301.
- [54] J.S. Mitchell, D.M. Mount, C.H. Papadimitriou, The discrete geodesic problem, *SIAM J. Comput.* 16 (4) (1987) 647–668.
- [55] E.W. Dijkstra, A note on two problems in connexion with graphs, *Numer. Math.* 1 (1) (1959) 269–271.
- [56] D.C. Feng, Y.P. Liang, X. Ren, J. Li, Random fields representation over manifolds via isometric feature mapping-based dimension reduction, *Comput.-Aided Civ. Infrastructure Eng.* 37 (5) (2022) 593–611.
- [57] Y.P. Liang, X. Ren, D.C. Feng, Efficient stochastic finite element analysis of irregular wall structures with inelastic random field properties over manifold, *Comput. Mech.* 69 (1) (2022) 95–111.
- [58] K. Crane, C. Weischedel, M. Wardetzky, The heat method for distance computation, *Commun. ACM* 60 (11) (2017) 90–99.
- [59] E. Del Castillo, B.M. Colosimo, S.D. Tajbakhsh, Geodesic gaussian processes for the characterization of a free-form surface, *Technometrics* 57 (1) (2015) 87–99.
- [60] G. Christakos, D.T. Hristopoulos, P. Bogaert, On the physical geometry concept at the basis of space/time geostatistical hydrology, *Adv. Water Resour.* 23 (8) (2000) 799–810.
- [61] E. Anderes, J. Müller, J.G. Rasmussen, Isotropic covariance functions on graphs and their edges, *Ann. Statist.* 48 (4) (2020) 2478–2503.
- [62] M.A. Oliver, *Modern Spatiotemporal Geostatistics*, Vol. 108, (1–2) 2002, pp. 149–151.
- [63] P. Blanchard, O. Coulaud, E. Darve, Fast hierarchical algorithms for generating Gaussian random fields, *Technical Report*, Inria Bordeaux Sud-Ouest, 2015.
- [64] M. Schevenels, B.S. Lazarov, O. Sigmund, Robust topology optimization accounting for spatially varying manufacturing errors, *Comput. Methods Appl. Mech. Engrg.* 200 (49–52) (2011) 3613–3627.
- [65] N. Wiener, Generalized harmonic analysis, *Acta Math.* 55 (C) (1930) 117–258.
- [66] S.R.S. Varadhan, On the behavior of the fundamental solution of the heat equation with variable coefficients, *Comm. Pure Appl. Math.* 20 (2) (1967) 431–455.
- [67] Diana FE5, DIANA Finite Element Analysis User's Manual Release 10.4, Technical Report, Delft, the Netherlands, 2020.
- [68] R.D. Cook, D.S. Malkus, M.E. Plesha, R.J. Witt, *Concepts and Applications of Finite Element Analysis*, Vol. 4, Fourth, Wiley New York, 2002.
- [69] K. Crane, C. Weischedel, M. Wardetzky, Geodesics in heat: A new approach to computing distance based on heat flow, *ACM Trans. Graph.* 32 (5) (2013).
- [70] F.M. Dekking, C. Kraaikamp, H.P. Lopuhaä, L.E. Meester, *A Modern Introduction to Probability and Statistics: Understanding Why and How*, Springer Science & Business Media, 2005.
- [71] M. Vořechovský, D. Novák, Simulation of random fields for stochastic finite element analysis, *Icoscar* (2005) 2545–2552.
- [72] P. Joubert, S. Langdell, Fixing a broken correlation matrix, 2019, pp. 1–5.
- [73] R. Berger, B. Hofmeister, C.G. Gebhardt, R. Rolles, A two-objective design optimisation approach for blending repairs of damaged compressor blisks, *Aerosp. Sci. Technol.* 105 (2020) 106022.
- [74] V. Papadopoulos, G. Soimiris, M. Papadrakakis, Buckling analysis of I-section portal frames with stochastic imperfections, *Eng. Struct.* 47 (2013) 54–66.
- [75] D. Schillingler, V. Papadopoulos, M. Bischoff, M. Papadrakakis, Buckling analysis of imperfect I-section beam-columns with stochastic shell finite elements, *Comput. Mech.* 46 (3) (2010) 495–510.
- [76] F. Yang, L.D. Cohen, Geodesic distance and curves through isotropic and anisotropic heat equations on images and surfaces, *J. Math. Imaging Vis* 55 (2) (2016) 210–228.
- [77] K. Sepahvand, Spectral stochastic finite element vibration analysis of fiber-reinforced composites with random fiber orientation, *Compos. Struct.* 145 (2016) 119–128.
- [78] J.W. Harris, H. Stocker, *Handbook of Mathematics and Computational Science*, Springer Science & Business Media, 1998.
- [79] R.P. Brent, *Algorithms for Minimization Without Derivatives*, Courier Corporation, 2013.
- [80] A.H. Schoen, Infinite periodic minimal surfaces without self-intersections, *Nasa Tech. Note* D-5541 (1970) 92.
- [81] Z. Qin, G.S. Jung, M.J. Kang, M.J. Buehler, The mechanics and design of a lightweight three-dimensional graphene assembly, *Sci. Adv.* 3 (1) (2017) 1–9.
- [82] R. Tino, M. Leary, A. Yeo, M. Brandt, T. Kron, Gyroid structures for 3D-printed heterogeneous radiotherapy phantoms, *Phys. Med. Biol.* 64 (21) (2019) 0–11.
- [83] D. Li, W. Liao, N. Dai, G. Dong, Y. Tang, Y.M. Xie, Optimal design and modeling of gyroid-based functionally graded cellular structures for additive manufacturing, *Comput. Aided Des.* 104 (2018) 87–99.

S. van den Broek, E. Jansen and R. Rolfes

Thin-Walled Structures 179 (2022) 109646

- [84] J. Podroužek, M. Marcon, K.s. Ninčević, R. Wan-Wendner, Bio-inspired 3D infill patterns for additive manufacturing and structural applications, *Materials* 12 (3) (2019) 1–12.
- [85] J. Arboez, H. Abramovich, The initial imperfection data bank at the delft university of technology: Part 1. 1979, pp. 1–18.
- [86] C.A. Schenk, G.I. Schuëller, Buckling analysis of cylindrical shells with random geometric imperfections, *Int. J. Non-Linear Mech.* 38 (7) (2003) 1119–1132.
- [87] V. Papadopoulos, P. Iglésis, The effect of non-uniformity of axial loading on the buckling behaviour of shells with random imperfections, *Int. J. Solids Struct.* 44 (18–19) (2007) 6299–6317.
- [88] V. Papadopoulos, M. Papadrakakis, The effect of material and thickness variability on the buckling load of shells with random initial imperfections, *Comput. Methods Appl. Mech. Engrg.* 194 (12–16) (2005) 1405–1426.
- [89] V. Papadopoulos, G. Stefanou, M. Papadrakakis, Buckling analysis of imperfect shells with stochastic non-Gaussian material and thickness properties, *Int. J. Solids Struct.* 46 (14–15) (2009) 2800–2808.
- [90] W.A. Waters, Effects of Initial Geometric Imperfections on the Behavior of Graphite-Epoxy Cylinders Loaded in Compression, Old Dominion University, 1996.
- [91] J. Arboez, J.H. Starnes, M.P. Nemeth, On a high-fidelity hierarchical approach to buckling load calculations, in: 19th AIAA Applied Aerodynamics Conference, (c) 2001.
- [92] B. Kriegesmann, E.L. Jansen, R. Rolfes, Design of cylindrical shells using the single perturbation load approach - potentials and application limits, *Thin-Walled Struct.* 108 (2016) 369–380.
- [93] T. Rahman, A Perturbation Approach for Geometrically Nonlinear Structural Analysis Using a General Purpose Finite Element Code, (Ph.D. thesis), Delft University of Technology, 2009, p. 165.
- [94] M.W. Hilburger, M.P. Nemeth, Shell buckling design criteria based on manufacturing imperfection signatures, *AIAA J.* 44 (3) (2006) 654–663.

PAPER B: ENHANCING STRUCTURES

Measure what can be measured, and make measurable what cannot be measured.

— Galileo Galilei

The paper presented in this chapter introduces the approach used to generate enhancements in structures using random fields, it was first published as

van den Broek, S. *et al.* Enhanced deterministic performance of panels using stochastic variations of geometry and material. *AIAA Journal* **58**, 2307. ISSN: 00011452. doi:10.2514/1.J058962 (Jan. 2020)

AUTHOR CONTRIBUTIONS

SANDER VAN DEN BROEK The principal author of the paper, implementor of the approach described, and the corresponding author.

SERGIO MINERA Provided the structural code in which the method was implemented and supported the approach's implementation in his code. He also provided technical discussions to the principal author.

ALBERTO PIRRERA Provided technical suggestions during the development of the approach.

PAUL WEAVER Provided technical suggestions and input during the development of the approach.

EELCO JANSEN Provided technical suggestions and input during the development of the approach.

RAIMUND ROLFES Provided technical suggestions and input during the development of the approach.



Enhanced Deterministic Performance of Panels Using Stochastic Variations of Geometry and Material

Sander van den Broek*

*Leibniz University Hannover, 30167 Hannover, Germany*Sergio Minera,[†] Alberto Pirrera,[‡] and Paul M. Weaver[§]*University of Bristol, Bristol, England BS8 1TR, United Kingdom*
andEelco Jansen[¶] and Raimund Rolfes^{**}*Leibniz University Hannover, 30167 Hannover, Germany*<https://doi.org/10.2514/1.J058962>

The effect of stochastic variation in material and geometric properties on structural performance is important for robust design. Knowledge of such effects can be acquired by applying variation patterns to a structure using random fields through a Monte Carlo analysis. The output is postprocessed to show the correlation pattern between the stochastic variation of a structural property and a chosen mechanical response measure. The resulting patterns are used to identify areas most susceptible to variations, as well as areas that have the most potential to increase structural performance by varying the material parameter or geometry. By using these maps of local sensitivity to variations with respect to the structural response, it is possible to redistribute material properties or geometry to promote certain behavior. This is demonstrated on a flat plate and curved panel by varying either the Young's modulus or the thickness of the structure to increase the linear buckling load. In both of these variations the average property is set to remain the same as the original structure. Applying the redistribution increased the linear buckling load by up to 29%.

Nomenclature

cov	=	covariance operator
c_i	=	coordinates of element i
E	=	expectation operator
\mathbf{E}	=	strain tensor
\mathbf{E}	=	2D cross-section shape function
\mathbf{f}	=	force vector
\mathbf{g}_i	=	unit vector on i axis
\mathbf{H}	=	correlation pattern
$\hat{\mathbf{H}}$	=	normalized correlation pattern
\mathbf{h}	=	vector with correlated random values
\mathbf{K}	=	conventional stiffness matrix
\mathbf{K}_G	=	geometric stiffness matrix
L_c	=	correlation length
\mathbf{L}	=	decomposed correlation matrix
m	=	exponent used to rescale field
\mathbf{m}_{el}	=	vector with field values at element el
N	=	axial 1D shape function
N^{3D}	=	3D shape function of the geometric mesh
\mathbf{Q}	=	array with eigenvectors
\mathbf{R}	=	correlation matrix
\mathbf{S}	=	second Piola stress tensor

\mathbf{u}	=	displacement field
w	=	Gauss–Legendre integration weights
x	=	Gauss–Legendre integration points
$\mathbf{\Lambda}$	=	array with eigenvalues on the diagonal
λ	=	eigenvalue
μ	=	mean value
ρ	=	correlation
σ	=	standard deviation
χ	=	random vector with unit standard deviation and zero mean

I. Introduction

TRADITIONALLY structures are designed using constant, meaning uniform and deterministic, material properties throughout the structure and nominal geometry. This representation is not necessarily appropriate, as internal stresses, variations in production processes, and chemical composition can cause mechanical properties and geometry to vary stochastically. These variations exist not only within the structural topology but also between manufactured components thought to be identical. This means that one component coming from the production line may conform to expectations, but another one does not. These variations are usually included in safety factors used within a structural design. Understanding these variations and how they affect performance is a source of extensive research and literature [1–3].

One of the ways to calculate the effects of stochastic variations is by applying them through random fields [4]. In this way a parameter can vary throughout a structure and, by running sufficient analyses, the effects of the variation can be quantified. Previous uses of this approach have looked at how geometric or material variations can affect mechanical behavior [5–9].

These analyses usually make assumptions on the spatial distribution of statistical properties, or analyze a range of correlation lengths.^{††} The actual distribution depends on the specific structure, manufacturing processes, and environmental conditions. Limited information exists in the public domain, with only a few recent papers attempting to find spatial and statistical distributions [10–13]. The approaches discussed in these papers use coupon tests to quantify the variability of

Presented as Paper 2019-0511 at the AIAA SciTech 2019 Forum, San Diego, CA, 7–11 January 2019; received 14 August 2019; revision received 6 November 2019; accepted for publication 12 December 2019; published online 27 January 2020. Copyright © 2019 by Sander van den Broek. Published by the American Institute of Aeronautics and Astronautics, Inc., with permission. All requests for copying and permission to reprint should be submitted to CCC at www.copyright.com; employ the eISSN 1533-385X to initiate your request. See also AIAA Rights and Permissions www.aiaa.org/randp.

*Ph.D. Student and Research Associate, Institute of Structural Analysis, Appelstrasse 9A.

[†]Ph.D. Student, Bristol Composites Institute (Advanced Composites Collaboration for Innovation and Science).

[‡]Lecturer and Engineering and Physical Sciences Research Council Research Fellow, Bristol Composites Institute (ACCIS).

[§]Professor, Bristol Composites Institute (ACCIS) and Bernal Institute, School of Engineering; also University of Limerick, Limerick, Ireland.

[¶]Senior Faculty Member, Institute of Structural Analysis, Appelstrasse 9A.

**Professor, Institute of Structural Analysis, Appelstrasse 9A.

^{††}The correlation length, defined in Sec. III.B, can be thought of as a characteristic length scale within a random field.

mechanical properties and their distributions. This is a costly and time-consuming process, which may be affected by factors such as curing temperature, raw material batches, and even the technicians making the structure. A potential future alternative is to use nondestructive testing to find variations; within composites this could be used to analyze variations in fiber angle, void content, as well as other parameters that may affect material properties. This topic is an active field of research [14,15] that could potentially be used to gain statistical information about structures efficiently and cost effectively.

Variations of nominal material properties and geometry are sometimes introduced purposefully by changing material parameters spatially. One way of achieving local variations is by varying the fiber angle in composites, creating variable stiffness composites [16–18]. Materials can also have other spatially varying material properties; these are often referred to as functionally graded materials. These materials can be used to improve thermal properties [19] or improve the mechanical performance of a structure. This increase can also be achieved by adding variations in the geometry, thereby tailoring the response [20–22]. One example of such an improvement is where the buckling load of the structure can be increased. Solutions are usually based on a combination of linear buckling modes of the structure. Another approach is to locally vary the thickness, either empirically [23], using periodic functions [24], or by using arbitrary stepwise variations [25]. Some papers directly vary the stiffness by varying the Young's modulus [18,26]. A few papers combine multiple parameters [27,28]. There has been some research in optimizing the stiffness topology [26,28,29]. These approaches lead to (local) optima, but do not always give physical insight into the physical changes or evolution of the structure. This is possible because the topology is directly coupled with the average sensitivity to variations of the structure to its response. The changes made to the structure affect the stresses and strains and other mechanical parameters. It is therefore likely possible to make further improvements through an iterative approach. An iterative approach would reveal the nonlinear topological change of sensitivity between iterations.

The difference between stochastic approaches and traditional optimization methods is that the results take some degree of random variations into account. The patterns therefore should lead to a design that is less susceptible to deviations of the improved design. This process is different from traditional structural optimization techniques, in which the optimized design becomes increasingly sensitive to deviations from the optimized shape (as optima often lie on a Pareto front of design constraints). Robust optimization is a field of research that is becoming more prominent as engineers realize that uncertainties can have an ever-increasing effect on structural performance [30–32].

The work presented herein tries to identify where in the topology variations cause the most influence on a measure of the structural response, and can be considered a more generalized stochastic version of the approach presented by Minera [33] to improve linear buckling loads. Within the current approach a measure, which can be buckling load, stress, displacement, or any other output from an analysis is targeted to be improved. Property enhancement is achieved by analyzing the effects of fictitious local variations on the structure. This is done by looking at the correlation between these variations and its effect on the structural response. Calculating this correlation at points throughout a structure generates a pattern, which can be used to redistribute the parameter within the structure. This distribution can improve the understanding of the underlying structural mechanics. This knowledge can be used to improve the performance of the structure and identify areas most critical for inspection during manufacture. This approach could potentially be used in additive manufacturing, where there are fewer design constraints and potentially more variation in material properties due to the printing process. Additive manufacturing also makes it possible to vary the composition of the printing material, tailoring it to specific properties needed locally within a structure.

The patterns related to a structural measure are generated through Monte Carlo analyses. These are run using spatially random patterns of fictitious variations and then correlating how the patterns affect the mechanical response (e.g., buckling load, displacements, and stresses). The variations are analyzed on a flat plate and curved panel, by either varying the Young's modulus within a structure or by changing the

thickness locally. The variations used in this procedure are not related to actual variations in the structure, but are instead fictitious small variations that are purely used to generate the correlation pattern. The correlation pattern is used in turn to tailor the material properties or geometry of the structure to improve performance, as could be done using additive materials or additive manufacturing techniques. These techniques make it possible to theoretically vary the composition of the printing material locally, thereby changing its material properties. The printing process also allows designers to vary geometry such as thickness throughout the structure.

The remainder of this paper first introduces the methods used in Sec. II, starting with the structural model in Sec. II.A. Section II.B describes how random fields are generated, and how they are mapped is described in Sec. II.C. The procedure to apply thickness imperfections is explained in Sec. II.D. Section II.E specifies how correlation patterns are calculated, Sec. II.F discusses how they are applied to the structure. Results are shown in Sec. III, starting with the flat plate example in Sec. III.A, and continuing with a curved panel example in Sec. III.B. The paper finishes with a discussion of the results and method as well as some conclusions in Sec. IV.

II. Methods

A. Finite Element Formulation

The model used for the structural calculations is based on the unified formulation [34]. The implementation used is based on Serendipity Lagrange (SL) elements [35]. These elements use SL expansion functions in two dimensions $F(x, z)$, and Lagrange shape functions in the axial direction $N(y)$ of a 3D element. The implementation is developed for 3D structures with beam-like geometry, in which a cross section is extended axially. This can be done by warping the cross section in the axial direction (to include curvature or tapering), but requires element connectivity to remain the same [36].

The focus of this work is on linear buckling problems, which includes determining the geometric stiffness matrix K_G . This matrix captures the effect that in-plane forces have on the (out-of-plane) stiffness of the structure, which is essential in buckling problems.

1. Basic Formulation

The structural model consists of 3D elements. Different shape functions are used in the cross-sectional $F(x, z)$ and axial direction $N(y)$ to approximate the displacement field.

Starting with a displacement field $\mathbf{u} = [u, v, w]^T$ the Green–Lagrange strain tensor \mathbf{E} can be defined linearly as

$$E_{ij} = \frac{1}{2} (\mathbf{u}_i \cdot \mathbf{g}_j + \mathbf{u}_j \cdot \mathbf{g}_i) \quad (1)$$

where commas denote derivatives and \mathbf{g}_i denotes a unit vector on the i axis. The displacement field \mathbf{u} is approximated within the unified formulation as

$$\mathbf{u}_{(e)}(x, y, z) = F(x, z)N(y)\mathbf{u}_i, \quad \text{with } i = 1, \dots, N \quad (2)$$

where N is the number of degrees of freedom of the model. For quasi-static problems the elastic equilibrium is

$$\delta W_{\text{int}} = \delta W_{\text{ext}} \quad (3)$$

where W_{ext} and W_{int} are the external work and internal energy. Noting that the internal energy of the structure can be calculated as the sum of internal energy of all the elements $W_{\text{int}} = \sum_e W_{\text{int}}^{(e)}$, the internal energy can be expressed using the stress and strain tensors:

$$\delta W_{\text{int}}^{(e)} = \int_{V_{(e)}} \delta \mathbf{E} \cdot \mathbf{S} \, dV \quad (4)$$

where \mathbf{S} is the second Piola stress tensor. This can be written as

$$\delta W_{\text{int}}^{(e)} = \delta \mathbf{u}_i^T \mathbf{k}_{(e)}^{ijrs} \mathbf{u}_r^T \quad (5)$$

where $i, j = 1, \dots, N_e$, $\tau, s = 1, \dots, M, N_e$ is the number of Lagrange nodes in the axial direction, and M is the number of terms in the cross-section expansion [35], Eq. (11). The term $k_{(c)}^{ij\tau s}$ is referred to as the *fundamental nucleus*, the explicit form of which can be found in [34,37]. The fundamental nuclei can be assembled into a global stiffness matrix \mathbf{K} in the form

$$\mathbf{K}\mathbf{u} = \mathbf{f} \tag{6}$$

which can be solved to find generalized displacements.

To calculate the linear buckling load an additional geometric stiffness matrix \mathbf{K}_G is needed. For the sake of brevity the full form is omitted, but can be found in [33,38,39]. Linear buckling can be derived as an eigenvalue problem in the form ([40] Chap. 18)

$$(\mathbf{K} + \lambda_{cr} \mathbf{K}_G) \delta \mathbf{u} = \mathbf{0} \tag{7}$$

where $\delta \mathbf{u}$ represents a buckling mode with an indeterminate amplitude. The scalar value λ is a proportionality factor that relates the applied force \mathbf{f} and the stresses, which are used to generate the geometric stiffness matrix. The buckling load can be solved as the nontrivial solution to

$$\det(\mathbf{K} + \lambda_{cr} \mathbf{K}_G) = 0 \tag{8}$$

whereby solving for λ_{cr} and subsequently identifying the load factor as

$$\mathbf{f}_{cr} = \lambda_{cr} \mathbf{f} \tag{9}$$

where \mathbf{f}_{cr} is the buckling load.

2. Geometric Representation

The element stiffness matrix is obtained by integrating the terms of equation (5) throughout the element domain. When modeling complex geometries the correct geometrical description is of fundamental importance. The SL expansion functions defined in Sec. II.A are used to enrich the kinematics in the cross section. These functions are integrated over the cross section of the structure, which requires a transformation of coordinates. If the edges of a quadrilateral element are straight, the approximation of the geometry is obtained through linear mapping by using linear Lagrange polynomials, which in this case coincide with SL functions of order 1. This approach does not allow for an accurate representation of curved geometries. When using isogeometric formulations the same functions describe the displacement field and the geometry. The advantage of this approach is that modeling the geometry correctly automatically improves the accuracy of the field. This may, however, come with a high computational cost, especially when unified formulation is used. An alternative approach is to discretize the geometry and structure separately, as is done in the current approach. This approach uses higher order meshes for the geometry, and higher order Lagrange shape functions for coordinate transformations.

The hierarchical nature of the SL shape functions makes it possible to use them within curved elements, as the expansion order can be increased as needed. The approach adopted in the current structural model aims to do this without adding to the degrees of freedom of the structure. This can be done by blending the structure with higher order polynomials [41], which can become cumbersome for distorted or large meshes. Another approach is to use exact geometric descriptions through nonlinear functions ([42] Chap. 5). This approach requires an exact geometric description to be given analytically, limiting the geometry that can be analyzed. The approach used in the current model is non-isoparametric, using higher order Lagrange shape functions to describe geometry.

The current approach uses a higher order mesh generated using gmsh [43], generating a mesh with elements of 9 or 16 nodes in the cross section. This gives a 2D shape function $N^{2D}(\alpha, \beta)$ to describe the geometry of a cross section that is independent of the structural shape functions $F(x, z)$ and $N(y)$. The function $N^{2D}(\alpha, \beta)$ is defined

in the range $[-1, 1]^2$ and defines the mapping between the global coordinates and local element coordinates

$$\mathbf{x} = N_k^{2D}(\alpha, \beta) \mathbf{x}_k \tag{10}$$

where $\mathbf{x}_k \in \mathbb{R}^2$ are the position vectors of the nodes of the element, and $k = 1, \dots, N_{ne}$, with N_{ne} the number of nodes; 9 or 16 node Lagrange elements are supported by the current implementation.

To model varying thickness this approach is extended by changing the shape function of the cross section to vary at every integration point. This adds another dimension to the shape function $N^{2D}(\alpha, \beta)$ to account for the change in the axial direction. This new function, $N^{3D}(\alpha, \beta, \xi)$, can change the cross-section mapping as a function of ξ , making it possible to model tapered structures.

The number of nodes used to describe the geometry ($N^{3D}(\alpha, \beta, \xi)$) is independent from the number of degrees of freedom in the structural model $F(x, z)$ and $N(y)$. The degrees of freedom of the structural and geometric mesh are shown in Fig. 1. The 2D shape function N^{2D} is identical to N^{3D} in structures that are prismatic. For non-prismatic structures this shape function is calculated at every integration point in the ξ direction.

The current implementation uses 3D geometric Lagrange shape functions to take thickness variations into account efficiently. This geometric mesh overlaps the structural mesh, but uses higher order brick elements of 27 or 64 nodes. These shape functions reduce the amount of computation needed during assembly. The 3D geometric mesh shape functions are used in Secs. II.C and II.D to map variations to the structure, and to calculate the volume and average material properties of the structure.

B. Random Field Generation

Random fields, also known as stochastic fields, are fields in n -dimensional space that spread a parameter in space with a distribution. Values within a field are correlated with each other. There are many methods that can be used to generate random fields [4]. These methods have their own advantages and disadvantages. The technique used here is covariance matrix decomposition (CMD) ([44,45] Sec. 5.3.2). This choice is made due to the relative ease of implementing customized correlation functions. CMD creates fields directly from an autocorrelation matrix by decomposing it and multiplying the decomposed array with a random vector. The values of a random field are usually generated from a (log)normal distribution with an associated mean value (μ) and standard deviation (σ). Actual variations may not be in such a distribution, but are often assumed to be such as a simplification, or due to a lack of experimental data. These points are correlated in space, thus giving a relationship to the value of a coordinate and those in its vicinity. The mathematical definition ([46] Chap. 10) of correlation between points i and j of field h is

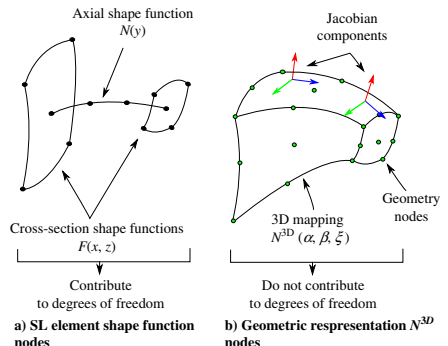


Fig. 1 Element discretization and shape functions [36].

$$\rho_{h_i, h_j} = \frac{\text{cov}(h_i, h_j)}{\sigma_i \sigma_j} = \frac{E[(h_i - \mu_i)(h_j - \mu_j)]}{\sigma_i \sigma_j} \quad (11)$$

where E is the expectation operator used in probability and equals the mean value of a distribution given an infinite amount of samples. Equation (11) can be used to calculate the autocorrelation between points; to generate fields these correlations have to be given as an input. The most common functions found in literature are based on an exponential function. The correlation function used to generate the fields here is

$$\rho_{s, \text{exp}} = e^{-(\Delta L/L_c)^2} \quad (12)$$

in which L_c is the correlation length, and ΔL the distance between two points. This relationship assumes stationarity, as the field is only dependent on distance, and does not change throughout the structure. The term ΔL traditionally refers to Euclidean distance, but as we are concerned with thin-walled structures, the geodesic length is used instead. Using geodesic lengths creates a more accurate measure for generating random fields than Euclidean distance, particularly for highly curved structures [47]. Structures that are relatively flat might have a bottom and top that are close to each other in a Euclidean sense, but distant in a geodesic sense. The geodesic lengths of the current implementation are calculated using the heat method of Crane et al. [48], using normalized heat gradients to calculate the shortest path through solving the Poisson's equation. This can be done with limited computational costs, as these turn out to be linear problems. The random field method used in this paper does not offer a continuous function and instead discretizes points into space, which are then coupled to points in the structure. The space between random field nodes should be between $(L_c/4)$ and $(L_c/2)$ for the correlation function used [49]. In the context of this paper the correlation length represents a measure of the resolution of the correlated structure. A shorter correlation length allows variations to be more local, allowing patterns to be more localized, at the cost of taking longer to converge. Having a large correlation length therefore makes it harder for smaller details to converge; large-scale variations make it easier to converge to a pattern.

Using CMD, random fields are calculated through multiplication of a matrix and a random vector:

$$\mathbf{h} = \mathbf{L}\boldsymbol{\chi} \quad (13)$$

in which \mathbf{L} is a decomposed version of the correlation matrix \mathbf{R} and $\boldsymbol{\chi}$, a vector with random entries of zero mean and unit variance. This decomposition has to be done in such a way as to generate a correlated vector \mathbf{h} with a mean of zero and unit variance.

The first step in generating random fields is to build a correlation matrix of all vertices of the field

$$R_{ij} = \frac{\text{cov}(h_i, h_j)}{\sigma_i \sigma_j} \rightarrow \mathbf{R} = \begin{bmatrix} 1 & \rho(h_1, h_2) & \dots & \rho(h_1, h_n) \\ \rho(h_2, h_1) & 1 & \dots & \rho(h_2, h_n) \\ \vdots & & \ddots & \vdots \\ \rho(h_n, h_1) & \rho(h_n, h_2) & \dots & \rho(h_n, h_n) \end{bmatrix} \quad (14)$$

in which $\rho(h_i, h_j) = \rho(h_j, h_i)$, noting that the correlation here can be calculated using Eq. (12).

Taking the definition of covariance

$$\text{cov}[h_i, h_j] = E[h_i h_j] - E[h_i]E[h_j] \quad (15)$$

and keeping in mind the field has a zero mean, it is possible to show that \mathbf{R} can be decomposed into two matrices:

$$\begin{aligned} \mathbf{R} &= \text{cov}[\mathbf{h}, \mathbf{h}] = E(\mathbf{h}, \mathbf{h}^T) - \mathbf{0} \cdot \mathbf{0} \\ &= E(\mathbf{L}\boldsymbol{\chi}(\mathbf{L}\boldsymbol{\chi})^T) = E(\mathbf{L}E(\boldsymbol{\chi}\boldsymbol{\chi}^T)\mathbf{L}^T) = \mathbf{L}\mathbf{I}\mathbf{L}^T = \mathbf{L}\mathbf{L}^T \quad (16) \end{aligned}$$

where \mathbf{I} is an identity matrix. Noting that from Eqs. (12) and (14) the matrix \mathbf{R} is symmetric and positive semidefinite, the eigenvalues should not be negative. This expression exploits the independence of the components of $\boldsymbol{\chi}$. Decomposing is done by using eigendecomposition in the form of

$$\mathbf{R} = \mathbf{Q}\boldsymbol{\Lambda}\mathbf{Q} \quad (17)$$

where $\boldsymbol{\Lambda}$ is a diagonal matrix with the eigenvalues of \mathbf{R} on the diagonal, and \mathbf{Q} contains the eigenvectors of the matrix. The matrix \mathbf{L} can be extracted as

$$\mathbf{R} = \mathbf{Q}\hat{\boldsymbol{\Lambda}}\mathbf{Q} = \mathbf{L}\mathbf{L}^T \rightarrow \mathbf{L} = \mathbf{Q}\hat{\boldsymbol{\Lambda}} \quad (18)$$

in which $\hat{\boldsymbol{\Lambda}} = \text{diag}(\sqrt{\lambda})$, where λ are the eigenvalues of the \mathbf{R} matrix. Using the decomposed correlation matrix \mathbf{L} it is possible to generate random fields using Eq. (13), requiring minimal additional computational costs.

C. Random Field Mapping to Structure

The random fields in the current implementation are generated on a surface, whereas the structural model is based on 3D elements. To assign material properties to each integration point using the values of the random field, it is necessary to implement a mapping procedure.

The mapping procedure used within this paper separates the random field mesh and the structural mesh. This is done so that in other applications the geodesic length can be calculated with a greater accuracy, being able to more accurately represent the curved geometry. It also makes it possible to refine the structure without at the same time refining the random field discretization.

By using the higher order shape functions of the geometric mesh (Sec. II.A.2) it is possible to include the curvature within an element in the mapping procedure. The mapping procedure starts by projecting each node of the geometric mesh to the random field surface, finding the shortest Euclidean distance. This has to be done only once, which saves time during Monte Carlo analyses. While initializing each analysis the values of the random field are calculated for every geometric node using the four-node shape function of the random field element.

During assembly, material properties of each integration point are interpolated using the shape function of the geometric mesh. This process has the advantage that by using higher order elements (e.g., 27 nodes) it is possible to have a nonlinear variation of properties within an element. It is therefore possible to represent the structure with larger elements and still have an accurate material property distribution. As a consequence the mapping procedure can have a higher fidelity than would be possible with the linear shape functions of the eight-node structural elements. The optimal discretization of the random field is therefore also dependent on the order of the geometric Lagrange elements, and the structural SL elements in addition to the correlation function used.

The illustration in Fig. 2 shows the mapping process, where at an integration point the coordinates within the element coordinate system are used to interpolate values of the geometric mesh, or mathematically as

$$h_i = \mathbf{m}_{ei} N_{ei}^{3D}(\alpha_i, \beta_i, \xi_i) \quad (19)$$

where h_i is the field value at a point i , \mathbf{m}_{ei} a vector with the field values at element ei , and $N_{ei}^{3D}(\alpha_i, \beta_i, \xi_i)$ the shape function evaluated at element coordinate i with components α, β, ξ . It should be noted that this approach has a constant value assumption through thickness, which is why the value is the same for β between $[-1, 1]$.

Random field values are normalized to zero mean and unit variance. Applying the field to a variation in the Young's modulus would require the addition of the mean and multiplication with the standard deviation as

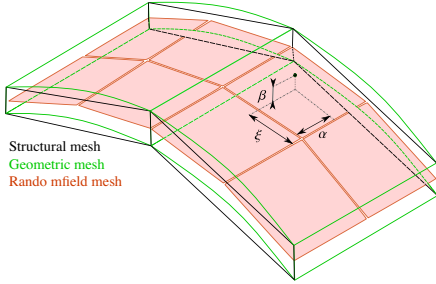


Fig. 2 Separate discretization of meshes and coordinates at point i .

$$E_i = E_\mu + h_i E_\sigma \quad (20)$$

in which E_i is the Young's modulus at point i , E_μ is the mean value of E , h_i is the value of the random field at the point, and E_σ is the standard deviation of the Young's modulus.

D. Applying Thickness Imperfections

Applying variations to the thickness in the structure requires changing the 3D mesh to reflect the new geometry. This is done by mapping the random field to perturbations to the structural mesh.

In Sec. II.C, a mapping between the random field and nodes of the geometric mesh (N^{3D}) is described. This process gives interpolated scalar values of the random field to every node in the geometric mesh. This scalar value is used to determine the amount of displacement that should be applied to the node.

The approach used in the current work determines the amount of displacement of a coordinate by scaling the displacement with the distance from the random field surface. This approach makes it possible to apply symmetric thickness variations, by having the random field in the middle of the structural mesh. It also makes it possible to vary in one direction, by having the random field intersect the surface that should not be varied.

The direction in which the node is displaced is taken from the derivative of the shape function with respect to the element normal direction. In the convention used within this paper this gives the normal direction relative to the surface of the structure. An unrotated element has its α, β, ξ components aligned with x, z, y , with the normal being defined as the component in z . With the convention used the normal direction is therefore equal to $\mathbf{g}_\beta = \mathbf{x}(\partial N^{3D} / \partial \beta)$, where \mathbf{g}_β is a unit length normal vector of a coordinate in the normal (β), and \mathbf{x} an array of the physical coordinates of an element. This solution may not be unique if a node is used in multiple elements. In those cases the average normal direction of all elements containing the node is used. The distance d between a physical node and the random field surface is calculated numerically. The displacement is applied to node i by adding an offset to the coordinates of the nodes

$$\mathbf{c}_{i,new} = \mathbf{c}_{i,old} + \delta d_i = \mathbf{c}_{i,old} + d_i \sigma_i \mathbf{g}_\beta h_i \quad (21)$$

in which d_i is the original distance between the node and random field surface and \mathbf{c}_i the coordinates of node i .

E. Calculating the Correlation of a Parameter on the Structure

By running an analysis n times it is possible to calculate how variations of material or geometric parameters affect the structure. This approach makes it possible to identify areas that most influence the mechanical response. In doing so, it offers valuable information on the relationship of buckling load to stiffness variation, stress to displacement, or any other combination of parameters.

The correlation is calculated at the same points in which the random field is discretized; the points are then evaluated for

parameters a and b . Using the definition of correlation of Eq. (11) the correlation of each point a on the structure is calculated relative to parameter b . For the examples discussed in the Results section, the parameter a would equal the Young's modulus or thickness and the parameter b the first linear buckling load. For this example the pattern can be evaluated as

$$H_i = \frac{\sum_{j=1}^n (f_j - \bar{f})(E_{i,j} - \bar{E})}{\sqrt{\sum_{j=1}^n (f_j - \bar{f})^2} \sqrt{\sum_{j=1}^n (E_{i,j} - \bar{E})^2}} \quad (22)$$

where H_i is the correlated value at point i , f_j the buckling load at run j , \bar{f} the sample mean buckling load over all n runs, $E_{i,j}$ the Young's modulus at point i at run j , and \bar{E} the sample mean Young's modulus over all runs.

F. Applying the Correlation Pattern to Improve Mechanical Response

The map of correlation gives a direct indication of how the structure responds to a variation of a parameter at a specific location. Changing the base state to incorporate the variation pattern of parameter a (e.g., Young's modulus) can therefore increase or decrease the parameter b (e.g., buckling load).

1. Applying Correlation Pattern to the Structure

To map this correlation pattern to the structure, it is first normalized by fitting it into a range [0, 1]. Using this normalized pattern it is used to redistribute the parameter with the function

$$a_i = a_{min} + (a_{max} - a_{min}) \hat{H}_i \quad (23)$$

where \hat{H}_i is the value of the normalized correlation pattern at a_i .

The distribution of \hat{H} is not necessarily symmetric, making it necessary to manipulate this pattern to improve performance or move the sample mean within a selected range. An extension is therefore introduced to Eq. (23) to

$$a_i = a_{min} + (a_{max} - a_{min}) \hat{H}_i^m \quad (24)$$

in which either the exponent m or range of $a \in [a_{min}, a_{max}]$ can be calculated to ensure that the average value of the property remains unchanged.

In the analyses shown in this paper, a is either a Young's modulus (a functionally graded material) or the thickness of the structure, the parameter b is the linear buckling load. In these analyses a large value for m would result in very local increases in the Young's modulus or thickness. A small value for m would cause localized low values of the distribution. The exponent m and range of the pattern are related. When m is decreased the average value of the pattern increases, whereas increasing m causes it to decrease. There is a unique value of m for every specified range in which the average value (Young's modulus or thickness) remains the same.

2. Calculating Volume and Average Properties in an Analysis

When enhancing the structure it is important to analyze the change in mass or average material property within a structure. Increasing the stiffness of a structure by adding mass or increasing the average Young's modulus is trivial. The volume of elements is calculated by using their shape functions, which represents a mapping between coordinate systems. Taking the definition of a volume element

$$dV = \rho(u_1, u_2, u_3) du_1 du_2 du_3 \quad (25)$$

The volume of an element can be found by integrating dV over the volume of an element. Using the 3D Jacobian

$$J3D = \begin{vmatrix} \frac{\partial N_1^{3D}}{\partial \alpha} & \frac{\partial N_1^{3D}}{\partial \beta} & \frac{\partial N_1^{3D}}{\partial \xi} \\ \frac{\partial N_2^{3D}}{\partial \alpha} & \frac{\partial N_2^{3D}}{\partial \beta} & \frac{\partial N_2^{3D}}{\partial \xi} \\ \frac{\partial N_3^{3D}}{\partial \alpha} & \frac{\partial N_3^{3D}}{\partial \beta} & \frac{\partial N_3^{3D}}{\partial \xi} \end{vmatrix} \quad (26)$$

and using Gauss–Legendre quadrature the volume of an element is integrated numerically as

$$V_i = \sum_{i=1}^N \sum_{j=1}^N \sum_{k=1}^N J3D(x_i, x_j, x_k) w_i w_j w_k \quad (27)$$

where $x_{i,j,k}$ are the integration points in the range $[-1, 1]$, $w_{i,j,k}$ are integration weights, and N is the integration order.

To calculate the average value of the property a weighed integration is done of the volume, which is then divided by the structure’s volume. For a property, n , within a structure this becomes

$$\mu_n = \frac{\sum_{i=1}^N \sum_{j=1}^N \sum_{k=1}^N J3D(x_i, x_j, x_k) p_n(x_i, x_j, x_k) w_i w_j w_k}{\sum_{i=1}^N \sum_{j=1}^N \sum_{k=1}^N J3D(x_i, x_j, x_k) w_i w_j w_k} \quad (28)$$

where $p_n(x_i, x_j, x_k)$ is the property n at integration point x_i, x_j, x_k .

III. Results

The methods discussed in the previous section were applied to two different structures: a square flat plate and a curved panel. Both of these examples analyze variations of the Young’s modulus and the thickness separately. These variations are applied intrusively, by perturbing the mesh in the case of thickness variations, and nonintrusively by changing the scalar value of material properties at integration points in the case of Young’s modulus variations.

A. Rectangular Plate

The first example consists of a rectangular plate of 1×1 m and a thickness of 3 mm, as shown in Fig. 3. It is modeled using a 20×20 mesh with Serendipity Lagrange third-order elements (described in Sec. II.A). The material properties used are $E = 181$ GPa and $\nu = 0.3$. A unit force is applied to the $y = 0$ and $y = 1$ edges as a uniform distributed load on the surface, with a total force of 1 N. Out-of-plane (z) displacement is restricted on all edges; x displacement is also restricted on the $x = 0$ and $x = 1$ edges. The linear buckling load is 16,892 N, with the buckling mode shown in Fig. 4. Before generating the correlation pattern the buckling load and mode were verified using the finite element code DIANA [50].

1. Young’s Modulus Variation

Five thousand runs were made in which a random field with a correlation length $L_c = 0.2$ m was applied to a standard deviation in the Young’s modulus of 1 GPa. An example of such a distribution can

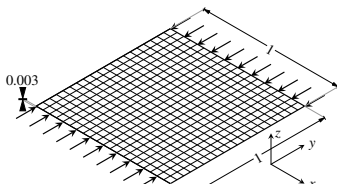


Fig. 3 Rectangular plate, dimensions in m.

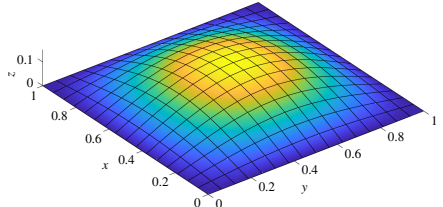


Fig. 4 First buckling mode of the rectangular plate.

be found in Fig. 5. The correlation pattern of the Young’s modulus to first buckling load among all 5000 runs is shown in Fig. 6a. These runs are used to generate correlation patterns with which the Young’s modulus is redistributed in order to increase the linear buckling load. This could be done by using functionally graded materials, where the stiffness varies throughout the geometry.

This pattern is normalized and used to redistribute the Young’s modulus of the plate in the range of 108–254 GPa, which is ± 73 GPa the baseline value. This range is an assumption using data of laser deposition range ratios in Ti6Al4V/TiC functionally graded materials achieved by Mahamood and Akinlabi [51]. Unfortunately, this paper does not include mechanical properties, and the Young’s modulus range is therefore assumed using the deposition ratios achieved. The average Young’s modulus of the analyses was kept equal to that of the baseline analysis (181 GPa). By having a fixed range and a set average in the pattern, it is possible to determine the exponent m in Eq. (24) to ensure that the average Young’s modulus in the plate equals that of the baseline. This procedure is repeated for a variety of property ranges, the trends of which are shown in Fig. 7. The largest increase was found for the range 108–254 GPa, using a scaling parameter of $m = 0.84$. This is a unique value for a specific material range, pattern, and average value of the pattern. The associated material distribution can be found in Fig. 6b; applying the same loads and boundary conditions to the plate results in an 8.6% increase in linear buckling load (18,363 N).

2. Thickness Variation

Thickness is varied over 5000 samples. The fictitious variations have a standard deviation of 5% of thickness with a correlation length of 0.2 m. The correlation of the thickness variation with the linear buckling load can be found in Fig. 8a. The load vector is updated

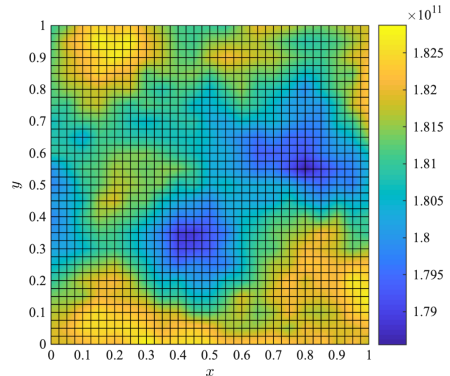


Fig. 5 Example of randomly distributed Young’s modulus on the flat plate, Pa.

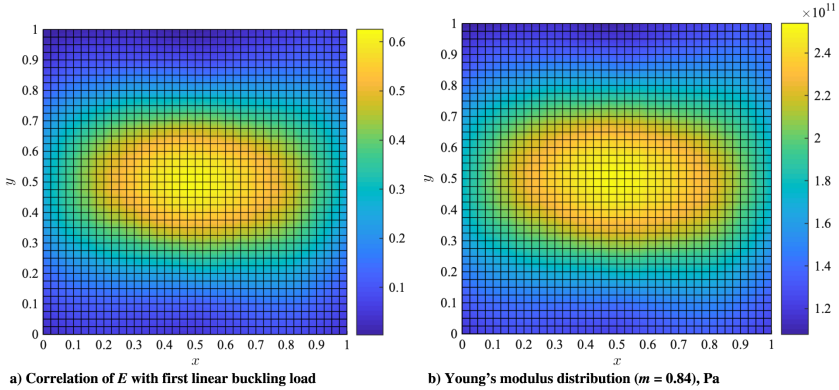


Fig. 6 Calculated correlation pattern and applied Young's modulus distribution of flat plate example.

every step to ensure that the total load magnitude is unit, and is distributed proportional to the local thickness. Analyses were run over a range of thickness between ± 5 and $\pm 50\%$, the results of which can be found in Fig. 9. The best result was found using a range of -50 to 35% of the original thickness (0.0015–0.00405 m), using a scaling coefficient $m = 0.7409$ to retain constant mass. In contrast to the Young's modulus example, the results here are not the best with the largest range. Using a large range causes the scaling parameter used to retain constant mass to be more focused in the material thickening. In this case this would cause a large local increase of bending stiffness while reducing the bending stiffness in other parts of the structure. An optimal is therefore found as a tradeoff between local stiffening and a decrease in stiffness in other areas. It is quite possible that extending the range through sequential iterative steps will provide a better result. Applying this pattern, shown in Fig. 8b increases the linear buckling load by 16.9% to 19,754 N.

3. Interpretation

An interpretation of the results is made using the effect on the prebuckling stress distribution, and the buckling state through buckling mode and strain energy density. The strain energy density gives

an indication of the local stresses and strains that are locally stored through elastic deformation. The center of the plate is stiffened in both parameter studies. By examining the strain energy density with definition $U = (1/2)\epsilon_{ij}\sigma_{ij}$ ([52] p. 122) shown in Fig. 10, it can be deduced that the strain energy density is lower at the center of the plate, where the buckle forms. The reduction is due to a redistribution where the strain energy density is relocated away from the center and toward the loaded edges. The redistribution of strain energy density is much more prominent than the redistribution of prebuckling stresses. The redistribution of the thickness and strain energy causes the buckling mode to change, moving the curvature of the buckled shape from the center toward the edges, as shown in Fig. 11. This effect is due to the local increase of stiffness in the center of the plate, which causes the mode shape to change where the curvature is more prominent at the edges.

B. Curved Panel

As a second example the curved panel shown in Fig. 12a is analyzed. It is a 90° arc of a cylindrical shell with a radius of 0.1 m, thickness of 2 mm, and a length of 0.15 m. A uniformly distributed pressure load 1 N in magnitude is applied on the curved

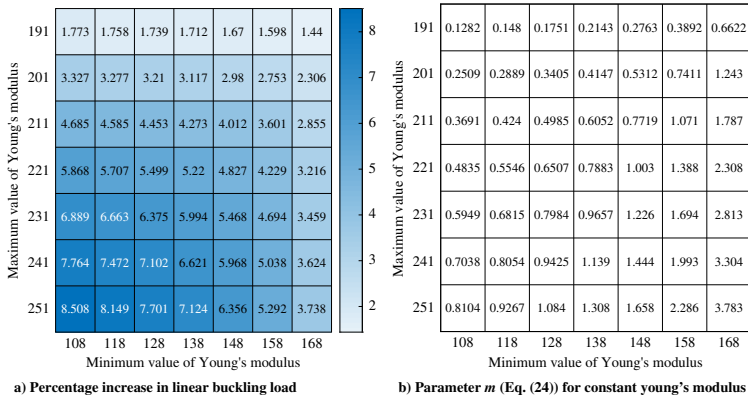


Fig. 7 Linear buckling load improvement of flat plate with Young's modulus variation, retaining baseline average.

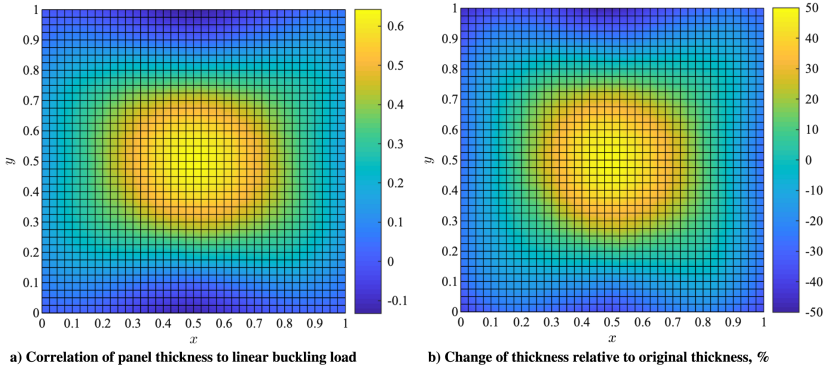


Fig. 8 Correlation pattern and redistribution of thickness within the flat plate.

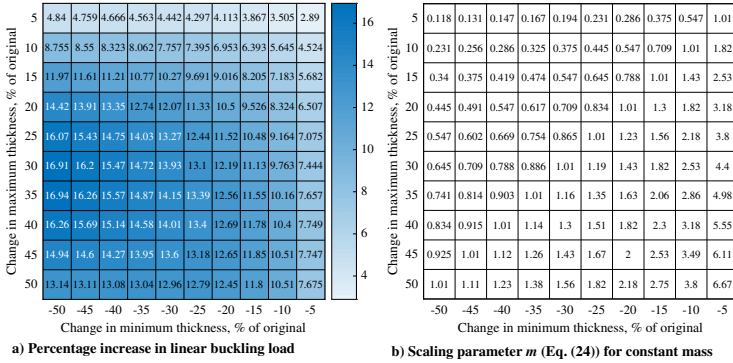


Fig. 9 Flat plate with thickness variation linear buckling load improvement, with constant mass.

edges of the panel, while restricting displacements in the plane of the loaded edges. These boundary conditions differ from an earlier version of this paper [53], in which the same boundary conditions were used for the prebuckling state but had the loaded edges clamped during the eigenvalue analysis. To restrict the rigid body mode in the load direction, two points on the ends of the curve at $y = 0.075$ m are fixed in the load direction. A discretization of 40 SL elements in

radial direction and 40 SL elements in the axial direction was used. Material properties of the previous example ($E = 181$ GPa, $\nu = 0.3$) are also used in this example. Using the CUF implementation the first buckling load of 102,504 N was calculated, and verified using DIANA [50] with a 930 Q20SH element shell model (107,280 N). Figure 13 shows the first linear buckling mode, calculated using the CUF implementation.

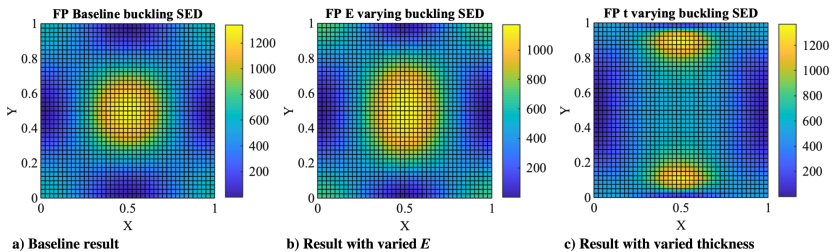


Fig. 10 Strain energy density of the first buckling mode (compression in y), outer surface, $J \cdot m^{-1}$.

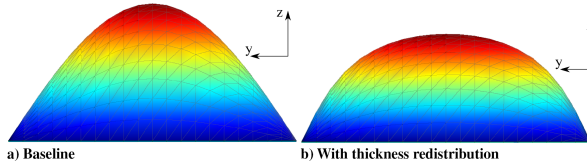


Fig. 11 Linear buckling mode of baseline and thickness varied structure, relative displacement (projection facing unloaded edge).

1. Young's Modulus Variation

A correlation pattern was generated using a total of 10,000 random samples using a correlation length of 0.01 m. During postprocessing the correlation of the structure's Young's modulus with the first buckling mode was computed, as shown in Fig. 14a. An examination of the pattern shows that the panel benefits the most from reinforcements in the center of the straight edges, in the area of the maximum buckling amplitude. Stiffened regions are focused into five zones around the center. As with the flat panel, the increase was studied under a range of minima and maxima. The trends of these analyses are shown in Fig. 15. Using the full range of 108–254 GPa the material distribution of Fig. 14b shows the largest increase in linear buckling load. Using this redistributed stiffness results in a 7.4% increase in linear buckling load to 113,820 N. Applying this stiffness redistribution also causes the prebuckling deformation to change, as is shown in Fig. 16b.

2. Thickness Variation

Thickness variations are analyzed by running 10,000 linear buckling analyses in which the mesh is perturbed proportional to the thickness by a 5% standard deviation. The load vector is updated at every sample, updating ensures that the magnitude on an edge remains unity, and the load is distributed evenly on the surface. Variations are applied to the structure using a correlation length of 0.01 m. Figure 17a shows the pattern of these correlations. A study was done to analyze the improvement in linear buckling load; the resulting trends are shown in Fig. 18. In these analyses the thickness range was changed together with an appropriate scaling parameter m , while retaining the original mesh volume (mass). The greatest increase was found using a range of -50 to 15% of the original thickness, using a scaling factor $m = 1.56$. As was the case with the flat plate example the optimal range is a tradeoff between localized bending stiffness increase and a reduction elsewhere in the structure (due to the constant mass constraint imposed). Applying these ranges improved the linear buckling load by 29%, to 136,702 N. Figure 17b shows the corresponding thickness distribution. The changes in the pre-buckling displacement are shown in Fig. 19, showing a significant decrease in displacement along the unloaded edges.

3. Interpretation

As was done for the flat plate the interpretation focused on the prebuckling stress and the strain energy density of the buckling mode. Changes in the prebuckling stress in the load (y) direction reduce in areas where buckles form, particularly for the thickness varying structure, as shown in Fig. 20c. At the same time the buckling strain energy density ($U = (1/2)\epsilon_{ij}\sigma_{ij}$ ([52] p. 122) of the structures was

also redistributed. The original structure had a concentration of strain energy along the unsupported edges, which decreased in the Young's modulus-tailored structure, and even more so in the thickness-tailored structure. Changes in the prebuckling stress pattern are more prominent than changes in strain energy density, which differs from the previous example. Increases in buckling strain energy density at the corners of the thickness-tailored structure is due to the local decrease in thickness, which causes a redistribution of the applied force. This influences the load path of forces applied to the structure, allowing these to be focused in areas less sensitive to high stresses.

C. Effect of Correlation Length

Patterns are generated using random variations of the Young's modulus or thickness throughout the structure. Variations are correlated to each other, meaning that points close to each other are related, more so than points far apart from each other. Patterns of correlations shown in this section are similarly related. A comparison of the curved panel thickness example is shown in Fig. 21, where the thickness correlation of the curved panel is shown for a correlation length of 0.05 and 0.01 m. Both analyses are run 10,000 times, but it is clear that the 0.05 m pattern appears to be more converged. It is also clear that the pattern with a correlation length of 0.01 m is different, preferring a fairly thin strip along the edges instead of the larger areas along the off center areas of the panel.

Similarly an analysis was run in which the flat panel analysis of Sec. III.A.1 was run with a correlation length of 1 m. A round pattern was generated instead of an oval pattern. The correlation length in this context can be interpreted as a characteristic pattern minimum feature length. A shorter length, while giving more resolution to the pattern, also causes the pattern to take longer to converge.

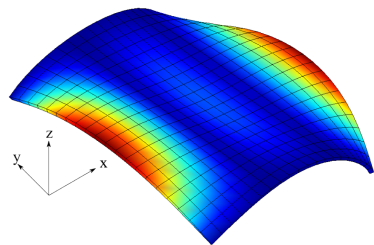


Fig. 13 First linear eigenmode of the curved panel, compression in y.

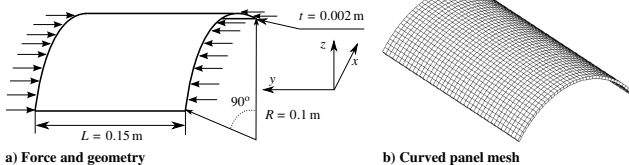


Fig. 12 Curved panel structure.

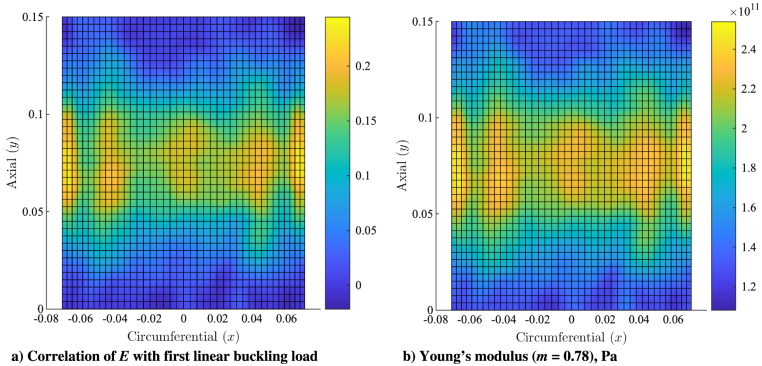


Fig. 14 Calculated correlation pattern and applied stiffness distribution.

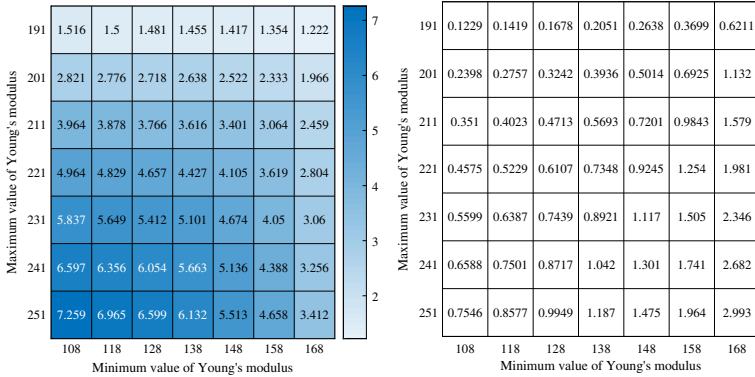


Fig. 15 Improvement over a range of Young's modulus of the curved panel, with average value equalling the baseline Young's modulus.

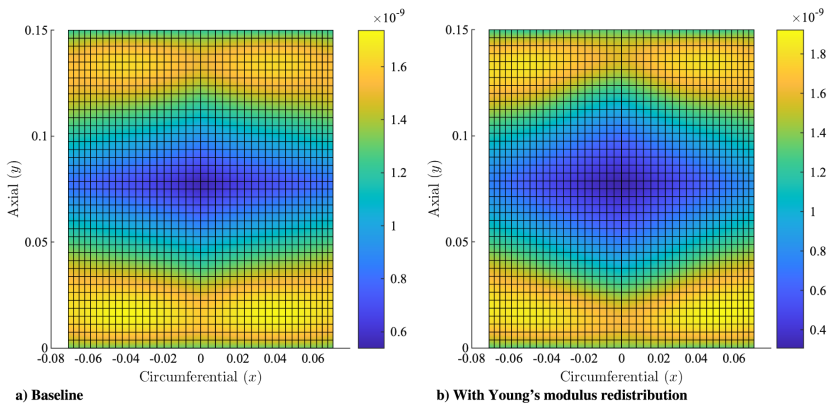
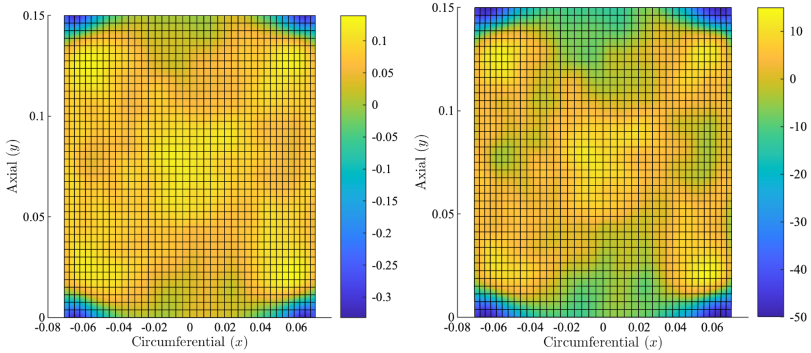
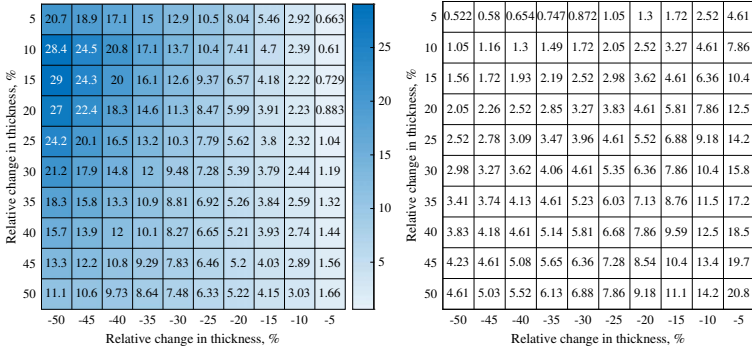


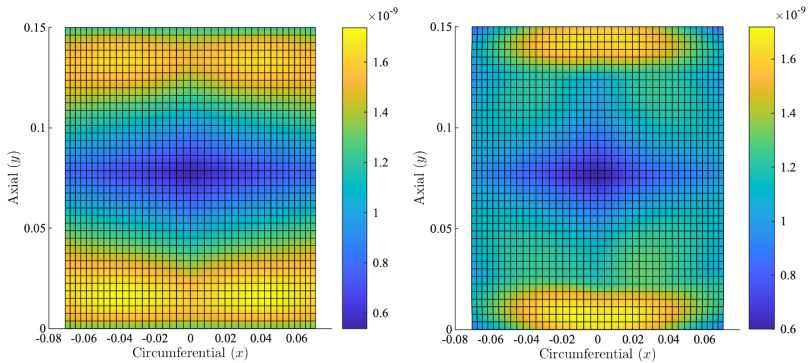
Fig. 16 Prebuckling displacement of curved panel, m .



a) Correlation of thickness with first linear buckling load b) Thickness change ($m = 1.56$), % of original thickness
Fig. 17 Calculated correlation pattern and applied thickness distribution of curved panel.



a) Percentage increase in linear buckling load b) Scaling parameter m (Eq. (24)) for constant mass
Fig. 18 Improvement of buckling load of curved panel over a range of thickness ranges, with constant mass.



a) Baseline b) With thickness distribution
Fig. 19 Prebuckling displacement of curved panel change with thickness variation, m .

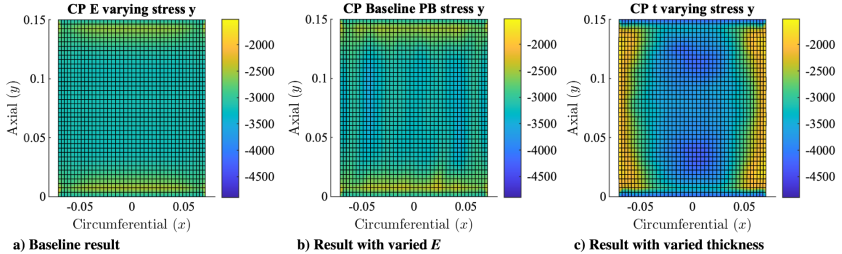


Fig. 20 Prebuckling stress in the y direction for three different curved panel analyses with compression in y , Pa.

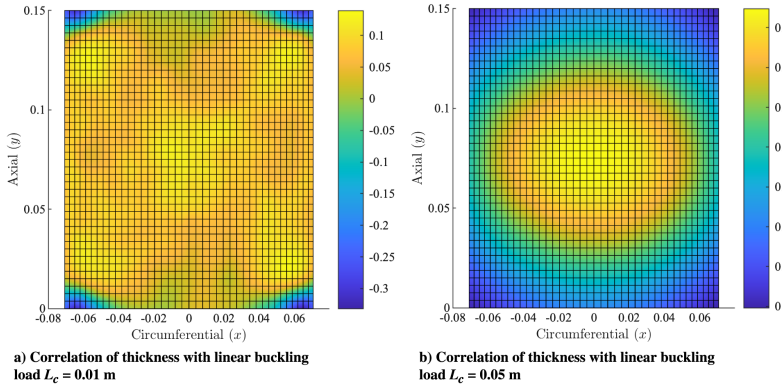


Fig. 21 Comparison to correlation patterns of thickness variations of curved panel with different correlation lengths.

To analyze how the two patterns compare, analyses were done in which the thickness variation was compared. The 0.01 m pattern of Fig. 21a shows an increase of 29% using $m = 1.56$ over a range of change from -50 to 15% of the original thickness. A similar analysis was done for a correlation length of 0.05 m. The best improvement was found in the range -50 to 15% , which showed an increase of the linear buckling load of 9.4% , using a scaling factor of $m = 0.44$. Comparing this to the result generated with a smaller correlation length gives only a third of the increase. A shorter correlation length has a better potential enhancement, at a higher computational expense.

IV. Conclusions

Through stochastic analyses of randomized local variations of, for example, thickness, it is possible to glean information on the average local sensitivity of the structure to a variation of that parameter. Using this information it is possible to tailor structures to enhance their mechanical response. Numerical examples have demonstrated such effects through examples that improve the linear buckling load of two structures through stiffness redistribution, by varying either the Young's modulus or the thickness locally. The new stiffness distributions cause the bending stiffness to increase in areas where buckling deformation is most significant. Another effect is that the prebuckling stress tends to reduce in those areas; the combined effect of the stiffness and stress redistributions is that the strain energy density of sensitive areas reduces. Analyses over multiple correlation lengths were accomplished. An overall trend shows that correlation patterns with a shorter length generate patterns that perform better. This result is due to the pattern having a higher resolution (i.e., is less smooth), allowing enhancements to be more localized.

Correlation patterns are different depending on which parameter (e.g., Young's modulus or thickness) is varied; in the examples shown, this is due to two effects: the first being the effect variations have on the stiffness. Both parameters increase in-plane stiffness linearly with their variation. Bending stiffness, on the other hand, is proportional to $E t^3$; thickness variations therefore affect the bending stiffness of the structure much more than varying the Young's modulus. Variations of the thickness cause another effect; force is applied to the edge of the structure as a distributed load. When the thickness decreases, the load is redistributed away from the area and into other areas (as the area decreases locally); this can help redirect load to parts of the structure that are less sensitive. The corners of the curved panel depict this; these areas are thinner so as to decrease the relative amount of load applied in those areas close to the edge. In this way the thickness distribution also tailors the load path while tailoring the stiffness.

Future extensions can broaden the use of the method. Local stress amplitude reduction during cyclic loading could also be decreased, which could lead to an improved fatigue life. The results so far are limited to linear results, and it is also possible to run these analyses using nonlinear analyses at a specific load level or buckling load.

Potential use of this approach on additive manufactured materials and structures is also of interest. Extra design freedoms facilitated by these production processes make it possible to create complex geometry, which would not be economical with traditional manufacturing processes. When the manufacturing process is well understood and the variations can be quantified in a representative fashion, the effects on the structural performance of the tailored structure can be directly compared, potentially enabling the structure simultaneously to be

more highly tailored and have excellent performance through the same design process.

Adding multiple design iterative stages can also lead to further improvement of linear and, potentially, nonlinear problems. Results shown in Figs. 9a and 18a indicate that maximizing the parameter range does not automatically lead to the best improvement. To find an optimal distributions, successive iterations will likely be needed. By applying the random fields to out-of-plane displacements it may also be possible to add tailored variations to affect the behavior. Fields can be generated in 2D, as done here, but random fields can also be generated for 3D structures. Optimization using these methods does not necessarily require a converged correlation pattern; the patterns could be perturbed and modified in successive iterations each time an improvement is found. It is noted that convergence would likely improve by postprocessing on the patterns, using symmetry, for instance.

Acknowledgments

This project has received funding from the European Union's Horizon 2020 research and innovation program under the Marie Skłodowska-Curie grant agreement No. 642121. This work was carried out using the computational facilities of the Advanced Computing Research Centre, University of Bristol (<http://www.bris.ac.uk/acrc/>) as well as computational facilities within the Institute of Structural Analysis at Leibniz University Hannover. Paul M. Weaver would like to thank the Science Foundation Ireland for support under its Research Professor scheme (Variacomp: 15/RP/2773) and the Royal Society for its Wolfson Merit Award.

References

- [1] Stefanou, G., "The Stochastic Finite Element Method: Past, Present and Future," *Computer Methods in Applied Mechanics and Engineering*, Vol. 198, Nos. 9–12, 2009, pp. 1031–1051. <https://doi.org/10.1016/j.cma.2008.11.007>
- [2] Ghanem, R. G., and Spanos, P. D., "Spectral Stochastic Finite-Element Formulation for Reliability Analysis," *Journal of Engineering Mechanics*, Vol. 117, No. 10, 1991, pp. 2351–2372. [https://doi.org/10.1061/\(ASCE\)0733-9399\(1991\)117:10\(2351\)](https://doi.org/10.1061/(ASCE)0733-9399(1991)117:10(2351))
- [3] Der Kiureghian, A., and Ke, J.-B., "The Stochastic Finite Element Method in Structural Reliability," *Probabilistic Engineering Mechanics*, Vol. 3, No. 2, 1988, pp. 83–91. [https://doi.org/10.1016/0266-8920\(88\)90019-7](https://doi.org/10.1016/0266-8920(88)90019-7)
- [4] Spanos, P. D., and Zeldin, B. A., "Monte Carlo Treatment of Random Fields: A Broad Perspective," *Applied Mechanics Reviews*, Vol. 51, No. 3, 1998, pp. 219–237. <https://doi.org/10.1115/1.3098999>
- [5] Papadopoulos, V., Stefanou, G., and Papadrakakis, M., "Buckling Analysis of Imperfect Shells with Stochastic Non-Gaussian Material and Thickness Properties," *International Journal of Solids and Structures*, Vol. 46, Nos. 14–15, 2009, pp. 2800–2808. <https://doi.org/10.1016/j.jssolstr.2009.03.006>
- [6] Vorechovsky, M., and Novák, D., "Simulation of Random Fields for Stochastic Finite Element Analysis," *Icoassur*, Vol. 5, June 2005, pp. 2545–2552. <https://pdfs.semanticscholar.org/0570/dac368ae71dd6d980ecc78bf25d8b755856.pdf>
- [7] Vryzidis, I., Stefanou, G., and Papadopoulos, V., "Stochastic Stability Analysis of Steel Tubes with Random Initial Imperfections," *Finite Elements in Analysis and Design*, Vol. 77, Dec. 2013, pp. 31–39. <https://doi.org/10.1016/j.finel.2013.09.002>
- [8] Tootkaboni, M., Graham-Brady, L., and Schafer, B. W., "Geometrically Non-Linear Behavior of Structural Systems with Random Material Property: An Asymptotic Spectral Stochastic Approach," *Computer Methods in Applied Mechanics and Engineering*, Vol. 198, Nos. 37–40, 2009, pp. 3173–3185. <https://doi.org/10.1016/j.cma.2009.05.014>
- [9] Van den Broek, S., Jansen, E., Minerá, S., Weaver, P. M., and Rolles, R., "Effect of Spatially Varying Material Properties on the Post-Buckling Behaviour of Composite Panels Utilising Geodesic Stochastic Fields," *Proceedings of the 6th Aircraft Structural Design Conference*, Bristol, 2018.
- [10] Sasikumar, P., Suresh, R., Vijayagosh, P. K., and Gupta, S., "Experimental Characterisation of Random Field Models for CFRP Composite Panels," *Composite Structures*, Vol. 120, Feb. 2015, pp. 451–471. <https://doi.org/10.1016/j.compstruc.2014.10.023>
- [11] Sriramula, S., and Chryssanthopoulos, M. K., "An Experimental Characterisation of Spatial Variability in GFRP Composite Panels," *Structural Safety*, Vol. 42, May 2013, pp. 1–11. <https://doi.org/10.1016/j.strusafe.2013.01.002>
- [12] Sriramula, S., and Chryssanthopoulos, M. K., "Quantification of Uncertainty Modelling in Stochastic Analysis of FRP Composites," *Composites Part A: Applied Science and Manufacturing*, Vol. 40, No. 11, 2009, pp. 1673–1684. <https://doi.org/10.1016/j.compositesa.2009.08.020>
- [13] Lekou, D. J., and Philippidis, T. P., "Mechanical Property Variability in FRP Laminates and Its Effect on Failure Prediction," *Composites Part B: Engineering*, Vol. 39, Nos. 7–8, 2008, pp. 1247–1256. <https://doi.org/10.1016/j.compositesb.2008.01.004>
- [14] Saenz-Castillo, D., Martín, M., Calvo, S., Rodríguez-Lence, F., and Güemes, A., "Effect of Processing Parameters and Void Content on Mechanical Properties and NDI of Thermoplastic Composites," *Composites Part A: Applied Science and Manufacturing*, Vol. 121, Jan. 2019, pp. 308–320. <https://doi.org/10.1016/j.compositesa.2019.03.035>
- [15] Manta, A., Gresil, M., and Soutis, C., "Infrared Thermography for Void Mapping of a Graphene/Epoxy Composite and its Full-Field Thermal Simulation," *Fatigue and Fracture of Engineering Materials and Structures*, Vol. 42, No. 7, 2019, pp. 1441–1453. <https://doi.org/10.1111/ffe.12980>
- [16] Gurdal, Z., and Olmedo, R., "In-Plane Response of Laminates with Spatially Varying Fiber Orientations—Variable Stiffness Concept," *AIAA Journal*, Vol. 31, No. 4, 1993, pp. 751–758. <https://doi.org/10.2514/3.11613>
- [17] Blom, A. W., Stickler, P. B., and Gurdal, Z., "Optimization of a Composite Cylinder Under Bending by Tailoring Stiffness Properties in Circumferential Direction," *Composites Part B: Engineering*, Vol. 41, No. 2, 2010, pp. 157–165. <https://doi.org/10.1016/j.compositesb.2009.10.004>
- [18] Burgueno, R., Hu, N., Heeringa, A., and Lajnef, N., "Tailoring the Elastic Postbuckling Response of Thin-Walled Cylindrical Composite Shells Under Axial Compression," *Thin-Walled Structures*, Vol. 84, Nov. 2014, pp. 14–25. <https://doi.org/10.1016/j.tws.2014.05.009>
- [19] Chi, S. H., and Chung, Y. L., "Mechanical Behavior of Functionally Graded Material Plates Under Transverse Load—Part I: Analysis," *International Journal of Solids and Structures*, Vol. 43, No. 13, 2006, pp. 3657–3674. <https://doi.org/10.1016/j.jssolstr.2005.04.011>
- [20] Hu, N., and Burgueno, R., "Elastic Postbuckling Response of Axially-Loaded Cylindrical Shells with Seeded Geometric Imperfection Design," *Thin-Walled Structures*, Vol. 96, Sept. 2015, pp. 256–268. <https://doi.org/10.1016/j.tws.2015.08.014>
- [21] Cox, B. S., Groh, R. M., Avitabile, D., and Pirrera, A., "Modal Nudging in Nonlinear Elasticity: Tailoring the Elastic Post-Buckling Behaviour of Engineering Structures," *Journal of the Mechanics and Physics of Solids*, Vol. 116, July 2018, pp. 135–149. <https://doi.org/10.1016/j.jmps.2018.03.025>
- [22] Hu, N., and Burgueno, R., "Harnessing Seeded Geometric Imperfection to Design Cylindrical Shells with Tunable Elastic Postbuckling Behavior," *Journal of Applied Mechanics*, Vol. 84, No. 1, 2017, Paper 011003. <https://doi.org/10.1115/1.4034827>
- [23] Hu, N., and Burgueno, R., "Cylindrical Shells with Tunable Postbuckling Features Through Non-Uniform Patterned Thickening Patches," *International Journal of Structural Stability and Dynamics*, Vol. 18, No. 2, 2018, Paper 1850026. <https://doi.org/10.1142/S0219455118500268>
- [24] Li, Y. W., Elishakoff, I., and Starnes, J. H., "Axial Buckling of Composite Cylindrical Shells with Periodic Thickness Variation," *Computers and Structures*, Vol. 56, No. 1, 1995, pp. 65–74. [https://doi.org/10.1016/0045-7949\(94\)00527-A](https://doi.org/10.1016/0045-7949(94)00527-A)
- [25] Chen, Z., Yang, L., Cao, G., and Guo, W., "Buckling of the Axially Compressed Cylindrical Shells with Arbitrary Axisymmetric Thickness Variation," *Thin-Walled Structures*, Vol. 60, Nov. 2012, pp. 38–45. <https://doi.org/10.1016/j.tws.2012.07.015>
- [26] Guest, J. K., "Optimizing the Layout of Discrete Objects in Structures and Materials: A Projection-Based Topology Optimization Approach," *Computer Methods in Applied Mechanics and Engineering*, Vol. 283, Jan. 2015, pp. 330–351. <https://doi.org/10.1016/j.cma.2014.09.006>
- [27] Li, Y. W., Elishakoff, I., Starnes, J. H., and Bushnell, D., "Effect of the Thickness Variation and Initial Imperfection on Buckling of Composite Cylindrical Shells: Asymptotic Analysis and Numerical Results by BOSOR4 and PANDA2," *International Journal of Solids*

- and Structures, Vol. 34, No. 28, 1997, pp. 3755–3767.
[https://doi.org/10.1016/S0020-7683\(96\)00230-2](https://doi.org/10.1016/S0020-7683(96)00230-2)
- [28] Lagaros, N. D., and Papadopoulos, V., “Optimum Design of Shell Structures with Random Geometric, Material and Thickness Imperfections,” *International Journal of Solids and Structures*, Vol. 43, Nos. 22–23, 2006, pp. 6948–6964.
<https://doi.org/10.1016/j.jsoistr.2006.02.019>
- [29] Sliiseri, J., and Rocens, K., “Optimal Design of Composite Plates with Discrete Variable Stiffness,” *Composite Structures*, Vol. 98, April 2013, pp. 15–23.
<https://doi.org/10.1016/j.compstruct.2012.11.015>
- [30] Lee, K. H., and Park, G. J., “Robust Optimization Considering Tolerances of Design Variables,” *Computers and Structures*, Vol. 79, No. 1, 2001, pp. 77–86.
[https://doi.org/10.1016/S0045-7949\(00\)00117-6](https://doi.org/10.1016/S0045-7949(00)00117-6)
- [31] Chen, X., Hasselman, T., Neill, D., Chen, X., Hasselman, T., and Neill, D., “Reliability Based Structural Design Optimization for Practical Applications,” AIAA Paper 1997-1403, 2013.
<https://doi.org/10.2514/6.1997-1403>
- [32] Guo, X., Zhang, W., and Zhang, L., “Robust Structural Topology Optimization Considering Boundary Uncertainties,” *Computer Methods in Applied Mechanics and Engineering*, Vol. 253, Jan. 2013, pp. 356–368.
<https://doi.org/10.1016/j.cma.2012.09.005>
- [33] Minera, S., “Analysis and Design of Buckling Resistant Thin-Walled Structures via Computationally Efficient 3D Stress Analysis,” Ph.D. Thesis, Univ. of Bristol, Bristol, England, U.K., 2019.
- [34] Carrera, E., Cinefra, M., Petrolo, M., and Zappino, E., *Finite Element Analysis of Structures Through Unified Formulation*, Wiley Online Library, 2014, Chap. 5.
<https://doi.org/10.1002/9781118536643>
- [35] Minera, S., Patni, M., Carrera, E., Petrolo, M., Weaver, P. M., and Pirrera, A., “Three-Dimensional Stress Analysis for Beam-Like Structures Using Serendipity Lagrange Shape Functions,” *International Journal of Solids and Structures*, Vols. 141–142, June 2018, pp. 279–296.
<https://doi.org/10.1016/j.jsoistr.2018.02.030>
- [36] Patni, M., “An Efficient Numerical Framework for Capturing Localised 3D Stress Fields in Laminated Composites,” Ph.D. Thesis, Univ. of Bristol, Bristol, U.K., 2019.
- [37] Carrera, E., Giunta, G., and Petrolo, M., *Beam Structures: Classical and Advanced Theories*, Wiley, Chichester, England, U.K., 2011.
<https://doi.org/10.1002/9781119978565>
- [38] Pagani, A., and Carrera, E., “Unified Formulation of Geometrically Nonlinear Refined Beam Theories,” *Mechanics of Advanced Materials and Structures*, Vol. 25, No. 1, 2018, pp. 15–31.
<https://doi.org/10.1080/15376494.2016.1232458>
- [39] Patni, M., Minera, S., Bisagni, C., Weaver, P., and Pirrera, A., “Geometrically Nonlinear Finite Element Model for Predicting Failure in Composite Structures,” *Composite Structures*, Vol. 225, May 2019, Paper 111068.
<https://doi.org/10.1016/j.compstruct.2019.111068>
- [40] Cook, R. D., Malkus, D. S., Plesha, M. E., and Witt, R. J., *Concepts and Applications of Finite Element Analysis*, 4th ed., Vol. 4, Wiley, New York, 2002. <https://www.wiley.com/en-us/Concepts+and+Applications+of+Finite+Element+Analysis>.
- [41] Pagani, A., de Miguel, A. G., and Carrera, E., “Cross-Sectional Mapping for Refined Beam Elements with Applications to Shell-Like Structures,” *Computational Mechanics*, Vol. 59, No. 6, 2017, pp. 1031–1048.
<https://doi.org/10.1007/s00466-017-1390-7>
- [42] Szabó, B., and Babuška, I., *Introduction to Finite Element Analysis: Formulation, Verification and Validation*, Vol. 35, John Wiley & Sons Ltd., Chichester, U.K., 2011, Chap. 5.
<https://doi.org/10.1002/9781119993834>
- [43] Geuzaine, C., and Remacle, J. F., “Gmsh: A 3-D Finite Element Mesh Generator with Built-In Pre- and Post-Processing Facilities,” *International Journal for Numerical Methods in Engineering*, Vol. 79, No. 11, 2009, pp. 1309–1331.
<https://doi.org/10.1002/nme.2579>
- [44] Davis, M. W., “Production of Conditional Simulations via the LU Triangular Decomposition of the Covariance Matrix,” *Mathematical Geology*, Vol. 19, No. 2, 1987, pp. 91–98.
<https://doi.org/10.1007/BF00898189>
- [45] Sudret, B., and Kiureghian, A. D., *Stochastic Finite Element Methods and Reliability: A State-of-the-Art Report*, Univ. of California, Berkeley, Nov. 2000, p. 189, <https://www.1.ethz.ch/ibk/su/publications/Reports/SFE-report-Sudret.pdf>.
- [46] Dekking, F. M., Kraaikamp, C., Lophuää, H. P., and Meester, L. E., *A Modern Introduction to Probability and Statistics: Understanding Why and How*, Springer Science & Business Media, London, 2005, Chap. 10.
<https://doi.org/10.1007/1-84628-168-7>
- [47] Scarth, C., Adhikari, S., Cabral, P. H., Silva, G. H. C., do Prado, A. P., Higino, P., Silva, G. H. C., and do Prado, A. P., “Random Field Simulation over Curved Surfaces: Applications to Computational Structural Mechanics,” *Computer Methods in Applied Mechanics and Engineering*, Vol. 345, March 2019, pp. 283–301.
<https://doi.org/10.1016/j.cma.2018.10.026>
- [48] Crane, K., Weischedel, C., and Wardetzky, M., “The Heat Method for Distance Computation,” *Communications of the ACM*, Vol. 60, No. 11, 2017, pp. 90–99.
<https://doi.org/10.1145/3131280>
- [49] Li, C.-C., and Der Kiureghian, A., “Optimal Discretization of Random Fields,” *Journal of Engineering Mechanics*, Vol. 119, No. 6, 1993, pp. 1136–1154.
[https://doi.org/10.1061/\(ASCE\)0733-9399\(1993\)119:6\(1136\)](https://doi.org/10.1061/(ASCE)0733-9399(1993)119:6(1136))
- [50] “DIANA Finite Element Analysis User’s Manual Release 10.3,” Tech. Rept., Diana FEA, 2019, <https://dianafea.com/manuals/d103/Diana.html>.
- [51] Mahamood, R. M., and Akinlabi, E. T., “Laser Metal Deposition of Functionally Graded Ti6Al4V/TiC,” *Materials and Design*, Vol. 84, Nov. 2015, pp. 402–410.
<https://doi.org/10.1016/j.matdes.2015.06.135>
- [52] Sadd, M. H., *Elasticity-Theory, Applications, and Numerics*, 2nd ed., Academic Press, Oxford, U.K. and Waltham, MA, 2014, p. 122.
<https://doi.org/10.1016/c2012-0-06981-5>
- [53] van den Broek, S., Minera, S., Pirrera, A., Weaver, P. M., Jansen, E. L., and Rolles, R., “Enhanced Deterministic Performance of Panels Using Stochastic Variations of Geometric and Material Parameters,” *Proceedings of the 2019 AIAA Science and Technology Forum and Exposition*, AIAA Paper 2019-0511, 2019.
<https://doi.org/10.2514/6.2019-0511>

R. Ghanem
Associate Editor

PAPER C: IMPROVING FATIGUE LIFE OF PRINTED STRUCTURES

Imperfection inspires invention, imagination, creativity. It stimulates. The more I feel imperfect, the more I feel alive.

— Jhumpa Lahiri

The paper presented in this chapter describes how local thickness changes analyzed in stochastic analyses can be used to increase the fatigue life of a structure. Validation of the results is done on 3D-printed samples. First published as

van den Broek, S. *et al.* Improving the fatigue life of printed structures using stochastic variations. *Progress in Additive Manufacturing*. ISSN: 2363-9520. doi:10.1007/s40964-022-00296-5 (2022)

AUTHOR CONTRIBUTIONS

SANDER VAN DEN BROEK The principal author of the paper, implementor of the approach described, and the corresponding author.

JOHANNES WOLFF Provided input on the 3D-printing process, and provided the samples used for validation.

SVEN SCHEFFLER Provided technical suggestions and support during testing.

CHRISTIAN HÜHNE Provided technical suggestions during the development of the approach.

RAIMUND ROLFES Provided technical suggestions and input during the development of the approach.



Improving the fatigue life of printed structures using stochastic variations

Sander van den Broek¹ · Johannes Wolff² · Sven Scheffler¹ · Christian Hühne² · Raimund Rolfes¹

Received: 10 July 2021 / Accepted: 27 March 2022
© The Author(s) 2022

Abstract

Additive manufacturing allows designers to create geometries that would not be possible or economical to manufacture using traditional manufacturing processes. Production with these technologies does, however, introduce a large amount of variation and additional unknowns. These random variations from idealized geometry or material properties can harm the performance of the design. The current work presents an approach to improve the fatigue life of such structures, and simultaneously reduce its influence from random variations in local thickness. Following an initial numerical study, the results are experimentally validated. Experimental results show a significant improvement in fatigue life in the redesigned sample with a tailored thickness distribution.

Keywords Random field · Robust design · Fatigue improvement · Thickness tailoring · Additive manufacturing

1 Introduction

Load conditions of structures often change during operation. Cyclic changes in the stress state of a structure can cause cumulative damage, leading to fatigue failure after a certain number of cycles. Certain structural features, such as holes, slots, and sharp edges, cause stress concentrations that accelerate fatigue failure. For many of these features, it is best to avoid them, but holes are sometimes necessary due to cable routing, water drainage, pressure-equalizing, or other reasons. Designs can be adapted in these cases to minimize any adverse effects and reduce the effects of stress concentrations, which can induce fatigue failure.

Additive Manufacturing (AM) is a term used for different manufacturing technologies that create a structure by successively adding material layer by layer [15, 16]. A wide range of materials can be used with these techniques, including metals, polymers, and resins. These techniques selectively place or harden material using direct printing, laser sintering, photopolymerization, or another process.

The extra design freedom offered by AM techniques allows for an economical fabrication of components with very complex geometries, which are not feasible with traditional manufacturing techniques [28]. Nevertheless, since different AM techniques exhibit different design limitations, it is crucial to keep process type and necessary support structures in mind during planning and designing. Manufacturability can be assured by adding constraints to the topology optimization by adding length-scale controls [25, 39], non-enclosed void [27], and overhang constraints that limits the geometry to shapes which are less likely to collapse during manufacturing [23, 31]. Some AM technologies also cause an anisotropic behavior of the printed components, which must be taken into account during the design process [7].

The fatigue behavior can be improved using a design process that shapes the structure to minimize stresses within a given design volume [30]. Keshavarzzadeh et al. [20] showed that a more robust design with respect to random variations of geometry, material, and loads is possible by taking random variations into account during the design process. When it comes to fatigue, there are some hurdles to overcome in specific AM processes.

The most popular process used for polymers is Fused Filament Fabrication (FFF). FFF involves extruding molten plastic filament through a movable nozzle. Strands between 0.05 and 0.8 mm in diameter are deposited parallel in two-dimensional layers and fused to the previous layer during

✉ Sander van den Broek
s.vandenbroek@isd.uni-hannover.de

¹ Institute of Structural Analysis, Leibniz University Hannover, Appelstr. 9A, 30167 Hannover, Germany

² Deutsches Zentrum für Luft- und Raumfahrt (DLR), Lilienthalplatz 7, 38108 Brunswick, Germany

deposition. In this way, a layer-by-layer manufacturing process generates three-dimensional components. Within the FFF process, Chacón et al. and Wu et al. [5, 38] showed that the stiffness, strength, and fatigue performance of a printed component are directly influenced by manufacturing process parameters such as the printing direction as well as the equipment used. Generally, the build-up direction is less robust and more susceptible to brittle failure than other directions [5]. Another parameter is the raster angle, referring to the printing direction which dominates in a layer. The ideal raster angle depends on the load and resulting stresses in the structure, the desired stiffness [26, 38], and fatigue requirements [13]. The extrusion and nozzle movement also influences the thickness of printed layers. The exact effects of the change in layer thickness vary depending on the build-up direction and stress state of the structure.

In most cases, it is advantageous to orient the raster angle in the main direction of the load, thereby orienting the filaments into the principal stress. Other design and process parameters can also influence the material parameters, such as the type of reinforcement used in fiber-reinforced filaments and the fiber volume fraction [6]. Predicting the exact mechanical properties of the manufactured materials becomes quite complex, especially when variations introduced by machine and filament batch are also taken into account. Work done by Zou et al. [40] tries to predict mechanical properties while varying some of the discussed parameters, but these are still only estimates given to the inherent complexity.

These parameters can affect the semi-crystalline structure of an FFF structure, but more importantly, affect the bonding of filaments added at every layer. With the right printing parameters, Young's modulus within a printed layer can be nearly identical in longitudinal and transverse directions. In the build-up direction the Young's modulus can vary due to inter-layer contact differences and polymer crystallization. Conversely, the ultimate tensile stress in the build-up direction is usually significantly lower, showing more brittle behavior than in the printing plane [33]. Analysis of experimental results by Ezeh and Susmel [13] shows that the logarithmic slope in an s - n curve is the same in all directions when scaled from the ultimate tensile stress.

Even when the best effort is made to control manufacturing parameters, an increase relative to traditional approaches still exists in the uncertainty in the material's strength, stiffness, and fatigue resilience. Controlling the process and assuring consistent performance is much more complex with an additive manufacturing technique such as FFF than traditional approaches, e.g., injection molding. Many opportunities exist in the FFF process for improper adhesion to form between filaments and for voids to form between filaments and layers in a structure, to name two sources of imperfections. Work done by Iragi et al. [19] has shown that a large

amount of deviation from the expected performance can be traced down to such microstructure imperfections that are introduced during manufacturing.

Overcoming these uncertainties introduced by FFF manufacturing to improve fatigue life requires a robust design that is not as quickly affected by variations. This paper presents an approach for improving the fatigue life of a thin-walled, FFF-manufactured structure by a mass-neutral shape adaptation. Herein, only the thickness is varied, which is of particular interest for thin-walled structures in which the shape is fixed due to e.g., aerodynamic flow considerations. An example of this would be the inner structure of a suction-panel wing-box designed to facilitate laminar flow over the outer surface of an aircraft wing. Such a structure may consist of gyroid unit cells of varying sizes to facilitate a specific pressure drop. Herein, the thickness of the unit cells can be varied to reduce stress-induced fatigue while not having a significant effect on the internal airflow. The approach used in this paper utilizes stochastic analyses to simulate the effects of local changes in thickness. Then, through post-processing, the correlation is computed between local thickness changes and the estimated influence on the fatigue life. Such a correlation pattern gives a map of the influence local changes have on fatigue life. Applying this pattern to modify the local thickness of the structure tailors the structure to increase its fatigue life. Using an open-hole structure as an example the approach is demonstrated numerically in Sect. 3, leading to a modified thickness distribution of the original design. Following numerical analyses, a series of experiments demonstrate the potential of this approach on an actual FFF open-hole specimen is presented in Sect. 4.

2 Methodology

The approach used to improve the fatigue life of a structure is based on earlier work on buckling loads presented in [3, 4]. This approach uses random fields to generate random patterns of thickness distributions within a thin-walled structure. These variations are compared to their effect on initial fatigue failure, generating a pattern of correlated values. Using this pattern material is redistributed, postponing initial failure, while at the same time creating a more robust structure.

2.1 Random field generation

Random thickness distributions are generated using random fields. Many techniques exist to generate random fields [18, 34]. Fields can be represented through continuous functions in space, usually a sum of functions. Sums of functions can be generated through a Karhunen-Loève (KL) expansion [35] or Fourier series for instance [22]. Another approach is to

generate fields directly on points in space (such as nodes in a finite element model). Fields can be generated on those points through decomposition of the covariance matrix [8], using spatial averaging [36] or fast Fourier transformations [32].

Vectors representing values of the field on finite element nodes are generated using a technique known as Covariance Matrix Decomposition (CMD). CMD makes it possible to create random vectors in which entries have a specified correlation to each other. The choice for CMD is made because it is easy to implement, accurate, and has few limitations, especially for small to mid-sized models. The current approach generates fields using the finite element model nodes, giving thickness values at every structural node. Within the current work, correlation is a function of the physical distance between points on the structure. Correlation of two points i and j in field \mathbf{h} is defined as [9, ch. 10]

$$\rho_{h_i, h_j} = \frac{\text{cov}(h_i, h_j)}{\sigma_i \sigma_j} = \frac{E[(h_i - \mu_i)(h_j - \mu_j)]}{\sigma_i \sigma_j}, \tag{1}$$

where E is the expectation operator and equals the mean value over an infinite amount of samples. Parameters μ and σ are the mean and standard deviation. The functions used within this work to determine the correlation of points on the structure to each other are

$$\rho_I = e^{-\frac{\Delta L}{L_c}} \tag{2}$$

and

$$\rho_{II} = e^{-\left(\frac{\Delta L}{L_c}\right)^2}, \tag{3}$$

where ΔL is the distance between points, and L_c is the correlation length. These two functions will, from now on, be referred to as type I and type II correlation functions. Both type I and II correlation functions are commonly used in literature, but generate fields that have different types of imperfections. Both types of fields are used in this work as a comparison, and in an analysis of imperfection sensitivity.

Generating a field requires first calculating the distances between nodes; these distances are then used to generate a correlation matrix using Eqs. (2) and (3). Assembly results in a symmetric positive definite correlation matrix with indices and matrix representation in the form of

$$R_{ij} = \frac{\text{cov}(h_i, h_j)}{\sigma_i \sigma_j} \tag{4}$$

$$\mathbf{R} = \begin{bmatrix} 1 & \rho(h_1, h_2) & \dots & \rho(h_1, h_n) \\ \rho(h_2, h_1) & 1 & \dots & \rho(h_2, h_n) \\ \vdots & \vdots & \ddots & \vdots \\ \rho(h_n, h_1) & \rho(h_n, h_2) & \dots & 1 \end{bmatrix}. \tag{5}$$

CMD makes it possible to generate many fields without any additional computational cost. Most of the computing time is spent factorizing the correlation matrix, which has to be done only once. After precomputing, simple matrix multiplication can generate additional fields using a random zero-mean unit variance vector χ in the form

$$\mathbf{h} = \mathbf{L}\chi, \tag{6}$$

where \mathbf{L} is a decomposed version of the correlation matrix \mathbf{R} of Eq. (5).

Determining the decomposed correlation matrix is done by first taking the definition of covariance

$$\text{cov}[h_i, h_j] = E[h_i h_j] - E[h_i]E[h_j], \tag{7}$$

keeping in mind that the field has a zero mean value. The correlation matrix \mathbf{R} can be decomposed into two matrices as

$$\begin{aligned} \mathbf{R} &= \text{cov}[\mathbf{h}, \mathbf{h}] = E(\mathbf{h}, \mathbf{h}^T) - \mathbf{0} \cdot \mathbf{0} \\ &= E[\mathbf{L}\chi(\mathbf{L}\chi)^T] = \mathbf{L}E(\chi\chi^T)\mathbf{L}^T = \mathbf{L}\mathbf{I}\mathbf{L}^T = \mathbf{L}\mathbf{L}^T, \end{aligned} \tag{8}$$

where \mathbf{I} is an identity matrix. This approach exploits the independence of the components of χ . Decomposition can be done using a variety of methods, such as Cholesky or eigenvalue methods. Within the current implementation, the eigenvalue decomposition was utilized, as this was shown to be slightly more accurate by van der Have [17]. Eigendecomposition gives matrices in the form

$$\mathbf{R} = \mathbf{Q}\mathbf{\Lambda}\mathbf{Q}, \tag{9}$$

where $\mathbf{\Lambda}$ is a diagonal matrix with eigenvalues of \mathbf{R} on the diagonal, and \mathbf{Q} contains its eigenvectors.

From this decomposed matrix the decomposed matrix \mathbf{L} can be extracted as

$$\mathbf{R} = \mathbf{Q}\hat{\mathbf{\Lambda}}\mathbf{Q} = \mathbf{L}\mathbf{L}^T \rightarrow \mathbf{L} = \mathbf{Q}\hat{\mathbf{\Lambda}}, \tag{10}$$

in which $\hat{\mathbf{\Lambda}} = \text{diag}(\sqrt{\lambda})$, in which λ are the eigenvalues of the correlation matrix Eq. (5).

While solving the finite element model the thickness at integration points is evaluated at integration points using shape functions and field values at nodes. Fields are generated with unit variance and zero mean, the thickness at point i is therefore

$$t_i = t_\mu + h_i t_\sigma, \tag{11}$$

where h_i is the field value at point i and t_σ the standard deviation of thickness.

2.2 Improving the cycles until initial failure

Within the current approach, the number of cycles until initial failure is estimated using the highest stress within the structure. Structures printed using fused filament fabrication have a very similar Young’s modulus in the printing plane, and slightly less stiff between printed layers. Elastic behavior for thin-walled structures can, therefore, be approximated as isotropic [5, 33, 40]. Experimental work done by Afrose et al., [1, 11, 12, 26] have indicated that the slope of the s-n diagram of the material is not dependent on the orientation of the printing direction. The structure designed has a primary filament orientation aligned with the applied forces. Inter-layer stresses should be minimal. With this in mind, it is possible to estimate the effect on the number of cycles using the Von Mises yield criterion and the material’s SN curve. This allows the initial failure of the structure due to fatigue to be estimated from the stress state of the structure at a given thickness distribution.

Stress concentrations caused by the production process are not taken into account in this fatigue model, the estimated values are therefore a likely overestimation of the actual number of cycles until failure, and should therefore only be taken as a qualitative measure. Parameters affecting failure in tested specimens are further discussed in Sect. 4.4.1.

2.2.1 Calculating the correlation pattern

In a large set of random thickness patterns, some samples will show an increased number of cycles until failure, while others will show a decrease. A non-dimensional map of the average contribution of thickness to the critical stress state can be evaluated by computing the correlation of these at every point on the structure. If we create a pattern H of the thickness distribution and insert it into the mathematical definition of correlation (Eq. 1) we can compute its terms as

$$H_i = \frac{\sum_{j=1}^n (\sigma_{vm,j} - \bar{\sigma}_{vm})(t_{i,j} - \bar{t})}{\sqrt{\sum_{j=1}^n (\sigma_{vm,j} - \bar{\sigma}_{vm})^2} \sqrt{\sum_{j=1}^n (t_{i,j} - \bar{t})^2}} \quad (12)$$

where H_i is the correlated value of maximum Von Mises stress σ_{vm} found in the structure, and thickness at point i , while thickness of run j is described as $t_{i,j}$ with bar describing the mean value of each term.

2.2.2 Applying the correlation pattern to fatigue behavior

Patterns obtained in Sect. 2.2.1 can not be used directly; it gives a correlation pattern with values in the range $[-1, 1]$.

This pattern is normalized to the range $[0,1]$. Such a normalized pattern can easily be used to vary the thickness in the structure into a specified range as

$$t_i = t_{min} + (t_{max} - t_{min})\hat{H}_i, \quad (13)$$

where \hat{H}_i is the value of the normalized correlation pattern at point i . Directly applying Eq.(13) to the structure will most likely change the volume of the structure. Retaining the original volume, and therefore mass requires a scaling parameter m , extending Eq.(13) to

$$t_i = t_{min} + (t_{max} - t_{min})\hat{H}_i^m. \quad (14)$$

For each range $t \in [t_{min}, t_{max}]$ there exists a unique value of m where the volume of the original structure is retained. This value can be obtained numerically using numerical optimization and scalar minimization algorithms, within this paper; Brent’s method [2] is used.

3 Numerical analysis

To demonstrate the approach of Sect. 2, a numerical example was analyzed. The structure analyzed is an open-hole specimen, its baseline design is shown in Fig. 1. While this structure does not include bending stresses it does represent an easily reproducible stress state which can be repeated fairly easily. Nothing in the approach suggests that it does not work on more complex structures which include bending stresses. This structure is first modeled in finite elements, after which the approach described in Sect. 2 is used to improve the number of cycles until initial fatigue failure by redistributing the thickness of the structure. An additional study is done to analyze changes in stochastic response. Both the baseline

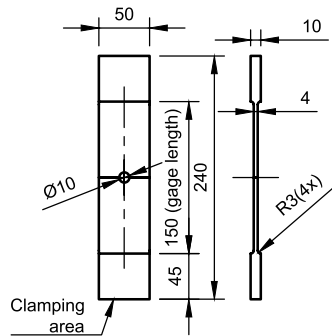


Fig. 1 Drawing of baseline specimen, dimensions in mm

and the improved design were then tested experimentally to demonstrate the potential use of this approach.

3.1 Finite element model

Modeling of the structure in finite elements is done using DIANA FEA [10]. A mean mesh sizing of 1 mm was used to generate a mesh of a quarter of the sample's gage length using 1858 Q8MEM linear shell elements. An image of the discretization can be found in Fig. 2.

The Young's modulus in printed structures depends on both printer settings and build direction [1, 5, 26, 33]. The assumptions listed in section 2.2 means that the qualitative response or improvement should not be affected by anisotropy, assuming the primary build direction and print parameters are maintained in the designs. Therefore, properties used in the analyses shown are assumed based on averaged experimental data in literature as $E = 3.368$ GPa and $\nu = 0.366$. It is important to note that the actual Young's modulus used in the numerical analysis does not significantly affect the linear analyses used to find the correlation between the highest stresses and local changes. Using the unifying fatigue curve for Polylactic Acid (PLA) proposed by [13] a relationship can be made between the maximum stress $\sigma_{max} = \sigma_{mean} + \sigma_{amp}$ relative to the ultimate tensile stress, and the approximate number of cycles until failure. Stresses in the specimen are expected to be minimal in the printing direction, while the ultimate stress in the printing plane is very similar. Figure 3 shows the expected number of cycles for stresses in the printing plane.

Symmetry boundary conditions are applied to the structure on its symmetry line. The left edge in Fig. 2 is fixed in the x-direction, the upper edge is fixed in the y-direction. The rigid body mode in the z-direction is fixed on the edge of the hole. The load is applied as a distributed tensile force on the bottom edge of 1 kN. Von Mises stress results and

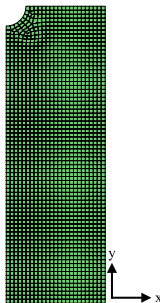


Fig. 2 Mesh discretization

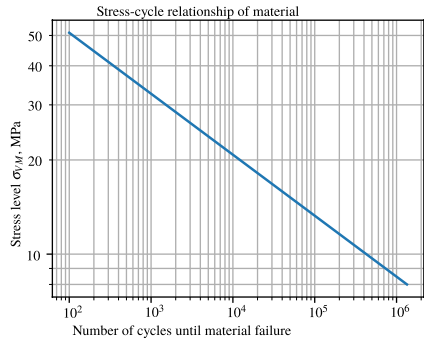


Fig. 3 SN curve used to approximate the number of cycles until initial failure in printing plane of printed PLA

the corresponding number of cycles estimated from the SN-curves of [13] for the baseline sample is shown in Fig. 4.

3.2 Increasing cycles until initial failure

Improvement of the baseline design is achieved using the approach described in Sect. 2.2. Thickness variations are applied through both the type I and type II correlation functions defined in Eqs.(2) and (3) with a correlation length of 5 mm. Figure 5 shows the relationship of distance to the correlation of field values. The correlation length helps

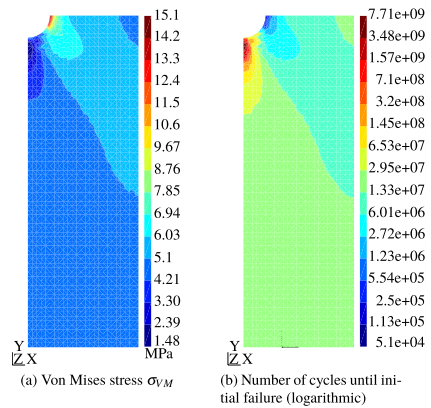


Fig. 4 Baseline results of the finite element model

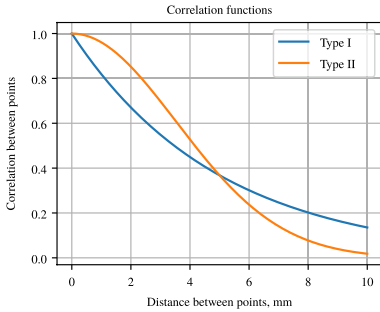


Fig. 5 Correlation functions used to generate thickness patterns, Eqs. (2) and (3) with $L_c = 5$ mm

determine how much distance is needed for the correlation pattern to change significantly within this approach. 5 mm gives reasonably local changes without any very abrupt changes. Fields define the thickness with a standard deviation of $t_\sigma = 0.5$ mm from the $t_\mu = 4$ mm baseline configuration. Changes applied are purely fictitious and only used to generate a correlation pattern. These values can be smaller or slightly larger as long as the response to the local change remains linear. Both of these correlation functions are used to generate two sets with 5000 samples each. The number of samples used was determined by optically checking when the correlation pattern converged and then rounding up. Figure 6 shows an example of a sample of each set.

To find the relative effect of thickness to initial fatigue failure, the Von Mises stress, and the corresponding number of cycles from Fig. 3 are calculated at every node. As described in Fig. 2.2 the initial failure is assumed to be defined by the maximum Von Mises stress and has a logarithmic direct relationship to the number of load cycles. Figure 7 shows the patterns of both types I and II correlation functions and the autocorrelation of each point.

The stress and cycles until failure patterns create a very similar pattern for each correlation function; this is expected as the number of cycles is defined as a function of the stress level. The number of cycles until failure increases with an increase of thickness while the stress decreases. Due to this, the correlation patterns are inverses of each other. Correlation patterns generated using a type II correlation function result in an overall smoother pattern; this is due to the higher correlation the function has at shorter distances (Fig. 5).

Both correlation patterns are used to generate a thickness distribution varying within the range of 2–6 mm. In order to retain the original volume of the structure, the scaling parameter m defined in Eq. (14) had to be computed. Computed values were $m_I = 0.397$ for the type I field and

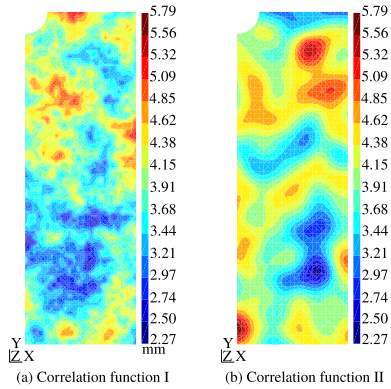


Fig. 6 Example of thickness distributions generated with two different correlation functions

$m_{II} = 0.411$ for the type II field. Figure 8 shows the thickness distributions obtained as well as the new stresses and cycles until initial failure related to the stresses in the structure.

Both patterns are similar and reinforce the hole in the high-stress area by increasing the thickness locally and reducing material in the low-stress area. The solution found can be deduced quite quickly to be more efficient than one obtained by simply adding thickness concentrically around the hole. Stresses vary in the topography around the hole, and sensitivity to local changes also varies significantly over the surface of the structure. Stresses at the top and bottom of the hole are very low, for instance, as forces flow around the hole as shown in Fig. 4a.

Comparing thickness patterns obtained through both correlation functions shows that they are slightly different. Type I correlation function results in a pattern which is less smooth overall, due to the lower correlation to nearby points. Table 1 gives an overview of how the results compare to each other. Both of the improved designs show a decreased stress of 36–38%, which results in having over 10× the number of cycles until initial fatigue failure in Fig. 3.

3.3 Robustness analysis

Designs of Sect. 3.2 are found using random variations, but no analyses are done on the stochastic response of the structure. Robust design can be defined as removing the negative effects of random variations on the performance of a structure. For the current design, this can be interpreted as the distribution of fatigue life in the presence of random thickness variations.

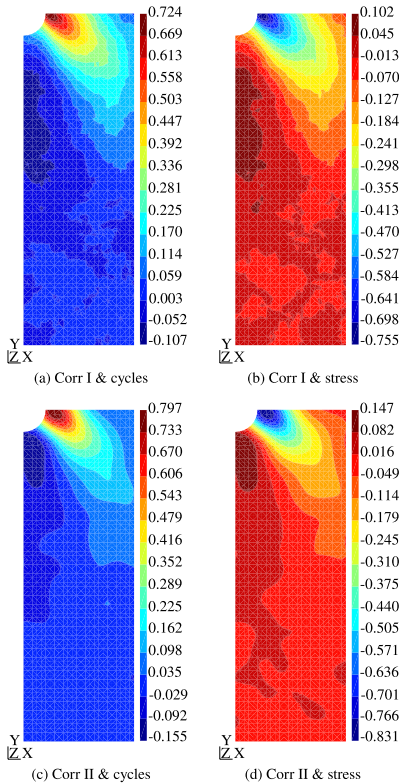


Fig. 7 Correlation patterns of type I and II correlation functions and the stress and number of cycles until initial failure

Robustness is analyzed by applying thickness variations generated using the same parameters as the thickness variations of Sect. 3.2, with two different correlation functions $t_{\sigma} = 0.5$ mm and $L_c = 5$ mm. These variations are applied to the baseline design, as well as the enhanced designs. The results of the maximum stress analyses are shown in Table 2. The statistical properties are shown for a normal distribution with a coefficient of variation (CoV) defined as $CoV = \frac{\sigma}{\mu}$. Estimated cycles until failure has been fit to a lognormal distribution, the parameters of the natural logarithm of these distributions are shown in Table 3,

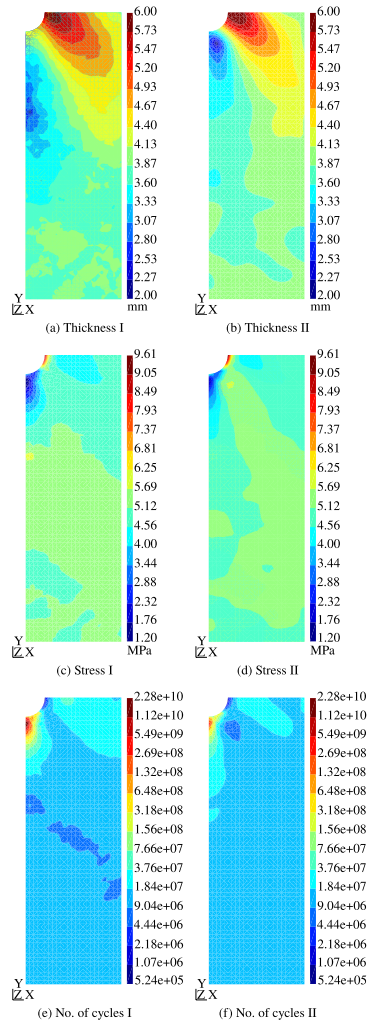


Fig. 8 Thickness distribution, Von Mises stress results and corresponding number of cycles until initial fatigue failure for designs obtained with type I and II correlation functions

Table 1 Comparison between the maximum Von Mises stress and corresponding number of cycles until initial failure for baseline and enhanced designs

	σ_{VM}		Cycles	
Baseline	15.1 MPa	–	5.1E4	–
Pattern I	9.35 MPa	– 38.1%	6.02E5	11.8×
Pattern II	9.61 MPa	– 36.4%	5.24E5	10.3×

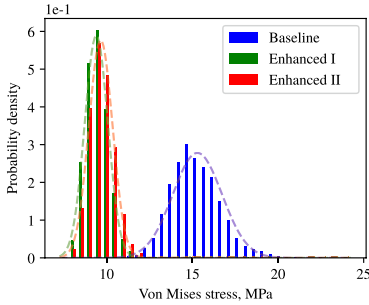


Fig. 9 Probability density function of maximum stress in structure subjected to type I thickness variations

Fig. 10 Probability density function of expected number of cycles until initial failure for structure subjected to type I thickness variations

where the coefficient of variation for lognormal distributions is defined as $CoV = \sqrt{e^{\sigma^2} - 1}$.

Enhancing the design has caused not only the deterministic design to be improved, but also has reduced the standard deviation of the response, significantly improving structural reliability. Figure 9 shows the normal distributions found, as well as a histogram of the 5000 analyses of baseline and enhanced designs. Distributions of the enhanced and baseline designs only have a small overlap at the tail of the distribution. Reducing the maximum stress in the structure greatly influences the expected number of cycles until initial failure. The lognormal distribution of cycles is shown in Fig. 10, showing that the expected number of cycles is approximately one order of magnitude higher for the enhanced designs.

4 Experimental validation

The numerical results of Sect. 3 show a great increase in the expected fatigue life of specimens with the specified thickness redistribution. Manufacturing panel structures with tailored thicknesses using a traditional manufacturing process is quite challenging, requiring multiple machining steps. This section tries to analyze the potential use of additive manufacturing to generate structures with these types of thickness redistributions.

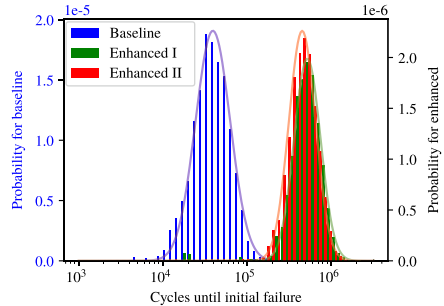


Table 2 Statistical stress σ_{VM} properties baseline and enhanced designs subjected to thickness variations generated with type I and II correlation functions with $L_c = 5$ mm and $t_e = 0.5$ mm

$X = \mu + \sigma Z$	Thickness variations of type I						Thickness variations of type II					
	μ , MPa	δ	σ , kPa	δ	CoV	δ	μ , MPa	δ	σ , kPa	δ	CoV	δ
Baseline	15.30	(–)	1430	(–)	9.35%	(–)	15.31	(–)	1470	(–)	9.60%	(–)
Enhanced I	9.40	(– 38.6%)	678	(– 52.6%)	7.22%	(– 22.8%)	9.39	(– 38.7%)	683	(– 53.5%)	7.27%	(– 24.3%)
Enhanced II	9.66	(– 36.9%)	692	(– 51.6%)	7.17%	(– 23.3%)	9.65	(– 37.0%)	700	(– 52.4%)	7.26%	(– 24.4%)

Table 3 Statistical parameters of the number of cycles until failure distribution's natural logarithm, of baseline and enhanced designs subjected to thickness variations generated using type I and II correlation functions with $L_c = 5$ mm and $t_\sigma = 0.5$ mm

$X = e^{\mu+\sigma Z}$	Thickness variations of type I					Thickness variations of type II						
	μ	δ	σ	δ	CoV	μ	δ	σ	δ	CoV	δ	
Baseline	10.81	(-)	0.475	(-)	0.503	(-)	10.80	(-)	0.485	(-)	0.515	(-)
Enhanced I	13.29	(- 22.9%)	0.361	(- 24.0%)	0.361	(- 25.8%)	13.30	(- 23.1%)	0.365	(- 24.7%)	0.378	(- 26.6%)
Enhanced II	13.16	(- 21.7%)	0.365	(- 23.2%)	0.378	(- 24.9%)	13.16	(- 21.9%)	0.370	(- 23.7%)	0.383	(- 25.6%)

The test campaign contained two types of tests. The first test has the objective of finding the failure load. Researchers have already published the ultimate tensile stress of PLA structures produced with FFF, but the numbers vary from 15.5–72.2 MPa [21, 24], depending on the chosen filament and production parameters [5, 37]. As the objective of the test is to observe an increase in fatigue life of the structure, it is not necessary to obtain an exact tensile strength for the experimental campaign. What does have to be obtained is an appropriate load level to perform the fatigue test on, this is done by performing a static test series.

Using a load level derived from the static test, an oscillating sinusoidal load with varying amplitude ($R = \frac{F_{\min}}{F_{\max}} = 0.1$) is applied to the structure until structural failure occurs. This fatigue test is first done on the baseline constant thickness sample and then repeated with the redesigned sample featuring a thickness redistribution.

4.1 Test specimen manufacturing using FFF technique

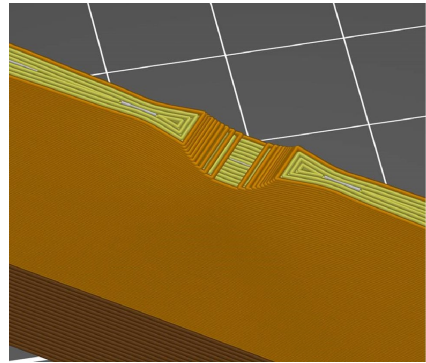
Samples were manufactured by importing the design from Sect. 3 and adding transitional radii between the clamping and gage areas. Sample manufacturing was done using the FFF technique and Poly-lactic Acid (PLA) filament.

Manufacturing of the samples was done at the institute of adaptronics and function integration (IAF) of TU Braunschweig. Using a nozzle diameter of 0.4 mm, a heating chamber temperature of 220 °C, and a print bed temperature of 55 °C. The layer height used during printing was 0.2 mm.

The test specimens were printed as solid pieces, while most filament strands in the gauge area are routed in the direction of force with the help of a concentric arrangement as shown in Fig. 11. The test samples were spray-painted with a speckled pattern after printing, for deformation tracking with a digital image correlation system, as is visible in Fig. 12.

4.2 Test setup

Tests were performed at the testing facility of the Institute of Structural Analysis in Hannover, Germany. Samples

**Fig. 11** Orientation of filament in the printing of the improved sample

were tested in a servo-hydraulic test machine with an attached 12.5 kN load cell. The machine clamps the sample on both ends, as shown in Fig. 12, where the bottom end is free in rotation, eliminating any unwanted torque in the test setup.

A digital image correlation (DIC) system constantly monitored the sample during testing. This system allows for real-time tracking of displacements (and resulting strains) of the test sample. Within the fatigue tests, the hole elongation is measured as a measure of damage evolution. An overview of the system operating during testing is shown in Fig. 13.

4.3 Static pretesting

The goal of the static test series is to find an appropriate load level for the succeeding fatigue test series. During the test, specimens were elongated at a rate of 1 mm/min, while continually recording the resulting force. The test was repeated 3 times, and showed a high degree of reproducibility, with ultimate loads of around 8.5 kN. The force-displacement graphs of these three tests can be found in Fig. 14.



Fig. 12 Test sample clamped into test machine

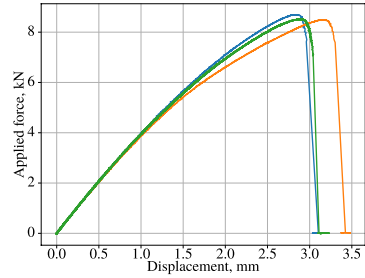


Fig. 14 Static pretest results of baseline samples

4.4 Fatigue testing

In order to assess the fatigue performance of both designs fatigue tests are performed under an oscillating load until failure. Force is applied as a sinusoid with a load level of 25%, 50% and 70% of the ultimate load of Fig. 4.3, and a minimum load of a tenth of that, giving a stress ratio of $R = \frac{F_{min}}{F_{max}} = 0.1$.

At least three samples are used at each load level. The data points were used to fit a curve using the Basquin equation of $N = \frac{B}{S_r^m}$, where N is the number of cycles, S the stress level, B and m are fitting parameters. A curve was fit using the Levenberg-Marquardt algorithm, leading to the following least-squares fits

$$N_{BL} = \frac{340.58}{S_r^{4.49}}, \tag{15}$$

for the baseline sample and

$$N_{Imp} = \frac{1661.9}{S_r^{4.24}}, \tag{16}$$

for the improved sample.

The results shown in Fig. 15 make it clear that the redistributed thickness found in Sect. 3 results in a significant improvement in the fatigue life. Accurately quantifying this improvement requires more testing, but it seems to be in the order of 4 to 5 times the original design on average.

The spread between results is relatively small. Tests done by [11] show an order of magnitude difference between the top and bottom 10% of samples. Results of the experiments performed in this paper all show a difference of the highest and lowest results of less than an order of magnitude. Any possible effects the load level has on this spread can not be extrapolated from the data as the sample size is not large enough.

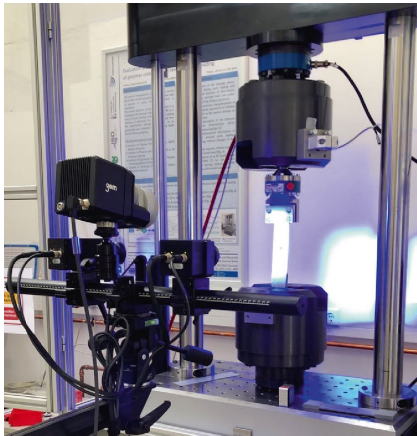


Fig. 13 Test setup with digital image correlation system

Pretesting determines an appropriate load level and indicates reproducibility. As tests on the improved samples are performed on the same load levels, pretesting is not repeated for those designs.

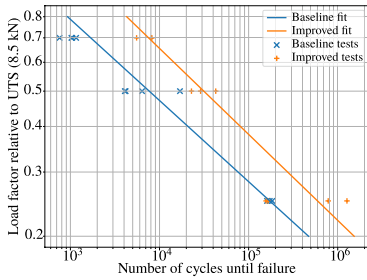


Fig. 15 SN data of tested specimens and fitted curves

4.4.1 Analysis of fatigue failure of specimens

Failure in the numerical studies was taken as an instantaneous event, without any progressive damage, which can cause stresses to redistribute. Within this section, this assumption is analyzed using data obtained during testing. Hole elongation is used as a measure of damage progression. The relative progression towards failure is shown in Fig. 16. Within this diagram, the elongation of the hole is plotted using a virtual extensometer generated using digital image correlation during testing. Values in the y-direction are set to

$$D = \frac{\frac{F_1}{u_n}}{\frac{F_n}{u_n}} = \frac{F_1 u_n}{F_n u_1} \triangleq \frac{E_1}{E_n} \tag{17}$$

where values $\frac{E_1}{u_1}$ is the original stiffness, and $\frac{E_n}{u_n}$ the apparent stiffness during the test. The original stiffness is calculated as the average stiffness as the load is increased from 1 to 25% of the maximum load level at the start of the test.

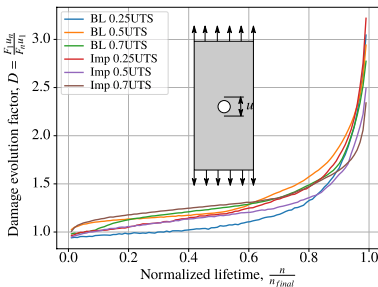


Fig. 16 Evolution of apparent elasticity during testing

Figure 16 shows that there is a significant amount of progressive damage, and therefore stress redistribution during testing. Stress redistribution and internal damage cause the stress distribution to evolve during the lifetime of the structure. The figures show an approximately linear increase in the damage evolution up to 60-80% of their lifetime. At this point, stress redistribution and crack forming cause an accelerated increase in the damage evolution until final failure occurs. Numerical analysis of Sect. 3 does not take any evolution or stress redistribution into account.

The mechanism resulting in ultimate failure seems to be identical in the baseline and improved designs. Relative progression of damage shown in Fig. 16 shows that the evolutionary characteristic of damage is very similar. Samples also showed cracks initiate at the same areas within both designs. It is, therefore, reasonable to assume that the primary mechanism leading to fatigue life improvement is the reduced tensile stress at critical locations. Lowering the stresses results in a slowing down damage progression and increase in the structural lifespan.

Also, fracture initiation found in the samples is not in the highest stress area in the finite element model. Figure 4 shows that the highest von Mises stress in the structure is at the 3 and 9 o'clock locations of the hole. Fractures in the tested specimens were shown to initiate slightly above or below this location, i.e., 2, 4, 8, or 10 o'clock positions. Figure 17 shows a typical fracture forming during testing. The topography of the immediate area can be seen in Fig. 11. The area that was found most critical in the finite element analysis consists of filaments oriented in the tensile direction. Immediately to the side of the critical areas, transversely oriented filaments effectively introduce notches into the structure. Notches such as these naturally attract stress concentrations, leading to crack initiation and crack growth leading to final failure. Such topological features are not included within the numerical model. The structure is modeled using ideal geometry. Manufacturing with FFF means

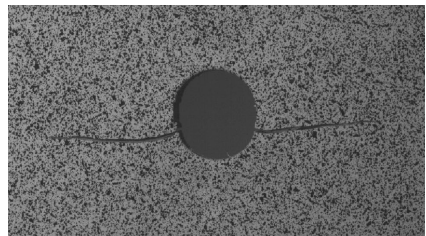


Fig. 17 Evolving crack pattern formed during testing, just before final failure

that the actual topology differs, making it easy for stresses to concentrate at irregularities not included in the model.

5 Conclusion and discussion

This paper has presented a numerical approach to increase the fatigue life of structures by tailoring the distribution of local thickness. By applying this approach to a test specimen, the simulated fatigue life was increased by order of magnitude. Numerical results also show that the approach decreases the sensitivity of the structure to random variations of thickness.

Experiments showed the potential use of this approach on structures manufactured using additive techniques. The experiments show that the number of cycles until failure is increased to around 4 to 5 the original baseline design. The method discussed is not designed to predict the number of cycles until failure but only to improve it. Nevertheless, analyzing this difference can show how the approach can be extended to include other effects.

This discrepancy between numerical and experimental results could be resolved by extending the fatigue model to consider additional effects. The two main areas identified are printer orientation and stress redistribution. Extending the numerical model to take these effects into account will likely improve the experimental results.

Additive manufacturing using FFF causes a topology within the final structure that can have areas more sensitive to crack initiation. The printing layout can be adapted to remove these sensitive areas if this is considered in the numerical model. In cases where the topology must have these sensitive areas, the stresses can be lowered by adopting a scaling function to the fatigue relation used to generate a correlation pattern.

Compared to standard topology optimization methods used in additive manufacturing [14, 29], the approach discussed in this paper differentiates itself by including stochastic variations in the design. By including these, the design can become more robust towards imperfections and enable evaluation of robustness during and after design using the same procedure. In addition to this, a transitory length scale can be specified through a correlation function and length used to generate variations. These length scales can assure continuity of thickness patterns, making it easier to assure manufacturability. Solutions obtained using density-based topology optimization may also create additional holes or end up with lattice-type solutions instead of continuous surfaces, which may be undesirable in structures such as wings panels. Extensive quantitative comparisons between approaches are left for the next phase of development.

Though this paper only deals with improving the fatigue life by redistributing the material thickness, it is possible to

have a similar approach towards other parameters in AM. Process parameters, such as print speed, can directly affect the quality of a printed structure. The optimal values are usually a compromise between manufacturing time and quality. A similar analysis to that done in this paper could be performed to tailor the local use of process parameters, increasing the manufacturing speed while retaining high accuracy and a good finish in critical areas.

Acknowledgments The authors thank Gerd-Jan Schreppers from DIANA FEA B.V. for his support with the numerical analyses in DIANA. Our final thanks go to Christian Gerendt, Martin Brod, Oliver Dorn, and Jens Breyer for their assistance in experimental work.

Funding Open Access funding enabled and organized by Projekt DEAL. We would like to acknowledge the funding by the Deutsche Forschungsgemeinschaft (DFG, German Research Foundation) under Germany's Excellence Strategy-EXC 2163/1- Sustainable and Energy Efficient Aviation-Project-ID 390881007.

Data availability Test data and numerical results are available upon request

Code availability Results are generated using DIANA, a commercially available finite element solver, pre and postprocessing is done using a series of python scripts. These python scripts can be made available to researchers upon request.

Declarations

Conflict of interest The authors declare that they have no conflict of interest.

Open Access This article is licensed under a Creative Commons Attribution 4.0 International License, which permits use, sharing, adaptation, distribution and reproduction in any medium or format, as long as you give appropriate credit to the original author(s) and the source, provide a link to the Creative Commons licence, and indicate if changes were made. The images or other third party material in this article are included in the article's Creative Commons licence, unless indicated otherwise in a credit line to the material. If material is not included in the article's Creative Commons licence and your intended use is not permitted by statutory regulation or exceeds the permitted use, you will need to obtain permission directly from the copyright holder. To view a copy of this licence, visit <http://creativecommons.org/licenses/by/4.0/>.

References

1. Afrose MF, Masood SH, Iovenitti P, Nikzad M, Sbarski I (2016) Effects of part build orientations on fatigue behaviour of FDM-processed PLA material. *Prog Addit Manuf* 1(1–2):21–28. <https://doi.org/10.1007/s40964-015-0002-3>
2. Brent RP (2013) Algorithms for minimization without derivatives. Courier Corporation
3. van den Broek S, Minera S, Pirrera A, Weaver PM, Jansen E, Rolfes R (2020) Enhanced deterministic performance of panels using stochastic variations of geometry and material. *AIAA J* 58(5):2307–2320. <https://doi.org/10.2514/1.J058962>

4. van den Broek S, Minera S, Jansen E, Rolles R (2021) Robust improvement of the asymmetric post-buckling behavior of a composite panel by perturbing fiber paths. *Compos Struct* 270:114011. <https://doi.org/10.1016/j.compstruct.2021.114011>
5. Chacón JM, Caminero MA, García-Plaza E, Núñez PJ (2017) Additive manufacturing of PLA structures using fused deposition modelling: effect of process parameters on mechanical properties and their optimal selection. *Mater Des* 124:143–157. <https://doi.org/10.1016/j.matdes.2017.03.065>
6. Chacón JM, Caminero MA, Núñez PJ, García-Plaza E, García-Moreno I, Reverte JM (2019) Additive manufacturing of continuous fibre reinforced thermoplastic composites using fused deposition modelling: effect of process parameters on mechanical properties. *Compos Sci Technol* 181:107688. <https://doi.org/10.1016/j.compscitech.2019.107688>
7. Dapogny C, Estevez R, Faure A, Michailidis G (2019) Shape and topology optimization considering anisotropic features induced by additive manufacturing processes. *Comput Methods Appl Mech Eng* 344:626–665. <https://doi.org/10.1016/j.cma.2018.09.036>
8. Davis MW (1987) Production of conditional simulations via the LU triangular decomposition of the covariance matrix. *Math Geol* 19(2):91–98. <https://doi.org/10.1007/BF00898189>
9. Dekking FM, Kraaikamp C, Lohpuhaä HP, Meester LE (2005) A modern introduction to probability and statistics: understanding why and how. Springer Science & Business Media. <https://doi.org/10.1007/1-84628-168-7>
10. Diana FEA (2020) DIANA Finite Element Analysis User's Manual Release 10.4. Tech. rep., Delft, the Netherlands. <https://diana.fea.com/manuals/d1/04/Diana.html>. Accessed 1 July 2021
11. Ezech OH, Susmel L (2018) Fatigue behaviour of additively manufactured polylactide (PLA). *Procedia Struct Integr* 13:728–734. <https://doi.org/10.1016/j.prostr.2018.12.121>
12. Ezech OH, Susmel L (2018) On the fatigue strength of 3D-printed polylactide (PLA). *Procedia Struct Integr* 9:29–36. <https://doi.org/10.1016/j.prostr.2018.06.007>
13. Ezech OH, Susmel L (2019) Fatigue strength of additively manufactured polylactide (PLA): effect of raster angle and non-zero mean stresses. *Int J Fatigue* 126:319–326. <https://doi.org/10.1016/j.ijfatigue.2019.05.014>
14. Fu YF (2020) Recent advances and future trends in exploring Pareto-optimal topologies and additive manufacturing oriented topology optimization. *Math Biosci Eng* 17(5) 4631–4656. <https://doi.org/10.3934/mbe.2020255>
15. Gao W, Zhang Y, Ramanujan D, Ramani K, Chen Y, Williams CB, Wang CC, Shin YC, Zhang S, Zavatieri PD (2015) The status, challenges, and future of additive manufacturing in engineering. *CAD Comput Aided Des* 69:65–89. <https://doi.org/10.1016/j.cad.2015.04.001>
16. Gibson I, Rosen DW, Stucker B (2010) Additive manufacturing technologies. Springer Science & Business Media. <https://doi.org/10.1007/978-1-4419-1120-9>
17. Van der Have R (2015) Random fields for non-linear finite element analysis of reinforced concrete. <https://repository.tudelft.nl/islandora/object/uuid:2578069a-49c4-4085-9a65-af73119d97a7?collection=education>. Accessed 1 July 2021
18. Hristopulos D (2020) Random fields for spatial data modeling. Springer Nature B.V. <https://doi.org/10.1007/978-94-024-1918-4>
19. Iragi M, Pascual-González C, Esnaola A, Lopes CS, Aretxabaleta L (2019) Ply and interlaminar behaviours of 3D printed continuous carbon fibre-reinforced thermoplastic laminates; effects of processing conditions and microstructure. *Addit Manuf.* <https://doi.org/10.1016/j.addma.2019.100884>
20. Keshavarzadeh V, Kirby RM, Narayan A (2020) Stress-based topology optimization under uncertainty via simulation-based Gaussian process. *Comput Methods Appl Mech Eng* 365:112992. <https://doi.org/10.1016/j.cma.2020.112992>
21. Kotlinski J (2014) Mechanical properties of commercial rapid prototyping materials. *Rapid Prototyp J* 20(6):499–510. <https://doi.org/10.1108/RPJ-06-2012-0052>
22. Kriegesmann B, Rolles R, Hühne C, Teßmer J, Arboz J (2010) Probabilistic design of axially compressed composite cylinders with geometric and loading imperfections. *Int J Struct Stab Dyn* 10(04):623–644. <https://doi.org/10.1142/S0219455410003658>
23. Langelaar M (2016) Topology optimization of 3D self-supporting structures for additive manufacturing. *Addit Manuf* 12:60–70. <https://doi.org/10.1016/j.addma.2016.06.010>
24. Lanzotti A, Grasso M, Staiano G, Martorelli M (2015) The impact of process parameters on mechanical properties of parts fabricated in PLA with an open-source 3-D printer. *Rapid Prototyp J* 21(5):604–617. <https://doi.org/10.1108/RPJ-09-2014-0135>
25. Lazarov BS, Wang F (2017) Maximum length scale in density based topology optimization. *Comput Methods Appl Mech Eng* 318:826–844. <https://doi.org/10.1016/j.cma.2017.02.018>
26. Letcher T (2014) Material Property Testing of 3D-printed Specimen in PLA on an Entry-level 3D Printer. In: Proceedings of the ASME 2014 International Mechanical Engineering Congress & Exposition IMECE2014, pp 1–8
27. Liu S, Li Q, Chen W, Tong L, Cheng G (2015) An identification method for enclosed voids restriction in manufacturability design for additive manufacturing structures. *Front Mech Eng* 10(2):126–137. <https://doi.org/10.1007/s11465-015-0340-3>
28. Lyons B (2014) Additive manufacturing in aerospace: examples and research outlook. *Bridge* 42(1):13–19. <https://www.nae.edu/58467/Additive-Manufacturing-in-Aerospace-Examples-and-Research-Outlook>. Accessed 11 April 2022
29. Meng L, Zhang W, Qian D, Shi G, Tang L, Hou Y, Breitkopf P, Zhu J, Gao T (2020) From topology optimization design to additive manufacturing: today's success and tomorrow's roadmap. *Arch Comput Methods Eng* 27(3):805–830. <https://doi.org/10.1007/s11831-019-09331-1>
30. Picelli R, Townsend S, Brampton C, Norato J, Kim HA (2018) Stress-based shape and topology optimization with the level set method. *Comput Methods Appl Mech Eng* 329:1–23. <https://doi.org/10.1016/j.cma.2017.09.001>
31. Qian X (2017) Undercut and overhang angle control in topology optimization: a density gradient based integral approach. *Int J Numer Methods Eng* 111(3):247–272. <https://doi.org/10.1002/nme.5461>
32. Shinozuka M, Deodatis G (1996) Simulation of multi-dimensional Gaussian stochastic fields by spectral representation. *Appl Mech Rev* 49(1):29–53. <https://doi.org/10.1115/1.3101883>
33. Song Y, Li Y, Song W, Yee K, Lee KY, Tagarielli VL (2017) Measurements of the mechanical response of unidirectional 3D-printed PLA. *Mater Des* 123:154–164. <https://doi.org/10.1016/j.matdes.2017.03.051>
34. Spanos PD, Zeldin BA (1998) Monte carlo treatment of random fields: a broad perspective. *Appl Mech Rev* 51(3):219. <https://doi.org/10.1115/1.3098999>
35. Sudret B, Der Kiureghian A (2000) Stochastic Finite Element Methods and Reliability: A State-of-the-Art Report. University of California Berkeley (November):189. <https://ethz.ch/content/dam/ethz/special-interest/baug/ibk/risk-safety-and-uncertainty-dam/publications/reports/SFE-report-Sudret.pdf>. Accessed 11 April 2022
36. Vanmarcke E, Grigoriu M (1983) Stochastic finite element analysis of simple beams. *J Eng Mech* 109(5):1203–1214. [https://doi.org/10.1061/\(asce\)0733-9399\(1983\)109:5\(1203\)](https://doi.org/10.1061/(asce)0733-9399(1983)109:5(1203))
37. Witbrodt B, Pearce JM (2015) The effects of PLA color on material properties of 3-D printed components. *Addit Manuf* 8:110–116. <https://doi.org/10.1016/j.addma.2015.09.006>
38. Wu W, Geng P, Li G, Zhao D, Zhang H, Zhao J (2015) Influence of layer thickness and raster angle on the mechanical properties of

-
- 3D-printed PEEK and a comparative mechanical study between PEEK and ABS. *Materials* 8(9):5834–5846. <https://doi.org/10.3390/ma8095271>
39. Zhou M, Lazarov BS, Wang F, Sigmund O (2015) Minimum length scale in topology optimization by geometric constraints. *Comput Methods Appl Mech Eng* 293:266–282. <https://doi.org/10.1016/j.cma.2015.05.003>
40. Zou R, Xia Y, Liu S, Hu P, Hou W, Hu Q, Shan C (2016) Isotropic and anisotropic elasticity and yielding of 3D printed material. *Compos B Eng* 99:506–513. <https://doi.org/10.1016/j.compositesb.2016.06.009>
- Publisher's Note** Springer Nature remains neutral with regard to jurisdictional claims in published maps and institutional affiliations.

PAPER D: ROBUST BUCKLING LOAD IMPROVEMENT OF AN ASYMMETRIC COMPOSITE STRUCTURE

The road to perfection winds through a land called imperfection.

— Bangambiki Habyarimana

The paper presented in this chapter describes how random fiber generations can be analyzed to create a robust fiber path which gives a higher buckling load for certain asymmetric structures. First published as van den Broek, S. *et al.* Robust improvement of the asymmetric post-buckling behavior of a composite panel by perturbing fiber paths. *Composite Structures* **270**, 114011. ISSN: 02638223. doi:10.1016/j.compstruct.2021.114011 (2021)

AUTHOR CONTRIBUTIONS

SANDER VAN DEN BROEK The principal author of the paper, implementor of the approach described, and the corresponding author.

SERGIO MINERA Provided the structural code in which the method was implemented and provided technical discussions with the principal author.

EELCO JANSEN Provided technical suggestions and input during the development of the approach.

RAIMUND ROLFES Provided technical suggestions and input during the development of the approach.



ELSEVIER

Contents lists available at ScienceDirect

Composite Structures

journal homepage: www.elsevier.com/locate/compstruct

Robust improvement of the asymmetric post-buckling behavior of a composite panel by perturbing fiber paths

Sander van den Broek^{a,*}, Sergio Minera^b, Eelco Jansen^c, Raimund Rolfes^a

^a Leibniz University Hannover, Hannover, Germany

^b National Composites Centre, Bristol, United Kingdom

^c Rotterdam University of Applied Sciences, Rotterdam, The Netherlands

ARTICLE INFO

Keywords

Random field
Robust design
Fiber misalignment
Buckling
Composites
Steered fiber path

ABSTRACT

The buckling behavior of structures is highly sensitive to imperfections, i.e., deviations from the geometry and material properties of the ideal structure. In this paper, an approach is presented in which the effects of spatially varying fiber misalignments in composite structures are assessed through random field analysis and are subsequently used to improve the structure while simultaneously making it more robust to fiber misalignments. Effects of misalignments are quantified by applying random fields on the structure, which represent fiber misalignments. Using analyses of the effect of the random local stiffness changes due to fiber misalignments, a pattern of the relative influence these local changes have on the buckling load is created. By applying a small change to local fiber orientation corresponding to this pattern to the original structure, the performance of the design is improved. Additional stochastic analyses are performed using the improved design, reanalyzing the effects local fiber misalignments have on the structural performance and the subsequent changes in robustness. Stochastic results show an overall increase in the mean buckling load and a reduction in the coefficient of variation in the analysis of the perturbed structure. The approach is applied to a composite panel exhibiting asymmetric post-buckling behavior, i.e., having an unstable post-buckling branch and an (initially) stable branch. Results show that perturbations in the fiber path can nudge a structure into a more stable post-buckling path by promoting a post-buckling path using local changes in structural stiffness. The robustness of improved designs can also increase, making structures less susceptible to local fiber misalignments.

1. Introduction

It has long been the habit of designers to design structures using idealized homogeneous material properties within a structure. Deviations of these assumptions are taken into consideration by using a safety factor. Material properties found in manufactured composite structures can vary spatially. Variations occur due to manufacturing processes and allowable tolerances and can affect the shape [1], thickness [2], void content [3], fiber alignment [4], and other material properties [5,6].

Quantifying the effects of such local variations have on structures can be done using random fields [7–12]. Random fields are continuous spatial fields generated in one, two, or three dimensions. Fields contain random values associated with coordinates on the field; the coordinates' values are correlated with each other using a predefined correlation function, allowing for continuous variations of parameters.

Varying parameters can also improve performance or generate different behavior. Buckling loads can be improved by tailoring the thickness [13], applying seeded geometric changes to geometry [14–16], or tailoring the fiber path. Composite structures with engineered fiber paths are also known as variable stiffness composites and enable more careful tailoring of stiffnesses and tailor the buckling and out of plane behavior of structures [17–20]. Variable stiffness structures also allow for bistability, in which a stable equilibrium exists in multiple configurations utilizing a combination of pre-stress and varying stiffnesses [21].

Several manufacturing techniques are suited to manufacture variable stiffness composites. Automated fiber placement (AFP) is one such technology in which tows of fibers are placed following curved paths. Conventional AFP machines use a compaction head that is perpendicular to the tangential placement direction. Shear in tows, which results due to in-plane bending deformation, can not be compensated. As tow-

* Corresponding author.

E-mail addresses: S.vandenBroek@isd.uni-hannover.de (S. van den Broek), Sergio.Minera@nccuc.com (S. Minera), E.L.Jansen@hr.nl (E. Jansen), R.Rolfes@isd.uni-hannover.de (R. Rolfes).

<https://doi.org/10.1016/j.compstruct.2021.114011>

Received 17 March 2021; Accepted 20 April 2021

Available online 27 April 2021

0263-8223/© 2021 Elsevier Ltd. All rights reserved.

width increases and bending radius decreases, fiber breakage or wrinkling can become more of an issue. A lack of shear variability causes the width of the tow to vary with the bending radius, leading to overlaps or gaps between tows [22]. Gaps can be filled in using 3D printing technologies [23], where fiber-reinforced matrix material is deposited on any gaps formed, though this is a tedious and time-consuming process for mass production. Continuous tow shearing alleviates these issues by allowing shear within tows and compensating for deformation during placement using a pinching device, making much tighter turning radii possible [24,25].

Tolerances in the placement and curing process cause small changes in the fiber angle, resin richness, and other material parameters. Local variations in stiffness caused by these changes can adversely affect the deterministic result. The argument could be made that any optimum found should be resilient enough to be insensitive to common variations [26]. Variable stiffness composites make it possible to make structures less sensitive to imperfections [27].

Structures with asymmetric post-buckling behavior have a stable and an unstable branch, corresponding to the two alternative directions of the relevant buckling mode and initial geometric imperfection shape. Which equilibrium path dominates depends on the imperfections found in the structure, making the structure very sensitive to imperfections. Imperfections can consist of deviations from a nominal geometry or, to a lesser extent, parameters affecting stiffness.

Tailoring a structure to incorporate small changes in its original design can improve the buckling load by increasing stiffness locally. This paper presents an approach to find patterns in which to apply local changes to the fiber angle of composite structures. Local variations are applied to the structure using random fields, affecting its buckling load. Analyzing the influence of local variations on the buckling load of a structure can give a non-dimensional pattern of influence of a structural parameter. Previous work of the authors has improved the deterministic linear buckling load of isotropic structures by tailoring the local thickness and Young's modulus [28]. Developments presented in this paper include its application on a non-linear problem, fiber angles of composite structures, and robustness analyses.

Developments are demonstrated on a composite curved panel by varying fiber angles using its nominal geometry. Deviations from a nominal fiber path can be achieved using existing techniques used to fabricate variable-stiffness composites. Fiber misalignments are generated on the structure using geodesic random fields. Running a Monte Carlo analysis quantifies the likelihood of reaching a particular limit-point buckling load. Patterns of the perturbed fiber paths are generated by analyzing the effects of local fiber misalignments and finding the local correlation between these variations and the buckling load. Deterministic results are analyzed from perturbed designs, after which the effects of introducing random fiber angle changes indicate the sensitivity of a perturbed fiber path to imperfections introduced during manufacturing.

The remainder of this paper introduces the methods used in Section 2, starting with the structural model in Section 2.1. Random variations to the fiber angle are generated using random fields. The generation and mapping of random fields is discussed in Section 2.2. Analyzing stochastic results can lead to a pattern in which fibers are perturbed. Applying this pattern to the fiber paths leads to a deterministic improvement discussed in Section 2.3. The robustness of improved designs can be analyzed by applying random fiber misalignments, this is discussed in Section 2.4. An example of a curved composite panel is described in Section 3.1, with baseline mechanical results without variations applied are shown in Section 3.2. Section 3.3 adds perturbations on top of the baseline structure, quantifying and analyzing the effects fiber misalignments can have. Deterministic improvements are discussed in Section 3.4, after which random variations are applied to analyze the perturbed fiber paths' sensitivity in Section 3.5. The overall conclusions are discussed in Section 4.

2. Methods

2.1. Structural formulation

Results are generated by using a structural model based on a Unified Formulation, making use of Serendipity Lagrange shape functions [29]. Extensions to the unified formulation enable the analysis of geometric non-linearity and curved elements [30]. Non-linearity is taken into account using an arc-length based solver.

2.1.1. Basic formulation

The structural model is a non-linear three-dimensional model. It utilizes a displacement field using two different shape functions in the cross-sectional plane ($F(x, z)$) and axial direction ($N(y)$).

Starting with a displacement field, $u = [u, v, w]^T$, the Green–Lagrange stress tensor E can be defined as

$$E_{ij} = \frac{1}{2}(u_{,i} \cdot g_j + u_{,j} \cdot g_i + u_{,i} \cdot u_{,j}), \quad (1)$$

where commas denote derivatives and g_i denotes a unit vector on the i axis. Displacement field u is approximated within the Unified Formulation as

$$u_{(e)}(x, y, z) = F(x, z)N(y)u_i, \quad \text{with } i = 1, \dots, n, \quad (2)$$

where n are the degrees of freedom of the model. For quasi-static problems, the elastic equilibrium is

$$\delta W_{\text{int}} = \delta W_{\text{ext}} \quad (3)$$

where W_{ext} and W_{int} are the external work and internal energy. Noting that the internal energy of the structure can be calculated as the sum of internal energy of all the elements $W_{\text{int}} = \sum_e W_{\text{int}}^{(e)}$ the internal energy can be expressed using the stress and strain tensors

$$\delta W_{\text{int}}^{(e)} = \int_{V_{(e)}} \delta E \cdot S dV \quad (4)$$

in which S is the second Piola stress tensor. For non-linear analyses, it is of interest to create tangential matrices. Changes in internal energy are expressed as [31, Section 3.1.1]

$$\begin{aligned} \delta(\delta W_{\text{int}}^{(e)}) &= \int_{V_{(e)}} \delta(\delta E \cdot S) dV, \\ &= \int_{V_{(e)}} \delta E \cdot \delta S dV + \int_{V_{(e)}} \delta(\delta E) \cdot S dV, \end{aligned}$$

where V is the volume of an element. Rewriting these in terms of non-linear contributions of the tangential and geometric stiffness matrices results in [32]

$$\delta(\delta W_{\text{int}}^{(e)}) = \delta u_i^T K_{(e)}^{(t)} u_i + \delta u_i^T K_{(e)}^{(g)} u_i. \quad (7)$$

Rewriting the tangential stiffness matrix using Eq. (7) leads to

$$K_{(T)}^{(e)} = K_{(e)}^{(t)} + K_{(e)}^{(g)}, \quad (8)$$

where $K_{(e)}^{(t)}$ is the non-linear contribution and $K_{(e)}^{(g)}$ the geometric stiffness matrix. Explicit forms of these matrices can be found in [33,34].

2.1.2. Formulation for curved elements

Returning to the displacement field approximation of Eq. (2), the model used in the presented research uses Serendipity Lagrange shape functions in the cross-section (F) and Lagrange shape functions in the axial (N) direction. These shape functions are used to approximate the displacement field of the structure. The cross-sectional shape function F has either 4, 8, 12, 17, 23, or 30 degrees of freedom, depending on the order chosen. Hierarchical elements with four nodes are used in the current implementation.

Unlike most finite element formulations, different shape functions are used for the displacement field and the geometry. Using this approach, it is possible to have a higher fidelity representation of the geometry without increasing the degrees of freedom of the structural problem. This additional shape function $N^{3D}(\alpha, \beta, \xi)$ is defined within $[-1, 1]^3$. Shape functions are defined in brick (e.g., 8, 27, or 64 nodes) elements. The three shape functions N^{3D} , $F(x, z)$, and $N(y)$ come together in a Jacobian matrix consisting of the shape derivatives of the shape function. These can represent curvilinear basis vectors [33].

2.2. Assigning random material variations

Variations analyzed in this paper are generated and applied by combining several different techniques and methods. These techniques have been previously applied and discussed in [28]. Geodesic distances define the correlation between points on a random field. Computing and mapping geodesic distances add complexity to the generation of fields in curved structures. This section will discuss the methods used to generate the geodesic distance array, generate the field, and map it to the structure.

2.2.1. Geodesics

Geodesic distance refers to the distance between points as it would be on a (curved) surface. On the other hand, Euclidean distance calculates the distance between two coordinates in space as a straight line. Finding the geodesic distance can be done with a variety of approaches. The most straightforward approach for this problem would be to find the shortest path between two points using the connectivity of a mesh. Utilizing a forward front in all directions to iteratively find the shortest distance is the most simplistic approach and first discussed by Dijkstra [35]. Such an approach tends to overestimate the distance, as it follows the edges of elements, while the shortest distance usually crosses over the face of an element (usually a polyhedron).

Finding the actual shortest distance over a mesh is a classic field of research in computational geometry, with many approaches being proposed and extended on over the years [36]. The approach used within this paper is based on the idea first published by Varadhan [37] and recently extended by Crane et al. [38]. In this approach, heat is introduced at a point on a mesh for a time t . Applying heat at a point generates a vector field of the heat flux on the surface. Normalizing this vector field generates a vector field of the shortest distances from the origin point, after which the geodesic distance is calculated by solving the Poisson heat equation. Crane has shown how this approach can be pre-factored, significantly reducing the computational time when distances between many points are required, as is the case for random fields.

Geodesic distances used to generate the field are computed on a surface within the 3D model. The surface used spans the mid-plane of the structure. Using a surface reduces the number of distances to points that have to be computed, reducing the computational effort of generating a distance array and the decomposition to generate random fields.

2.2.2. Generating random fields

Random fields are stochastically generated distributions of a parameter in n dimensional space. Fields generated within this work are generated on a 2D plane within 3D space. These random variables' values are not entirely unrelated to each other, and actual variations are usually related to their neighboring variations. Defining how close points are to each other is why the geodesic length of Section 2.2.1 is used to relate points. There are many different techniques to generate random fields [39]. Many of these methods have assumptions in space or correlation function. The method used within this work is called

Covariance Matrix Decomposition (CMD) and has the advantage of its relative ease in implementation and combining with geodesic length.

Correlation of two sets X and Y is defined mathematically as [40, ch. 10]

$$\rho_{X,Y} = \frac{\text{cov}(X, Y)}{\sigma_X \sigma_Y} = \frac{E[(X - \mu_X)(Y - \mu_Y)]}{\sigma_X \sigma_Y}, \tag{9}$$

where ρ is the correlation, cov the covariance operator, μ_i the mean of set i , σ_i the standard deviation of set i , and E the expectation operator, within random fields, these sets represent points in a field and how they relate to each other. The correlation varies between 1 and -1 and indicates the relationship between the two sets. It is useful for generating random fields to define functions, which define the correlation as a function of distance. The fields generated in this paper use the correlation function

$$\rho_{kl} = e^{-\left(\frac{l}{l_c}\right)^2}, \tag{10}$$

in which l_c is called the correlation length, and Δl the (geodesic) distance between points k and l . This correlation function is widely used in literature and produces smooth continuous fields, well suited for in-plane fiber-angle variations [41]. Correlation length defines a length scale at which the correlation function of Eq. (10) deteriorates. Experimentally measured correlation functions are not available in published literature and are highly dependant on the geometry and manufacturing process used. Studies analyzing random-field generated fiber imperfections on variable stiffness composites generally utilize a correlation length defined scale of curvature [42,41] or a set distance, generally shorter than the scale of the structure [43].

The CMD method uses discretized points in space and assigns a random value to that value [44]. The field must be discretized fine enough to represent the transition in variation amplitude. The necessary refinement was studied by Li & Kiureghian [45] and found to be between $\frac{1}{2}$ and $\frac{1}{3}$ for the correlation function of Eq. (10).

The CMD method decomposes the correlation matrix. This decomposed matrix can be used to calculate random fields through simple multiplication with a random vector χ with unit variance, and zero mean. The first step in generating fields is to build a correlation matrix of all points h_i of the field,

$$R_{ij} = \frac{\text{cov}(h_i, h_j)}{\sqrt{\sigma_{h_i} \sigma_{h_j}}} \rightarrow \mathbf{R} = \begin{bmatrix} 1 & \rho(h_1, h_2) & \dots & \rho(h_1, h_n) \\ \rho(h_2, h_1) & 1 & \dots & \rho(h_2, h_n) \\ \vdots & \vdots & \ddots & \vdots \\ \rho(h_n, h_1) & \rho(h_n, h_2) & \dots & \rho(h_n, h_n) \end{bmatrix}, \tag{11}$$

where $\rho(y_i, y_j) = \rho(y_j, y_i)$, noting that the correlation here can be calculated using Eq. (10).

Taking the definition of covariance

$$\text{cov}[X, Y] = E[XY] - E[X]E[Y], \tag{12}$$

and keeping in mind the field has a mean of zero, it is possible to show that \mathbf{R} can be decomposed into two matrices,

$$\begin{aligned} \mathbf{R} &= \text{cov}[x, x] = E[x \cdot x^T] - 0 \cdot 0 \\ &= E[(\mathbf{L}\chi)(\mathbf{L}\chi)^T] = E[\mathbf{L}\chi\chi^T\mathbf{L}^T] = \mathbf{L}\mathbf{\Lambda}\mathbf{L}^T = \mathbf{L}\mathbf{L}^T. \end{aligned} \tag{13}$$

From Eqs. (10) and (11) the matrix \mathbf{R} is symmetric and positive definite, the eigenvalues should all be positive and real. This decomposition is done by using eigendecomposition in the form of

$$\mathbf{R} = \mathbf{Q}\mathbf{\Lambda}\mathbf{Q} \tag{14}$$

in which $\mathbf{\Lambda}$ is a diagonal matrix with the eigenvalues of \mathbf{R} , and \mathbf{Q} contains the eigenvectors of the matrix. Matrix \mathbf{L} can be extracted from this as

$$\mathbf{R} = \mathbf{Q}\hat{\Lambda}\mathbf{Q} = \mathbf{L}\mathbf{L}^T - \mathbf{L} = \mathbf{Q}\hat{\Lambda}, \quad (15)$$

in which $\hat{\Lambda} = \text{diag}(\sqrt{\lambda})$, λ being the eigenvalues of the \mathbf{R} matrix. Using the decomposed correlation matrix \mathbf{L} , it is possible to generate random fields using

$$\mathbf{f} = \mathbf{L}\chi. \quad (16)$$

Decomposing is only necessary once, after which random fields are generated with a minimal computational cost.

2.2.3. Mapping random fields to structure

Fields are generated on a 2D (surface) within a 3D structure, not having any variability through the thickness of the structure, which is considered negligible for thin-walled structures. 3D brick elements described in Section 2.1.2 are used to map the field into a 3D space. Discretization of fields are not directly related and can be refined independently depending on their optima. Structures containing much curvature may benefit from a finely discretized random field (as the geodesic distances would be more accurate) while not necessarily needing a considerable refinement in structural elements to converge to accurate results.

While initializing, the analysis nodes of the geometric mesh are projected on the random field mesh. Random field element numbers and local coordinates are stored, creating a mapping between the two meshes. As this mapping is the same for all analyses, it only has to be done once and can be reused during the stochastic analysis. Values of the random field are evaluated using the shape function of the geometric mesh. Fig. 1 shows how a point in the structure i has element coordinates within the geometric mesh α, β, ξ .

During assembly of the stiffness matrix, the material properties are assigned as

$$\theta_{pe} = \theta_p + f_{pe}\theta_\sigma \quad (17)$$

in which θ_{pe} is the material orientation at point pe , θ_p is the mean value of θ , f_{pe} is the value of the random field at the point and θ_σ is the standard deviation of material parameter θ .

2.3. Deterministic improvement

Deterministic improvement of the buckling load of the baseline structure is achieved by analyzing the effects of random variations applied to the fiber angle. The authors' previous work has led to an increase of linear buckling loads by varying the thickness of Young's modulus in similar structures [28]. Similar to that approach, correlation patterns of fiber angle variations of every layer show the local

influence of fiber angle changes. Improvement in the buckling load is achieved by scaling this correlation pattern, perturbing the fiber paths of the baseline design.

2.3.1. Generating correlation patterns

Independent random fields are generated for every layer of a structure. These random fields represent small angle variations of the fiber paths in each layer. Variations generated can be modeled to be similar to real fiber path deviations but can also be fictitious.

Extending Eq. (9), it is possible to generate the local correlation pattern over n samples using

$$H_{ij} = \frac{\sum_{k=1}^n (f_{im,k} - \bar{f}_{im})(\theta_{i,j,k} - \bar{\theta}_i)}{\sqrt{\sum_{k=1}^n (f_{im,k} - \bar{f}_{im})^2} \sqrt{\sum_{k=1}^n (\theta_{i,j,k} - \bar{\theta}_i)^2}} \quad (18)$$

where H_{ij} is the correlated value of the buckling load f_{im} , and fiber angle variation at point i at layer j . Parameter $\theta_{i,j,k}$ is the fiber angle variation at point i , layer j , and sample k . Mean values of parameters are indicated using $\bar{\cdot}$.

The pattern generated infers the average influence a local fiber angle variation has on the buckling load. Applying this field to perturb the fiber path can thereby lead to an improvement in the buckling load of the structure. Patterns formed inherit the correlation of points to the distance defined by the correlation function of Eq. (10). Correlation in the distance within random variations leads to a continuity in the correlation pattern and defines its length scale. Correlation patterns generated using a large correlation length will vary over a relatively large distance. Shorter correlation lengths will lead to correlation patterns with more localized deviations, and a higher potential improvement [28]. Which correlation length to use while generating correlation patterns may also be determined by manufacturing considerations. As tighter fiber-placement curvatures are possible, the correlation length can become shorter.

2.3.2. Applying correlation pattern onto structure

Values of the correlation pattern show a non-dimensional relative influence of local variations. Applying these patterns to a structure first requires proper scaling. Normalization is first applied to the fields so that they fit in the range $[-1,1]$. Analyses within this paper utilize a normalization in which the global minima and maxima (over all fields) correspond to this range, not the individual layers minima and maxima.

Using this normalized field $\hat{\mathbf{H}}$ variations are computed using a maximum variation parameter ϕ , and a scaling parameter m . During matrix assembly, these parameters are used to evaluate material orientation using

$$\theta_{ij} = \theta_{0,ij} + \hat{H}_{ij}^m \phi_{ij}, \quad (19)$$

where $\theta_{0,ij}$ is the original material orientation.

Optimal values of m and ϕ depend on the structure in question and the desired reliability if there are stochastic variations present of the parameter in the structure.

2.4. Robustness analysis

The approach described in Section 2.3 can deterministically improve the structural performance by adding small variations in the material orientation (e.g., fiber angle). During manufacturing, random variations of material orientation can occur due to production processes. Robustness defines the effect that such imperfections have on the structure. When a design becomes more robust, the response becomes less sensitive to variations [46].

Improvements found using deterministic methods may be more sensitive to these random variations. These deterministic solutions are subjected to small local variations in fiber angle to analyze the

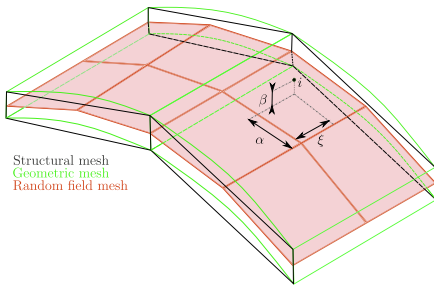


Fig. 1. Discretizations found in the structure, and the coordinates of i as projected into the geometric mesh [28]. Coordinates are then used to evaluate the value of a random field in the volume of the element.

robustness of the deterministic design with respect to fiber misalignments. Ideally, these would reflect real-world manufacturing tolerances, but even fictional variations can give a qualitative representation of the sensitivity of a structure to spatial fiber misalignments.

The fiber-alignment sensitivity of improved structures can be evaluated by comparing the statistical distribution of the buckling load of the baseline structure under random influences to that of the improved structure. Material orientation at every point i at layer j can be evaluated as

$$\theta_{ij} = \underbrace{\theta_{0,ij}}_{\text{Original}} + \underbrace{\mathbf{H}_{ij}^m \phi_{ij}}_{\text{Deterministic perturbation}} + \underbrace{\mathbf{f}_{ij} \theta_{\sigma}}_{\text{Random variation}}, \quad (20)$$

where the deterministic perturbation \mathbf{H} equals zero for the baseline configuration.

3. Numerical example

To demonstrate the approach discussed in Section 2, the approach is applied to a composite curved panel similar to the one analyzed in [10]. Analyses of the baseline structure without any variations applied show the linear and non-linear behavior of a structure without any variations applied. Following these baseline results, stochastic variations are applied to the structure, providing information on the effects of variations on the buckling load of the structure. Effects of these stochastic runs are then processed to find a correlation pattern across the structure. Perturbations of the fiber paths are made on the structure to improve the buckling load. These deterministic solutions are finally evaluated to quantify their ability to withstand spatial fiber misalignments.

3.1. Structure and solver

Dimensions of the panel are shown in Fig. 2. Three layers of anisotropic material are applied in a [90°,0°,90°] configuration, where 0° aligns with the y-axis. Table 1 lists the material properties of the layers.

The discretization of the structure consists of 10x3 third-order Serendipity Lagrange elements in the cross-section and ten elements in the axial direction. The structure has a total of 17670 degrees of freedom over all these elements.

Boundary conditions and loads consist of distributed loads applied on the edges of $y = 0$ and $y = 0.15$ totaling 1 N. Constraints limit out of plane displacement on the loaded edges. Axial displacement is constrained using two points on one of the loaded edges in the axial (y) direction.

Variations of the material orientation/fiber angle are applied of $\theta_{\sigma} = 2^\circ$. Fiber deviations, studied by Yurgartis, showed a measured range of up to this value [4]. Fields generated in this study use a correlation length of 25 mm for both correlation pattern generation and robustness analyses.

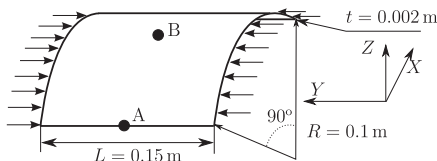


Fig. 2. Curved panel geometry.

Table 1 AS4 carbon fiber properties, taken from [47].

Material properties			
E_1	142 GPa	$E_2 = E_3$	10.3 GPa
G_{23}	4.28 GPa	$G_{13} = G_{12}$	7.2 GPa
ν_{23}	0.4	$\nu_{13} = \nu_{12}$	0.27

Analyses done in the following sections all utilize a non-linear solver. Buckling loads of the configurations are determined by using an arc-length based solver. Load is slowly increased until it ceases 5 sequential steps, the (limit-point) buckling load is the highest load found in the analysis.

3.2. Baseline analysis

Baseline results of the structure reach a buckling load of 22.1 kN. Deformations are in the form shown in Fig. 3b. Curved panels have asymmetric bifurcation behavior with an initially stable, as well as unstable equilibrium. Deformations indicate that the baseline solution follows the unstable branch of the asymmetric bifurcation.

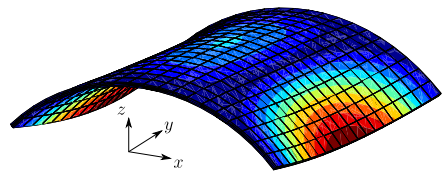
3.3. Stochastic analysis

Effects of fiber variations are analyzed by applying independent random fields to the three layers' fiber angles. Samples with random fields are generated and run 5000 times, generating the probability density shown in Fig. 4.

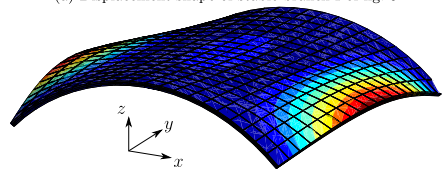
Displacements in the z-direction show distinct branching in responses. Fig. 5 shows displacement results of all the stochastic runs, highlighting four representative responses showing the different load–displacement paths. Branches I and II both have two mirrored versions of each other, depending on which side of the structure forms the buckle. Scaled initial post-buckling displacements corresponding to these paths are shown in figure Fig. 6.

Both of the equilibrium paths generate distinctly different responses. Lower load levels between 0.8–1.05 belong to the unstable branch II shown in Fig. 3b, the initially stable branch I of Fig. 3a has a buckling load that's approximately 50% higher.

Analyzing the two equilibrium paths, 62% of samples follow the unstable branch II, and 38% follow the initially stable branch I. Due



(a) Displacement shape of stable branch I of fig. 5



(b) Displacement shape of initially unstable branch II of fig. 5

Fig. 3. Scaled deformation shapes of the curved panel at buckling load.

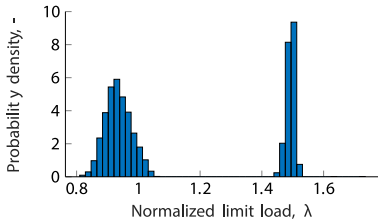
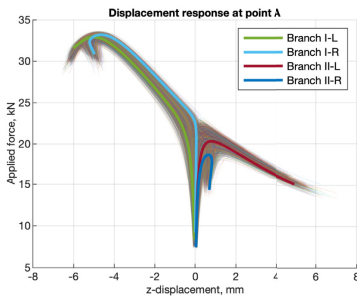
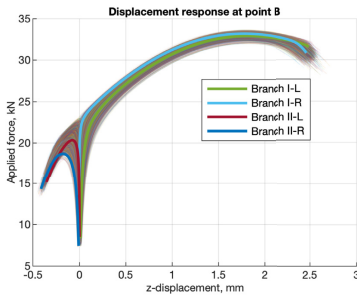


Fig. 4. Probability density plot of the buckling load of the baseline structure subjected to 2° variations of fiber angles, normalized to the baseline load.



(a) Results of z-displacements at point A



(b) Results of z-displacements at point B

Fig. 5. z-displacement results of stochastic runs at points A and B shown in Fig. 2, highlighting runs following different equilibrium branches.

to these two branches’ distinctly different characteristics, both branches are analyzed separately.

The unstable branch II, with λ between 0.8–1.1 has a mean value of 20.67 kN (0.935 λ) with a standard deviation of 934 N (0.042 λ), corresponding to a coefficient of variation of 4.52%. Branch II with initial stable behavior has a normalized buckling load around $\lambda = 1.5$, equaling a mean value of 32.99 kN (1.494 λ), with a standard deviation of 322 N (0.0147 λ) equalling a coefficient of variation of 0.975%.

3.4. Deterministic improvement

Improving the design is done by analyzing the runs done in Section 3.3, finding the correlation between local variations and the buckling load found, as discussed in Section 2.3. Doing these calculations leads to the patterns found in Fig. 7. Such patterns indicate the relative influence fiber angle variations have on the buckling load achieved. Patterns are continuous because variations are coupled to local distances through a correlation function, as discussed in Section 2.2.2 and [28].

Applying the correlation function to the structure, changing the predefined fiber paths is done by scaling the fields, as discussed in Section 2.3.2. Changing the scaling parameter m (Eq. (19)) affects how the pattern applies to the fiber paths. Figs. 9 to 11, shows examples with a scaling parameter m of 0.1, 1, and 10. Extreme scaling parameters used show how the pattern changes as the scaling parameter changes. Lower values for scaling parameter m lead to very aggressive fiber variations, with stronger curvatures in the path. Using high values leads to very local changes of orientation changes, retaining the original path in most of the structure. Scaling parameters close to 1 lead to a very smooth continuous fiber path without any quick changes.

A series of deterministic analyses are performed using a range of 1–20° maximum fiber variation ϕ , with a logarithmically spaced range of 21 different values between 0.1 and 10 for the scaling parameter m . Fig. 8 shows these deterministic analyses’ results, comparing the buckling load achieved with that of the baseline analysis done in Section 3.2. Results show that the most significant deterministic improvement is achieved using small local changes in the fiber path. Using a maximum variation of 1°, a scaling parameter of $m = 10$ led to the largest increase in the buckling load by 51.1%. Such a small deviation is enough to nudge the structure into the stable branch II path shown in Fig. 3a, which has a higher buckling load. As the fiber path perturbation increases in magnitude, the stiffness in the load-direction decreases, which reduces the buckling load, even when post-buckling branch II is triggered.

3.5. Robustness analysis

Stochastic results of Section 3.3 shows that the equilibrium path of the baseline structure can switch due to localized fiber variations. Variation also exists within these equilibrium branches, in which these variations can positively or negatively influence the load achieved before instability occurs.

Robustness, in the context of this paper, refers to the influence such variations have on a structure. Quantitatively, this entails reducing the spread of the buckling load, ensuring that the stable equilibrium branch is followed while simultaneously reducing the standard deviation of the response.

Stochastic analyses were performed on a selection of the configurations analyzed in Section 3.3. Each configuration had 1000 samples computed, in which random fiber angle variations were applied. Variations were generated using the same parameters used in Section 3.3, with $\sigma = 2^\circ$ and a correlation length $L_c = 25$ mm.

Results indicate that the mean values shown in Fig. 12 of specific configurations differ substantially from the deterministic results of Section 3.4. Comparing the graph with that of the coefficient of variation in Fig. 13, it is clear that this is due to different equilibrium paths being followed in specific configurations.

Fig. 14 shows results of the structure with a maximum fiber variation of 2°, and a scaling factor of $m = 10$. 56% of the samples follow the stable path, with 44% following the unstable path followed in the baseline configuration. Compared to the 38% of the baseline structure, this is an improvement but still shows a significant unpredictability.

Seeking an optimal series of parameters of imperfect structures requires a reliability target under stochastic inputs. If, for example,

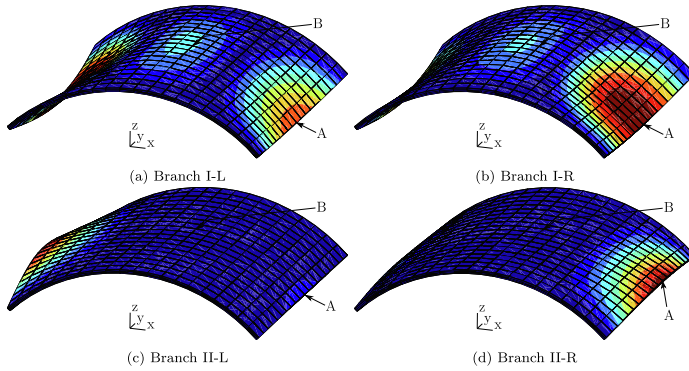


Fig. 6. Scaled deformation shapes just past the buckling load, color indicates total relative deformation.

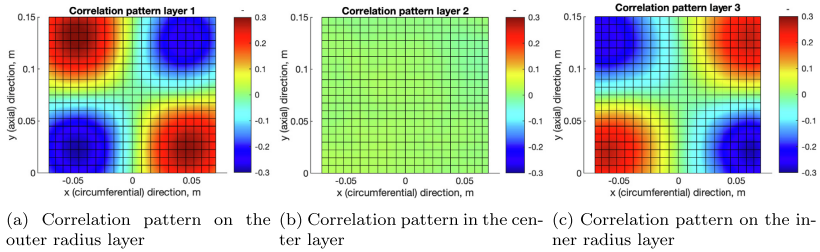


Fig. 7. Correlation of local fiber angle variations and buckling load achieved.

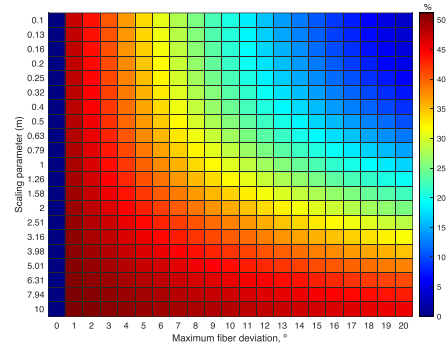


Fig. 8. Percent increase in buckling load in deterministic results achieved by applying correlation patterns using Eq. (19).

the buckling load for 99% of the structures should exceed a target value, the statistical properties of the lower 1% can be analyzed. For the inputs given, the 1% values of the configurations are shown in

Fig. 15. Values are generated using either a fit Gaussian distribution (Fig. 15a) or taking the lowest 1% of samples computed (Fig. 15b). Configurations that consistently stay within one branch will show similar results in both of these figures. Configurations that follow both equilibrium paths will not fit Gaussian distributions. Comparing these figures shows which configurations are sensitive to branch jumping with the set variation and which are not.

Several configurations show similar performance. The ideal setup might, therefore, be related to manufacturing-related considerations. For example, the configuration with a maximum fiber variation of 8° and a scaling parameter of $m = 6.31$, with the fiber paths shown in Fig. 17 has the distribution shown in Fig. 16. Samples generated using those parameters follow the stable equilibrium path, 99.7% of all runs. Increasing the likelihood that the more stable branch II is followed significantly decreases the variability in the post-buckling response. Decreasing the variance while increasing the expectant value of the response of a structure makes the structure more robust while also increasing reliability [46].

4. Conclusion

Misalignments in fiber angles can be represented using random fields. These stochastically generated misalignments can simulate the effects any local misalignments have on the structure. Analyzing the effects of local changes on the limit load of the structure gives the local

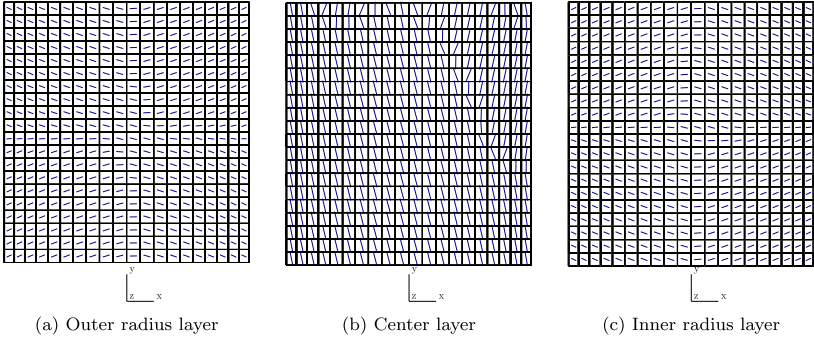


Fig. 9. Fiber orientation for configuration with maximum variation of $\phi = 20^\circ$ and scaling factor $m = 0.1$.

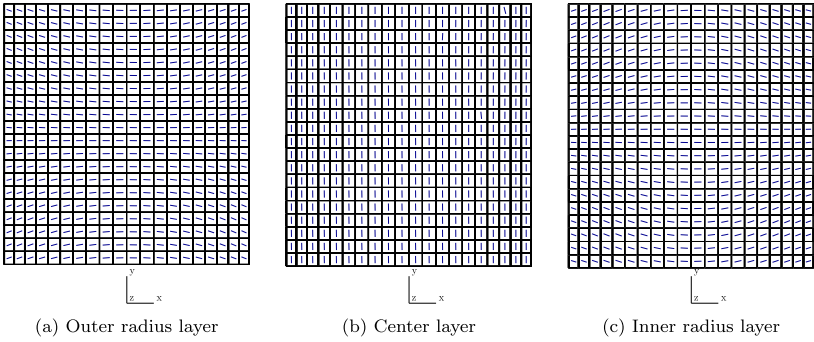


Fig. 10. Fiber orientation for configuration with maximum variation of $\phi = 20^\circ$ and scaling factor $m = 1$.

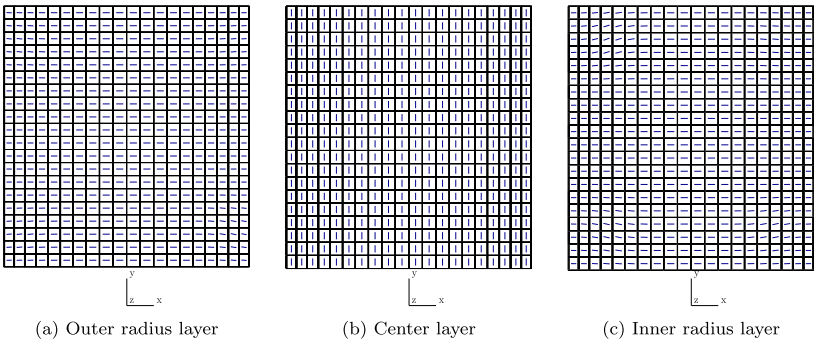


Fig. 11. Fiber orientation for configuration with maximum variation of $\phi = 20^\circ$ and scaling factor $m = 10$.

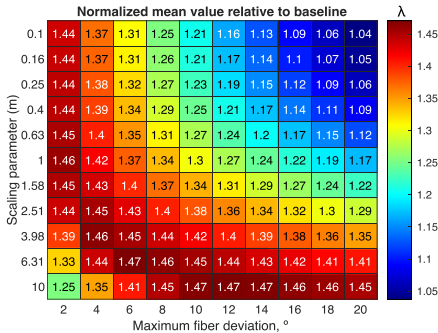


Fig. 12. Mean value of buckling load for configurations with fiber angle variations of $\theta_0 = 2^\circ$ with $L_c = 25$ mm applied.

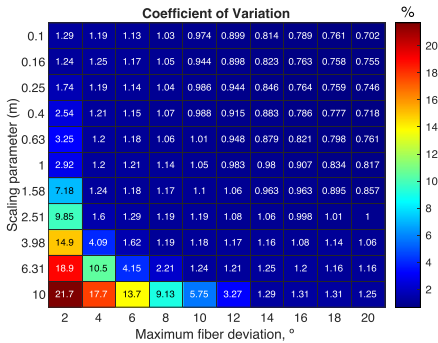


Fig. 13. Coefficient of variation of configurations with fiber angle variations of $\theta_0 = 2^\circ$ with $L_c = 25$ mm applied.

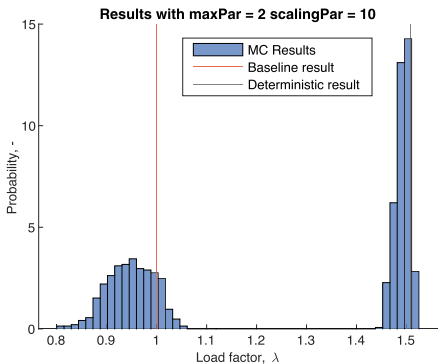
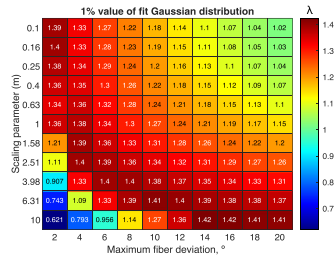
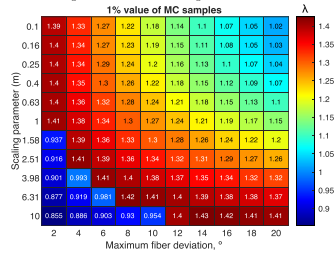


Fig. 14. Probability density of samples with perturbed fiber paths with a maximum variation of $\phi = 2^\circ$ and scaling parameter $m = 10$.



(a) 1% values of configurations obtained using Gaussian fit over numerical results



(b) 1% values of configurations obtained numerically

Fig. 15. Lowest 1% values for the normalized buckling load for configurations with scaling parameters m and maximum fiber deviations ϕ applied according to Eq. (19).

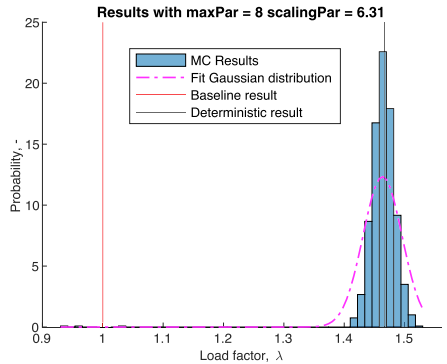


Fig. 16. Probability density of samples with perturbed fiber paths with a maximum variation $\phi = 8^\circ$ and scaling parameter $m = 6.31$.

effects of small perturbations on the buckling load. Thus, perturbing the design of a structure by incorporating minor changes to the fiber path can promote a more desirable post-buckling response.

Combining perturbed fiber paths in structures with random local misalignments makes it possible to quantify the chance that the desired equilibrium path is followed in an imperfect structure. Using statistical analysis on such combined runs makes it possible to compute the minimum load for a specific configuration. Parameters used to scale the field are a trade-off between mean improvement in the

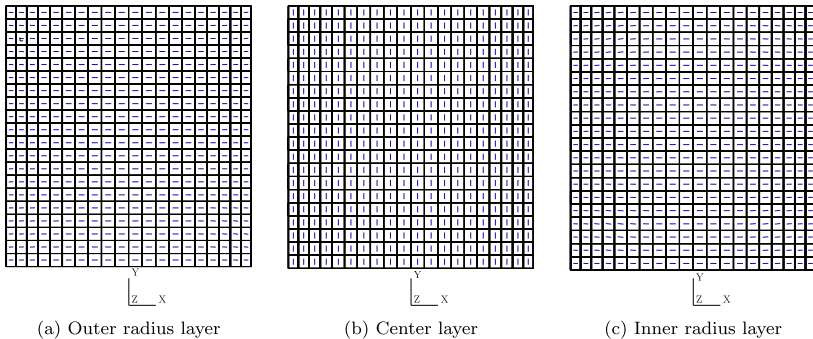


Fig. 17. Fiber orientation for configuration with maximum variation of $\phi = 8^\circ$ and scaling factor $m = 6.31$.

buckling load and the robustness of the structure, defined by the likelihood to follow the more stable post-buckling path in the presence of fiber misalignments.

Improvements found in the numerical example show increases in the order of 50%. The magnitude of improvement varies a lot by the specific structure analyzed and which equilibrium paths exist. Improvements can be higher than those of the example or lower. Improvements will also exist for other structures without a more stable post-buckling path nearby but will not be as significant. Instead of nudging the post-buckling path, the approach will redistribute the stiffnesses of a structure to increase the buckling load. Robustness, quantified by a reduction in variance, should be present in most structures.

The approach presented in this paper perturbs the design of a structure by applying small changes in the fiber orientation. Such perturbations can directly influence the deterministic solution (without random local misalignments applied) of the structural response and make the response more robust to simulated imperfections in fiber alignment. The ideal scaling parameters used to perturb the structure depend on the fiber misalignments expected in the structure, which affects the robustness of the structure.

Analyses presented in this work focus solely on fiber angle variations. Imperfections are not limited to such variations, and future work should take others, such as geometric, into account. No limits are present in the approach itself, as similar approaches have already been used for thickness and Young's modulus tailoring [28]. Combining multiple sources of variations can potentially further improve the insensitivity, and deterministic improvements presented.

5. Data availability

The raw data required to reproduce these findings may be available on request.

Declaration of Competing Interest

The authors declare that they have no known competing financial interests or personal relationships that could have appeared to influence the work reported in this paper.

Acknowledgements

This research work has been carried out within the project FULLCOMP (FULLY integrated analysis, design, manufacturing and

health-monitoring of COMposite structures), funded by the European Union Horizon 2020 Research and Innovation program under the Marie Skłodowska-Curie grant agreement No. 642121.

The calculations presented here were partially carried out on the computing cluster system of the Leibniz University of Hannover, Germany.

References

- [1] Calladine CR. Understanding imperfection-sensitivity in the buckling of thin-walled shells. *Thin-Walled Struct* 1995;23:215–35.
- [2] Kettle J, Herath MT, Pearce G, Gangadhara Prusty B, Thomson R, Degenhardt R. Stochastic analysis of imperfection sensitive unstiffened composite cylinders using realistic imperfection models. *Compos Struct* 2015;126:159–73.
- [3] Manta A, Gresil M, Soutis C. Infrared thermography for void mapping of a graphene/epoxy composite and its full-field thermal simulation. *Fatigue Fract Eng Mater Struct* 2019:1–13.
- [4] Yurgartis SW. Measurement of small angle fiber misalignments in continuous fiber composites. *Compos Sci Technol* 1987;30:279–93.
- [5] Sankumar P, Suresh R, Vijaygosh PK, Gupta S. Experimental characterisation of random field models for CFRP composite panels. *Compos Struct* 2015;120:451–71.
- [6] Sriramula S, Chryssanthopoulos MK. An experimental characterisation of spatial variability in GFRP composite panels. *Struct Saf* 2013;42:1–11.
- [7] Dodwell TJ, Kinston S, Butler R, Hafika RT, Kim NH, Scheichl R. Multilevel Monte Carlo simulations of composite structures with uncertain manufacturing defects 2019.
- [8] Stefanou G, Savvas D, Papadrakakis M. Stochastic finite element analysis of composite structures based on mesoscale random fields of material properties. *Comput Methods Appl Mech Eng* 2017;326:319–37.
- [9] Scarth C, Adhikari S, Cabral PH, Silva GHC, Prado APD, Higinio P, Silva GHC, Prado APD. Random field simulation over curved surfaces: applications to computational structural mechanics. *Comput Methods Appl Mech Eng* 2019;345:283–301.
- [10] van den Broek S, Jansen E, Minerá S, Weaver PM, Rolles R. Effect of spatially varying material properties on the post-buckling behaviour of composite panels utilising geodesic stochastic fields. In: Proceedings of the 6th aircraft structural design conference, Bristol, United Kingdom.
- [11] Papadopoulos V, Papadrakakis M. The effect of material and thickness variability on the buckling load of shells with random initial imperfections. *Comput Methods Appl Mech Eng* 2005;194:1405–26.
- [12] Tootkabanli M, Graham-Brady L, Schafer BW. Geometrically non-linear behavior of structural systems with random material property: An asymptotic spectral stochastic approach. *Comput Methods Appl Mech Eng* 2009;198:3173–85.
- [13] Hu N, BURGUEÑO R. Cylindrical shells with tunable postbuckling features through non-uniform patterned thickening patches. *Int J Struct Stab Dyn* 2018;18:1850026.
- [14] Hu N, BURGUEÑO R. Harnessing seeded geometric imperfection to design cylindrical shells with tunable elastic postbuckling behavior. *J Appl Mech* 2017;84:011003.
- [15] Cox BS, Groh RM, Avitabile D, Pirrera A. Modal nudging in nonlinear elasticity: Tailoring the elastic post-buckling behaviour of engineering structures. *J Mech Phys Solids* 2018;116:135–49.
- [16] Cox BS, Groh RM, Pirrera A. Nudging axially compressed cylindrical panels toward imperfection insensitivity. *J Appl Mech Trans ASME* 2019;86.
- [17] Hyer MW, Charette RF. Use of curvilinear fiber format in composite structure design. *AIAA J* 1991;29:1011–5.

- [18] Grdal Z, Tatting BF, Wu CK. Variable stiffness composite panels: Effects of stiffness variation on the in-plane and buckling response. *Compos Part A* 2008;39:911–22.
- [19] Wu Z, Raju G, Weaver PM. Postbuckling analysis of variable angle tow composite plates. *Int J Solids Struct* 2013;50:1770–80.
- [20] Goburn BH, Wu Z, Weaver PM. Buckling analysis of stiffened variable angle tow panels. *Compos Struct* 2014;111:259–70.
- [21] Haldar A, Groh RM, Jansen E, Weaver PM, Rolfes R. An efficient semi-analytical framework to tailor snap-through loads in bistable variable stiffness laminates. *Int J Solids Struct* 2020;195:91–107.
- [22] Blom AW, Lopes CS, Kromwijk PJ, Grdal Z, Camanho PP. A theoretical model to study the influence of tow-drop areas on the stiffness and strength of variable-stiffness laminates. *J Compos Mater* 2009;43:403–25.
- [23] Rakhshbahar M, Sinapius M. A novel approach: combination of automated fiber placement (AFP) and additive layer manufacturing (ALM). *J Compos Sci* 2018;2:42.
- [24] Kim BC, Potter K, Weaver PM. Continuous tow shearing for manufacturing variable angle tow composites. *Compos Part A* 2012;43:1347–56.
- [25] Dodwell TJ, Butler R, Rhead AT. Optimum fiber steering of composite plates for buckling and manufacturability. *AIAA J* 2016;54:1139–42.
- [26] Marczyk J. Stochastic multidisciplinary improvement – Beyond optimization. In: 8th Symposium on multidisciplinary analysis and optimization.
- [27] White SC, Raju G, Weaver PM. Initial post-buckling of variable-stiffness curved panels. *J Mech Phys Solids* 2014;71:132–55.
- [28] van den Broek S, Minera S, Pirrera A, Weaver PM, Jansen E, Rolfes R. Enhanced deterministic performance of panels using stochastic variations of geometry and material. *AIAA J* 2020;58:2307–20.
- [29] Minera S, Patni M, Carrera E, Petrolo M, Weaver PM, Pirrera A. Three-dimensional stress analysis for beam-like structures using serendipity lagrange shape functions. *Int J Solids Struct* 2018;141–142:279–96.
- [30] Patni M, Minera S, Weaver PM, Pirrera A. Efficient modelling of beam-like structures with general non-prismatic, curved geometry. *Comput Struct* 2020;240:106339.
- [31] De Borst R, Crisfield MA, Remmers JJ, Verhoosel CV. *Nonlinear finite element analysis of solids and structures*. John Wiley & Sons; 2012.
- [32] Pagani A, Carrera E. Unified formulation of geometrical nonlinear refined beam theories. *Mech Adv Mater Struct* 2018;25:15–31.
- [33] Minera S. Analysis and design of buckling resistant thin-walled structures via computationally efficient 3d stress analysis, Ph.D. thesis, University of Bristol; 2019.
- [34] Patni M, Minera S, Bisagni C, Weaver P, Pirrera A. Geometrically nonlinear finite element model for predicting failure in composite structures. *Compos Struct* 2019;225:111068.
- [35] Dijkstra EW. A note on two problems in connexion with graphs. *Numer Math* 1959;1:269–71.
- [36] Bose P, Maheshwari A, Shu C, Whrer S. A survey of geodesic paths on 3D surfaces. *Comput Geom Theor Appl* 2011;144:486–98.
- [37] Varadhan SRS. On the behavior of the fundamental solution of the heat equation with variable coefficients. *Commun Pure Appl Math* 1967;20:431–55.
- [38] Crane K, Weischedel G, Wardetzky M. The heat method for distance computation. *Commun ACM* 2017;60:90–9.
- [39] Spanos PD, Zeldin BA. Monte Carlo treatment of random fields: a broad perspective. *Appl Mech Rev* 1998;51:219.
- [40] Dekking FM, Kraaikamp C, Løpuha HP, Meester LE. *A modern introduction to probability and statistics: Understanding why and how*, Springer Science & Business Media; 2005.
- [41] Pagani A, Sanchez-Majano AR. Stochastic stress analysis and failure onset of variable angle tow laminates affected by spatial fibre variations. *Compos Part C* 2021;4:100091.
- [42] Pagani A, Sanchez-Majano AR. Influence of fiber misalignments on buckling performance of variable stiffness composites using layerwise models and random fields. *Mech Adv Mater Struct* 2020;1–15.
- [43] Sepahvand K. Spectral stochastic finite element vibration analysis of fiber-reinforced composites with random fiber orientation. *Compos Struct* 2016;145:119–28.
- [44] Davis MW. Production of conditional simulations via the LU triangular decomposition of the covariance matrix. *Math Geol* 1987;19:91–8.
- [45] Li C-C, Der Kiureghian A. Optimal discretization of random fields. *J Eng Mech* 1993;119:1136–54.
- [46] Yao W, Chen X, Luo W, Van Tooren M, Guo J. Review of uncertainty-based multidisciplinary design optimization methods for aerospace vehicles. *Prog Aerosp Sci* 2011;47:450–79.
- [47] Barbero EJ. *Introduction to composite materials design*, CRC Press. 2nd ed, 2011.

SUMMARY AND FUTURE WORK

We demand rigidly defined areas of doubt and uncertainty!

— Douglas Adams

6.1 SUMMARY

This thesis aimed to present a general approach to improve a structure's performance by applying small perturbations to material or geometric parameters. Improvements come forth from analyzing stochastic analyses, which use geodesic random fields.

Geodesic distances refer to the distances using the structure's geometry rather than Euclidian space. Random fields using geodesic distances can better simulate spatially varying structural parameters on curved structures.

Applying a point source of heat onto a structure gives a gradient of heat flowing away from the point. Normalizing this gradient gives a general direction of heat flow in the structure, thereby creating the path with the shortest distance. Integrating the distance of the path followed then gives the geodesic distance between points.

Extensions of this heat method generating random fields make it possible to generate anisotropic or inter-correlated fields. Extensions such as these are particularly interesting when analyzing specific types of structures. Anisotropic fields are useful for, e.g., generating geometric imperfections in cylinders, which may vary in circumferential and axial directions. Anisotropic fields use anisotropic heat conductivity to define the gradients of the heat flow. Parametric studies show that the pseudo-distance computed is not the exact scaled geodesic distance but rather a parameter that gives a more smoothed pseudo-distance.

Another extension introduced is the simultaneous generation of multiple fields that are correlated with each other. Such fields are both correlated internally by a correlation function but also show similarities among the set of simultaneously generated fields. Using these types of fields, imperfection patterns can be generated that show many similarities (correlation) between each other. Intercorrelated fields can help analyze the effects of fiber misalignments in a composite structure. Misalignments can originate from

different sources, such as fiber placement and curing. Some variations may affect a single layer (lamina), while others affect the complete laminate. Sets of correlated fields can represent global misalignments and simultaneously add local misalignments to the fields.

Stochastic analyses using geodesic random fields make it possible to quantify the effects of random imperfections of structures given a correlation function and distribution. The correlation function describes the shape and distribution of local variation of a parameter, while the distribution describes the statistical distribution from which local variations are sampled. Such analyses make it possible to quantify the robustness and reliability of a structure.

Analyzing structures with randomly generated local imperfections can reveal the local effects of a change in a parameter. Patterns generated by correlating local structural parameters (such as thickness) and a structural measure, such as maximum stress or buckling load, can be obtained using realistic or fictional variations. Patterns generated indicate the local trend of a parameter on the effects of a structural measure. Perturbing the design using this information makes it possible to redistribute thickness to increase the buckling load, for example.

Patterns generated by correlating local changes of a parameter with a structural measure vary depending on the correlation function and length used. As variations become more localized in a random field (e.g., by applying fields with a shorter correlation length), correlated patterns can become less smooth than larger lengths.

Using correlation patterns obtained from stochastic analyses, varying the material or structural parameter deterministically becomes possible. Analyzing the effects of thickness variations on the linear buckling load can lead to a pattern relating thickness changes to the buckling load. Using this pattern to redistribute material by varying the local thickness makes it possible to increase the buckling load.

Additive manufacturing validated a thickness redistribution of an open-hole specimen in which the number of cycles until fatigue failure was used as a structural measure. Numerical results indicated that using a thickness-redistributed design would increase the fatigue life by an estimated factor of approximately 10x. Stochastic analyses were done on the baseline constant-thickness design and the design with a tailored thickness distribution. A reduction in the standard deviation was found in the tailored structure, indicating that the improved design is more robust than the original.

Applying the approach to a composite curved panel using variations in the fiber angle led to a series of steered fiber path designs. The analyzed structure had an asymmetric post-buckling behavior, in which two post-buckling paths are near each other but have significantly different buckling loads. Deterministic improvements were best when very minute changes were applied, pushing an ideal structure into a more-stable path. Applying random fiber misalignments showed that the best deterministic improvement configurations were the most sensitive to random misalignments. Optimal fiber path perturbations are determined by taking realistic fiber misalignments (and other variations when possible) into account.

Methods shown in this thesis can be used to readily analyze the effects of local imperfections on curved thin-walled structures and analyze the sensitivity to changes in geometry or material properties. The developed approach has successfully been applied to tailor different structures, including cylindrical shells, open-hole specimens and curved panels. Structural parameters used to tailor structures include Young's modulus, thickness, and fiber path (material orientation). In addition to deterministic improvements, the robustness of improved design is also analyzed, showing that this can be improved using the method.

6.2 FUTURE WORK

Studies performed in this thesis have been on a limited amount of parameters and relatively small structures. Future work should involve applying this approach to larger, more complex structures, varying multiple parameters simultaneously. Doing so will increase the number of degrees of freedom and parameters varied, potentially slowing down the enhancement process. Improvements to the algorithm can increase computational efficiency in several ways:

SAMPLING Sampling in the work shown is entirely random, not taking prior fields into account. Generating fields that are sampled orthogonally to each other can improve the convergence of patterns, requiring fewer samples.

PERTURBATION APPROACH Applying the approach within a perturbation-type stochastic analysis could improve computational efficiency. As shown in section 1.2.2.8, perturbation analyses represent the output of a stochastic problem as a Taylor-series expansion. Combining orthogonal fields with a Taylor series expansion could make correlation-

pattern generation much faster. Faster estimation of the standard deviation also makes optimization of scaling parameters of robust designs feasible, as doing this using Monte Carlo analyses can be time-consuming.

MACHINE LEARNING Instead of using a correlation between points and a structural measure to find a pattern and perturb the structure, it would also be possible to use this data to train a neural network. A trained neural network of structure would estimate the effects of local changes to the structure without running a full finite element analysis. Similar work done by Sun *et al.* [196] predicts stress levels of fiber-reinforced polymers based on microstructure imperfections. Work done by Giovanis & Papadopoulos [197] also improves in speeding up random field imperfections using a neural network. Such an approach can assist in increasing the speed in which patterns are computed, and robustness can be evaluated.

Increasing efficiency makes it possible to analyze larger structures with more complex and interconnected variations. Analysis with multiple layers of fibers has already been demonstrated in chapter 5. Analyzing different types of parameters, such as geometry and fiber path, would potentially make it possible to design perturbations that improve a structure in multiple ways while also making it more robust to multiple types of imperfections.

An aspect not thoroughly explored in this thesis is manufacturing applications using the tools developed in this thesis. Correlation patterns identify areas that influence the structure's response most when deviations occur of the material or geometric parameters.

Areas that are the most sensitive can be the target of non-destructive quality inspections. Rejecting structures with an unacceptable deviation in critical areas leads to an increase in accepted structures' robustness.

Manufacturing processes can also use correlation patterns to tweak the manufacturing process. Manufacturing processes often have the option to slow down in order to increase accuracy. Slowing down the manufacturing of an entire component can be expensive, but slowing down at certain stages/areas of manufacturing could be economical, especially if it helps achieve design objectives. Laying tapes with an AFP process, as an example, could be slowed down in certain areas in order to increase local accuracy. Such local slow-downs can increase the overall quality of the product without unnecessarily slowing down production too much.

BIBLIOGRAPHY

1. Yang, J., Liew, K. M. & Kitipornchai, S. Second-order statistics of the elastic buckling of functionally graded rectangular plates. *Composites Science and Technology* **65**, 1165. ISSN: 02663538. doi:10.1016/j.compscitech.2004.11.012 (2005).
2. Parthasarathy, J., Starly, B. & Raman, S. A design for the additive manufacture of functionally graded porous structures with tailored mechanical properties for biomedical applications. *Journal of Manufacturing Processes* **13**, 160. ISSN: 15266125. doi:10.1016/j.jmapro.2011.01.004 (2011).
3. Chi, S. H. & Chung, Y. L. Mechanical behavior of functionally graded material plates under transverse load-Part I: Analysis. *International Journal of Solids and Structures* **43**, 3657. ISSN: 00207683. doi:10.1016/j.ijsolstr.2005.04.011 (2006).
4. Hu, N. & Burgueño, R. Cylindrical Shells with Tunable Postbuckling Features Through Non-Uniform Patterned Thickening Patches. *International Journal of Structural Stability and Dynamics* **18**, 1850026. ISSN: 0219-4554. doi:10.1142/S0219455418500268 (2018).
5. Li, Y. W., Elishakoff, I. & Starnes, J. H. Axial buckling of composite cylindrical shells with periodic thickness variation. *Computers and Structures* **56**, 65. ISSN: 00457949. doi:10.1016/0045-7949(94)00527-A (1995).
6. Chen, Z., Yang, L., Cao, G. & Guo, W. Buckling of the axially compressed cylindrical shells with arbitrary axisymmetric thickness variation. *Thin-Walled Structures* **60**, 38. ISSN: 02638231. doi:10.1016/j.tws.2012.07.015 (2012).
7. Hu, N. & Burgueño, R. Elastic postbuckling response of axially-loaded cylindrical shells with seeded geometric imperfection design. *Thin-Walled Structures* **96**, 256. ISSN: 02638231. doi:10.1016/j.tws.2015.08.014 (2015).
8. Cox, B. S., Groh, R. M., Avitabile, D. & Pirrera, A. Modal nudging in nonlinear elasticity: Tailoring the elastic post-buckling behaviour of engineering structures. *Journal of the Mechanics and Physics of Solids* **116**, 135. ISSN: 00225096. doi:10.1016/j.jmps.2018.03.025 (2018).

9. Hu, N. & Burgueño, R. Harnessing Seeded Geometric Imperfection to Design Cylindrical Shells With Tunable Elastic Postbuckling Behavior. *Journal of Applied Mechanics* **84**, 011003. ISSN: 0021-8936. doi:10.1115/1.4034827 (2017).
10. Fina, M., Panther, L., Weber, P. & Wagner, W. Shell Buckling With Polymorphic Uncertain Surface Imperfections and Sensitivity Analysis. *ASCE-ASME Journal of Risk and Uncertainty in Engineering Systems, Part B: Mechanical Engineering* **7**. ISSN: 2332-9017. doi:10.1115/1.4050165 (2021).
11. Bielewicz, E., Górski, J., Schmidt, R. & Walukiewicz, H. Random fields in the limit analysis of elastic-plastic shell structures. *Computers and Structures* **51**, 267. ISSN: 00457949. doi:10.1016/0045-7949(94)90334-4 (1994).
12. Teixeira, Â. P. & Soares, C. G. *Ultimate strength of plates with random fields of corrosion in Structure and Infrastructure Engineering* **4** (2008), 363. ISBN: 0415399017 | 9780415399012. doi:10.1080/15732470701270066.
13. Pagani, A. & Sanchez-Majano, A. R. Influence of fiber misalignments on buckling performance of variable stiffness composites using layer-wise models and random fields. *Mechanics of Advanced Materials and Structures* **0**, 1. ISSN: 15376532. doi:10.1080/15376494.2020.1771485 (2020).
14. Herzog, D., Jaeschke, P., Meier, O. & Haferkamp, H. Investigations on the thermal effect caused by laser cutting with respect to static strength of CFRP. *International Journal of Machine Tools and Manufacture* **48**, 1464. ISSN: 08906955. doi:10.1016/j.ijmachtools.2008.04.007 (2008).
15. Staehr, R., Bluemel, S., Hansen, P., Jaeschke, P., Suttmann, O. & Overmeyer, L. The influence of moisture content on the heat affected zone and the resulting in-plane shear strength of laser cut thermo-plastic CFRP. *Plastics, Rubber and Composites* **44**, 111. ISSN: 17432898. doi:10.1179/1743289814Y.0000000114 (2015).
16. Gibson, I., Rosen, D. W. & Stucker, B. *Additive Manufacturing Technologies* ISBN: 9781441911193. doi:10.1007/978-1-4419-1120-9 (Springer Science & Business Media, 2010).
17. Blok, L. G., Longana, M. L., Yu, H. & Woods, B. K. An investigation into 3D printing of fibre reinforced thermoplastic composites. *Additive Manufacturing* **22**, 176. ISSN: 22148604. doi:10.1016/j.addma.2018.04.039 (2018).

18. Lindgren, L. E. & Lundbäck, A. Approaches in computational welding mechanics applied to additive manufacturing: Review and outlook. *Comptes Rendus - Mecanique* **346**, 1033. ISSN: 16310721. doi:10.1016/j.crme.2018.08.004 (2018).
19. Tymrak, B. M., Kreiger, M. & Pearce, J. M. Mechanical properties of components fabricated with open-source 3-D printers under realistic environmental conditions. *Materials and Design* **58**, 242. ISSN: 18734197. doi:10.1016/j.matdes.2014.02.038 (2014).
20. Chacón, J. M., Caminero, M. A., García-Plaza, E. & Núñez, P. J. Additive manufacturing of PLA structures using fused deposition modelling: Effect of process parameters on mechanical properties and their optimal selection. *Materials and Design* **124**, 143. ISSN: 18734197. doi:10.1016/j.matdes.2017.03.065 (2017).
21. Letcher, T. & Waytashek, M. *Material Property Testing of 3D-Printed Specimen in PLA on an Entry-Level 3D Printer in Volume 2A: Advanced Manufacturing* (American Society of Mechanical Engineers, 2014), 1. ISBN: 978-0-7918-4643-8. doi:10.1115/IMECE2014-39379.
22. Wu, W., Geng, P., Li, G., Zhao, D., Zhang, H. & Zhao, J. Influence of layer thickness and raster angle on the mechanical properties of 3D-printed PEEK and a comparative mechanical study between PEEK and ABS. *Materials* **8**, 5834. ISSN: 19961944. doi:10.3390/ma8095271 (2015).
23. Ezeh, O. H. & Susmel, L. Fatigue strength of additively manufactured polylactide (PLA): effect of raster angle and non-zero mean stresses. *International Journal of Fatigue* **126**, 319. ISSN: 01421123. doi:10.1016/j.ijfatigue.2019.05.014 (2019).
24. Barbero, E. J. *Introduction to Composite Materials Design, Third Edition* 2nd Editio. ISBN: 9781315296494. doi:10.1201/9781315296494 (CRC Press, 2017).
25. Campbell, F. C. *Structural composite materials* 1. ISBN: 978-1-61503-037-8 (ASM international, 2010).
26. Tuttle, M. E. & Tuttle, M. E. *Structural Analysis of Polymeric Composite Materials* 1. ISBN: 9780429169137. doi:10.1201/b13672 (Chapman and Hall/CRC, 2012).
27. Talreja, R. in *Polymer Composites in the Aerospace Industry* 83 (Elsevier, 2020). ISBN: 9780081026793. doi:10.1016/B978-0-08-102679-3.00004-6.

28. Sokołowski, D. & Kamiński, M. *Homogenization of carbon/polymer composites with anisotropic distribution of particles and stochastic interface defects* **9**, 3727. ISBN: 0070701821747. doi:10.1007/s00707-018-2174-7 (Springer Vienna, 2018).
29. Sokołowski, D. & Kamiński, M. Computational homogenization of carbon/polymer composites with stochastic interface defects. *Composite Structures* **183**, 434. ISSN: 02638223. doi:10.1016/j.compstruct.2017.04.076 (2018).
30. Kamiński, M. Stochastic Boundary Element Method analysis of the interface defects in composite materials. *Composite Structures* **94**, 394. ISSN: 02638223. doi:10.1016/j.compstruct.2011.07.026 (2012).
31. Czichon, S. *Multi scale Failure Analysis of Fibre Reinforced Polymers with production induced Porosity Defects* PhD thesis (Leibniz University Hannover, 2013).
32. Hyde, A., He, J., Cui, X., Lua, J. & Liu, L. Effects of microvoids on strength of unidirectional fiber-reinforced composite materials. *Composites Part B: Engineering* **187**, 107844. ISSN: 13598368. doi:10.1016/j.compositesb.2020.107844 (2020).
33. Liu, L., Zhang, B. M., Wang, D. F. & Wu, Z. J. Effects of cure cycles on void content and mechanical properties of composite laminates. *Composite Structures* **73**, 303. ISSN: 02638223. doi:10.1016/j.compstruct.2005.02.001 (2006).
34. Koushyar, H., Alavi-Soltani, S., Minaie, B. & Violette, M. Effects of variation in autoclave pressure, temperature, and vacuum-application time on porosity and mechanical properties of a carbon fiber/epoxy composite. *Journal of Composite Materials* **46**, 1985. ISSN: 00219983. doi:10.1177/0021998311429618 (2012).
35. Mehdikhani, M., Gorbatikh, L., Verpoest, I. & Lomov, S. V. Voids in fiber-reinforced polymer composites: A review on their formation, characteristics, and effects on mechanical performance. *Journal of Composite Materials* **53**, 1579. ISSN: 1530793X. doi:10.1177/0021998318772152 (2019).
36. Lukaszewicz, D. H., Potter, K. D. & Eales, J. A concept for the in situ consolidation of thermoset matrix prepreg during automated lay-up. *Composites Part B: Engineering* **45**, 538. ISSN: 13598368. doi:10.1016/j.compositesb.2012.09.008 (2013).

37. Kratmann, K. K., Sutcliffe, M. P., Lilleheden, L. T., Pyrz, R. & Thomsen, O. T. A novel image analysis procedure for measuring fibre misalignment in unidirectional fibre composites. *Composites Science and Technology* **69**, 228. ISSN: 02663538. doi:10.1016/j.compscitech.2008.10.020 (2009).
38. Yurgartis, S. W. Measurement of small angle fiber misalignments in continuous fiber composites. *Composites Science and Technology* **30**, 279. ISSN: 0266-3538. doi:10.1016/0266-3538(87)90016-9 (1987).
39. Potter, K., Khan, B., Wisnom, M., Bell, T. & Stevens, J. Variability, fibre waviness and misalignment in the determination of the properties of composite materials and structures. *Composites Part A: Applied Science and Manufacturing* **39**, 1343. ISSN: 1359835X. doi:10.1016/j.compositesa.2008.04.016 (2008).
40. Mehdikhani, M., Breite, C., Swolfs, Y., Wevers, M., Lomov, S. V. & Gorbatikh, L. Combining digital image correlation with X-ray computed tomography for characterization of fiber orientation in unidirectional composites. *Composites Part A: Applied Science and Manufacturing* **142**, 106234. ISSN: 1359835X. doi:10.1016/j.compositesa.2020.106234 (2021).
41. Heinecke, F. & Willberg, C. Manufacturing-Induced Imperfections in Composite Parts Manufactured via Automated Fiber Placement. *Journal of Composites Science* **3**, 56. ISSN: 2504-477X. doi:10.3390/jcs3020056 (2019).
42. Maass, D. Progress in automated ply inspection of AFP layups. *Reinforced Plastics* **59**, 242. ISSN: 0034-3617. doi:10.1016/j.repl.2015.05.002 (2015).
43. Lozano, G. G., Tiwari, A. & Turner, C. A design algorithm to model fibre paths for manufacturing of structurally optimised composite laminates. *Composite Structures*. ISSN: 0263-8223. doi:10.1016/j.compstruct.2018.07.088 (2018).
44. Lichtinger, R., Lacalle, J., Beier, U. & Drechsler, K. Simulation and experimental validation of gaps and bridging in the automated fiber placement process. **22**, 131. doi:10.1515/secm-2013-0158 (2015).
45. Lukaszewicz, D. H., Ward, C. & Potter, K. D. The engineering aspects of automated prepreg layup: History, present and future. *Composites Part B: Engineering* **43**, 997. ISSN: 13598368. doi:10.1016/j.compositesb.2011.12.003 (2012).

46. Perner, M., Algermissen, S., Keimer, R. & Monner, H. P. *Avoiding defects in manufacturing processes: A review for automated CFRP production* 2016. doi:10.1016/j.rcim.2015.10.008.
47. Sriramula, S. & Chryssanthopoulos, M. K. An experimental characterisation of spatial variability in GFRP composite panels. *Structural Safety* **42**, 1. ISSN: 01674730. doi:10.1016/j.strusafe.2013.01.002 (2013).
48. Sasikumar, P., Suresh, R., Vijayaghosh, P. K. & Gupta, S. Experimental characterisation of random field models for CFRP composite panels. *Composite Structures* **120**, 451. ISSN: 02638223. doi:10.1016/j.compstruct.2014.10.023 (2015).
49. Birt, E. A. & Smith, R. A. A review of NDE methods for porosity measurement in fibre-reinforced polymer composites. *Insight: Non-Destructive Testing and Condition Monitoring* **46**, 681. ISSN: 13542575. doi:10.1784/insi.46.11.681.52280 (2004).
50. Manta, A., Gresil, M. & Soutis, C. Infrared thermography for void mapping of a graphene/epoxy composite and its full-field thermal simulation. *Fatigue and Fracture of Engineering Materials and Structures*, **1**. ISSN: 14602695. doi:10.1111/ffe.12980 (2019).
51. Saenz-Castillo, D., Martín, M., Calvo, S., Rodriguez-Lence, F. & Güemes, A. Effect of processing parameters and void content on mechanical properties and NDI of thermoplastic composites. *Composites Part A: Applied Science and Manufacturing* **121**, 308. ISSN: 1359-835X. doi:10.1016/J.COMPOSITESA.2019.03.035 (2019).
52. Sutcliffe, M. P., Lemanski, S. L. & Scott, A. E. Measurement of fibre waviness in industrial composite components. *Composites Science and Technology* **72**, 2016. ISSN: 02663538. doi:10.1016/j.compscitech.2012.09.001 (2012).
53. Safdar, N., Daum, B., Scheffler, S. & Rolfes, R. Experimental determination of a probabilistic failure envelope for carbon fiber reinforced polymers under combined compression–shear loads. *International Journal of Solids and Structures* **244–245**, 111585. ISSN: 00207683. doi:10.1016/j.ijsolstr.2022.111585 (2022).
54. Safdar, N. *A stochastic failure investigation of composites under combined compression-shear loads* PhD thesis (Leibniz University Hannover, 2022). doi:10.15488/12829.

55. Safdar, N., Daum, B. & Rolfes, R. A numerical prediction of failure probability under combined compression-shear loading for unidirectional fiber reinforced composites. *Mechanics of Materials* **171**, 104352. ISSN: 01676636. doi:10.1016/j.mechmat.2022.104352 (2022).
56. Daum, B., Gottlieb, G., Safdar, N., Brod, M., Ohlendorf, J. H. & Rolfes, R. A numerical investigation of the statistical size effect in non-crimp fabric laminates under homogeneous compressive loads. *Journal of Composite Materials* **56**, 665. ISSN: 1530793X. doi:10.1177/00219983211057346 (2022).
57. Papadopoulos, V. & Papadrakakis, M. The effect of material and thickness variability on the buckling load of shells with random initial imperfections. *Computer Methods in Applied Mechanics and Engineering* **194**, 1405. ISSN: 00457825. doi:10.1016/j.cma.2004.01.043 (2005).
58. Koiter, W. T. *Over de stabiliteit van het elastisch evenwicht* PhD thesis (Delft University of Technology, 1945).
59. Calladine, C. R. Understanding imperfection-sensitivity in the buckling of thin-walled shells. *Thin-Walled Structures* **23**, 215. ISSN: 02638231. doi:10.1016/0263-8231(95)00013-4 (1995).
60. Jansen, E. *The influence of initial geometric imperfections on composite shell stability and vibrations* 509. ISBN: 9780081004296. doi:10.1016/B978-0-08-100410-4.00010-7 (Elsevier Ltd, 2017).
61. Meurer, A. D. *Filtering Geometric Imperfection patterns for analysis and design of composite shell structures* PhD thesis (Gottfried Wilhelm Leibniz Universität Hannover, 2017). doi:10.15488/9026.
62. Singer, J. & Abramovich, H. The development of shell imperfection measurement techniques. *Thin-Walled Structures* **23**, 379. ISSN: 02638231. doi:10.1016/0263-8231(95)94361-V (1995).
63. Degenhardt, R., Kling, A., Bethge, A., Orf, J., Kärger, L., Zimmermann, R., Rohwer, K. & Calvi, A. Investigations on imperfection sensitivity and deduction of improved knock-down factors for unstiffened CFRP cylindrical shells. *Composite Structures* **92**, 1939. ISSN: 02638223. doi:10.1016/j.compstruct.2009.12.014 (2010).
64. Hilburger, M. W. & Starnes, J. H. Effects of imperfections of the buckling response of composite shells. *Thin-Walled Structures* **42**, 369. ISSN: 02638231. doi:10.1016/j.tws.2003.09.001 (2004).

65. Lyssakow, P., Friedrich, L., Krause, M., Dafnis, A. & Schröder, K. U. Contactless geometric and thickness imperfection measurement system for thin-walled structures. *Measurement: Journal of the International Measurement Confederation* **150**, 107038. ISSN: 02632241. doi:10.1016/j.measurement.2019.107038 (2020).
66. Zhao, X., Tootkaboni, M. & Schafer, B. W. Development of a Laser-Based Geometric Imperfection Measurement Platform with Application to Cold-Formed Steel Construction. *Experimental Mechanics* **55**, 1779. ISSN: 17412765. doi:10.1007/s11340-015-0072-7 (2015).
67. Arbocz, J. & Abramovich, H. *The initial imperfection data bank at the Delft University of Technology: Part I* 1979.
68. Dancy, R. & Jacobs, D. *The initial imperfection data bank at the Delft University of Technology: Part II. DELFT University of Technology* (1988).
69. Singer, J., Arbocz, J. & Babcock, C. D. Buckling of imperfect stiffened cylindrical shells under axial compression. *AIAA Journal* **9**, 68. ISSN: 00011452. doi:10.2514/3.6125 (1971).
70. Vries, J. D. *The Imperfection Data Bank and its Applications* 190. ISBN: 9789088920127 (2009).
71. Timoshenko, S. P. *History of Strength of Materials* ISBN: 9780486611877 (McGraw-Hill, 1953).
72. Haldar, A. & Mahadevan, S. *Reliability assessment using stochastic finite element analysis* (John Wiley & Sons, 2000).
73. Králik, J. *Reliability Analysis of Structures Using Stochastic Finite Element Method* tech. rep. (Slovak University of Technology, 2009). doi:10.13140/2.1.4900.9924.
74. Ching, J. Equivalence between reliability and factor of safety. *Probabilistic Engineering Mechanics* **24**, 159. ISSN: 02668920. doi:10.1016/j.probengmech.2008.04.004 (2009).
75. Wang, X., Shi, Q., Fan, W., Wang, R. & Wang, L. Comparison of the reliability-based and safety factor methods for structural design. *Applied Mathematical Modelling* **72**, 68. ISSN: 0307904X. doi:10.1016/j.apm.2019.03.018 (2019).
76. Tinsley Oden, J., Belytschko, T., Babuska, I. & Hughes, T. J. Research directions in computational mechanics. *Computer Methods in Applied Mechanics and Engineering* **192**, 913. ISSN: 00457825. doi:10.1016/S0045-7825(02)00616-3 (2003).

77. Der Kiureghian, A. & Ke, J.-B. The stochastic finite element method in structural reliability. *Probabilistic Engineering Mechanics* **3**, 83. ISSN: 02668920. doi:10.1016/0266-8920(88)90019-7 (1988).
78. Sudret, B. & Kiureghian, A. D. Stochastic Finite Element Methods and Reliability: A State-of-the-Art Report. *University of California Berkeley*, 189 (2000).
79. Stefanou, G. The stochastic finite element method: Past, present and future. *Computer Methods in Applied Mechanics and Engineering* **198**, 1031. ISSN: 00457825. doi:10.1016/j.cma.2008.11.007 (2009).
80. Arregui-Mena, J. D., Margetts, L. & Mummery, P. M. Practical Application of the Stochastic Finite Element Method. *Archives of Computational Methods in Engineering* **23**, 171. ISSN: 18861784. doi:10.1007/s11831-014-9139-3 (2016).
81. Papadopoulos, V. & Giovanis, D. G. *Stochastic Finite Element Methods* ISBN: 978-3-319-64527-8. doi:10.1007/978-3-319-64528-5 (Springer International Publishing, 2018).
82. Courant, R. *et al.* Variational methods for the solution of problems of equilibrium and vibrations. *Lecture notes in pure and applied mathematics* **49**, 1. ISSN: 1063651X. doi:10.1103/PhysRevE.67.016108 (1943).
83. Turner, M. J., Clough, R. W., Martin, H. C. & Topp, L. J. Stiffness and Deflection Analysis of Complex Structures. *Journal of the Aeronautical Sciences* **23**, 805. doi:10.2514/8.3664 (1956).
84. Clough, R. W. The finite element method after twenty-five years: A personal view. *Computers and Structures* **12**, 361. ISSN: 00457949. doi:10.1016/0045-7949(80)90113-3 (1980).
85. Cook, R. D., Malkus, D. S., Plesha, M. E. & Witt, R. J. *Concepts and applications of finite element analysis* Fourth edi. ISBN: 978-0-471-35605-9 (Wiley New York, 2002).
86. Vanmarcke, E. *Random Fields* 382. ISBN: 978-981-256-297-5. doi:10.1142/5807 (World Scientific, 2010).
87. Spanos, P. D. & Zeldin, B. A. Monte Carlo Treatment of Random Fields: A Broad Perspective. *Applied Mechanics Reviews* **51**, 219. ISSN: 0003-6900. doi:10.1115/1.3098999 (1998).
88. Liu, Y., Li, J., Sun, S. & Yu, B. Advances in Gaussian random field generation: a review. *Computational Geosciences* **23**, 1011. ISSN: 15731499. doi:10.1007/s10596-019-09867-y (2019).

89. Dekking, F. M., Kraaikamp, C., Lopuhaä, H. P. & Meester, L. E. *A Modern Introduction to Probability and Statistics: Understanding why and how* ISBN: 9781846281686. doi:10.1007/1-84628-168-7 (Springer Science & Business Media, 2005).
90. Abrahamsen, P. *A review of Gaussian Random Fields and Correlation Functions* 2nd editio. doi:10.13140/RG.2.2.23937.20325 (1997).
91. Ghanem, R. G. & Spanos, P. D. *Stochastic Finite Elements: A Spectral Approach* 222. ISBN: 978-1-4612-7795-8. doi:10.1007/978-1-4612-3094-6 (Springer-Verlag New York, 1991).
92. Lauterbach, S., Fina, M. & Wagner, W. Influence of stochastic geometric imperfections on the load-carrying behaviour of thin-walled structures using constrained random fields. *Computational Mechanics* **62**, 1107. ISSN: 01787675. doi:10.1007/s00466-018-1554-0 (2018).
93. Spanos, P. D. & Ghanem, R. G. Stochastic Finite element expansion for random media. *Journal of Engineering Mechanics* **115**, 1035. ISSN: 0733-9399. doi:10.1061/(ASCE)0733-9399(1989)115:5(1035) (1989).
94. Betz, W., Papaioannou, I. & Straub, D. Numerical methods for the discretization of random fields by means of the Karhunen–Loève expansion. *Computer Methods in Applied Mechanics and Engineering* **271**, 109. ISSN: 00457825. doi:10.1016/j.cma.2013.12.010 (2014).
95. Latz, J., Eisenberger, M. & Ullmann, E. Fast sampling of parameterised Gaussian random fields. *Computer Methods in Applied Mechanics and Engineering* **348**, 978. ISSN: 00457825. doi:10.1016/j.cma.2019.02.003 (2019).
96. Davis, M. W. Production of conditional simulations via the LU triangular decomposition of the covariance matrix. *Mathematical Geology* **19**, 91. ISSN: 08828121. doi:10.1007/BF00898189 (1987).
97. Willoughby, R. A. Compact Numerical Methods for Computers: Linear Algebra and Function Minimization (J. C. Nash). *SIAM Review* **23**, 124. ISSN: 0036-1445. doi:10.1137/1023031 (1981).
98. Van der Have, R. *Random Fields for Non-Linear Finite Element Analysis of Reinforced Concrete* 2015.
99. Vořechovský, M. & Novák, D. Simulation of random fields for stochastic finite element analysis. *Icossar*, 2545 (2005).

100. Dietrich, C. R. & Newsam, G. N. Efficient generation of conditional simulations by chebyshev matrix polynomial approximations to the symmetric square root of the covariance matrix. *Mathematical Geology* **27**, 207. ISSN: 08828121. doi:10.1007/BF02083211 (1995).
101. Graham, I. G., Kuo, F. Y., Nuyens, D., Scheichl, R. & Sloan, I. H. Analysis of Circulant Embedding Methods for Sampling Stationary Random Fields. *SIAM Journal on Numerical Analysis* **56**, 1871. ISSN: 0036-1429. doi:10.1137/17M1149730 (2018).
102. Park, M. & Tret'yakov, M. V. A block circulant embedding method for simulation of stationary gaussian random fields on block-regular grids. *International Journal for Uncertainty Quantification* **5**, 527. ISSN: 21525099. doi:10.1615/Int.J.UncertaintyQuantification.2015013781 (2015).
103. Feischl, M., Kuo, F. Y. & Sloan, I. H. *Fast random field generation with H-matrices* **3**, 639. ISBN: 0021101809. doi:10.1007/s00211-018-0974-2 (Springer Berlin Heidelberg, 2018).
104. Blanchard, P., Coulaud, O. & Darve, E. *Fast hierarchical algorithms for generating Gaussian random fields* tech. rep. (Inria Bordeaux Sud-Ouest, 2015).
105. Shinozuka, M. & Deodatis, G. Simulation of stochastic processes by spectral representation. *Applied Mechanics Reviews* **44**, 191. ISSN: 00036900. doi:10.1115/1.3119501 (1991).
106. Shinozuka, M. & Deodatis, G. Simulation of multi-dimensional Gaussian stochastic fields by spectral representation. *Applied Mechanics Reviews* **49**, 29. ISSN: 00036900. doi:10.1115/1.3101883 (1996).
107. Fenton, G. A. *Simulation and Analysis of Random Fields* PhD thesis (1990), 189.
108. Fenton, G. A. Error Evaluation of Three Random-Field Generators. *Journal of Engineering Mechanics* **120**, 2478. ISSN: 0733-9399. doi:10.1061/(ASCE)0733-9399(1994)120:12(2478) (1994).
109. Emery, X., Furrer, R. & Porcu, E. A turning bands method for simulating isotropic Gaussian random fields on the sphere. *Statistics and Probability Letters* **144**, 9. ISSN: 01677152. doi:10.1016/j.spl.2018.07.017 (2019).

110. Mantoglou, A. & Wilson, J. L. The Turning Bands Method for simulation of random fields using line generation by a spectral method. *Water Resources Research* **18**, 1379. ISSN: 19447973. doi:10.1029/WR018i005p01379 (1982).
111. Oliver, D. S. Moving averages for Gaussian simulation in two and three dimensions. *Mathematical Geology* **27**, 939. ISSN: 08828121. doi:10.1007/BF02091660 (1995).
112. Fenton, G. A. & Vanmarcke, E. H. Simulation of Random Fields via Local Average Subdivision. *Journal of Engineering Mechanics* **116**, 1733. ISSN: 0733-9399. doi:10.1061/(ASCE)0733-9399(1990)116:8(1733) (1990).
113. Fenton, G. A. & Griffiths, D. in *Probabilistic Methods in Geotechnical Engineering* 201 (Springer Vienna, Vienna, 2007). doi:10.1007/978-3-211-73366-0_9.
114. Li, C.-C. & Der Kiureghian, A. Optimal discretization of random fields. *Journal of engineering mechanics* **119**, 1136. doi:10.1061/(ASCE)0733-9399(1993)119:6(1136) (1993).
115. Zeldin, B. A. & Spanos, P. D. On random field discretization in stochastic finite elements. *Journal of Applied Mechanics, Transactions ASME* **65**, 320. ISSN: 15289036. doi:10.1115/1.2789057 (1998).
116. Allaix, D. L. & Carbone, V. I. Discretization of 2D random fields: A genetic algorithm approach. *Engineering Structures* **31**, 1111. ISSN: 01410296. doi:10.1016/j.engstruct.2009.01.008 (2009).
117. Vanmarcke, E. & Grigoriu, M. Stochastic Finite Element Analysis of Simple Beams. *Journal of Engineering Mechanics* **109**, 1203. ISSN: 0733-9399. doi:10.1061/(asce)0733-9399(1983)109:5(1203) (1983).
118. Matthies, H. G., Brenner, C. E., Bucher, C. G. & Guedes Soares, C. Uncertainties in probabilistic numerical analysis of structures and solids-Stochastic finite elements. *Structural Safety* **19**, 283. ISSN: 01674730. doi:10.1016/S0167-4730(97)00013-1 (1997).
119. Jha, S. K., Ching, J. & Asce, M. Simulating Spatial Averages of Stationary Random Field Using the Fourier Series Method. *Journal of Engineering Mechanics* **139**, 594. doi:10.1061/(ASCE)EM.1943-7889.0000517. (2013).

120. Papadrakakis, M. & Papadopoulos, V. Robust and efficient methods for stochastic finite element analysis using Monte Carlo simulation. *Computer Methods in Applied Mechanics and Engineering* **134**, 325. ISSN: 00457825. doi:10.1016/0045-7825(95)00978-7 (1996).
121. Schuëller, G. I. Developments in stochastic structural mechanics. *Archive of Applied Mechanics* **75**, 755. ISSN: 09391533. doi:10.1007/s00419-006-0067-z (2006).
122. Schuëller, G. I., Pradlwarter, H. J. & Koutsourelakis, P. S. A critical appraisal of reliability estimation procedures for high dimensions. *Probabilistic Engineering Mechanics* **19**, 463. ISSN: 02668920. doi:10.1016/j.probengmech.2004.05.004 (2004).
123. Helton, J. C. & Davis, F. J. Latin hypercube sampling and the propagation of uncertainty in analyses of complex systems. *Reliability Engineering and System Safety* **81**, 23. ISSN: 09518320. doi:10.1016/S0951-8320(03)00058-9 (2003).
124. Koutsourelakis, P. S., Pradlwarter, H. J. & Schuëller, G. I. Reliability of structures in high dimensions, part I: Algorithms and applications. *Probabilistic Engineering Mechanics* **19**, 409. ISSN: 02668920. doi:10.1016/j.probengmech.2004.05.001 (2004).
125. Papadimitriou, C., Katafygiotis, L. S. & Beck, J. L. Approximate analysis of response variability of uncertain linear systems. *Probabilistic Engineering Mechanics* **10**, 251. ISSN: 02668920. doi:10.1016/0266-8920(95)00020-8 (1995).
126. Kriegesmann, B., Rolfes, R., Hühne, C. & Kling, A. Fast probabilistic design procedure for axially compressed composite cylinders. *Composite Structures* **93**, 3140. ISSN: 02638223. doi:10.1016/j.compstruct.2011.06.017 (2011).
127. Kriegesmann, B. *Probabilistic design of thin-walled fiber composite structures* PhD thesis (Leibniz Universität Hannover, 2012), 163. doi:10.15488/7891.
128. Kriegesmann, B., Rolfes, R., Jansen, E. L., Elishakoff, I., Hühne, C. & Kling, A. Design optimization of composite cylindrical shells under uncertainty. *Computers, Materials and Continua* **32**, 177. ISSN: 15462218. doi:10.3970/cmcc.2012.032.177 (2012).

129. Kriegesmann, B., Jansen, E. L. & Rolfes, R. Semi-analytic probabilistic analysis of axially compressed stiffened composite panels. *Composite Structures* **94**, 654. ISSN: 02638223. doi:10.1016/j.compstruct.2011.08.033 (2012).
130. Wiener, N. The Homogeneous Chaos. *American Journal of Mathematics* **60**, 897. ISSN: 00029327. doi:10.2307/2371268 (1938).
131. Jha, D. K., Kant, T. & Singh, R. K. A critical review of recent research on functionally graded plates. *Composite Structures* **96**, 833. ISSN: 02638223. doi:10.1016/j.compstruct.2012.09.001 (2013).
132. Sobczak, J. J. & Drenchev, L. B. *Metal Based Functionally Graded Materials* (eds J. Sobczak, J. & B. Drenchev, L.) ISBN: 9781608050383. doi:10.2174/97816080503831090101 (BENTHAM SCIENCE PUBLISHERS, 2009).
133. Ford, R. G. *Functionally gradient materials, design, process, and applications* 330. ISBN: 9780412607608 (1999).
134. Saleh, B., Jiang, J., Fathi, R., Al-hababi, T., Xu, Q., Wang, L., Song, D. & Ma, A. 30 Years of functionally graded materials: An overview of manufacturing methods, Applications and Future Challenges. *Composites Part B: Engineering* **201**, 108376. ISSN: 13598368. doi:10.1016/j.compositesb.2020.108376 (2020).
135. Mortensen, A. & Suresh, S. Functionally graded metals and metal-ceramic composites: Part 1 processing. *International Materials Reviews* **40**, 239. ISSN: 17432804. doi:10.1179/imr.1995.40.6.239 (1995).
136. Zhang, C., Chen, F., Huang, Z., Jia, M., Chen, G., Ye, Y., Lin, Y., Liu, W., Chen, B., Shen, Q., Zhang, L. & Lavernia, E. J. Additive manufacturing of functionally graded materials: A review. *Materials Science and Engineering A* **764**, 138209. ISSN: 09215093. doi:10.1016/j.msea.2019.138209 (2019).
137. Yin, H. M., Sun, L. Z. & Paulino, G. H. Micromechanics-based elastic model for functionally graded materials with particle interactions. *Acta Materialia* **52**, 3535. ISSN: 13596454. doi:10.1016/j.actamat.2004.04.007 (2004).
138. Lozano, G. G., Tiwari, A., Turner, C. & Astwood, S. A review on design for manufacture of variable stiffness composite laminates. *Proceedings of the Institution of Mechanical Engineers, Part B: Journal of Engineering Manufacture* **230**, 981. ISSN: 20412975. doi:10.1177/0954405415600012 (2016).

139. Gurdal, Z. & Olmedo, R. In-plane response of laminates with spatially varying fiber orientations - Variable stiffness concept. *AIAA Journal* **31**, 751. ISSN: 0001-1452. doi:10.2514/3.11613 (1993).
140. Khani, A., Ijsselmuiden, S. T., Abdalla, M. M. & Gürdal, Z. Design of variable stiffness panels for maximum strength using lamination parameters. *Composites Part B: Engineering* **42**, 546. ISSN: 13598368. doi:10.1016/j.compositesb.2010.11.005 (2011).
141. Gürdal, Z., Tatting, B. F. & Wu, C. K. Variable stiffness composite panels: Effects of stiffness variation on the in-plane and buckling response. *Composites Part A: Applied Science and Manufacturing* **39**, 911. ISSN: 1359835X. doi:10.1016/j.compositesa.2007.11.015 (2008).
142. Wu, Z., Raju, G. & Weaver, P. M. Postbuckling analysis of variable angle tow composite plates. *International Journal of Solids and Structures* **50**, 1770. ISSN: 00207683. doi:10.1016/j.ijsolstr.2013.02.001 (2013).
143. Coburn, B. H., Wu, Z. & Weaver, P. M. Buckling analysis of stiffened variable angle tow panels. *Composite Structures* **111**, 259. ISSN: 02638223. doi:10.1016/j.compstruct.2013.12.029 (2014).
144. Haldar, A., Reinoso, J., Jansen, E. & Rolfes, R. Thermally induced multistable configurations of variable stiffness composite plates: Semi-analytical and finite element investigation. *Composite Structures* **183**, 161. ISSN: 02638223. doi:10.1016/j.compstruct.2017.02.014 (2018).
145. Haldar, A., Groh, R. M., Jansen, E., Weaver, P. M. & Rolfes, R. An efficient semi-analytical framework to tailor snap-through loads in bistable variable stiffness laminates. *International Journal of Solids and Structures* **195**, 91. ISSN: 00207683. doi:10.1016/j.ijsolstr.2020.02.018 (2020).
146. Lincoln, R. L., Weaver, P. M., Pirrera, A. & Groh, R. M. Imperfection-insensitive continuous tow-sheared cylinders. *Composite Structures* **260**, 113445. ISSN: 02638223. doi:10.1016/j.compstruct.2020.113445 (2021).
147. Nguyen, H. D., Hoang, V. N. & Jang, G. W. Moving morphable patches for three-dimensional topology optimization with thickness control. *Computer Methods in Applied Mechanics and Engineering* **368**, 113186. ISSN: 00457825. doi:10.1016/j.cma.2020.113186 (2020).

148. Townsend, S. & Kim, H. A. A level set topology optimization method for the buckling of shell structures. *Structural and Multidisciplinary Optimization* **60**, 1783. ISSN: 16151488. doi:10.1007/s00158-019-02374-9 (2019).
149. Steltner, K., Kriegesmann, B. & Pedersen, C. B. Robust sizing optimization of stiffened panels subject to geometric imperfections using fully nonlinear postbuckling analyses. *Thin-Walled Structures* **175**, 109195. ISSN: 02638231. doi:10.1016/j.tws.2022.109195 (2022).
150. Cox, B. S., Groh, R. M. & Pirrera, A. Nudging Axially Compressed Cylindrical Panels Toward Imperfection Insensitivity. *Journal of Applied Mechanics, Transactions ASME* **86**. ISSN: 15289036. doi:10.1115/1.4043284 (2019).
151. Minera, S., Patni, M., Pirrera, A. & Weaver, P. Buckling-resistant topological design using sensitivities to variations in localised nominal stiffness. *Thin-Walled Structures* **167**, 108150. ISSN: 02638231. doi:10.1016/j.tws.2021.108150 (2021).
152. Minera, S. *Analysis and Design of Buckling Resistant Thin-Walled Structures via Computationally Efficient 3D Stress Analysis* PhD thesis (University of Bristol, 2019), 230.
153. Doltsinis, I. & Kang, Z. Robust design of structures using optimization methods. *Computer Methods in Applied Mechanics and Engineering* **193**, 2221. ISSN: 00457825. doi:10.1016/j.cma.2003.12.055 (2004).
154. Yao, W., Chen, X., Luo, W., Van Tooren, M. & Guo, J. Review of uncertainty-based multidisciplinary design optimization methods for aerospace vehicles. *Progress in Aerospace Sciences* **47**, 450. ISSN: 03760421. doi:10.1016/j.paerosci.2011.05.001 (2011).
155. Papadopoulos, V. & Papadrakakis, M. Finite-element analysis of cylindrical panels with random initial imperfections. *Journal of Engineering Mechanics* **130**, 867. ISSN: 07339399. doi:10.1061/(ASCE)0733-9399(2004)130:8(867) (2004).
156. Papadopoulos, V. & Iglisis, P. The effect of non-uniformity of axial loading on the buckling behaviour of shells with random imperfections. *International Journal of Solids and Structures* **44**, 6299. ISSN: 00207683. doi:10.1016/j.ijsolstr.2007.02.027 (2007).

157. Papadopoulos, V., Stefanou, G. & Papadrakakis, M. Buckling analysis of imperfect shells with stochastic non-Gaussian material and thickness properties. *International Journal of Solids and Structures* **46**, 2800. ISSN: 00207683. doi:10.1016/j.ijso1str.2009.03.006 (2009).
158. Shang, S. & Yun, G. J. Stochastic finite element with material uncertainties: Implementation in a general purpose simulation program. *Finite Elements in Analysis and Design* **64**, 65. ISSN: 0168874X. doi:10.1016/j.finel.2012.10.001 (2013).
159. Do, D. M., Gao, K., Yang, W. & Li, C. Q. Hybrid uncertainty analysis of functionally graded plates via multiple-imprecise-random-field modelling of uncertain material properties. *Computer Methods in Applied Mechanics and Engineering* **368**, 113116. ISSN: 00457825. doi:10.1016/j.cma.2020.113116 (2020).
160. Scarth, C., Adhikari, S., Cabral, P. H., Silva, G. H. & Prado, A. P. d. Random field simulation over curved surfaces: Applications to computational structural mechanics. *Computer Methods in Applied Mechanics and Engineering* **345**, 283. ISSN: 00457825. doi:10.1016/j.cma.2018.10.026 (2019).
161. Pagani, A. & Sanchez-Majano, A. R. Stochastic stress analysis and failure onset of variable angle tow laminates affected by spatial fibre variations. *Composites Part C: Open Access* **4**, 100091. ISSN: 2666-6820. doi:https://doi.org/10.1016/j.jcomc.2020.100091 (2021).
162. Balokas, G., Czichon, S. & Rolfes, R. Neural network assisted multiscale analysis for the elastic properties prediction of 3D braided composites under uncertainty. *Composite Structures* **183**, 550. ISSN: 02638223. doi:10.1016/j.compstruct.2017.06.037 (2018).
163. Balokas, G., Kriegesmann, B., Czichon, S. & Rolfes, R. Stochastic modeling techniques for textile yarn distortion and waviness with 1D random fields. *Composites Part A: Applied Science and Manufacturing* **127**. ISSN: 1359835X. doi:10.1016/j.compositesa.2019.105639 (2019).
164. Balokas, G., Kriegesmann, B. & Rolfes, R. Data-driven inverse uncertainty quantification in the transverse tensile response of carbon fiber reinforced composites. *Composites Science and Technology* **211**, 108845. ISSN: 02663538. doi:10.1016/j.compscitech.2021.108845 (2021).

165. Balokas, G., Kriegesmann, B., Czichon, S. & Rolfes, R. A variable-fidelity hybrid surrogate approach for quantifying uncertainties in the nonlinear response of braided composites. *Computer Methods in Applied Mechanics and Engineering* **381**, 113851. ISSN: 00457825. doi:10.1016/j.cma.2021.113851 (2021).
166. Schenk, C. A. & Schuëller, G. I. Buckling analysis of cylindrical shells with random geometric imperfections. *International Journal of Non-Linear Mechanics* **38**, 1119. ISSN: 00207462. doi:10.1016/S0020-7462(02)00057-4 (2003).
167. Schenk, C. A. & Schuëller, G. I. Buckling analysis of cylindrical shells with cutouts including random boundary and geometric imperfections. *Computer Methods in Applied Mechanics and Engineering* **196**, 3424. ISSN: 00457825. doi:10.1016/j.cma.2007.03.014 (2007).
168. Alfano, M. & Bisagni, C. Probability-based methodology for buckling investigation of sandwich composite shells with and without cut-outs. *International Journal of Computational Methods in Engineering Science and Mechanics* **18**, 77. ISSN: 15502295. doi:10.1080/15502287.2016.1276353 (2017).
169. Schillinger, D., Papadopoulos, V., Bischoff, M. & Papadrakakis, M. Buckling analysis of imperfect I-section beam-columns with stochastic shell finite elements. *Computational Mechanics* **46**, 495. ISSN: 01787675. doi:10.1007/s00466-010-0488-y (2010).
170. Papadopoulos, V., Soimiris, G. & Papadrakakis, M. Buckling analysis of I-section portal frames with stochastic imperfections. *Engineering Structures* **47**, 54. ISSN: 01410296. doi:10.1016/j.engstruct.2012.09.009 (2013).
171. Vryzidis, I., Stefanou, G. & Papadopoulos, V. Stochastic stability analysis of steel tubes with random initial imperfections. *Finite Elements in Analysis and Design* **77**, 31. ISSN: 0168874X. doi:10.1016/j.finel.2013.09.002 (2013).
172. Fina, M., Weber, P. & Wagner, W. Polymorphic uncertainty modeling for the simulation of geometric imperfections in probabilistic design of cylindrical shells. *Structural Safety* **82**, 101894. ISSN: 0167-4730. doi:10.1016/J.STRUSAFE.2019.101894 (2020).

173. Kriegesmann, B., Rolfes, R., Hühne, C., Teßmer, J. & Arbocz, J. Probabilistic Design of Axially Compressed Composite Cylinders With Geometric and Loading Imperfections. *International Journal of Structural Stability and Dynamics* **10**, 623. ISSN: 0219-4554. doi:10.1142/S0219455410003658 (2010).
174. Meurer, A., Kriegesmann, B., Dannert, M. & Rolfes, R. Probabilistic perturbation load approach for designing axially compressed cylindrical shells. *Thin-Walled Structures* **107**, 648. ISSN: 02638231. doi:10.1016/j.tws.2016.07.021 (2016).
175. Chen, G., Zhang, H., Rasmussen, K. J. & Fan, F. Modeling geometric imperfections for reticulated shell structures using random field theory. *Engineering Structures* **126**, 481. ISSN: 01410296. doi:10.1016/j.engstruct.2016.08.008 (2016).
176. Stefanou, G., Savvas, D. & Papadrakakis, M. Stochastic finite element analysis of composite structures based on mesoscale random fields of material properties. *Computer Methods in Applied Mechanics and Engineering* **326**, 319. ISSN: 00457825. doi:10.1016/j.cma.2017.08.002 (2017).
177. Martins, J. R. R. A. & Ning, A. *Engineering Design Optimization* ISBN: 9781108980647. doi:10.1017/9781108980647 (Cambridge University Press, 2021).
178. Beyer, H. G. & Sendhoff, B. Robust optimization - A comprehensive survey. *Computer Methods in Applied Mechanics and Engineering* **196**, 3190. ISSN: 00457825. doi:10.1016/j.cma.2007.03.003 (2007).
179. Marczyk, J. Stochastic multidisciplinary improvement - Beyond optimization. *8th Symposium on Multidisciplinary Analysis and Optimization*. doi:10.2514/6.2000-4929 (2000).
180. Taguchi, G., Chowdhury, S. & Wu, Y. *Taguchi's Quality Engineering Handbook* 1. ISBN: 9780470258354. doi:10.1002/9780470258354 (2007).
181. Mourelatos, Z. P. & Liang, J. A methodology for trading-off performance and robustness under uncertainty. *Journal of Mechanical Design, Transactions of the ASME* **128**, 856. ISSN: 10500472. doi:10.1115/1.2202883 (2006).
182. Schuëller, G. I. & Jensen, H. A. Computational methods in optimization considering uncertainties - An overview. *Computer Methods in Applied Mechanics and Engineering* **198**, 2. ISSN: 00457825. doi:10.1016/j.cma.2008.05.004 (2008).

183. Spall, J. C. in *Handbook of Computational Statistics* 173 (Springer Berlin Heidelberg, Berlin, Heidelberg, 2012). ISBN: 9783642215513. doi:10.1007/978-3-642-21551-3_7.
184. Schevenels, M., Lazarov, B. S. & Sigmund, O. Robust topology optimization accounting for spatially varying manufacturing errors. *Computer Methods in Applied Mechanics and Engineering* **200**, 3613. ISSN: 00457825. doi:10.1016/j.cma.2011.08.006 (2011).
185. Lazarov, B. S., Wang, F. & Sigmund, O. Length scale and manufacturability in density-based topology optimization. *Archive of Applied Mechanics* **86**, 189. ISSN: 14320681. doi:10.1007/s00419-015-1106-4 (2016).
186. Lazarov, B. S., Schevenels, M. & Sigmund, O. Topology optimization with geometric uncertainties by perturbation techniques. *International Journal for Numerical Methods in Engineering* **90**, 1321. doi:10.1002/nme (2012).
187. Lazarov, B. S., Schevenels, M. & Sigmund, O. Topology optimization considering material and geometric uncertainties using stochastic collocation methods. *Structural and Multidisciplinary Optimization* **46**, 597. ISSN: 1615147X. doi:10.1007/s00158-012-0791-7 (2012).
188. Kharmanda, G., Olhoff, N., Mohamed, A. & Lemaire, M. Reliability-based topology optimization. *Structural and Multidisciplinary Optimization* **26**, 295. ISSN: 1615147X. doi:10.1007/s00158-003-0322-7 (2004).
189. Jansen, M., Lombaert, G. & Schevenels, M. Robust topology optimization of structures with imperfect geometry based on geometric nonlinear analysis. *Computer Methods in Applied Mechanics and Engineering* **285**, 452. ISSN: 00457825. doi:10.1016/j.cma.2014.11.028 (2015).
190. Crane, K., Weischedel, C. & Wardetzky, M. The Heat Method for Distance Computation. *Communications of the ACM* **60**, 90. ISSN: 0001-0782 (print), 1557-7317 (electronic). doi:0.1145/3131280 (2017).
191. Lazarov, B. S. & Sigmund, O. Filters in topology optimization based on Helmholtz-type differential equations. *International Journal for Numerical Methods in Engineering* **86**, 765. ISSN: 00295981. doi:10.1002/nme.3072 (2011).

192. Van den Broek, S., Jansen, E. & Rolfes, R. Efficient generation of geodesic random fields in finite elements with application to shell buckling. *Thin-Walled Structures* **179**, 109646. ISSN: 02638231. doi:10.1016/j.tws.2022.109646 (2022).
193. Van den Broek, S., Minera, S., Pirrera, A., Weaver, P. M., Jansen, E. & Rolfes, R. Enhanced deterministic performance of panels using stochastic variations of geometry and material. *AIAA Journal* **58**, 2307. ISSN: 00011452. doi:10.2514/1.J058962 (2020).
194. Van den Broek, S., Wolff, J., Scheffler, S., Hühne, C. & Rolfes, R. Improving the fatigue life of printed structures using stochastic variations. *Progress in Additive Manufacturing*. ISSN: 2363-9520. doi:10.1007/s40964-022-00296-5 (2022).
195. Van den Broek, S., Minera, S., Jansen, E. & Rolfes, R. Robust improvement of the asymmetric post-buckling behavior of a composite panel by perturbing fiber paths. *Composite Structures* **270**, 114011. ISSN: 02638223. doi:10.1016/j.compstruct.2021.114011 (2021).
196. Sun, Y., Hanhan, I., Sangid, M. D. & Lin, G. Predicting mechanical properties from microstructure images in fiber-reinforced polymers using convolutional neural networks. *arXiv*, 1. ISSN: 23318422. doi:10.48550/arXiv.2010.03675 (2020).
197. Giovanis, D. G. & Papadopoulos, V. Spectral representation-based neural network assisted stochastic structural mechanics. *Engineering Structures* **84**, 382. ISSN: 1873-7323. doi:10.1016/j.engstruct.2014.11.044 (2015).

CURRICULUM VITAE

PERSONAL DATA

Name Sander Friso van den Broek
Date of Birth May 26, 1987
Place of Birth Amsterdam, the Netherlands
Citizen of Netherlands & United States

EDUCATION

2006 – 2010 Hogeschool van Amsterdam,
Amsterdam, the Netherlands
Final degree: Bachelor of Engineering

2010 – 2013 Technische Universiteit Delft
Delft, the Netherlands
Final degree: Master of Science

2016 – 2023 Leibniz University Hannover
Hannover, Germany
Final degree: Doktor-Ingenieur

EMPLOYMENT

Jan 2014 – Jan 2016 R&D Engineer
*Allseas Engineering B.V.,
Delft, the Netherlands*

April 2016 – Sep 2020 Research Associate
*Leibniz University Hannover,
Hannover, Germany*

June 2021 – Research Associate
*University of Bristol,
Bristol, United Kingdom*

DISSEMINATION

Articles in peer-reviewed journals:

1. van den Broek, S., Jansen, E. & Rolfes, R. Efficient generation of geodesic random fields in finite elements with application to shell buckling. *Thin-Walled Structures* **179**, 109646. ISSN: 0263-8231. doi:10.1016/j.tws.2022.109646 (2022).
2. Van den Broek, S., Wolff, J., Scheffler, S., Hühne, C. & Rolfes, R. Improving the fatigue life of printed structures using stochastic variations. *Progress in Additive Manufacturing*. ISSN: 2363-9520. doi:10.1007/s40964-022-00296-5 (2022).
3. Van den Broek, S., Minera, S., Jansen, E. & Rolfes, R. Robust improvement of the asymmetric post-buckling behavior of a composite panel by perturbing fiber paths. *Composite Structures* **270**, 114011. ISSN: 02638223. doi:10.1016/j.compstruct.2021.114011 (2021).
4. Van den Broek, S., Minera, S., Pirrera, A., Weaver, P. M., Jansen, E. & Rolfes, R. Enhanced Deterministic Performance of Panels Using Stochastic Variations of Geometry and Material. *AIAA Journal*, **1**. ISSN: 0001-1452. doi:10.2514/1.J058962 (2020).

Book chapters:

5. Van den Broek, S., Minera, S., Jansen, E., Pirrera, A., Weaver, P. M. & Rolfes, R. in *Advances in Predictive Models and Methodologies for Numerically Efficient Linear and Nonlinear Analysis of Composites* (ed Petrolo, M.) 143 (Springer International Publishing, Cham, 2019). ISBN: 978-3-030-11969-0. doi:10.1007/978-3-030-11969-0_9.

Invited talks:

6. Van den Broek, S., Patni, M., Hii, A., Weaver, P., Greaves, P. & Pirrera, A. *Structural analysis of horizontal-axis wind turbine blades* Invited lecture. Jiangu, China: Jiangu University of Technology, 2023.

Conference contributions:

7. Van den Broek, S., Patni, M., Hii, A., Weaver, P., Greaves, P. & Pirrera, A. *Nonlinear Analysis of Wind Turbine Blades Using Finite Elements with Anisotropic Variable Kinematics* in *AIAA SCITECH 2023 Forum* (National Harbor, MD, USA, 2023). doi:10.2514/6.2023-1921.

8. Van den Broek, S., Patni, M., Hii, A., Greaves, P., Weaver, P. & Pirrera, A. *Three-dimensional Stress Fields in Tapered Laminated Composites with Internal Ply Drops* in *Proceedings of the 15th World Congress on Computational Mechanics* (Yokohama, Japan, 2022).
9. Van den Broek, S., Patni, M., Hii, A., Greaves, P., Weaver, P. & Pirrera, A. *Nonlinear 3D analysis of laminated composite structures using variable kinematics elements* in *Proceedings of the 8th European Congress on Computational Methods in Applied Sciences and Engineering* (Oslo, Norway, 2022).
10. Van den Broek, S., Minera, S., Pirrera, A., Weaver, P. M., Jansen, E. L. & Rolfes, R. *Enhanced Deterministic Performance of Panels Using Stochastic Variations of Geometric and Material Parameters* in *Proceedings of the 2019 AIAA Science and Technology Forum and Exposition* (San Diego, CA, USA, 2019). doi:10.2514/6.2019-0511.
11. Van den Broek, S., Jansen, E., Minera, S., Weaver, P. M. & Rolfes, R. *Effect of spatially varying material properties on the post-buckling behaviour of composite panels utilising geodesic stochastic fields* in *Proceedings of the 6th Aircraft Structural Design conference* (Bristol, United Kingdom, 2018).
12. Van den Broek, S., Jansen, E. L. & Rolfes, R. *Effect of random spatial stiffness variations on the post- buckling behavior of layered structures* in *Proceedings of the First International Conference on Mechanics of Advanced Materials and Structures* (Turin, Italy, 2018), 86.
13. Van den Broek, S., Jansen, E. L., Rahman, T. & Rolfes, R. *Post-buckling behavior of a composite panel with spatially varying stochastic material parameters using Koiter's initial post-buckling method* in *ICCS20 - 20th International Conference on Composite Structures* (Paris, France, 2017), 6.
14. Van den Broek, S., Jansen, E. L., Rahman, T. & Rolfes, R. *Effect of spatially varying stochastic material properties on the post- buckling behavior of composite panels using a reduced order model* in *ECCOMAS Thematic Conference on the Mechanical Response of Composites* (Eindhoven, the Netherlands, 2017).
15. Jansen, E. L., van den Broek, S. & Rolfes, R. *Modal Interaction and Mode Switching in Post- buckling Analysis of Plates Using a Multi-mode Finite Element Based Reduced Order Model* in *ICCS19 19th International Conference on Composite Structures* (Porto, Portugal, 2016), 162.

Reviewer for the following journals:

1. Composite Structures
2. Frontiers in Materials - Mechanics of Materials
3. Thin-Walled Structures

MITTEILUNGEN DES INSTITUTS FÜR STATIK UND
DYNAMIK DER LEIBNIZ UNIVERSITÄT HANNOVER

1	R. Rolfes/ C. Hühne	Eröffnungskolloquium (Tagungsband)	2005
2	H. Rothert/ M. Kaliske/ L. Nasdala	Entwicklung von Materialmodellen zur Alterung von Elastomerwerkstoffen unter besonderer Berücksichtigung des Sauerstoffeinflusses (DFG-Abschlußbericht)	2005
3	L. Nasdala	Simulation von Materialinelastizitäten bei Nano-, Mikro- und Makrostrukturen – Stabilitätsprobleme, Schädigungs- und Alterungsprozesse bei Kohlenstoffnanoröhren und Elastomerwerkstoffen (Habilitationsschrift)	2005
4	C. Hühne	Robuster Entwurf beulgefährdeter, unversteifter Kreiszyinderschalen aus Faserverbundwerkstoff (Dissertationsschrift)	2006
5	L. Nasdala/ K.-U. Schröder	Finite Element Applications in Structural Analysis (Skript zur Hörsaalübung)	2006
6		Klausuraufgabensammlung, 4. Auflage	2007
7	R. Rolfes/ W.-J. Gerasch/ D. Rotert	Vorlesung Tragwerksdynamik	2007
8	K.-H. Elmer/ K. Betke/ Th. Neumann	Standardverfahren zur Ermittlung und Bewertung der Belastung der Meeresumwelt durch die Schallimmission von Offshore-Windenergieanlagen (Abschlussbericht zum BMU-Forschungsvorhaben)	2007
9	K.-U. Schröder	Zur nichtlinearen Berechnung von Stahlbeton- und Verbundbauteilen (Dissertationsschrift)	2007
10	G. Ernst	Multiscale Analysis of Textile Composites – Stiffness and Strength (Dissertationsschrift)	2008
11	G. Haake	Systemidentifikation mit Autoregressiven Modellen und Validierung numerischer Strukturmodelle bei Offshore-Windenergieanlagen (Dissertationsschrift)	2010
12	T. Griefsmann	Dynamisches Tragverhalten von Stahlbetonbiegebalken im Experiment und in der Simulation (Dissertationsschrift)	2011

13	S. Zerbst	Global Approach for Early Damage Detection on Rotor Blades of Wind Energy Converters (Dissertationsschrift)	2011
14	N. Wieczorek	Semiaktive Schwingungsdämpfung leichter Fußgängerbrückenkonstruktionen (Dissertationsschrift)	2011
15	B. Kriegesmann	Probabilistic Design of Thin-Walled Fiber Composite Structures (Dissertationsschrift)	2012
16	J. Reetz	Schadensdiagnose an Tragstrukturen von Windenergieanlagen mit der Multiparameter-Eigenwertproblem-Methode (Dissertationsschrift)	2012
17	R. Rolfes/ D. Rotert	Vorlesung Baustatik	2012
18	R. Rolfes/ D. Rotert	Vorlesung Stabtragwerke	2012
19	H. Krüger	Ein physikalisch basiertes Ermüdungsschädigungsmodell zur Degradationsberechnung von Faser-Kunststoff-Verbunden (Dissertationsschrift)	2012
20	S. Czichon	Multi scale Failure Analysis of Fibre Reinforced Polymers with production induced Porosity Defects (Dissertationsschrift)	2013
21	T. Pahn	Inverse Load Calculation for Offshore Wind Turbines (Dissertationsschrift)	2013
22	M. Fricke/ B. Neddermann/ A. Lübben/ J. Gabriel	Realistische Hydroschallszenarien auf der Basis von Prognosemodellen und Monitoring für den Bau von Offshore-Windparks in der deutschen Nordsee („HyproWind“) (Abschlussbericht zum BMU-Forschungsvorhaben)	2014
23	M. Vogler	Anisotropic Material Models for Fiber Reinforced Polymers (Dissertationsschrift)	2014
24	M. Fricke	Ein physikalisch basiertes Gesamtmodell für hydroakustische Immissionsprognosen bei Offshore-Pfahlrammungen (Dissertationsschrift)	2015
25	M. Häckell	A holistic evaluation concept for long-term structural health monitoring (Dissertationsschrift)	2015
26	J. Rustemeier	Optimierung von Blasenschleiern zur Minderung von Unterwasser-Rammschall (Dissertationsschrift)	2016
27	S. Hühne	A two-way loose coupling procedure for buckling and damage analysis of composite structures (Dissertationsschrift)	2016
28	A. Meurer	Filtering Geometric Imperfection Patterns for Analysis and Design of Composite Shell Structures (Dissertationsschrift)	2017

29	A. Dean	Material Modeling of Short Fiber Reinforced Polymeric Composites: Theory, Numerical Aspects, and Applications (Dissertationsschrift)	2017
30	M. Bishara	Compressive Failure of Polymer Composites Including Fiber Kinking and Interaction of Failure Mechanisms (Dissertationsschrift)	2017
31	K. Schröder	Advanced Model Updating Strategies for Structural Dynamic Systems (Dissertationsschrift)	2018
32	S. Tsiapoki	Transmissibility-Based Monitoring and Combination of Damage Detection Decisions within a Holistic Structural Health Monitoring Framework (Dissertationsschrift)	2018
33	S. R. Nabavi	Failure analysis of polycrystalline silicon-based photovoltaic modules considering the effects of residual stresses and mechanical loading (Dissertationsschrift)	2018
34	S. Scheffler	Ein neuer Modellierungsansatz zur systematischen numerischen Untersuchung des Versagensverhaltens von Verbindungen in FVK (Dissertationsschrift)	2018
35	J. Häfele	A numerically efficient and holistic approach to design optimization of offshore wind turbine jacket substructures (Dissertationsschrift)	2019
36	C. Hübler	Efficient probabilistic analysis of offshore wind turbines based on time-domain simulations (Dissertationsschrift)	2019
37	M. Akterskaia	Global-local progressive failure analysis of composite panels including skin-stringer debonding and intralaminar damage (Dissertationsschrift)	2019
38	C. Gebhardt	Robust computational procedures for the nonlinear dynamic analysis of beam and shell structures (Habilitationsschrift)	2020
39	A. Haldar	Multistable morphing structures using variable stiffness laminates (Dissertationsschrift)	2020
40	R. Unger	Multi-scale constitutive modelling of nanoparticle/epoxy nanocomposites: Molecular simulation-based methods and experimental validation (Dissertationsschrift)	2020
41	J. Fankhänel	A Multi-Scale Framework for Nanocomposites including Interphase and Agglomeration Effects (Dissertationsschrift)	2020
42	N. Penner	Monitoring ambient angeregter baodynamischer Systeme durch mehrschichtige Perzeptren (Dissertationsschrift)	2021
43	C. Gerendt	A finite element-based continuum damage model for mechanical joints in fiber metal laminates under static and fatigue loading: Theory and experimental validation (Dissertationsschrift)	2022

44	M. Brod	Damage prediction of unidirectional fiber composites under cyclic loading with different amplitudes (Dissertationsschrift)	2022
45	R. Berger	Multi-Objective Structural Optimization of Repairs of Blisk Blades (Dissertationsschrift)	2022
46	G. Balokas	Metamodel-based uncertainty quantification for the mechanical behavior of braided composites (Dissertationsschrift)	2022
47	S. Wernitz	Damage Localization in Data-Driven Vibration-Based Structural Health Monitoring Using Linear Quadratic Estimation Theory (Dissertationsschrift)	2022
48	B. Daum	On the computational analysis of microbuckling via mesoscale approaches (Habilitationsschrift)	2022
49	N. Safdar	A Stochastic Failure Investigation of Composites under Combined Compression-Shear Loads (Dissertationsschrift)	2022
50	S. van den Broek	Tailoring Structures Using Stochastic Variations of Structural Parameters (Dissertationsschrift)	2023